Università
Ca'Foscari
Venezia

Graduate School

Dottorato di ricerca
in Scienze Chimiche
Ciclo XXIX
Anno di discussione 2016

Bismuth-based advanced luminescent (nano)materials: from design to application

SETTORE SCIENTIFICO DISCIPLINARE DI AFFERENZA: CHIM/02

Tesi di Dottorato di Michele Back, matricola 812891

Coordinatore del Dottorato	**Tutore del Dottorando**
Prof. Maurizio Selva	**Dr. Enrico Trave**

Contents

Abstract

Bismuth-based luminescent materials have been recognized as promising candidates for the design of next-generation phosphors, in virtue of the peculiar emission activity exhibited by Bi ions and the optical characteristics of Bi based hosts, together with technologically appealing properties like low toxicity and low costs. In this view, this thesis is focused on the synthesis and the characterization of novel bismuth-based oxide materials, proposing new strategies of control of the light emission through careful dopant selection and host band structure tailor. Therefore, the main research activity has been devoted on the optical characterization and, in particular, on the determination and modeling of the luminescence mechanisms characterizing the studied systems. With the aim to reliably describe the optical processes involved, a combined experimental and theoretical approach was considered. Moreover, in order to increase the efficiency and the manipulation of the emission response, the research has also focused on the optimization of the synthesis procedures and subsequent material processing for suitable structural modification.

One topic of this work concerns the possibility to use bismuth oxide-based nanoparticles (NPs) as upconverting photoluminescence (UC PL) nanophosphors, going deep inside the key parameters for the optimization of PL output control. We have investigated two families of NPs: (i) Bi_2O_3 NPs and (ii) bismuth silicate NPs. Regarding Bi_2O_3 UCNPs nanophospors, we have analyzed the Y^{3+} doping effect on the crystalline and band structures of the material, evidencing the possibility to finely control the bandgap of the oxide host in a wide range of energies. This bandgap engineering has been demonstrated to effectively affect the overall UC emission output of Er^{3+} ions, then determining a novel strategy for a careful tuning of the UC PL chromaticity. In addition, by Bi_2O_3 NPs codoping with Yb^{3+}-Ln^{3+} (Ln^{3+}=Er^{3+}, Ho^{3+}, Tm^{3+}) ions, together with a remarkable UC PL quantum yield estimates, a similar bandgap controlled emission selectivity was observed, and in the case of Yb-Tm pair this results in a NIR single band emission spectrum. Concerning bismuth silicates as host for UCNPs, we have proposed a new synthetic procedure based on wet impregnation of mesoporous silica nanoparticles

(MSNs), that allows the formation of a core-shell system, where the outer region consists in a glassy shell of dense silica and the core is built upon the stabilization of the metastable Bi_2SiO_5 phase. To figure out the formation process, the effect of both the bismuth loading into the MSNs and of the temperature were investigated, showing a concentration driven self-assembly mechanism. It was also demonstrated that the UC emission of the lanthanide-doped $Bi_2SiO_5@SiO_2$ systems can be tuned over the whole CIE diagram by carefully choosing the suitable doping ions and the relative concentrations.

Another theme addressed by this thesis consists in the development of a new ratiometric luminescent thermal sensor. The distortion of the Cr^{3+} site induced by the crystal field in $Bi_2Ga_4O_9$ (with stereochemically active Bi^{3+} lone pairs of electrons), has allowed to design a novel single-doped dual-NIR emitting thermometer with promising properties for applications in the biological field. To the best of our knowledge, this is the first example of Cr single-doped material used as thermal sensor.

Although in the past an intense research activity aimed to investigate the bismuth ions properties has been developed, nowadays many intriguing aspects are still unclear and under debate. Therefore, part of the research activity has been focused on the definition of guidelines for the design of new bismuth-activated phosphors. In particular, we have determined the critical parameters explaining the PL trend for the bismuth-doped perovskite-type $CaBO_3$ hosts (*B*=Ti,Sn,Zr). Regarding Bi-doped $CaSnO_3$, the simultaneous stabilization of Bi^{3+} and Bi^{2+} ions was achieved and the persistent luminescence (PersL) properties of the system were addressed, suggesting a PersL mechanism by means of the VRBE diagram construction.

Furthermore, it is well known that the performance of a luminescent species can be improved through an energy transfer process triggered by a suitable sensitizing agent, resulting in both enhanced absorption window and excitation cross section. In this regard, a new, simple and effective model for the estimation of the critical distance between donor and acceptor pairs in crystals was also proposed and checked for the Y_2O_3:Bi,Er system. An efficient energy transfer process between Bi^{3+} and Er^{3+} ions in Y_2O_3 nanocrystals was discussed and the spread of the Er^{3+} absorption window due to the Bi^{3+} ion in C_2 site was demonstrated.

Finally, due to the peculiar luminescent properties exhibited by the investigated materials, it is worth pointing out that interesting potentialities for applications like (nano)phosphors in the photonics field, biolabels, thermal sensors and anti-counterfeiting agents are expected.

CHAPTER 1

General Introduction

Abstract This thesis deals with the optical properties of novel bismuth-based luminescent materials for advanced photonic applications. The main aim is the investigation of the luminescence properties of bismuth-based materials in which bismuth can act as a constituent of the host or a luminescent center, developing new (nano)systems for emerging applications such as biological imaging and optical thermal sensing. In this context, we focused, from one hand, on the synthesis and the optimization of the optical systems and, on the other hand, on the deep chemical-physical characterization. An overall understanding of the optical properties is achieved by combining an experimental and theoretical approach, modelling the luminescent processes and designing the energy level diagrams of the systems.

1.1 New Frontiers for Inorganic Luminescent Materials

Nowadays light emitting materials have a big impact in our daily life, promoting an ongoing search for luminescent materials with new and ever more efficient optical properties. The development of new models for the prediction of the optical properties is a key point for the design of efficient materials. At the same time, new synthetic approaches are of fundamental importance for the discovery of new luminescent materials, with increasing attention to the development of low-toxicity materials.

Over the last two decades, aimed by the increasing ability in manipulate materials at the nanoscale, the development of luminescent nanomaterials has become an active research area. Luminescent nanomaterials can have advantages over bulk materials (*e.g.* tunability and possibility to form

transparent dispersions) opening the way for the application of inorganic luminescent materials in new fields such as biological imaging[1-3] and theranostic nanomedicine[2-4] but also anti-counterfeiting[1,5] and optical thermal sensing at the nanoscale.[6,7]

By designing luminescent phosphors for uses as optical probes in biological environments, a fundamental aspect to take into account for a deep-tissue penetration is the match of absorption and emission of the probes with the *biological optical transparency window* (650-1800 nm). This region (Figure 1.1) accounts for the absorption and scattering due to the different skin layers and can be divided into the three distinctive regions: the so-called first biological window (NIR-I) ranging from 650 to 950 nm, the second biological window (NIR-II) from 1000 to 1350 nm and the third biological window covering the 1550-1800 nm range (NIR-III).[8-11]

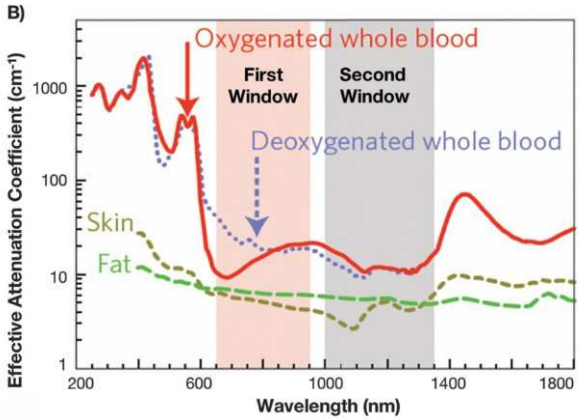

Figure 1.1 Effective attenuation coefficient (log scale) in the two first optical window in biological tissue and fluids (oxygenated and deoxygenated blood, skin and fatty tissue). From ref. 11.

Among the great variety of systems proposed for bio-imaging (*e.g.* QDs, polymers, nanodiamonds, dyes), rare-earth doped upconverting nanoparticles (UCNPs) have emerged as a new class of luminescent probes because of their ability to convert low-energy photons (usually NIR) into higher-energy photons *via* anti-Stokes process[1,12,13] (see Section 2.5.2). Based on UCNPs, multiphoton excited fluorescence microscopy allows deep tissue bioimaging minimizing background autofluorescence[14] without the need of intense coherent excitation sources. In fact, in contrast with conventional two-photon absorption processes that require excitation of 10^4-10^6 Wcm^{-2} as for quantum dots (QDs) and organic dyes, upconverting bioprobes are effectively excited by NIR diode lasers at 1 Wcm^{-2}.[3] Moreover, this class of nanoparticles has the advantage to allow multicolour emission tunability in a wide spectral range (Figure 1.2a), because of the characteristic emissions determined by the ladder-like energy level of each lanthanide ion and a relatively low cytotoxicity.

The big impact of this class of biolabels, has led to a massive effort aiming at optimizing the parameters to enhance the optical response, in virtue of a proper selection of both suitable (crystalline) host and luminescent ions with optical activity (absorption and emission) into the biological windows. For instance, Figure 1.2 shows the UC PL image of a mouse injected with

UC nanoparticles and a sketch of the NIR-to-NIR UC process for α-($NaYbF_4$:0.5% Tm^{3+})/CaF_2 core/shell nanosystem.[15] Moreover, the design of UC nanoparticles with selective NIR emission is highly demanding for multiplexing[16,17] (simultaneous detection of multiple targets with different probes).

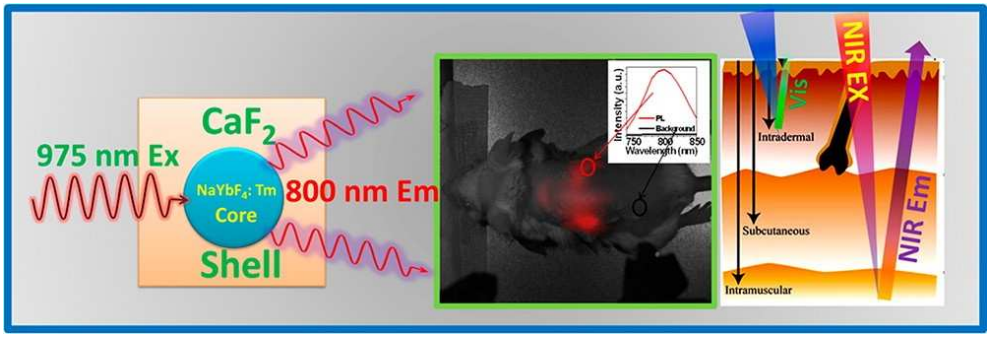

Figure1.2 Sketch of the potentialities of NIR-to-NIR UC nanoparticles for *in vivo* UC imaging of (α-$NaYF^4$:Tm^{3+})/CaF_2 core/shell NPs (from ref. 15).

In order to reduce energy losses via multiphonon relaxation and to maximize radiative emission, low phonon energy lattice hosts are usually chosen,[18] thus fluoride-based hosts[19-23] (*i.e.* $NaYF_4$, $NaGdF_4$, LaF_3, CaF_2, SrF_2) have been the most investigated hosts for upconverting nanoparticles. Furthermore, a critical role in the optical properties and efficiency of the upconverting processes is demonstrated to be played by the crystal field.[24-27] Recently, Wisser *et al.*[28] demonstrated the strong influence of the local symmetry distortion on the efficiency of the processes (Figure 1.3), increasing by a factor 1.6 the UC quantum yield of the unmodified β-$NaYF_4$ system by tailoring the structure with simultaneous Gd and Lu cooping (β-$NaY_{0.8-2x}Gd_xLu_xF_4$:$Yb_{0.18}Er_{0.02}$ system). In addition to fluorides, oxide hosts such as Y_2O_3 [29,30] and Gd_2O_2S [31,32] are also considered promising materials.

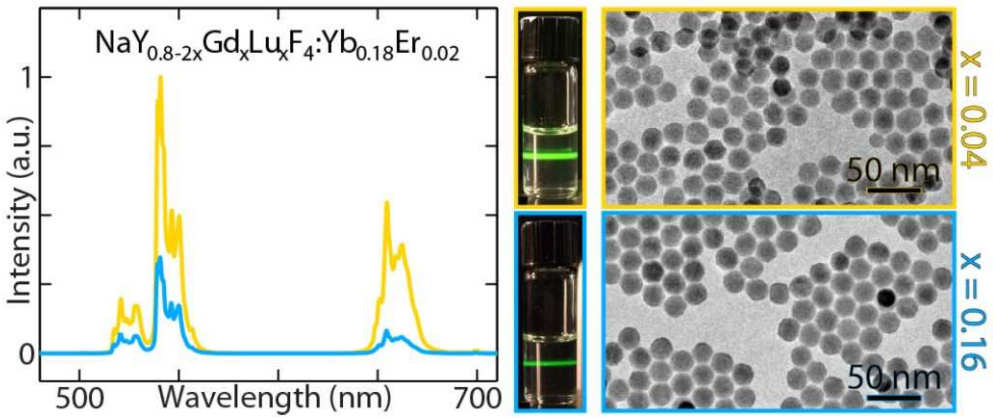

Figure 1.3 Enhancement effect of Gd and Lu codoping on β-$NaYF_4$:Yb,Er UC emission (from ref. 28).

The increasing knowledge on the key parameters and the design of new nanostructures (such as core-shell architectures) has led to very attractive results. However, the main drawback is that UC nanocrystals-based imaging in aqueous solutions still suffers from the significant cell death and tissue damage induced by the 980 nm excitation source. Hence, the solution of this problem is still a challenge. To overcome such a problem many strategies were proposed, by considering other excitation wavelengths within the biological windows (*e.g.* 800 nm) or trying to improve the efficiency engineering the electromagnetic environment experienced by upconverting materials using antenna dyes,[33] quantum dots[34] or plasmonic structures.[35] However, with the aim to develop an ideal upconverting system based on a single UC nanocrystal without the need of other complex structures, the research of novel high-performances upconverting nanocrystals is highly desirable and challenging.

In addition to biological applications, as summarized by Figure 1.4 (from ref. 1 and references therein), the progresses in upconverting nanocrystals preparation, have led to their use in a wide variety of different applications such as RGB printing, security systems, barcoding and 3D displays.

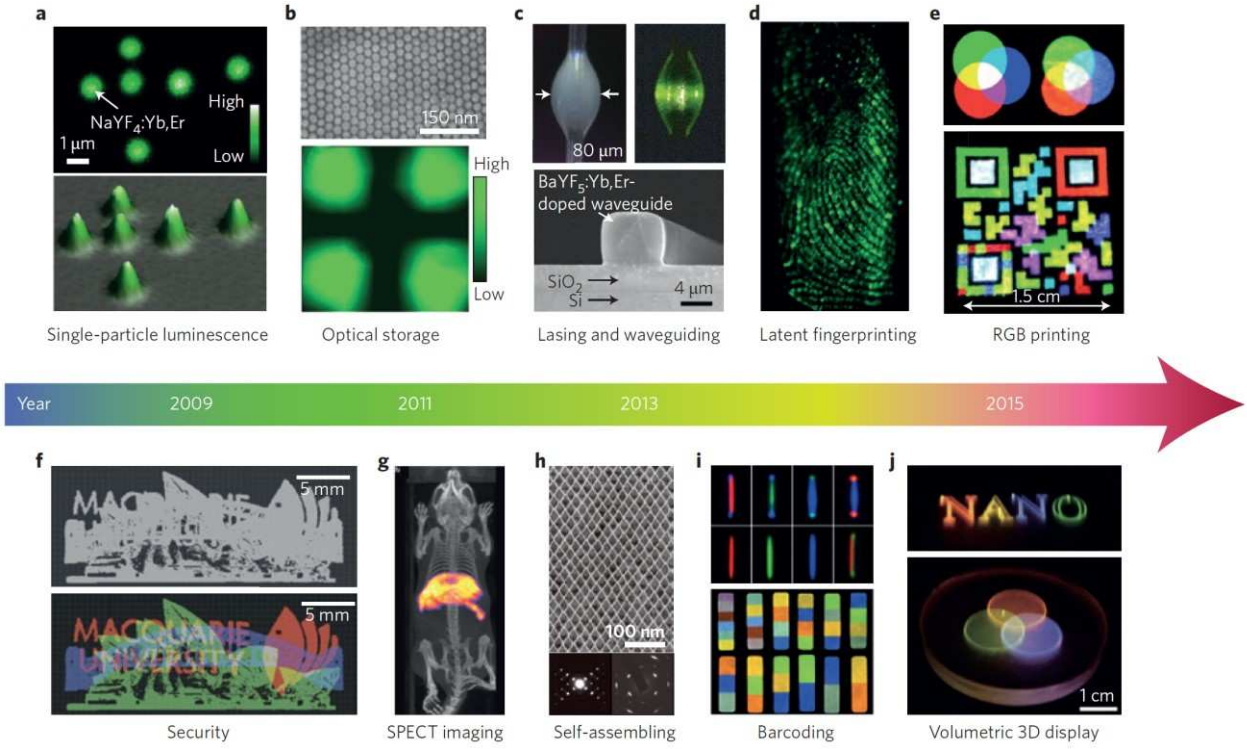

Figure 1.4 Summary of some of the relevant applications for multifunctional upconverting nanoparticles. From ref. 1.

In 2007, Chermont *et al.*[36] demonstrated the possibility to use persistent luminescent nanocrystals (PersLNCs) as effective probes for *in vivo* imaging, introducing a new concept for biological

imaging. Persistent luminescent (PersL) materials are characterized by the ability to store the excitation energy by means of electron(hole) traps and to release the carrier (electrons or holes) for long time, producing the long-lasting luminescent emission (see Section 2.6). As schematically reported in Figure 1.5, this new strategy allows to completely overcome the limitations coming from the excitation sources during the analysis needed for the other common luminescent systems, becoming one of the most attractive bioprobes class of the next generation. In fact, the nanoparticle suspension can be charged and successively injected into the mouse to monitor the glow emission.

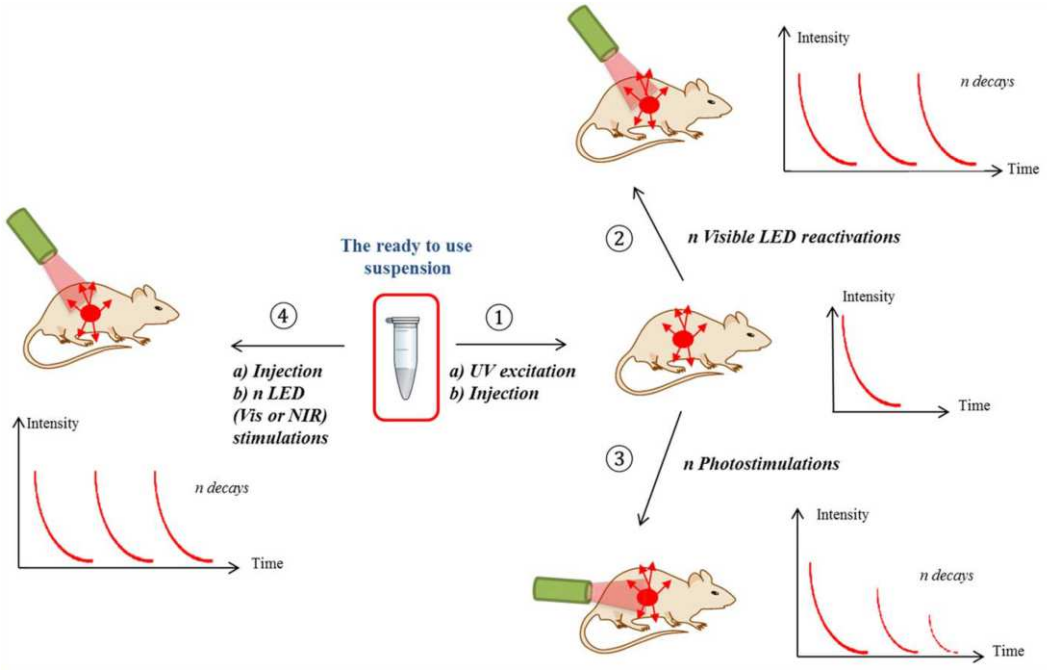

Figure 1.5 Concept scheme of the use of PersL nanoparticles in biological imaging (from ref. 3).

Also in this case, NIR emission is necessary and most recent advances in the development of PerL materials for bioimaging are based on transition metal ions[37] (in particular Cr^{3+}). It has been demonstrated that PersL nanocrystals present a much less intensive signal compare to QDs, but the signal-to-noise ratio can be much higher than for QDs.[3] As schematically reported in Figure 1.6, the key for the design of effective PersL materials with long afterglow, is the control of suitable "trap depth" between electron trap and the bottom of the conduction band of the material. To date, PersLNCs emission can be detected, after the injection, for very short time respect to the persistent behaviour of the bulk material. However, a careful design allows the excitation of the PersLNCs also after injection to recharged the material by visible LED or photostimulation (see right side of Figure 1.5). Maldiney *et al.* [38] reported that $ZnGa_2O_4:Cr^{3+}$ nanocrystals functionalized with polyethylene glycol chains, could image colon cancer cells (CT26) subcutaneously implanted into Balb/c mice, 4 h after NP injection and Chuang *et al.* [39] showed the possibility to detect the emission signal of $LiGa_5O_8:Cr^{3+}$ nanocrystals also after 10 days by means of photostimulation with white-LED light.

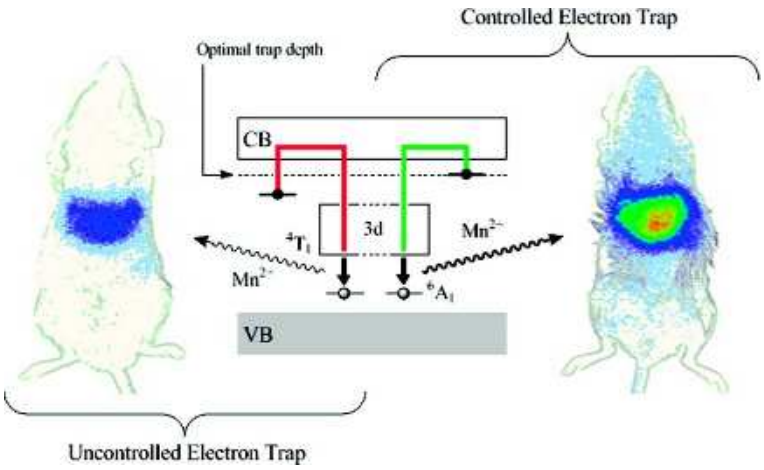

Figure 1.6 Energy level diagram of Mn^{2+}-doped $CaMgSi_2O_6$ with (right side) and without (left side) suitable electron trap (from ref. 40).

Even if these materials are very promising for biological purposes, to date, only few example of suitable PersL nanoparticles are reported.[36,38-44] This kind of materials are very sensible to the preparation method, being based on precise trap depth distributions. Therefore, synthetic procedure able to produce highly pure and crystalline PersLNCs, where anhanced optical performance at the nanoscale can be achieved also in virtue of a full control on the presence of detrimental defects, is highly demanding. In addition, the design of novel NIR emitting PersL materials is a hot topic.

It is also worth mentioning that the development of luminescent inorganic bioprobes, gave the opportunity to take advantage of some specific energy level configurations of the activators of the used phosphors to monitor the temperature in biological environments by means of luminescence output.[6,7,45-48] This new possibility drives the scientific community to the development of new systems able to discriminate also very small temperature fluctuations. Outstanding preliminary results were achieved in mapping the intracellular temperature not only with green fluorescent protein,[49] fluorescent polymers[50] or nanodiamonds,[51,52] but also with lanthanide-doped nanocrystals.[53,54] Recently, this possibility introduced a new active research area focused on the development of high performing inorganic luminescent thermometers.

It was demonstrated that, the more effective configuration for reliable measurements of the temperature is based on dual emitting systems (internally referred rational scheme).[46] In particular, single-doped systems ensure the reliability also by changing the environment because of the population distribution ratio ensured by the Boltzmann law.[46] In 2015, Balabhadra *et al.*[56] reported a Nd^{3+}-single-doped based luminescent thermometer (Gd_2O_3:Nd^{3+} system) with high relative sensitivity. Figure 1.7 shows the experimental analysis reported by Carrasco *et al.*[55] for Nd^{3+}-doped LaF_3 nanocrystals, evidencing the interesting possibility to follow the infrared fluorescence and to simultaneously use it as thermal sensor for the tumor.

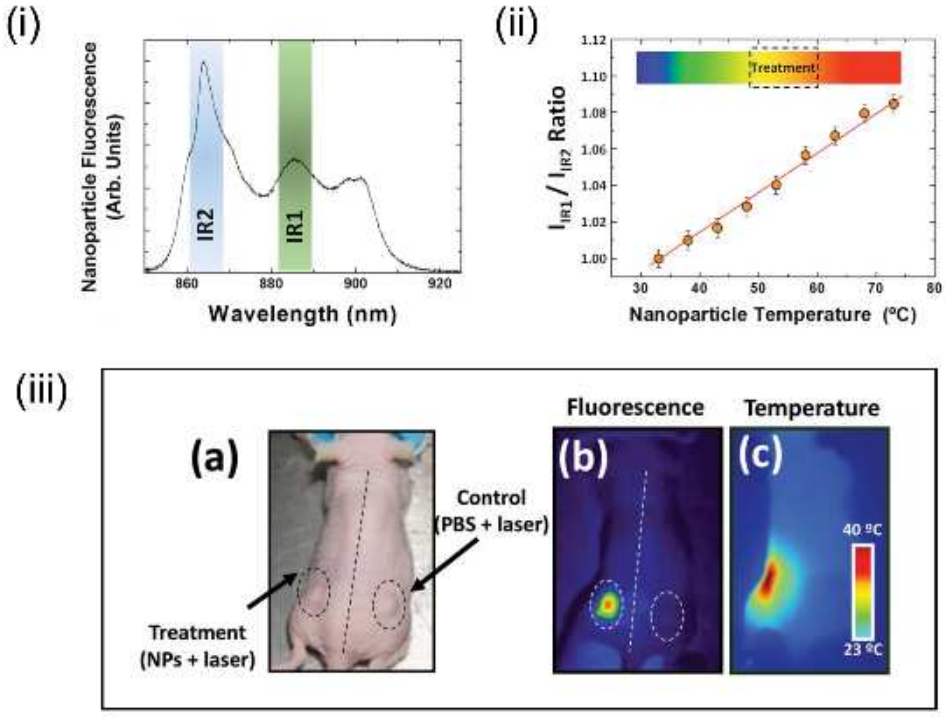

Figure 1.7 (i) NIR PL emission spectrum of LaF_3:Nd system with schematic indication of the spectral range (IR1 and IR2) used for ratiometric thermal sensing. (ii) Temperature dependence of the intensity ratio IR1/IR2. (iii) Optical image of a mouse with two tumors (a) and infrared fluorescence and thermal images (b,c) under 808 nm laser irradiation (4 Wcm^{-2}). From ref. 55).

In this view, it is straightforward to understand that the ever increasing performance requirements for applications involving luminescent systems claims for novel phosphors with high efficiency and low cost. In this thesis we investigate bismuth-based luminescent materials as promising systems for different optical applications. In particular, we have focused, from one hand, on the role of bismuth oxide-based compounds on the luminescent properties of lanthanides and Cr^{3+} ions, and, on the other hand, on the behaviour of bismuth ions (Bi^{3+} and Bi^{2+}) as luminescent centres in specific compounds (as donor or sensitizer).

Bismuth-based materials are characterized by low toxicity[57-61] and low cost, becoming very promising for the development of next generation phosphors. In addition, with the idea to develop high efficient luminescent materials it must be pointed out that Bi^{3+} is characterized by allowed transitions, differently from the typical f-f forbidden ones occurring in lanthanide ions.

The remarkable non-toxicity of bismuth compounds[59] is primarily due to their insolubility in neutral aqueous solutions such as biological fluids and, as can be seen from the comparison of LD_{50} values reported in Table 1.1, most of these are even less toxic than sodium chloride.

Table 1.1 Comparison of LD_{50} values for bismuth compounds and comparable salts (from ref. 59).

Compound	LD_{50} (g/Kg)	Species and Route
Sodium Chloride, NaCl	3.8	Rat, Oral
Bismuth Oxide, Bi_2O_3	5.0	Rat, Oral
Bismuth nitrate, $Bi(NO_3)_3 \cdot 5H_2O$	4.4	Rat, Oral
Bismuth oxychloride, BiOCl	22	Rat, Oral
Triphenylbismuthine, Ph_3Bi	180	Dog, Oral
Mercury chloride, $HgCl_2$	0.001	Rat, Oral
Cerium chloride, $CeCl_3$	2.1	Rat, Oral
Indium chloride, $InCl_3$	1.1	Rat, Oral

Given that the low toxicity makes bismuth-based phosphors very attractive for the development of biological probes, from the point of view of optical performances, specific properties characterizing these compounds, like lone pair electrons and high refractive index, open intriguing perspectives, inducing high emission probability rates and the possibility of unusual optical responses arising by the local electron cloud distortions (see Section 3.2).

Furthermore, it is worth considering that, to date, almost all the lighting devices commercially available contain rare-earth-doped phosphors (*e.g.* cerium and/or europium activated crystals).[62] The constant growth of the white LEDs market prompts the research, from one hand, to the development of new strategies to effectively improve the efficiency of the devices and, on the other hand, to find new alternatives to reduce the costs (keeping in mind the monopoly of China's rare-earth industries). In this context, bismuth seems to be a suitable candidate because of the rather low cost, and promising properties for white LEDs development, based on the ability of Bi^{2+} ions to absorb the excitation light of blue-LED and to emit in the red region.[63]

Finally, in the optic of designing the next-generation multimodal probes, moving toward multifunctional nanoplatforms, bismuth-based materials have also the intriguing characteristic to be suitable for computed X-ray tomography[64] (CT), photoacoustic tomography[65] (PAT) and single-photon emission CT[66] (SPECT).

1.2 Outline of the Thesis

In this thesis, new bismuth-based luminescent materials are presented. Synthesis and optical studies of these materials are provided, discussing their applicability in different field such as upconverting nanoparticles for bioimaging, ratiometric optical thermometer for biological environments, persistent luminescence in the visible and near-infrared regions and broadband sensitization of the Er^{3+} emissions at the telecommunication wavelengths via Bi^{3+} mediated energy transfer.

After providing necessary theoretical insights and basic knowledge, from the point of view of the systems investigated this thesis can be divided into two parts. At first, bismuth-based oxide materials as host for the luminescence properties of lanthanide and transition metal ions are addressed (Chapters 4, 5 and 6), while the following focus is the investigation of the optical properties of Bi^{3+} and Bi^{2+} ions as luminescent centers in perovskite $CaSnO_3$ and Bi^{3+} as sensitizer of Er^{3+} ions in codoped Y_2O_3 nanocrystals (Chapters 7 and 8).

The thesis is organized as follows:

The basic theoretical aspects and the important concepts explored in the thesis are presented in Chapter 2. After an introduction of the general luminescence phenomena of the localized luminescent centers, the chapter focuses on the theoretical background regarding quenching (concentration and thermal activated), energy transfer, upconversion and persistent luminescence processes.

Chapter 3 provides a brief overview of the luminescent properties of bismuth ions (Bi^{3+} and Bi^{2+}) and luminescent bismuth-based compounds, highlighting the strong effects of the interaction with the host. Moreover, an introduction on the potentialities of bismuth oxide-based compounds as host for luminescent centers is given, with an insight on the different Bi_2O_3 polymorphs.

In Chapter 4, Bi_2O_3-based nanoparticles are proposed as a new class of host for upconverting nanoparticles. The Y^{3+} doping effect is investigated by considering the upconverting emission properties of Er^{3+} ions used as optical probe in the activated Bi_2O_3 nanoparticles. The direct role played by the host bandgap in determining the nanophosphor optical performance is demonstrated. In addition, Yb^{3+}-Ln^{3+} codoped systems are reported for Ln=Er, Ho and Tm. The upconversion emission features and the quantum efficiency determined for the investigated nanoparticles evidence their suitability for possible applications as upconverting systems.

In Chapter 5, we investigate the lanthanide-doped Bi_2SiO_5 nanocrystal formation inside mesoporous silica nanoparticles (MSNs). The role of both the processing temperature and the concentration of precursor salts impregnated into the MSNs are discussed and a mechanism for the formation of Bi_2SiO_5/SiO_2 core-shell nanosystem is proposed. In addition, the easy tunability of the color output of the upconverting system is demonstrated by suitable choice of the doping lanthanide ions.

Chapter 6 introduces $Bi_2Ga_4O_9$ doped with Cr^{3+} as a new material for ratiometric optical thermal sensing. A detailed spectroscopic investigation is provided to estimate the crystal field experienced by Cr^{3+}, designing the Tanabe-Sugano diagram and the configurational coordinate diagram. With the aim to access the suitability of the material for thermal sensing, the temperature dependence of PL and decay curves are reported and the key parameters, such as the relative sensitivity and the temperature uncertainty, are calculated.

In Chapter 7 we focus on the persistent luminescence of Bi-activated $CaSnO_3$. We demonstrated the simultaneous stabilization of Bi^{3+} and Bi^{2+} ions, discussing the energy transfer between the

two luminescent centers. The observed luminescence features are compared to other Bi-activated Ca*B*O_3 perovskites (*B*=Ti, Sn, Zr); moreover, the factors responsible for the metal-to-metal charge transfer character of the transitions are discussed. Temperature dependence trends determined for the photoluminescence emission intensities, combined with empirical models and persistent luminescence analysis, are considered for designing the energy level diagram of the luminescent centers respect to the host conduction and valence band energies, and then for proposing a tentative mechanism for the observed persistent emissions. Finally, the effect of the codoping with Tb^{3+} or with Cr^{3+} is also investigated.

Chapter 8 discusses the energy transfer process between Bi^{3+} and Er^{3+} ions in codoped Y_2O_3 nanocrystals prepared by Pechini type sol-gel process. The effectiveness of the Bi^{3+} mediated enhancement and the broadening of the lanthanide absorption window as well as the crystalline site hosting the Bi^{3+} sensitizer are investigated. To get deeper insight the energy transfer process, we propose a simple model for the calculation of the critical transfer distance and a tentative determination of the interaction mechanism.

In Chapter 9, we summarize the main results of this thesis, and a perspective on the future research driven by the obtained results is given.

References

1. B. Zhou, B. Shi, D. Jin and X. Liu. Controlling upconversion nanocrystals for emerging applications. *Nat. Nanotechnol.* **2015**, 10, 924-936.
2. G. Chen, I. Roy, C. Yang and P.N. Prasad. Nanochemistry and nanomedicine for nanoparticle-based diagnostics and therapy. *Chem. Rev.* **2016**, 116, 2826-2885.
3. D. Jaque, C. Richard, B. Viana, K. Soga, X. Liu and J. García Solé. Inorganic nanoparticles for optical bioimaging. *Adv. Opt. Photonics* **2016**, 8, 1-103.
4. S.S. Lucky, K.C. Soo and Y. Zhang. Nanoparticles in photodynamic therapy. *Chem. Rev.* **2015**, 115, 1990-2042.
5. P. Kumar, S. Singh and B.K. Gupta. Future prospects of luminescent nanomaterial based security inks: from synthesis to anti-counterfeiting applications. *Nanoscale* **2016**, 8, 14297-14340.
6. C.D.S. Brites, A. Millán and L.D. Carlos. Lanthanide in luminescent thermometry. In J.-C. Bünzli and V.K. Pecharsky Eds., *Handbook on the Physiscs and Chemistry of Rare Earth*, Elsevier, 2016, Chapter 281, vol. 49, pp. 339-427.
7. C.D.S. Brites, P.P. Lima, N.J.O. Silva, A. Millán, V.S. Amaral, F. Palacio and L. D. Carlos. Thermometry at the nanoscale. *Nanoscale* **2012**, 4, 4799-4829.
8. A. M. Smith, M. C. Mancini and S. Nie. Second window for *in vivo* imaging. *Nat. Nanotechnol.* **2009**, 4, 710-711.

9. E. Hemmer, N. Venkatachalam, H. Hyodo, A. Hattori, Y. Ebina, H. Kishimoto and K. Soga. Upconverting and NIR emitting rare earth based nanostructures for NIR-bioimaging. *Nanoscale* **2013**, 5, 11339-11361.

10. L. Prodi, E. Rampazzo, F. Rastrelli, A. Speghini and N. Zaccheroni. Imaging agents based on lanthanide doped nanoparticles. *Chem. Soc. Rev.* **2015**, 44, 4922-4952.

11. E. Hemmer, A. Benayas, F. Légaré and F. Vetrone. Exploiting the biological windows: current perspectives on fluorescent bioprobes emitting above 1000 nm. *Nanoscale Horiz.* **2016**, 1, 168-184.

12. G. Chen, H. Qiu, P.N. Prasad and X. Chen. Upconversion nanoparticles: Design, nanochemistry, and applications in theranostics. *Chem. Rev.* **2014**, 114, 5161-5214.

13. X. Wu, G. Chen, J. Shen, Z. Li, Y. Zhang and G. Han. Upconversion nanoparticles: A versatile solution to multiscale biological imaging. *Bioconjugate Chem.* **2015**, 26, 166-175.

14. Y.I. Park, K.T. Lee, Y.D. Suh and T. Hyeon. Upconverting nanoparticles: a versatile platform for wide-field two-photon microscopy and multi-modal *in vivo* imaging. *Chem. Soc. Rev.* **2015**, 44, 1302-1317.

15. G. Chen, J. Shen, T. Y. Ohulchanskyy, N.J. Patel, A. Kutikov, Z. Li, J. Song, R.K. Pandey, H. Agren, P.N. Prasad and G. Han. (α-$NaYbF_4$:Tm^{3+})/CaF_2 core/shell nanoparticles with efficient near-infrared to near-infrared upconversion for high-contrast deep tissue bioimaging. *ACS Nano*, **2012**, 6, 8280-8287.

16. H.H. Gorris and O.S. Wolfbeis. Photon-upconverting nanoparticles for optical encoding and multiplexing of cells, biomolecules, and microspheres. *Angew. Chem. Int. Ed.* **2013**, 52, 3584-3600.

17. L. Zhou, R. Wang, C. Yao, X. Li, C. Wang, X. Zhang, C. Xu, A. Zeng, D. Zhao and F. Zhang. Single-band upconversion nanoprobes for multiplexed simultaneous *in situ* molecular mapping of cancer biomarkers. *Nat. Commun.* **2015**, 6, 6938.

18. J.F. Suyver, A. Aebischer, D. Biner, P. Gerner, J. Grimm, S. Heer, K.W. Krämer, C. Reinhard and H.U Güdel. Novel materials doped with trivalent lanthanides and transition metal ions showing near-infrared to visible photon upconversion. *Opt. Mater.* **2005**, 27, 1111-1130.

19. J.-C. Boyer, F. Vetrone, L.A. Cuccia and J.A. Capobianco. Synthesis of colloidal upconverting $NaYF_4$ nanocrystals doped with Er^{3+}, Yb^{3+} and Tm^{3+}, Yb^{3+} via thermal decomposition of lanthanide trifluoroacetate precursors. *J. Am. Chem. Soc.* **2006**, 128, 7444-7445.

20. N.-N. Dong, M. Pedroni, F. Piccinelli, G. Conti, A. Sbarbati, J.E. Ramírez-Hernández, L. Martínez Maestro, M.C. Iglesias-de la Cruz, F. Sanz-Rodriguez, A. Juarranz, F. Chen, F. Vetrone, J.A. Capobianco, J. García Sole, M. Bettinelli, D. Jaque and A. Speghini. NIR-to-NIR two-photon excited CaF_2:Tm^{3+},Yb^{3+} nanoparticles: multifunctional nanoprobes for highly penetrating fluorescence bio-imaging. *ACS Nano* **2011**, 5, 8665-8671.

21. R. Naccache, Q. Yu and J.A. Capobianco. The fluoride host: nucleation, growth, and upconversion of lanthanide-doped nanoparticles. *Adv. Optical Mater.* **2015**, 3, 482-509.

22. M. Quintanilla, I.X. Cantarelli, M. Pedroni, A. Speghini and F. Vetrone. Intense ultraviolet upconversion in water dispersible SrF_2:Tm^{3+},Yb^{3+} nanoparticles: the effect of the environment on light emissions. *J. Mater. Chem. C* **2015**, 3, 3108-3113.

23. C. Yan, H. Zhao, D.F. Perepichka and F. Rosei. Lanthanide ion doped upconverting nanoparticles: Synthesis, structure and properties. *Small*, 29, 3888-3907.

24. K.W. Krämer, D. Biner, G. Frei, H.U. Güdel, M.P. Hehlen and S.R. Lüthi. Hexagonal sodium yttrium fluoride based green and blue emitting upconversion phosphors. *Chem. Mater.* **2004**, 16, 1244-1251.

25. H. Schäfer, P. Ptacek, H. Eickmeier and M. Haase. Synthesis of hexagonal Yb^{3+}, Er^{3+}-doped $NaYF_4$ nanocrystals at low temperature. *Adv. Funct. Mater.* **2009**, 19, 3091-3097.

26. H. Dong, L.-D. Sun, Y.-F. Wang, J. Ke, R. Si, J.-W. Xiao, G.-M. Lyu, S. Shi and C.-H. Yan. Efficient tailoring of upconversion selectivity by engineering local structure of Lanthanides in Na_xREF_{3+x} nanocrystals. *J. Am. Chem. Soc.* **2015**, 137, 6569-6576.

27. M.D. Wisser, M. Chea, Y. Lin, D.M. Wu, W.L. Mao, A. Salleo and J.A. Dionne. Strain-induced modification of optical selection rules in lanthanide-based upconverting nanoparticles. *Nano Lett.* **2015**, 15, 1891-1897.

28. M.D. Wisser, S. Fischer, P.C. Maurer, N.D. Bronstein, S. Chu, A.P. Alivisatos, A. Salleo and J.A. Dionne. Enhancing quantum yield via symmetry distortion in lanthanide-based upconverting nanoparticles. *ACS Photonics* **2016**, 3, 1523-1530.

29. J.A. Capobianco, J.C. Boyer, F. Vetrone, A. Speghini and M. Bettinelli. Optical spectroscopy and upconversion studies of Ho^{3+}-doped bulk and nanocrystalline Y_2O_3. *Chem. Mater.* **2002**, 14, 2915-2921.

30. F. Vetrone, J.-C. Boyer, J.A. Capobianco, A. Speghini and M. Bettinelli. Concentration-dependent near-infrared to visible upconversion in nanocrystalline and bulk Y_2O_3:Er^{3+}. *Chem. Mater.* **2003**, 15, 2737-2743.

31. R. Martín-Rodríguez, S. Fischer, A. Ivaturi, B. Froehlich, K.W. Krämer, J.C. Goldschmidt, B.S. Richards and A. Meijerink. High efficient IR to NIR upconversion in Gd_2O_2S:Er^{3+} for photovoltaic applications. *Chem. Mater.* **2013**, 25, 1912-1921.

32. R. Martín-Rodríguez, F.T. Rabouw, M. Trevisani, M. Bettinelli and A. Meijerink. Upconversion dynamics in Er^{3+}-doped Gd_2O_2S: Influence of excitation power, Er^{3+} concentration, and defects. *Adv. Optical Mater.* **2015**, 3, 558-567.

33. W. Zou, C. Visser, J.A. Maduro, M.S. Pshenichnikov and J.C. Hummelen. Broadband dye-sensitized upconversion of near-infrared light. *Nat. Photonics* **2012**, 6, 560-564.

34. A.C. Pan, C. Del Cañizo, E. Cánovas, N.M. Santos, J.P. Leitão and A. Luque. Enhancement of up-conversion efficiency by combining rare earth-doped phosphors with PbS quantum dots. *Sol. Energy Mater. Sol. Cells* **2010**, 94, 1923-1926.

35. D.W. Wu, A. García-Etxarri, A. Salleo and J.A. Dionne. Plasmon-enhanced upconversion. *J. Phys. Chem. Lett.* **2014**, 5, 4020-4031.

36. Q. Chermont, C. Chanéac, J. Seguin, F. Pellé, S. Maîtrejean, J.-P. Jolivet, D. Gourier, M. Bessodes and D. Scherman. Nanoprobes with near-infrared persistent luminescence for *in vivo* imaging. *Proc. Natl. Acad. Sci. USA* **2007**, 104, 9266-9271.

37. Y. Zhuang, Y. Katayama, J. Ueda and S. Tanabe. A brief review on red to near-infrared persistent luminescence in transition-metal-activated phosphors. *Opt. Mater.* **2014**, 36, 1907-1912.

38. T. Maldiney, A. Bessière, J. Seguin, E. Teston, S.K. Sharma, B. Viana, A.J.J. Bos, P. Dorenbos, M. Bessodes, D. Gourier, D. Scherman and C. Richard. The *in vivo* activation of persistent nanophosphors for optical imaging of vascularization, tumours and grafted cells. *Nat. Mater.* **2014**, 13, 418-426.

39. Y.-J. Chuang, Z. Zhen, F. Zhang, F. Liu, J.P. Mishra, W. Tang, H. Chen, X. Huang, L. Wang, X. Chen, J. Xie and Z. Pan. Photostimulable near-infrared persistent luminescent nanoprobes for ultrasensitive and longitudinal deep-tissue bio-imaging. *Theranostics* **2014**, 4, 1112-1122.

40. T. Maldiney, A. Lecointre, B. Viana, A. Bessière, M. Bessodes, D. Gourier, C. Richard and D. Scherman. Controlling electron trap depth to enhance optical properties of persistent luminescence nanoparticles for in vivo imaging. *J. Am. Chem. Soc.* **2011**, 133, 11810-11815.

41. T. Maldiney, C. Richard, J. Seguin, N. Wattier, M. Bessodes and D. Scherman. Effect of core diameter, surface coating, and PEG chain length on the biodistribution of persistent luminescence nanoparticles in mice. *ACS Nano* **2011**, 5, 854-862.

42. A. Abdukayum, J.-T. Chen, Q. Zhao and X.-P. Yan. Functional near infrared-emitting Cr^{3+}/Pr^{3+} co-doped zinc gallogermanate persistent luminescent nanoparticles with superlong afterglow for *in vivo* targeted bioimaging. *J. Am. Chem. Soc.* **2013**, 135, 14125-14133.

43. T. Maldiney, B. Ballet, M. Bessodes, D. Scherman and C. Richard. Mesoporous persistent nanophosphors for *in vivo* optical bioimaging and drug-delivery. *Nanoscale* **2014**, 6, 13970-13976.

44. Z. Li, Y. Zhang, X. Wu, X. Wu, R. Maudgal, H. Zhang and G. Han. In vivo repeatedly charging near-infrared-emitting mesoporous $SiO_2/ZnGa_2O_4:Cr^{3+}$ persistent luminescence nanocomposites. *Adv. Sci.* **2015**, 2, 1500001.

45. D. Jaque and F. Vetrone. Luminescence nanothermometry. *Nanoscale* **2012**, 4, 4301-4326.

46. E.J. McLaurin, L.R. Bradshaw and D.R. Gamelin. Dual-emitting nanoscale temperature sensors. *Chem. Mater.* **2013**, 25, 1283-1292.

47. L.H. Fischer, G.H. Harms and O.S. Wolfbeis. Upconverting nanoparticles for nanoscale thermometry. *Angew. Chem. Int. Ed.* **2011**, 50, 4546-4551.

48. X.-D. Wang, O.S. Wolfbeis and R.J. Meier. Luminescent probes and sensors for temperature. *Chem. Soc. Rev.* **2013**, 42, 7834-7869.

49. J.S. Donner, S.A. Thompson, M.P. Kreuzer, G. Baffou and R. Quidant. Mapping intracellular temperature using green fluorescent protein. *Nano Lett.* **2012**, 12, 2107-2111.

50. K. Okabe, N. Inada. C. Gota, Y. Harada, T. Funatsu and S. Uchiyama. Intracellular temperature mapping with a fluorescent polymeric thermometer and fluorescence lifetime imaging microscopy. *Nat. Commun.* **2012**, 3, 705.

51. G. Kucsko, P.C. Maurer, N.Y. Yao, M. Kubo, H.J. Noh, P.K. Lo, H. Park and M.D. Lukin. Nanometre-scale thermometry in a living cell. *Nature* **2013**, 500, 54-58.

52. W.W.-W. Hsiao, Y.Y. Hui, P.-C. Tsai and H.-C. Chang. Fluorescent nanodiamond: A versatile tool for long-term cell tracking, super-resolution imaging, and nanoscale temperature sensing. *Acc. Chem. Res.* **2016**, 49, 400-407.

53. F. Vetrone, R. Naccache, A. Zamarrón, A.J. de la Fuente, F. Sanz-Rodríguez, L. Martinez Maestro, E. Martin Rodriguez, D. Jaque, J. García Solé and J.A. Capobianco. Temperature sensing using fluorescent nanothermometers. *ACS Nano* **2010**, 4, 3254-3258.

54. S. Hao, G. Chen and C. Yang. Sensing using rare-earth-doped upconversion nanoparticles. *Theranostics* **2013**, 3, 331-345.

55. E. Carrasco, B. del Rosal, F. Sanz-Rodríguez, A.J. De la Fuente, P. Haro Gonzalez, U. Rocha, K.U. Kumar, C. Jacinto, J. García Solé and D. Jaque. Intratumoral thermal reading during photo-thermal therapy by multifunctional fluorescent nanoparticles. *Adv. Funct. Mater.* **2015**, 25, 615-626.

56. S. Balabhadra, M.L. Debasu, C.D.S. Brites, L.A.O. Nunes, O.L. Malta, J. Rocha, M. Bettinelli and L.D. Carlos. Boosting the sensitivity of Nd^{3+}-based luminescent nanothermometers. *Nanoscale* **2015**, 7 17261-17267.

57. R. Mohan. Green bismuth. *Nat. Chem.* **2010**, 2, 336.

58. A.B. Seabra and N. Durán. Nanotoxicology of metal oxide nanoparticles. *Metals* **2015**, 5, 934-975.

59. H. Suzuki and Y. Matano. Organobismuth Chemistry. Ed. 1, Elsevier, Amsterdam, **2001**.

60. G.G. Briand and N. Burford. Bismuth compounds and preparations with biological or medicinal relevance. *Chem. Rev.* **1999**, *99*, 2601.

61. P. Riente, A. Matas Adams, J. Albero, E. Palomares and M.A. Pericàs. Light-driven organocatalysis using inexpensive, nontoxic Bi_2O_3 as the photocatalyst. *Angew. Chem. Int. Ed.* **2014**, *53*, 9613.

62. P. Pust, P.J. Schmidt and W. Schnick. A revolution in lighting. *Nat. Mater.* **2015**, 14, 454-458.

63. M. Peng and L. Wondraczek. Bi^{2+}-doped strontium borates for white-light-emitting diodes. *Opt. Lett.* **2009**, 34, 2885-2887.

64. O. Rabin, J.M. Perez, J. Grimm, G. Wojtkiewciz and R. Weissleder. An X-ray computed tomography imaging agent based on long-circulating bismuth sulphide nanoparticles. *Nat. Mater.* **2006**, 5, 118-122.

65. X. Zheng, J. Shi, Y. Bu, G. Tian, X. Zhang, W. Yin, B. Gao, Z. Yang, Z. Hu, X. Liu, L. Yan, Z. Gu and Y. Zhao. Silica-coated bismuth sulphide nanorods as multimodal contrast agents for a non-invasive visualization of the gastrointestinal tract. *Nanoscale* **2015**, 7, 12581-12591.

66. J. de Swart, H.S. Chan, M.C. Goorden, A. Morgenstern, F. Bruchertseifer, F.J. Beekman, M. de Jong and M.W. Konijnenberg. Utilizing high-energy γ-photons for high-resolution ^{213}Bi SPECT in mice. *J. Nucl. Med.* **2016**, 57, 486-492.

CHAPTER 2

Luminescence: Theoretical Background and Processes

Abstract In this chapter, the basics of fundamental theory and processes regarding the luminescence in solid materials are discussed. After the introduction of the fundamental concepts dealing with the description of the general key parameters commonly used, a brief overview of the optical and electronic properties of the main different types of luminescent centers will be introduced. Then, different pathways leading to non-radiative decay of the photoexcited emitter to the ground state (quenching processes) are described. Finally, energy transfer, upconversion and persistent luminescence processes are briefly reviewed.

2.1 Fundamentals of Luminescence

The term *luminescence* (from the Latin *lumen*, light) was first introduced in 1888 by Eilhardt Wiedmann, including both fluorescence and phosphorescence.[1] Nowadays, the word luminescence defines the phenomena in which the excitation of an electronic state results in the emission of light. Luminescence can be due to light emission from localized centers (doped ions, also called active or luminescent centers) or from delocalized centers (from host, as in the case of semiconductors). Localized luminescent centers are the main subject of this thesis and will be introduced in the next section.

The effect of a host material on the luminescence properties of an active center is different depending on the nature of the active center and, in particular, of the transition considered. For instance, if the f-f transitions in lanthanide ions are only weakly affected by the embedding matrix, on the other hand, the f-d transitions in lanthanides, the d-d transitions in transition metal ions and s-p transitions in ns^2-type ions strongly depend on the host material. The reason of this different behaviour is due to the specific nature of the orbitals involved. In fact, it is well known that the

4f-orbitals are "shielded" by electrons in the more extended 5s- and 5-p orbitals, while, 5d-orbitals (considered here as reference case for the class of the un-shielded orbitals) are more extended than the 4f-orbitals and thus their interaction with the lattice is much stronger.

When an optically active center (luminescent center) is incorporated in a crystal, the shape of the absorption and emission spectra is influenced by the interaction of the electronic energy levels with the lattice vibrations (phonons). The interaction between the electronic states and the vibrating modes is described in terms of *electron-phonon coupling*, resulting in the broadening of the absorption and emission bands and in the occurrence of the *Stokes-shift* (energy difference between the maxima of the absorption and emission bands belonging to the same electronic transition[2]).

In order to describe (qualitatively) the relative energy levels and luminescent processes of active centers in phosphors, *configurational coordinate diagram* is widely used. The *single configurational coordinate diagram* is a very useful simplified representation of the energy variation of the electronic levels of the active center with the nuclear displacements, in which only one vibrational coordinate is used. Figure 2.1a,b show the configurational coordinate diagrams of two electronic states with different displacement ΔQ_e (Q_e and Q_e' represent the equilibrium position of the ground and excited state respectively), where the configurational coordinate Q represents the deviation of ion-ligand distance from the equilibrium position. From the quantum mechanical point of view, the description of the energy potential of a system consisting of an active cation surrounded by coordinating anions (ligands) yields vibrational states with energy levels $\left(n+\frac{1}{2}\right)\hbar\omega$, where n is the vibrational quantum number and $\hbar\omega$ the energy of the vibrational mode.[3] In addition, the change in bonding between the central active cation and the ligands are responsible for the displacement ΔQ_e between the equilibrium positions of ground state and excited state.

The strength of the electron-phonon coupling is described by the *Huang-Rhys parameter*:[4]

$$S = \frac{1}{2}\frac{M\omega^2}{\hbar\omega}(\Delta Q_e)^2 \qquad (2.1)$$

where M is the effective ionic mass, ω the vibrational frequency and ΔQ_e is the effective mode offset between the excited state and the ground state. As evidenced in Figure 2.1c,d increasing S parameter the spectra become broader and the highest peak moves away from the zero-phonon line, with a clear increase of the Stokes-shift E_{Stokes}. Hence, a clear interconnection among the Huang-Rhys parameter, the Stokes-shift and the offset displacement is established.

As a result of the differences described above in the 4f- and 5d-orbitals (the same considerations can be applied to all the un-shielded orbitals) also the vibrational coupling extent is very different depending on the transitions involved.

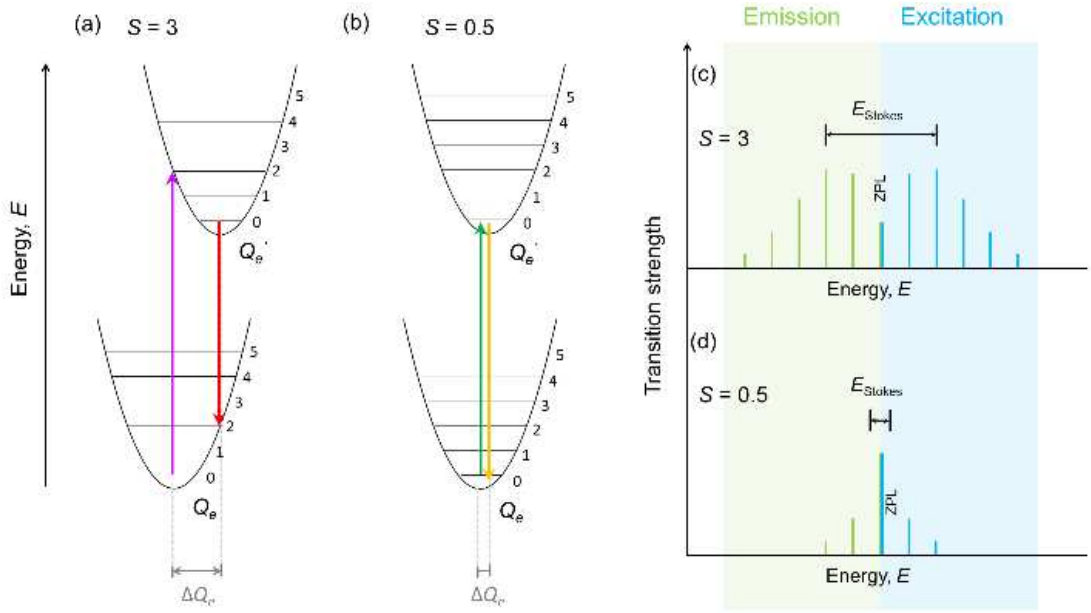

Figure 2.1 Configurational coordinate diagrams of electronic states for (a) S=3 and (b) S=0.5 and corresponding ((c) and (d), respectively) emission (green) and absorption (light-blue) spectra. The Stokes-shift E_{Stokes} increases with the Huang-Rhys parameter S.

This simplified model can be used to qualitatively explain several observations such as (i) the Stokes' law, (ii) the width of the absorption and emission bands and their temperature dependence and (iii) the thermal quenching mechanisms affecting the luminescence process.

2.2 Luminescence Centers

The typical (localized) luminescence centers in solid materials can be classified in three main groups: (i) lanthanide, (ii) transition metal and (iii) ns^2-type ions. The commonly observed transitions in lanthanide ions are between f-orbital to f-orbital or d-orbital (f-f or f-d transitions), while for transition metal ions these arise between d-orbitals (d-d transition) and in ns^2-type ions from s-orbitals to p-orbitals (s-p transitions).

Lanthanide ions: f-f and f-d transitions

Lanthanides are the elements with atomic numbers from 57 (La) to 71 (Lu). The most common oxidation state of lanthanides is +3 with an electronic configuration [Xe]$4f^n$, where n ranges from 0 to 14 moving across the series from La^{3+} to Lu^{3+}. These are characterized by unique luminescent properties, emitting in a wide range of energies from UV to the visible, up to the NIR region of the e.m. spectrum. The transitions are usually intraconfigurational f-f transitions, but also f-d transitions from $4f^n$ ground state to $4f^{n-1}5d^1$ excited state are also exhibited by some lanthanide ions.

The key to the spectroscopic properties of lanthanides ions is the shielding effect of the electrons in the 5s and 5p shells, that make the valence 4f orbitals "inner orbitals".[5] Hence, the 4f energy levels of free lanthanide ions are only slightly perturbed by the crystal field. These shielding effect allows to construct the Dieke diagram of the $4f^n$ energy levels for lanthanide ions, irrespective to the host materials (Figure 2.2).

As schematically depicted in Figure 2.3a, when a lanthanide ion is embedded into a crystal, the degeneracy of the free-ion levels is removed by (i) coulombic, (ii) spin-orbit and (iii) crystal-field interactions. The Coulomb interaction (electrostatic interaction) accounts for the repulsions between 4f electrons. Spin-orbit (SO) interactions split each ^{2S+1}L term into $(2J+1)$ states denoted $^{2S+1}L_J$. The energy levels of $4f^n$ configurations are identified by the so called $^{2S+1}L_J$ spectroscopic notation where S, L and J are the total spin angular momentum, the total orbital angular

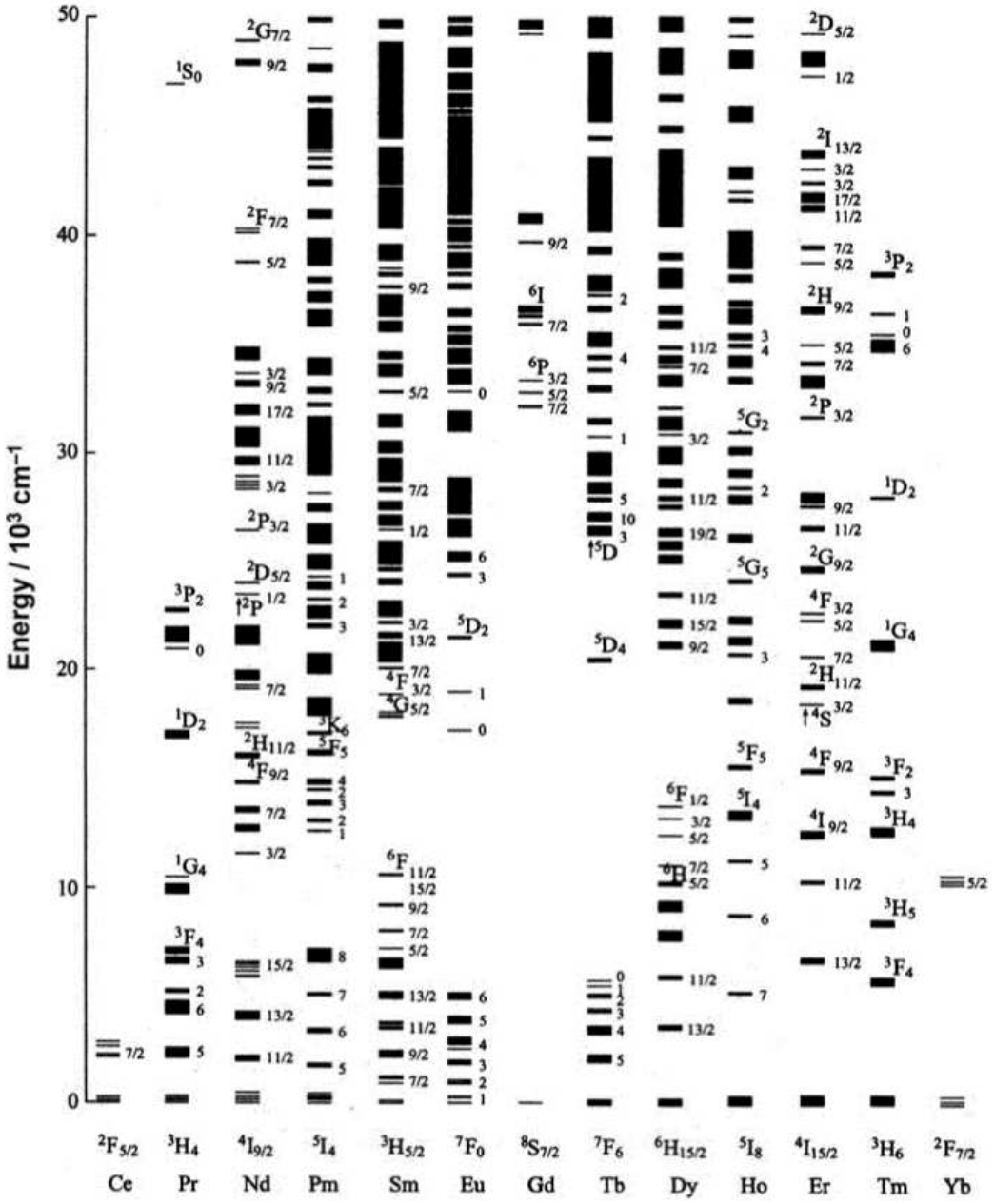

Figure 2.2 Energy level diagram for Ln^{3+} ions doped LaF_3 (from ref. 5).

momentum and the combined spin-orbit angular momentum of the electrons in the f orbitals, respectively. Moreover, the splitting induced by the crystal field interaction is smaller than the SO interaction.

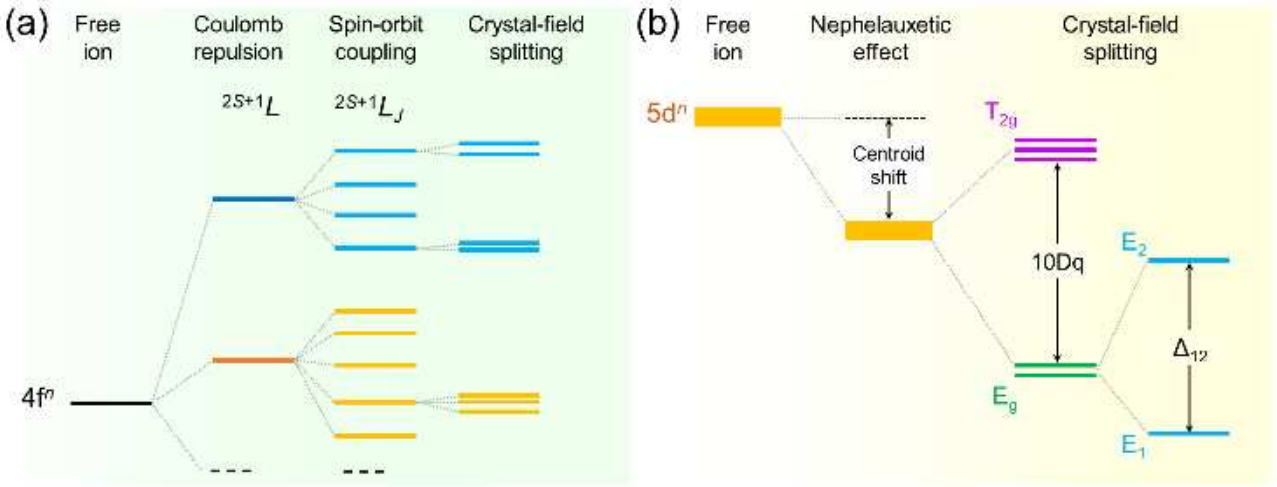

Figure 2.3 (a) Coulomb interaction split the degenerate states of the $4f^n$-state into *LS*-terms (^{2S+1}L), which split into different spin-orbit terms ($^{2S+1}L_J$). The crystal-field contribution is less effective. (b) Schematic effect of the host lattice on the $5d^n$ energy levels: centroid shift (nephelauxetic effect) and crystal-field splitting.

The outer 5d-orbitals are much more extended than 4f-orbitals and thus not shielded by filled 5s and 5p-orbitals. The f-d transitions are thus much more sensitive to the crystal field. In particular, if from one hand 5d energy is affected by the *nephelauxetic effect* due to the binding to the surrounding ligands (lowering the energy of the excited state), from the other hand, the crystal field can split the $4f^{n-1}5d^1$ state into several components (Figure 2.3b). The f-d transitions are common in trivalent lanthanide ions such as Ce^{3+}, Pr^{3+} and Tb^{3+}, as well as in divalent ions such as Eu^{2+} and Yb^{2+}. It is important to mention that the host effect on the 5d energies, is also commonly discussed in term of the *centroid shift* of 5d configurations, closely tied to the nephelauxetic effect.[6,7] Unlike f-f transitions, f-d ones are allowed, resulting in broad spectral bands and strong absorption cross-sections. The crystal field and the nephelauxetic effects[7-9] on the 5d energy levels are important to explain the color output in Eu^{2+} and Ce^{3+} doped phosphors[10,11] but they are critical parameters also for a better understanding of the processes involved in persistent luminescent materials, as reported by Ueda[12] for Ce^{3+}-doped garnets.

Transition metal ions: d-d transition

Transition metal ions are characterized by ground configurations with open *n*d shells, where the spin-orbit interaction increases with *n*. For instance, when the unfilled 3d-orbital elements are introduced into crystalline solids, they can exist in various oxidation states (from +1 to +6). As a result, the unfilled 3d shell becomes an outer electron shell with electronic states strongly affected by the nearest environment. In the simplest case of free Ti^{3+}, with $3d^1$ electron configuration, the

energies of the five 3d-orbitals are identical (degenerate orbitals). When the ion is incorporated into a crystal, if the cation is located into an octahedral crystal field (six red points in Figure 2.4a) the energies of x^2-y^2 and z^2 orbitals increase because of the electron repulsion from the anions with the same orientations, and the splitting into E_g (x^2-y^2, z^2) and T_{2g} (xy, yz, xz) levels occurs. In the case of tetrahedral crystal split (four blue point in Figure 2.4a) the orientation of the anions induces the opposite situation, with T_{2g} (xy, yz, xz) at higher energy than E_g (x^2-y^2, z^2) energy level (see Figure 2.4b).

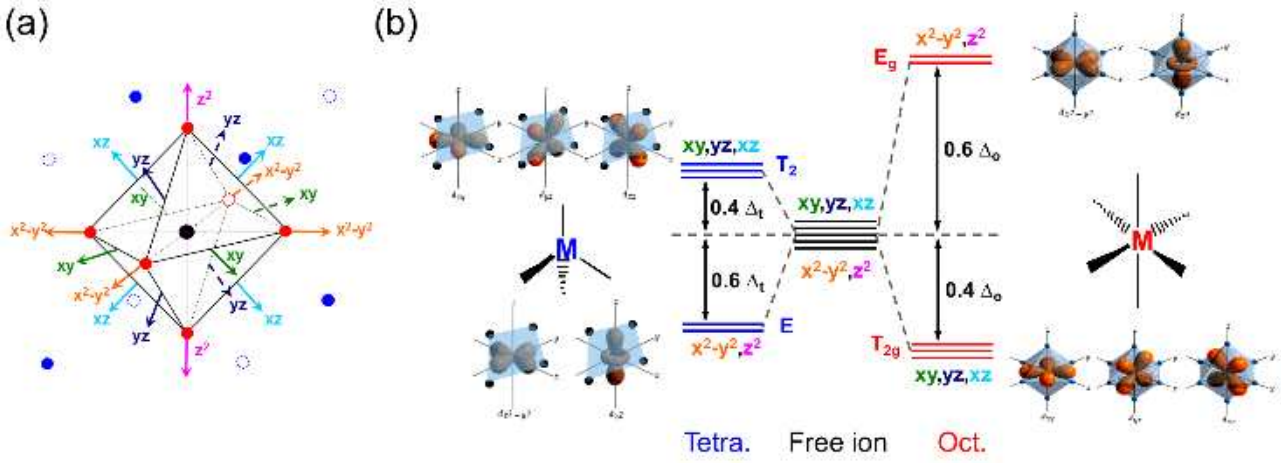

Figure 2.4 (a) Schematic representation of the orientation of the five d-orbitals xy, yz, xz, z^2 and x^2-y^2 distributed in tetrahedral coordinated state (4 blue anions) or in octahedral coordinated state (6 red anions) with transition metal ion at the center. (b) Splitting of energy levels for tetrahedral (blue) and octahedral (red) crystal fields.

For multi-electrons cations such as Cr^{3+}, the energy level splitting is much more complex and a detailed investigation was performed by Tanabe and Sugano,[13,14] that developed the famous Tanabe-Sugano diagrams for all the electronic configurations of transition metal ions, from d^2 to d^8. These diagrams are a very useful tools that has allowed to predict the optical properties of metal transition ions activated materials in terms of $10Dq$ and Racah parameter B. In Figure 2.5 a reproduction of the Tanabe-Sugano diagram for d^2 and d^3 is provided.

In 2013, Srivastava and Brik[15] introduced for the first time a new β_1 parameter (function of the Racah parameters B and C) for the prediction of the energy levels of Mn^{4+} by considering the nephelauxetic effect. In 2016, Brik *et al.*[16] applied the theory to Cr^{3+}, Mn^{4+} and Ni^{2+} in a wide variety of hosts, extrapolating an empirical equation for the determination of the lowest energy spin-forbidden transitions (from ^2E_g, ^2E_g and ^1E_g, excited state, respectively).

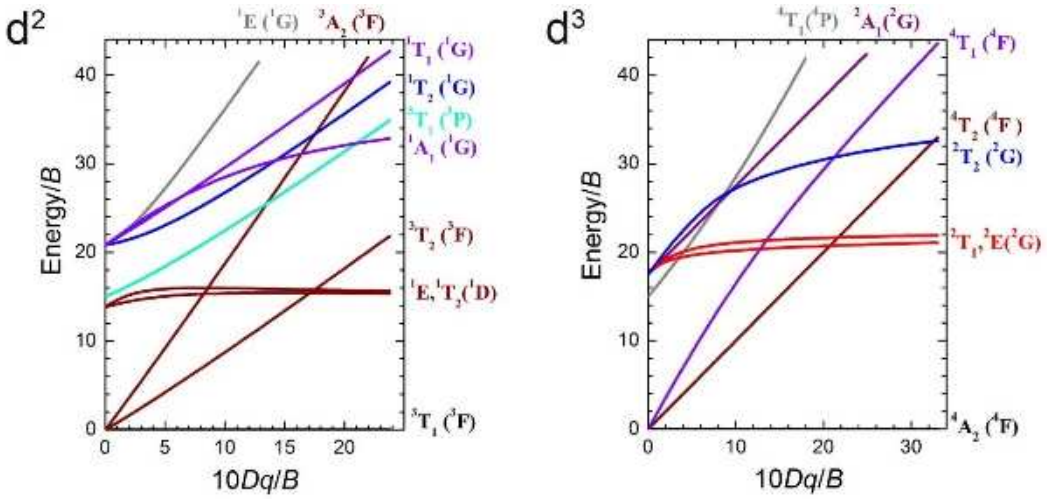

Figure 2.5 Tanabe-Sugano diagram for the d^2 and d^3 electronic configuration ions in octahedral coordination (*e.g.* Cr^{4+} for d^2 and Cr^{3+}, Mn^{4+} for d^3).

Another useful analysis to predict the energy level positions of Cr^{3+} and Mn^{4+} ions in solids was presented by Ogasawara *et al.*,[17] by means of first principle calculations. They calculated the multiplet energy level diagram as a function of the Cr-O bond length, allowing a prediction of the optical response of the materials by means of crystalline informations.

In Chapter 6, a detailed spectroscopic investigation of a Cr^{3+}-doped material will be presented.

ns^2-type ions: s-p transition

Ions with outer ns^2 configuration (Tl^+, Sn^{2+}, Pb^{2+}, Sb^{3+}, Bi^{3+}…) are considered strongly interacting with the surrounding host lattice, with a consequent effective influence on their luminescence properties.[18] The interest in this class of luminescent centers is due to their characteristic parity allowed $ns^2 \leftrightarrow nsnp$ electronic transitions that can result in efficient excitation and bright emissions.[18] Early studies have dealt with the optical properties of Tl^+ in crystalline host such as KCl,[19-22] so s^2 ions are also called Tl^+-like ions.[23]

The ns^2 ions are often characterized by off-center position due to the stereochemically active lone pair electrons (LEPs). The ns^2 pair, in principle, is spherically symmetric (without induction of distortion), thus the directed lone pair has been considered to be originated from a strong hybridisation of the *n*s states with the *n*p ones.[24] However, a more rigorous explanation is based on the pseudo-Jahn-Teller effect (PJTE), also known as second-order Jahn-Teller effect (SOJTE), that is a source of instability and distortions of high-symmetry configurations of any polyatomic system in nondegenerate states.[25] The distortions have thus a strong effect on the excited states. In addition, the excitation band position strongly depends also on the covalency (and polarizability) of the ns^2 ion-ligand bonds because of the electron cloud deformation induced by the so called *nephelauxetic effect*. As a result, the strong effect of host lattice to the energy levels of the ns^2 ions gives reason for a variety of emission energies, ranging from UV/blue to red. However, to date, even if the spectroscopic principles of the ns^2-type ions are well understood,[20]

the attribution of excitation and emission bands in many host lattices is still difficult and controversial.[26]

For an insight into the spectroscopic fundamentals of Bi^{3+} ion and a brief review on the models developed in the last years to predict the energy level positions, a focused introduction on Bi^{3+} and in general on Bi-doped materials is presented in Chapter 3. Moreover, two examples of Bi^{3+}-activated materials are shown in Chapter 7 and Chapter 8.

2.3 Selection Rules of Electronic Transitions

The electronic transitions are primarily of electric or magnetic character. In fact, in the *Fermi's golden rule*, defining the transition probability rate W_{mn} between $|m\rangle$ and $|n\rangle$ states,

$$W_{mn} = \frac{2\pi}{\hbar}|\langle n|\boldsymbol{H}|m\rangle|^2\rho(\hbar\omega) \tag{2.2}$$

the perturbation responsible for optical transitions (described by the operator $\boldsymbol{H}$) can result from the change of the center in the electric dipole moment (E_D), magnetic dipole moment (M_D) or electric quadrupole moment (E_Q). However, roughly: $W_{E_D}\sim10^8$ s^{-1}, $W_{M_D}\sim10^3$ s^{-1} and $W_{E_Q}\sim10$ s^{-1}.

2.3.1 Laporte (symmetry) selection rules

Laporte's rule states that, electric dipole transitions occur when

$$\Delta l = \pm 1$$

(l orbital quantum number), that means that the initial and final states must have opposite parity. Hence, based on Laporte's rule, transitions can be classified in parity allowed transitions and parity forbidden transitions. In particular, the parity of s and d orbitals is even, while that one of p and f orbitals is odd. Consequently, d-d and f-f transitions are parity forbidden, while f-d transitions and s-p transitions are parity allowed. Moreover, the parity rule generally determines the transition probability, explaining, for example, the very intense absorptions due to f-d transition in Ce^{3+}-doped materials or s-p transitions of Bi^{3+} in many hosts.

It should be point out that, although the electronic transition process mainly depends on the electronic dipole transition (parity allowed), magnetic dipole and electronic quadrupole (both parity forbidden) also give minor contributions in the real process. In fact, the real transition moment is:[27]

$$|M_{mn}|^2 = |(e\boldsymbol{r})_{mn}|^2 + \left|\left(\frac{e}{2mc}\boldsymbol{r}\times\boldsymbol{p}\right)_{mn}\right|^2 + \frac{3\pi\omega_{mn}^2}{40c^2}|(e\boldsymbol{r}\cdot\boldsymbol{r})_{mn}|^2 \tag{2.3}$$

where, the first term on the right hand side is the electronic dipole momentum (E_D), the second term represents the magnetic dipole momentum (M_D) and the third is the electronic quadrupole momentum (E_Q). Although the E_D-transition is parity forbidden for f-f and d-d transitions of free

lanthanide ions and transition metal ions, in crystals, the transition become partially allowed by the odd component of the crystal field.

2.3.2 Spin and total quantum number selection rules

The conditions describing the selection rules governing the dipole transitions are reported:

1. In the case of weak coupling (LS-coupling scheme) between the orbital angular momentum (l) and spin angular momentum (s), the transition occurs if:
   $\Delta S = 0$ (spin-allowed transition);
   $\Delta L = 0$ or ± 1;
   $\Delta J = 0$ or ± 1 ($J = 0 \rightarrow J = 0$ is forbidden).
2. In the case of strong coupling (JJ-coupling scheme) between the orbital angular momentum (l) and spin angular momentum (s), the transition occurs if:
   $\Delta J \leq 6$ ($J = 0 \rightarrow J = 0,1,2,3,5$ are forbidden).

For magnetic dipole transitions, the selection rule is: $|\Delta J| = 0, \pm 1$ ($J = 0 \rightarrow J = 0$ is forbidden).

2.4 Concentration and Thermal Quenching Processes

The term *quenching* is usually used to include any phenomenon which leads to an undesirable reduction of the emission intensity generated by a luminescent center. Even if the causes of this phenomenon are multiple and different (*e.g.* temperature, doping concentration), the presence of a competitive deactivation mechanism, leading to the non-radiative relaxation process, always affects the emission yield of a radiative transition involving the relaxation from an excited to a low-lying energy state.

In this section, the main radiationless processes for an excited center are presented.

Concentration quenching

High dopant concentration favours high energy transfer rates between dopants and, if the average distance between the luminescent centers is smaller than the critical Förster radius R_0 (a parameter that depends on the nature of host and activator), the energy can migrate among the donor species until a quenching site is reached (*i.e.* trapped into a non-luminescent defect or impurity). The loss of excitation energy by non-radiative process leads to a reduction of the luminescence quantum yield. Auzel *et al.*[28] described the quantum efficiency η_{em} of the lowest excited state depending on the luminescent ion concentration x through the following relationship:

$$\eta_{em}(x) = \left[1 + \frac{9}{2\pi}\left(\frac{x}{x_0}\right)^2\right]^{-1}, \tag{2.4}$$

where x_0 is the critical concentration.

In this regard, it is important to note that large Stokes-shift reduces the energy transfer probability and thus the concentration quenching impact.[29]

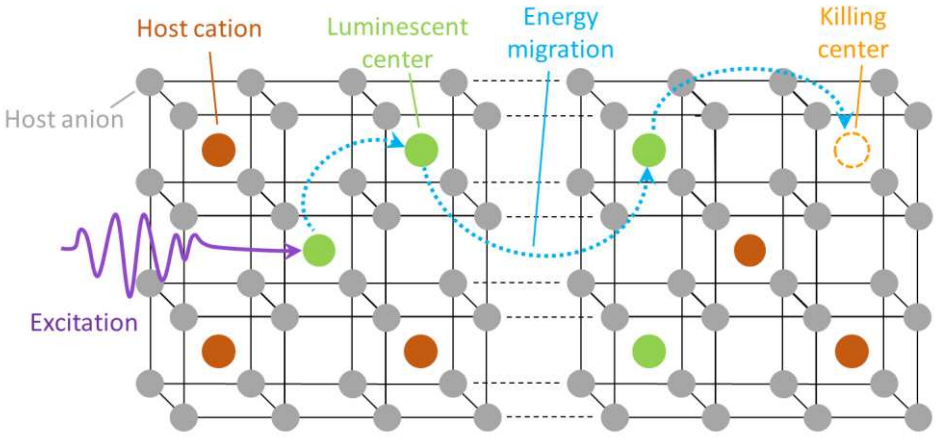

Figure 2.6 Scheme of concentration quenching in doped crystal. When luminescent centers are close together, the excitation can migrate and reach a quenching site in the crystal where be lost as heat. Grey and brown spheres represent the host anion and cation, respectively, green spheres the luminescent centers, orange dashed circle the killing center (quenching site such as a vacancy) and the light blue dotted arrows the energy migration through the crystal.

Thermal quenching

It is well known that high temperature can be detrimental for the luminescence in inorganic solids, leading to an overall decrease of the emission intensity. This process is generally known as *thermal quenching*.

Describing thermal quenching process, an energy barrier ΔE_T can be usually associated to the quenching process.[30] Experimentally, the thermal quenching profile of a material is described by

$$(T) = I(0)\left(1 + \frac{\tau_R}{\tau_{NR}} e^{-\Delta E_T / k_B T}\right)^{-1} \tag{2.5}$$

where τ_R is the intrinsic radiative decay constant of the ion, τ_{NR} is the decay constant for the non-radiative process and k_B is the Boltzmann constant. An alternative way to estimate ΔE_T is provided by considering the relationship with the specific temperature $T_{50\%}$, that is the temperature at which the intensity decreases down to 50% of the largest value recorded at low temperature:

$$T_{50\%} = \frac{\Delta E_T}{k_B T \ln \frac{\tau_R}{\tau_{NR}}} \tag{2.6}$$

As previously mentioned, the thermal quenching of luminescence is usually described in term of configurational coordinate model of non-radiative relaxation processes. Referring to Figure 2.7a, if the temperature is high enough to populate the energy levels in proximity or above the crossing point between the two parabolas, the system relaxes non-radiatively through the vibrational levels of the equilibrium ground state. As a result, the energy is given up as phonons to lattice during the process.[18]

Unlike the concentration quenching, the thermal quenching process drastically increase with Stokes-shift increasing. In fact, the bigger the Stokes-shift, the lower the energy between the bottom of the excited state (equilibrium position) and the crossing point of the parabolas.

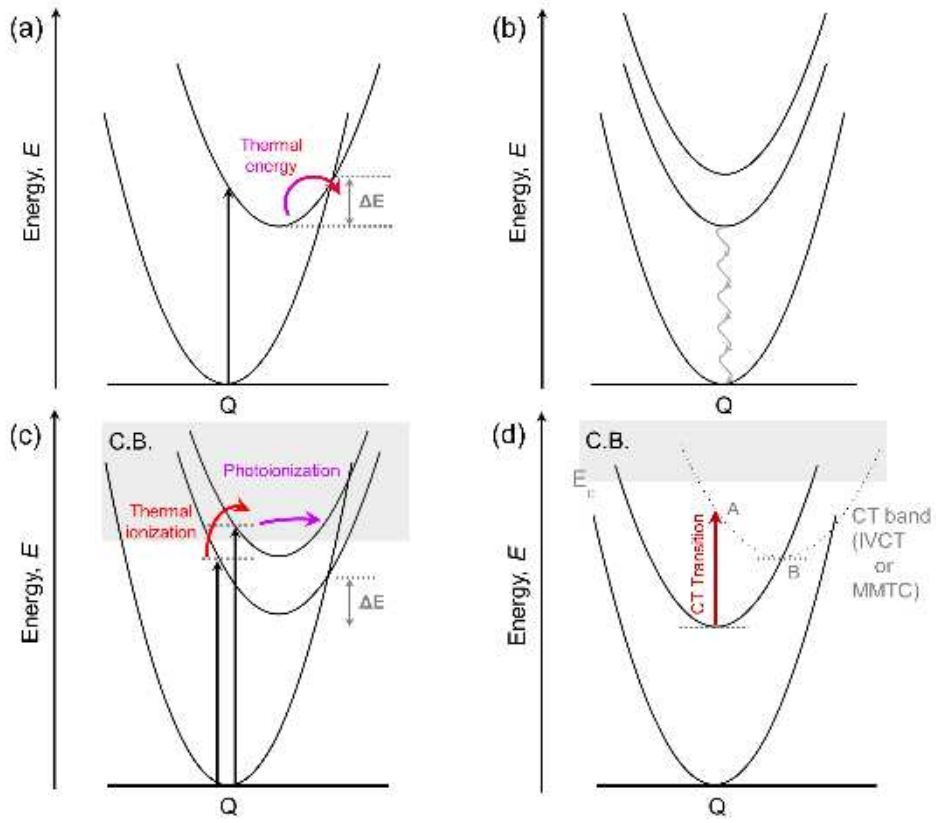

Figure 2.7 Schematic representation of luminescence quenching mechanisms; models based on (a) thermally activated crossover, (b) multiphonon relaxation, (c) thermally activated ionization and photoionization and (d) quenching process induced by charge transfer states (IVCT and MMCT).

In the case of weak coupling ($S \approx 0$) there is no crossover point between the GS and ES parabolas (*e.g.* for the trivalent lanthanide f-f transitions). However, if the separation between two levels ΔE (the so called *energy gap*) is equal to or less than 4-5 times the vibrational energy $\hbar\omega$ typical of the host, the excited emitter rapidly relaxes non-radiatively. This non-radiative process is called *multi-phonon relaxation*. This process can thus reduce the quantum efficiency and shorten the lifetime of an emitting state depending on the coupling with the surrounding vibrations.

The dependence of non-radiative probability W_{NR} on energy gap to the next lowest level ΔE and on the number of effective phonons p (where $p = \Delta E / \hbar\omega_{eff}$) is expressed by:[4]

$$W_{NR} = Ae^{-\alpha\Delta E} = Ae^{-(\alpha\hbar\omega_{eff})p} \tag{2.7}$$

the so called *energy gap law*. Here, $\hbar\omega_{eff}$ is the effective phonons, the highest energy phonons that are expected to participate in the non-radiative de-excitation process. At low temperature and small Huang-Rhys parameter, the temperature dependent multi-phonon relaxation rate can be express as:[31]

$$W_{NR}(T) = W_{NR}(0)\{1 + n_{eff}\}^{p} \tag{2.8}$$

where the occupancy of the effective phonon modes (Bose-Einstein occupation number):

$$n_{eff} = \left[exp\left(\hbar\omega_{eff}/k_B T\right) - 1\right]^{-1} \quad (2.9)$$

and p is the order of the multi-phonon process ($\Delta E/\hbar\omega_{eff}$).

In addition to the thermally activated crossover, the thermal quenching process can be driven also by thermally activated *photoionization process* (Figure 2.7c). In fact, if an emitting state is situated just below the conduction band, the ionization of an electron from the excited state to the conduction band can take place.[18,32] This is the case for Eu^{2+} 5d-4f emission in some hosts, in which 5d electron is thermally excited to the conduction band states.[32-34] Moreover, the same quenching process was considered to explain the absence of Ce^{3+} luminescence in different hosts[35] and it was recently stated as the thermal quenching mechanism in the most famous phosphor for white LEDs (w-LEDs), YAG:Ce^{3+}.[36]

In this context, as will reported in Section 2.6, the vacuum referred binding energy diagram (VRBE) is a powerful tool to investigate the absolute energy position of valence and conduction band edges relative to the excited states of luminescence centers, making light on the mechanisms involved in the luminescence processes.

Finally, another path that can bring to the quenching of luminescence involves the *charge transfer states* (CT). In the case of Y_2O_3:Eu^{3+} the fast radiationless transition from the CT state to the excited ^5D levels is responsible of the useful properties of this material, however, a CT state with large offset can induce the population of the ground state strongly reducing the luminescence (scheme in Figure 2.7d). As will be described in detail in Chapter 3 about the case of Bi^{3+}, depending on the nature of the dopant pairs in solid host, two different charge transfer states are defined: *intervalence charge transfer* (IVCT) states of mixed valence pairs and *metal-to-metal charge transfer* (MMCT) states of heteronuclear pairs.[37]

2.5 Energy Transfer and Upconversion Processes

In this section, energy transfer processes between a donor and an acceptor (also called sensitizer and activator) is described. The energy transfer between two optically active species embedded in a crystal can result in a wide variety of interesting phenomena, still object of an intense research activity in the field. After the introduction to the general knowledge on mechanisms involving the non-radiative energy transfer theory developed by Förster[38] and Dexter,[39] we briefly discuss the basic concepts of the upconversion processes (topic of the Chapters 4 and 5).

2.5.1 Energy transfer

When the energy level structure is adequate, an excited center can act as an energy donor for an acceptor. In general, energy transfer from a donor to an acceptor may take place *via* three different processes depending on the coupling regime (Figure 2.8a): exchange interaction, non-radiative multipole-multipole interaction and radiative transfer.

In the case of a *radiative energy transfer*, no actual coupling of ions exists, and the transfer of the energy occurs through the radiative reabsorption by an acceptor of a real photon emitted by a donor (also called reabsorption mechanism). For a radiative energy transfer by dipole-dipole interaction, $W_{rad}^{DA} \propto 1/R^2$. From the experimental point of view, a radiative energy transfer is characterized by (i) spectral dips in the emission spectra of the donor corresponding to the absorptions of the acceptor and (ii) unchanged decay time of the donor.

Unlike radiative ET, when the ions are closely spaced (strong-coupling, in a range of few angstroms) the transfer of excitation energy takes place by direct electron transfer exchange among the ions, while in a weak-coupling regime (several nanometers), the ions interact through coulombic interactions with a non-radiative energy transfer process governed by multipolar interactions. According to Fermi's golden rule, the probability W_{DA} of energy transfer between an excited donor D^* and a relaxed acceptor A is:

$$W_{DA} = \frac{2\pi}{\hbar} |\langle D^*, A | \boldsymbol{H}_{DA} | D, A^* \rangle|^2 \int f_{em}^{D}(E) f_{abs}^{A}(E) dE \qquad (2.10)$$

where $\boldsymbol{H}_{DA}$ is the interaction Hamiltonian between donor and acceptor (with energy transfer process described as $D^* + A \rightarrow D + A^*$; the asterisk denotes excited states), and the integral indicates the spectral overlap between the emission spectrum of the donor $f_{em}^{D}(E)$ and the absorption spectrum of the acceptor $f_{abs}^{A}(E)$ (Figure 2.8b,c).

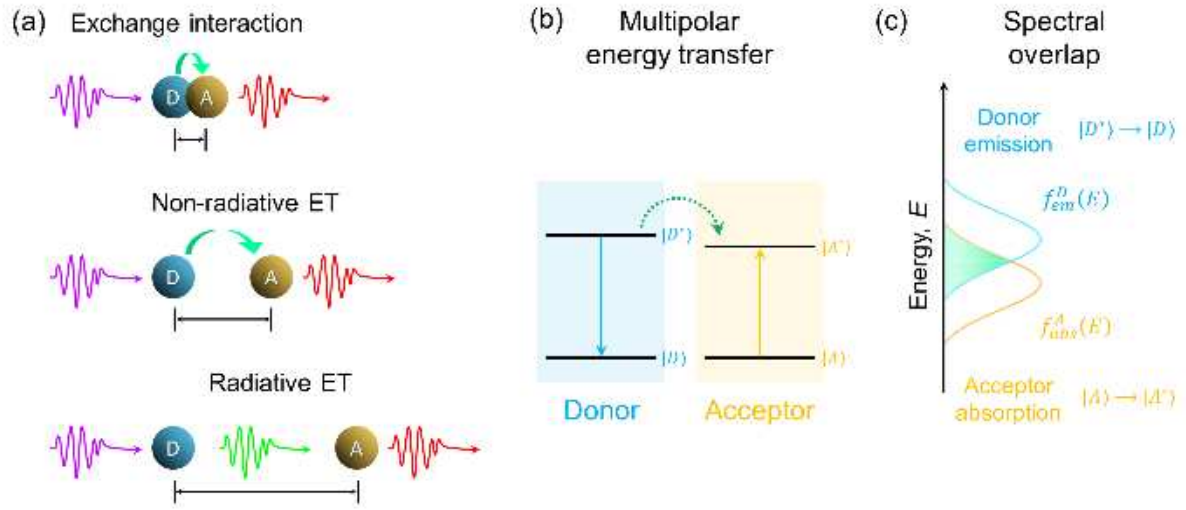

Figure 2.8 (a) Scheme of the possible energy transfer mechanisms (radiative, non-radiative and exchange interaction) and (b) energy level diagram for the non-radiative energy transfer process between a D-A pair with (c) the spectral overlap between donor emission ($f_{em}^{D}(E)$) and acceptor absorption ($f_{abs}^{A}(E)$) profiles.

If an energy donor D and an acceptor A are close enough that their electronic wavefunctions overlap, a non-radiative energy transfer by *exchange interaction* can occur (also known as Dexter transfer). If the wavefunctions overlap varies as e^{-R/a_0},[40] the transfer probability due to exchange interaction is given by:[39]

$$W_{exc}^{DA}(R) = \left(\frac{2\pi}{\hbar}\right) A^2 e^{-\frac{2R}{a_0}} \int f_{em}^{D}(E) f_{abs}^{A}(E) dE \qquad (2.11)$$

where A^2 is a constant, R the separation between D and A, $f_{em}^{D}(E)$ and $f_{abs}^{A}(E)$ the spectral shape of the D emission and A absorption, respectively, and a_0 the Bohr effective radius. When the distance R between the donor and the acceptor increases, the probability decreases exponentially.

In the *electrostatic interaction* range, the resonant energy transfer mechanisms depend on the character of D and A transitions. The strongest transitions are usually electric dipole transitions, thus an electric dipole transition of the donor couples an electric dipole transition of the acceptor (Förster-energy transfer type) with a transfer probability given by:[38]

$$W_{dd}^{DA}(R) = \frac{3c^4\hbar^4\sigma_A}{4\pi n^4 \tau_D R^6} \int \frac{f_{em}^{D}(E) f_{abs}^{A}(E)}{E^4} dE \tag{2.12}$$

with σ_A absorption cross-section of the acceptor, τ_D radiative lifetime of the donor and n refractive index of the crystal. In order to describe the strength of energy transfer for a donor-acceptor couple, a convenient parameter introduced by Förster is the critical radius R_0, defined as the D-A separation at which the probability of transfer equals the probability of radiative emission of the donor (*i.e.* $W_{dd}^{DA} \cdot \tau_D = 1$). The energy transfer probability can thus be expressed as:

$$W_{dd}^{DA}(R) = \frac{1}{\tau_D}\left(\frac{R_0}{R}\right)^6. \tag{2.13}$$

Other electric multipolar interactions become relevant at shorter distances, with dipole-quadrupole (dq) interaction that varies as R^{-8} and quadrupole-quadrupole (qq) interaction that depends as R^{-10}. Dexter demonstrated that the energy transfer probability can be generalized:[39]

$$W_{DA}(R) = \frac{1}{\tau_D}\left(\frac{R_0}{R}\right)^s \tag{2.14}$$

where s=6 for dipole-dipole interactions, s=8 for dipole-quadrupole interactions and s=10 for quadrupole-quadrupole interactions.

Moreover, in general, the dependence of the transfer probability $W_{DA}(R)$ on R due to the multipolar interaction can be written as:[4]

$$W_{DA}(R) = \frac{\alpha_{dd}}{R^6} + \frac{\alpha_{dq}}{R^8} + \frac{\alpha_{qq}}{R^{10}} + \cdots \tag{2.15}$$

where α_{dd}, α_{dq} and α_{qq} are factors that weight the different interactions depending also on the overlap. The equation states that, if the electric dipole transitions are not completely allowed, higher interaction processes (d-q or q-q) can have larger transfer probabilities at short distances.

If, from one hand, energy transfer processes can be detrimental for the overall luminescent quantum yield (as for the case of *energy migration* induced by high concentration described in Section 2.4), on the other hand, many different types of energy transfer processes can occur between ions, leading also to interesting phenomena such as upconversion and downconversion (Figure 2.9).

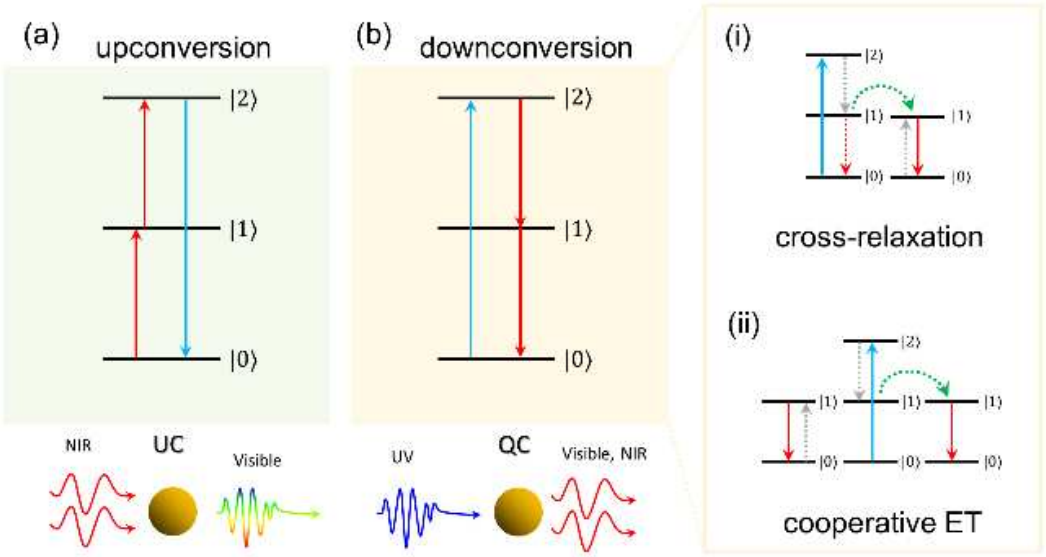

Figure 2.9 Schematic diagram of the upconversion (a) and downconversion (b) processes. The two main mechanism involved in downconversion process: (i) cooperative energy transfer consists in the simultaneous transfer of energy to two nearby acceptors, while (ii) cross-relaxation deals with the transfer of partial excitation energy of a donor to an acceptor.

Upconversion process (UC) refers to the generation of one high-energy photon from two or more low-energy absorbed photons (Figure 2.9a). Chapters 4 and 5 deal with bismuth-based upconverting nanoparticles and Section 2.5.2 summarized the main upconversion mechanisms involved in lanthanide doped materials.

Downconversion process (or quantum-cutting) consists in the generation of two low-energy photons from one high-energy absorbed photon. Figure 2.9b shows the quantum cutting of a single ion (for a simple schematic description), however this process is inefficient and an energy transfer process is usually involved. This process can be ascribed to different energy transfer pathways involving mechanisms such as cooperative energy transfer (Figure 2.9b) or cross-relaxation (Figure 2.9c). Downconversion processes are beyond the scope of the present thesis and will not be discussed further. For a detailed description refers to reff. 41,42.

2.5.2 Upconversion

An anti-Stokes process consists in the emission of photons with higher energy than the absorbed ones. In general, this non-linear process occurs, in order of increasing efficiency, in three main ways:[43,44] two-photon absorption (TPA), second harmonic generation (SHG) and upconversion (UC).

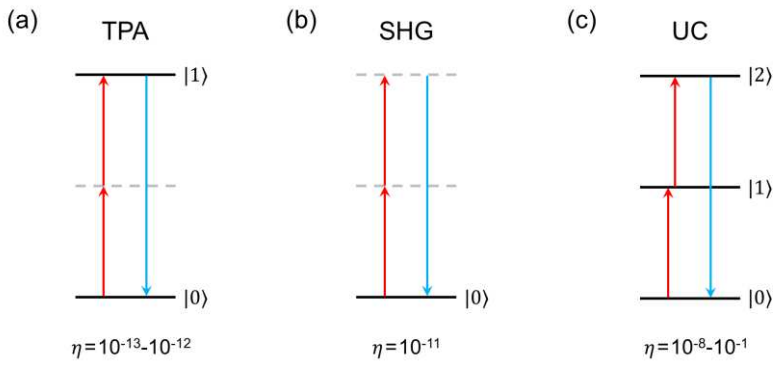

Figure 2.10 Simplified energy level diagrams of the typical anti-Stokes processes: (a) two-photon absorption (with an efficiency η of 10^{-13}-10^{-12} cm^2W^{-1}), (b) second harmonic generation (with η in the order of 10^{-11} cm^2W^{-1}) and (c) upconversion (with an efficiency η in the range of 10^{-8}-10^{-1} cm^2W^{-1}, depending on the mechanism).

TPA and SHG are characterized by a virtual intermediated level involved in the process. In SHG, also the emitting level is virtual (coherent excitation is needed). Hence, these two processes are very inefficient (η in the range of 10^{-13}-10^{-11} cm^2W^{-1} [44,45]) and very high excitation power is required. Unlike TPA and SHG, UC process depends on a real intermediate energy state leading to higher efficiency (up to 10^{-1} cm^2W^{-1}). The existence of a real long-lived intermediate state between the ground state and the emitting state is required to store the energy up to the absorption of the second low-energy photon, leading the excitation to a higher-lying excited state. It is important to underline that the rich energy-level scheme (as described in Section 2.2) makes lanthanide ions ideal candidates for photon upconversion.

The theoretical concept of upconversion was firstly introduced in 1959 by Bloembergen,[46] but only in 1966, Auzel[44] and Ovsyankin and Feofilov[47] independently showed experimentally the upconversion process for the first time. Since this year, many efforts were devoted, from one hand, to the comprehension of the mechanisms and the key parameters involved for the design of efficient upconverting materials and, on the other hand, to the application of such materials in many technological fields. In particular, in the last two decades, with the rapid emergence of nanotechnologies, enormous attention was attracted by the use of upconverting nanoparticles in biological applications such as bio-imaging and nanothermometry.

The schematic energy level diagram of UC process illustrated in Figure 2.11 is a simplified view of the real process. Hereinafter, the main upconversion mechanisms involved, such as (a) excited-state absorption (ESA), (b) energy transfer upconversion (ETU), (c) sensitized energy transfer upconversion (sensitized ETU), (d) cooperative luminescence upconversion (CLU) and (e) cooperative sensitization upconversion (CSU) are presented.

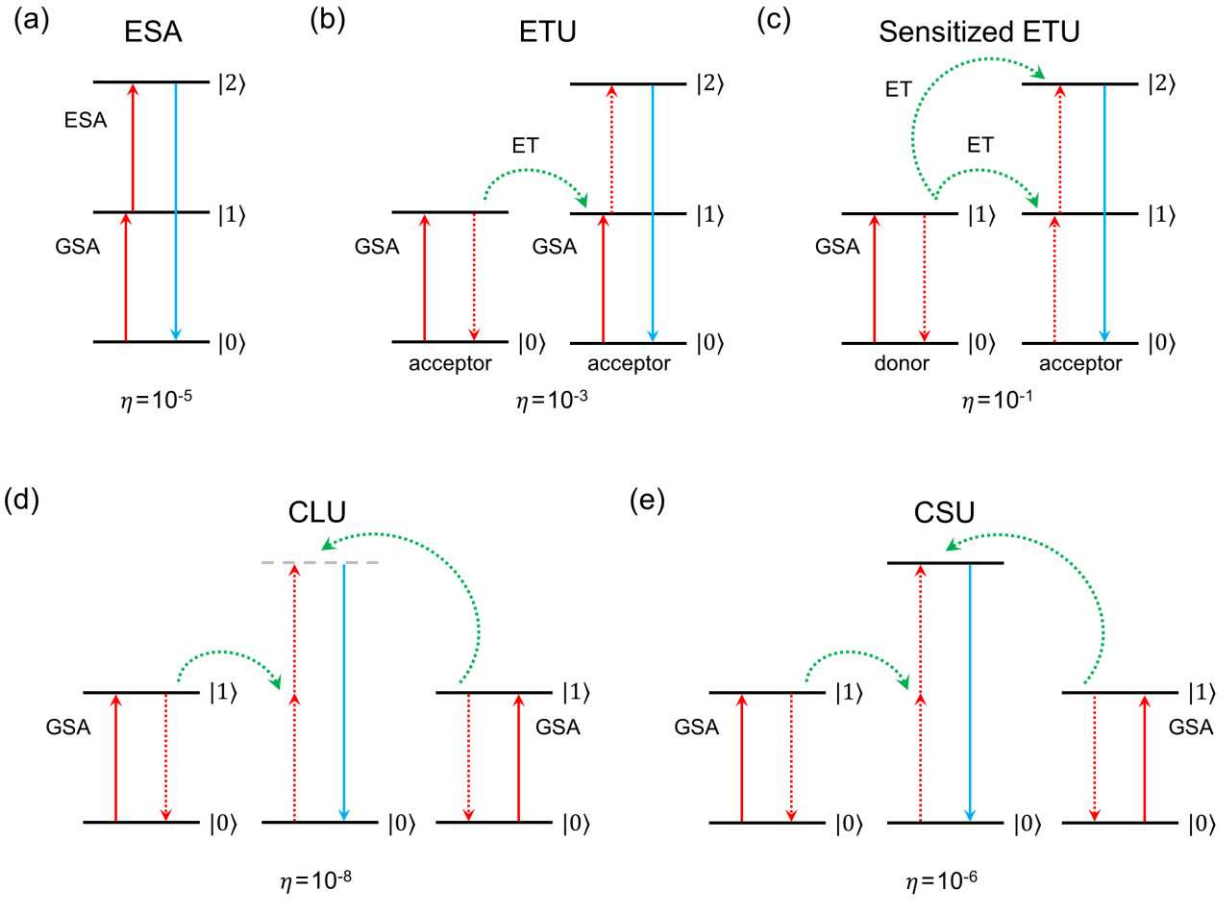

Figure 2.11 Principal UC mechanisms: (a) excited-state absorption ESA, (b,c) sensitized energy transfer upconversion ETU, (d) cooperative luminescence upconversion CLU and (e) cooperative sensitization upconversion CSU.

Excited-State Absorption (ESA)

Ground state absorption/excited state absorption (GSA/ESA) is the simplest upconversion mechanism involving only one dopant (Figure 2.11a). The mechanism consists in the first absorption of the exciting photon by the ground state $|0\rangle$ populating the intermediate state $|1\rangle$. If the lifetime of the intermediate state $|1\rangle$ is long enough, a second photon can be absorbed, exciting the ion to the higher-lying excited state $|2\rangle$ from which upconversion luminescence originates. Among the lanthanide ions with a suitable ladder-like energy level structure for ESA process, Er^{3+}, Ho^{3+}, Tm^{3+} and Nd^{3+} can be mentioned.

Energy Transfer Upconversion (ETU)

Upconversion through energy transfer mechanism (ETU) (Figure 2.11b,c) is the most efficient upconversion mechanism. It involves non-radiative energy transfers between two dopants and it exists in two different types. It can involve a pair of identical ions (donor-donor pair) where

intermediate states of the identical centers are excited by GSA and then one of the centers is excited to a higher energy level *via* energy transfer (Figure 2.11b). This is the case, for example, of Er^{3+}. Alternatively, the mechanism (GSA/ETU) occurs between two different centers: a donor (*e.g.* Yb^{3+}) and an acceptor (*e.g.* Er^{3+}, Ho^{3+}, Tm^{3+}). In the case of donor-acceptor pair, the donor absorbs the incident photon and then it relaxes to a lower-energy state (the ground state for Yb^{3+}) by transferring the energy to a neighbouring acceptor that eventually emits (Figure 2.11c).

The sensitized energy transfer upconversion mechanism is the key mechanism in the materials with the highest efficiency that are used in biological applications.

Cooperative Luminescence Upconversion (CLU)

Upconversion by cooperative luminescence (Figure 2.11d), consists in the sequential absorption of two exciting photons by two different ions. Consequently, both ions decay simultaneously with the emission of a single photon of an energy that is the sum of the energies of the ions. The cooperative luminescence emission occurs from a virtual level, with a very low emission probability.

Cooperative Sensitisation Upconversion (CSU)

The cooperative sensitization upconversion process (CSU) is similar to the CLU mechanism, with the difference that, after the double absorption of the photons, the energies of the two ions are transferred to a third ion that is brought to a higher-lying level with energy equal to the sum of those of the former two ions. The main difference is thus the presence of a real emitting state with a consequent higher efficiency respect to the CLU process. CSU has been reported in a variety of Yb^{3+}-Tb^{3+} codoped systems, such as $SrCl_2$,[48] $Cs_3Tb_2Br_9$ [48,49] and $LaPO_4$.[50]

Among the possible mechanisms depicted in Figure 2.11, it should be noted that UC process is strongly dominated by the contributions of ETU processes occurring between a donor-acceptor pair (sensitized ETU). This is the case for the most famous couples Yb^{3+}-Ln^{3+} with Ln=Er, Tm or Ho. In such case, the energy transfer from the donor (Yb^{3+}) to the acceptor (Ln^{3+}) is dominates by dipole-dipole interactions, with an energy transfer probability that follows the Eq. 2.12. From this equation, it is clear that the requirement for an efficient energy transfer is a high absorption cross-section of the acceptor (σ_A) at the emission wavelength of the donor, as for Yb^{3+}-Er^{3+} couple exciting at 980 nm. In the case of the well-known Yb^{3+}-Ho^{3+} and Yb^{3+}-Tm^{3+} couples, the energy mismatch is compensated by *phonon-assisted* energy transfer.

As reported by Pollnau *et al.*,[51] the UC photoluminescence intensity I_{UC} has a non-linear dependence on the excitation density:

$$I_{UC} = k_{mat} P^n \tag{2.16}$$

where k_{mat} is a coefficient related to the material, P is the power of the pump laser and n is the number of the photon required to produce UC photoluminescence. A very useful way for the determination of n consists in evaluating this parameter as the slop of the linear relationship resulting from the log-log graphic representation of the I_{UC} *vs.* P trend (see Section 4.3.3). Moreover, it is clear that the n estimate can be affected by many competing processes (*e.g.* the decay rate at the intermediated states) and at high excitation density a saturation effect can take place.[51-53] Moreover, by considering the strong dependence of the upconversion process on the excitation density, it is interesting to derive the power dependence of the upconversion quantum yield (UCQY), defined as the ratio of the emitted photons to the number of absorbed NIR photon:

$$UCQY = \frac{I_{UC}}{\alpha P} \propto P^{n-1} \tag{2.17}$$

Because of this dependence, the UCQY for an UC peak must be referred to the particular excitation density used during the measurements.

In addition to the above mechanisms, the so called *photon avalanche* (PA) effect must be mentioned. PA is a process that produce UC above a threshold of excitation power. This particular effect consists in a looping process (Figure 2.12) involving several absorption and energy transfer processes (*i.e.* excited state absorption (ESA) and efficient cross-relaxation (CR) processes).

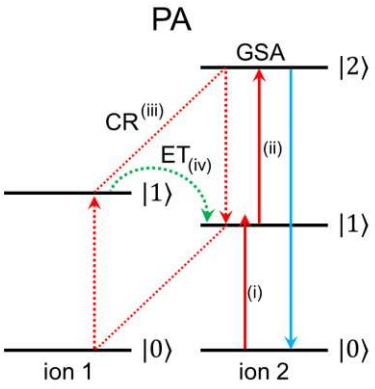

Figure 2.12 Photon avalanche (PA) process.

The looping process occurs following the scheme in Figure 2.12: (i) weak non-resonant GSA populates the $|1\rangle$ state of ion 2, then (ii) ESA process bring the ion to the emitting level $|2\rangle$, following by (iii) efficient CR process between the two ions $|2\rangle_{ion2} + |0\rangle_{ion1} \rightarrow |1\rangle_{ion2} + |1\rangle_{ion1}$ and finally (iv) the loop is complete with the transfer of energy of ion 1 to ion 2, populating the $|1\rangle$ state.[45,54] The net effect of the looping process is the generation of two ions excited at the metastable $|1\rangle$ state starting from one, with the production of four in the second cycle, eight in the third, and so on, with an avalanche effect. However, it should be point out that the PA effect is seldom observed in UC nanoparticles, probably because of the particular requirements for the avalanche regime.

2.6 Persistent Luminescence

Persistent luminescence (PersL), also called phosphorescence, afterglow or long lasting phosphorescence (LLP), is generally known as the phenomenon of emission of light for appreciable time (from seconds to days) ones the excitation radiation is removed. Even if the first observations of such phenomenon dates 1602,[55] only from the discovery by Matsuzawa (in 1993) and the early studies[56,57] of very bright and long afterglow in $SrAl_2O_4:Eu^{2+},Dy^{3+}$, the design and development of new persistent luminescent materials became an active research area.

As well reviewed by Smet *et al.*,[58,59] the extensive research on persistent luminescent materials of the last two decades has resulted in the discovery of a wide variety of materials that can be mainly divided in Eu^{2+}-doped and non-Eu^{2+}-doped compounds (in these two review, PerL compounds are listed). Figure 2.13 shows how, nowadays, the emissions of the persistent luminescent materials cover almost the whole visible spectrum.

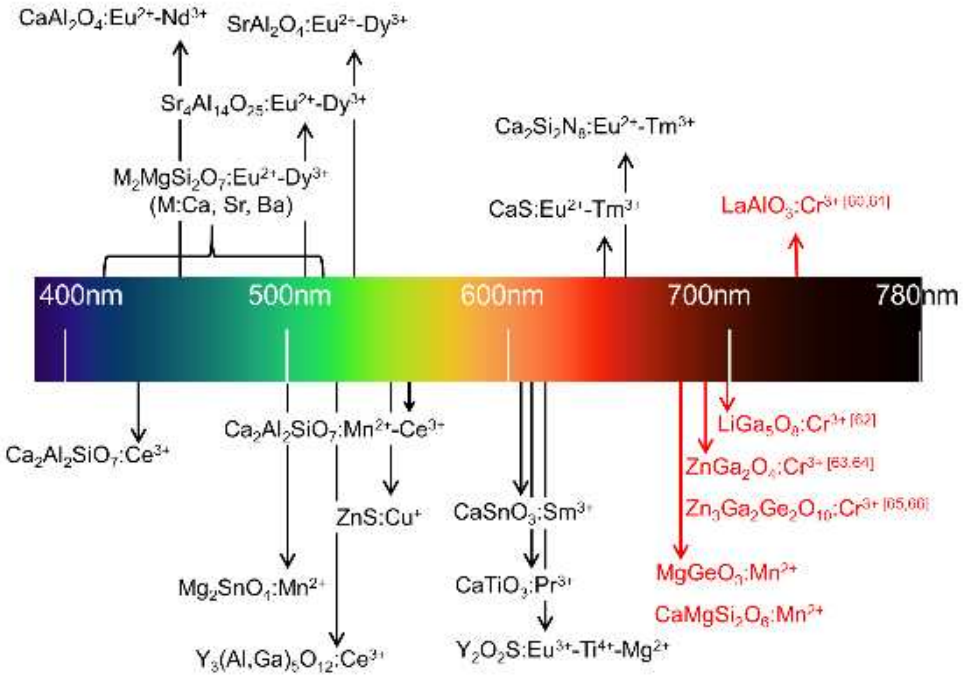

Figure 2.13 Main persistent luminescent materials respect to the emission wavelengths. All the value reported for the materials emitting in the blue-red region (without superscripts) come from reff. 58,59. The values reported for the red-NIR emitting materials are taken from reff. 60-66 (superscripts).

In 2007, the use of the red to NIR persistent nanoparticles was introduced as a new concept for bio-imaging applications by Chermont *et al.*.[67] The possibility to charge these optical labels before the injection allowed to completely remove the problems of autofluorescence in biological environment, improving significantly the signal to noise ratio. Hence, the design of persistent materials able to emit in the red to NIR region became an active research area in the last decade, showing great results for transition metal-activated oxide materials, in particular for Cr^{3+}-doped

persistent phosphors[68] (some of which are reported in red in Figure 2.13). Among the Cr^{3+}-doped materials with long-lasting potentiality suitable for *in vivo* imaging, $ZnGa_2O_4:Cr^{3+}$ system showed high performances[63] becoming one of the most investigated materials from the fundamental and applied point of view.[64,69-73] Moreover, other worth mentioning Cr^{3+}-activated persistent systems are $LiGa_5O_8:Cr^{3+}$,[62] $Zn_3Ga_2Ge_2O_{10}:Cr^{3+}$ [65,66] and $LaAlO_3:Cr^{3+}$.[60,61]

An afterglow phosphor is composed by (i) the host lattice, (ii) the luminescent (recombination) center and (iii) the trapping center. In a simplified view, the mechanism is based on the ability to storage the excitation energy by traps (intrinsic or induced) and the slow release of trapped charge carriers by thermal excitation with subsequent photon emission from luminescent centers. Figure 2.14 shows the sketch of the energy level diagram with the typical electron trapping process generally accepted as the mechanism for the $SrAl_2O_4:Eu^{2+},Dy^{3+}$ system and for the general Cr^{3+}-doped persistent materials.

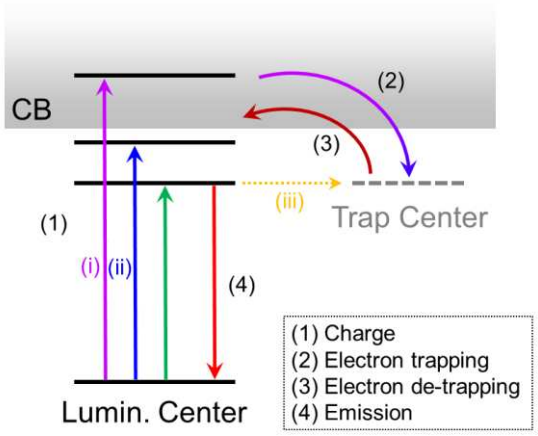

Figure 2.14 Schematic energy level diagram of the persistent luminescence mechanism with different electron trapping processes: (i) direct excitation into the CB, (ii) thermally assisted photoionization process and (iii) quantum tunnelling effect.

In this view, the electron trapping process to the conduction band can be achieved by different paths:[68] (i) excitation from the GS directly in the CB, (ii) from GS to the energy level slightly below the CB followed by a thermally assisted photoionization process that bring the electron into the CB or (iii) quantum tunnelling effect from an energy level far below the bottom of the CB.

On the basis of the knowledge gained in the recent years, the key point for the design of the effective persistent phosphors is the ability to tune and control the so-called *trap depth*, the energy difference between the bottom of the conduction band and the electron trap ($\Delta\varepsilon$ in Figure 2.14). In this view, the bandgap engineering technique was recently exploited as a very effective method to adjust and optimize the trap depth in different systems, such as $Y_3Al_{5-x}Ga_xO_{12}:Ce^{3+},Cr^{3+}$,[74,75] $Y_3Al_{5-x}Ga_xO_{12}:Cr^{3+}$,[76] $Gd_3Al_{5-x}Ga_xO_{12}:Cr^{3+},Eu^{3+}$,[77] $Zn(Ga_{1-x}Al_x)_2O_4:Cr^{3+},Bi^{3+}$ [78] and $Mg_3Y_2(Ge_{1-x}Si_x)_3O_{12}:Ce^{3+}$.[79]

The mechanism of persistent luminescence briefly described above, considers electron trap as trapping center to store the excitation energy, however, also hole-trapping and -detrapping mechanism *via* the valence band (VB) was recently evidenced in some hosts.[80]

The model proposed by Dorenbos,[81] based on a combination of the energy level structures of the host (top of the VB and bottom of the CB energies), of the luminescence centers and of the co-dopants (acting as traps), has brought to a real deeper understanding of the persistence mechanism. In fact, even if the model makes several simplifying assumptions (*e.g.* the role of co-dopants is not explained), it was demonstrated to be successfully used to design efficient persistent luminescence phosphors. The vacuum referred binding energy (VRBE) diagram is thus a powerful tool for the realization of persistent luminescence materials as well as for a better comprehension of those mechanisms involved in luminescent systems in which a key role is played by the relative positions of the energy levels of the emitting centers respect to that of the VB and CB of the host. With this aim, the use and the potentiality of the VRBE diagram approach will be discuss in detail in Chapter 4 and 7. Figure 2.15 summarizes the main data needed for the design of the VRBE diagram in the case of lanthanide ions in a host *A*:[9,82,83] (1) the bandgap value of the host E_g, (2) the charge transfer (CT) transition energy of Eu ($Eu^{3+} + e^-[O(2p)] \longrightarrow Eu^{2+}$) for assessing the Eu^{2+} ground state energy (also Ce CT can be used) and (3) the vacuum referred binding energy of an electron in the $4f^7$ ground state of Eu^{2+} in the chemical environment *A*, E_{4f} (7, 2+, *A*), defined as

$$E_{4f}(7,2+,A) = -24.92 + \frac{18.05 - U(6,A)}{0.777 - 0.0353U(6,A)} \qquad (2.18)$$

where -24.92 eV is the VRBE for the free ion and *U*(6,*A*) is the Coulomb repulsion energy.

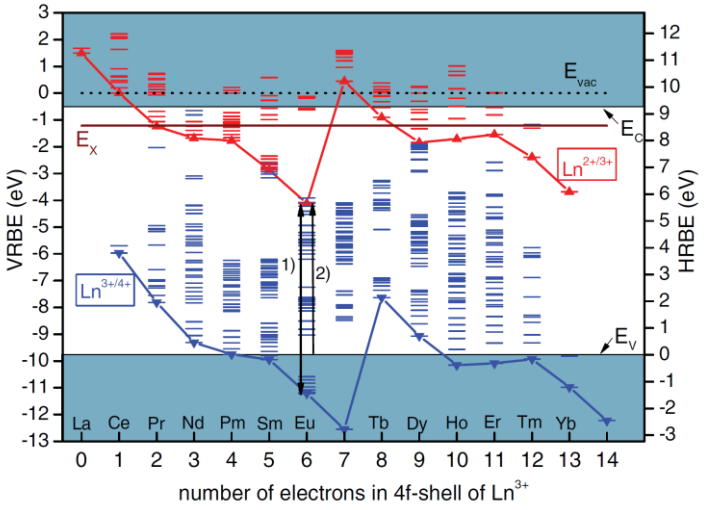

Figure 2.15 VRBE diagram of 4f levels in YPO_4 with the parameters needed for its design: arrows 1 and 2 indicate *U*(6,YPO_4) and the electron transfer from the VB to Eu^{3+}, respectively (from ref. 83).

It is important to underline that, in principle, all these data come from "standard" photoluminescence studies (except for very high bandgap materials for which synchrotron or other VUV excitation source are needed to determine the bandgap energy value). In addition,

thermoluminescence analyses are usually performed to study the trap depth distribution generated by intrinsic defects or doping ions intentionally embedded in the host with such purpose.

The thermally stimulated luminescence emission due to the recombination of electrons thermally released from traps during heating process, after the excitation at low temperature, is called thermoluminescence (TL).[84] The temperature dependence of the emission intensity is called TL glow curve which is used to estimate the activation energy of traps. As schematically depicted in Figure 2.16, the TL glow curve measurement consists of: (a) cooling of the sample at low temperature, and UV excitation of the sample to fill the traps with electrons or holes, (b) stop of the excitation, waiting of the detrapping for the shallowest levels for few minutes and then (c) record of the intensity during the temperature rising at constant rate.

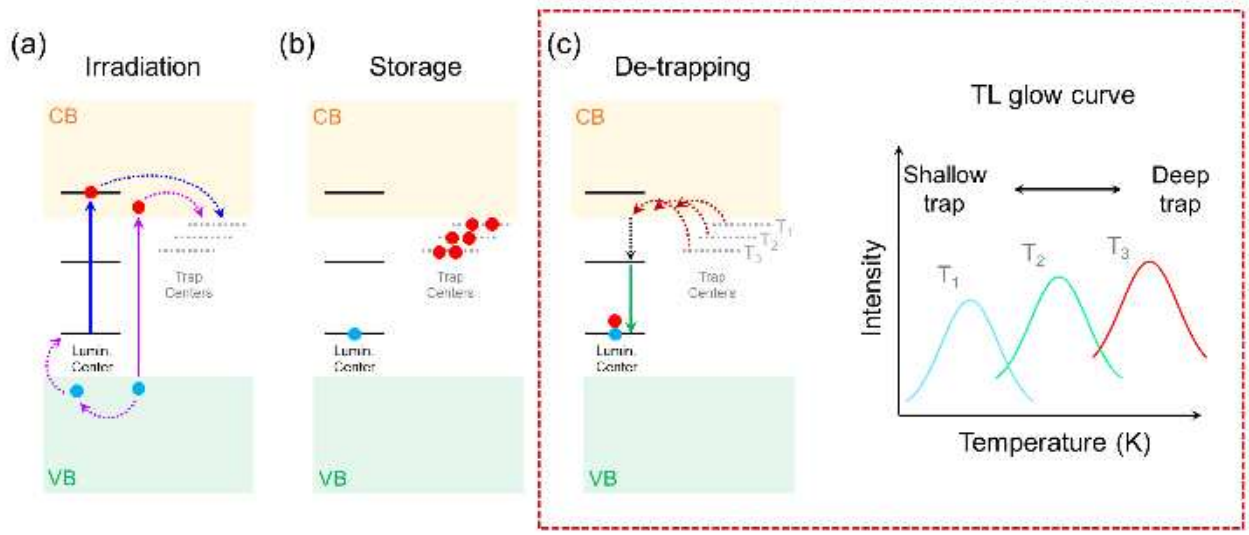

Figure 2.16 Simplified sketch of the basic principles of the TL analysis (a,b,c) and the glow curve (d). Intensity peaks of glow curves are caused by different energy differences between traps and the conduction band. Since different stimulation energies are needed, electrons from different traps are released at different temperatures.

Finally, it should be pointed out that many different models were proposed, however, the precise mechanism for the persistent luminescence process is still under debate (like the nature of the trap centers) and not completely understood.[58,85]

For a detailed review on the Eu^{2+}-doped and non-Eu^{2+}-doped persistent phosphors, on the mechanism of PersL and the red to NIR persistent phosphors, it is worth referring to the review reported by Smet *et al.*,[58,59] Hölsä *et al.*[85] and Tanabe *et al.*,[68] respectively.

2.7 Absorption Edge for Direct and Indirect Transitions

As previously introduced, the description of the energy level diagram respect to the energy position of the valence and conduction bands (in absolute scale) is an important step to design

new phosphors and discuss luminescent properties. In this view, a key role is played by the bandgap of the host.

The band structures of semiconductors are intensively investigated by means of optical absorption and/or diffuse reflectance spectroscopy. In presence of a specific band structure, typical light absorption features are the ones associated to electrons transitions from the valence (VB) to the conduction (CB) bands, occurring only at photon energy suitable for bridging the gap separating the two bands.

Considering the case of VB-CB transitions for electrons with the same momentum (*direct transition*) as shown in Figure 2.17a, the absorption coefficient $\alpha(h\nu)$ is written as:

$$\alpha(h\nu) = A\left(h\nu - E_g\right)^{1/2} \tag{2.19}$$

where A is a constant and E_g is the energy bandgap; the materials with this type of band structure are called as *direct gap materials*. For some of these, the transition at **k**=0 is forbidden by the selection rules and the absorption coefficient becomes:

$$\alpha(h\nu) = A'\left(h\nu - E_g\right)^{3/2}. \tag{2.20}$$

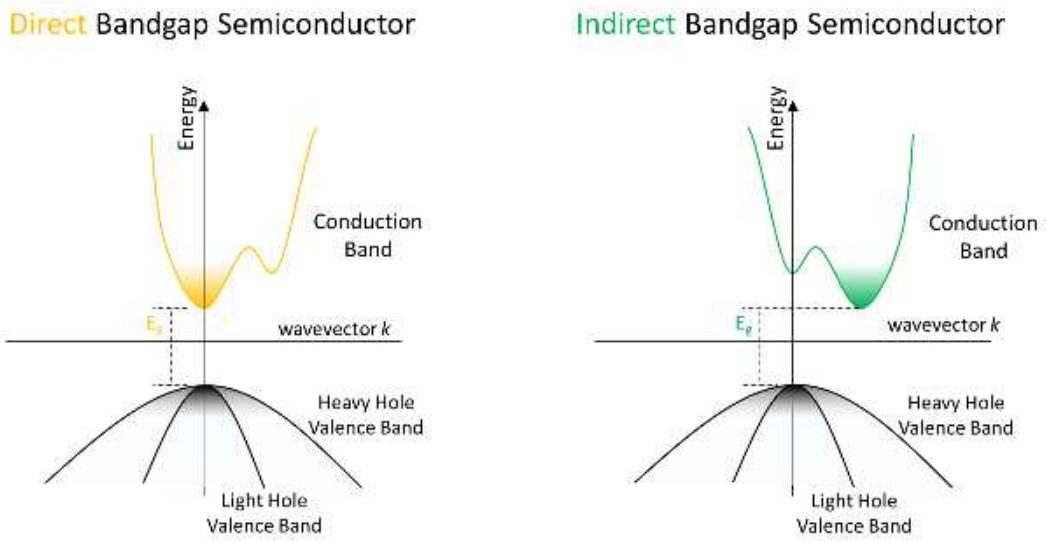

Figure 2.17 Simplified electronic band structure of direct- and indirect-bandgap semiconductors.

In the case depicted in Figure 2.17b, both the energy and the momentum of the electrons are changed and this process is known as *indirect transition*. This type of transition is accompanied by the excitation (or the absorption) of phonons and the absorption coefficient including these phonon-related mechanism can be written as:

$$\alpha(h\nu) = A\left(h\nu - E_g + E_p\right)^2 \left(e^{\frac{E_p}{k_B T}} - 1\right)^{-1} \tag{2.21}$$

where E_p is the phonon energy; the materials with this type of band structure are called as *indirect gap materials*.[27]

Many different methods can be used to calculate the bandgap energy of semiconductors. As adopted for some of the studies presented in the following chapters, a common method is based on the combination of the Kubelka-Munk function[86] and Tauc plot[87] approaches, starting from the spectra obtained by diffuse reflectance analysis. The conversion of the reflectance spectra into Kubelka-Munk function $F(R)$ is achieved with the equation:

$$F(R) = \frac{K}{S} = \frac{(1-R)^2}{2R} \tag{2.22}$$

where R is the reflectance, K the absorption coefficient and S the scattering coefficient. Then, by considering the Tauc plot,[87] the following equation can be considered:

$$(F(R) \times h\nu)^n = A(h\nu - E_g) \tag{2.23}$$

where n equal 0.5 or 2 depending on the nature of the semiconductor (indirect or direct gap material, respectively).

Finally, the bandgap energy E_g of the semiconductor can be estimated by extrapolating the value at the intersection of the tangent to the curve with the horizontal axis.

References

1. S. Shionoya. Introduction to the handbook. In W.M. Yen, S. Shionoya and H. Yamamoto Eds., *Phosphor Handbook* 2nd Edition, CRC Press, Boca Raton, USA **2007**.
2. P. Tanner. Some misconceptions concerning the electronic spectra of tri-positive europium and cerium. *Chem. Soc. Rev.* **2013**, 42, 5090-5101.
3. M. de Jong, L. Seijo, A. Meijerink and F.T. Rabouw. Resolving the ambiguity in the relation between Stokes shift and Huang-Rhys parameter. *Phys. Chem. Chem. Phys.* **2015**, 17, 16959-16969.
4. B. Henderson and G.F. Imbusch. Optical Spectroscopy of Inorganic Solids. Clarendon Press, Oxford 1989.
5. J.-C.G. Bünzli and S.V. Eliseeva. Basics of Lanthanide Photophysics. In P. Hänninen and H. Härmä editors, *Lanthanide Luminescence: Photophysical, Analytical and Biological Aspects*, Springer Berlin Heidelberg, 2010.
6. P. Dorenbos, J. Andriessen and C.W.E. van Eijk. $4f^{n-1}5d$ centroid shift in lanthanides and relation with anion polarizability, covalency, and cation electronegativity. *J. Solid State Chem.* **2003**, 171, 133-136.
7. P. Dorenbos. Lanthanide 4f-electron binding energies and the nephelauxetic effect in wide band gap compounds. *J. Lumin.* **2013**, 136, 122-129.
8. P. Dorenbos. The 5d level positions of the trivalent lanthanides in inorganic compounds. *J. Lumin.* **2000**, 91, 155-176.

9. P. Dorenbos. Electronic structure and optical properties of the lanthanide activated $RE_3(Al_{1-x}Ga_x)_5O_{12}$ (RE=Gd, Y, Lu) garnet compounds. *J. Lumin.* **2013**, 134, 310-318.

10. G. Li, Y. Tian, Y. Zhao and J. Lin. Recent progress in luminescence tuning of Ce^{3+} and Eu^{2+}-activated phosphors for pc-WLEDs. *Chem. Soc. Rev.* **2015**, 44, 8688-8713.

11. H. Terraschke and C. Wickleder. UV, Blue, Green, Yellow, Red, and Small: Newest Developments on Eu^{2+}-Doped Nanophosphors. *Chem. Rev.* **2015**, 115, 11352-11378.

12. J. Ueda. Analysis of optoelectronic properties and development of new persistent phosphor in Ce^{3+}-doped garnet ceramics. *J. Ceram. Soc. Japan* **2015**, 123, 1059-1064.

13. Y. Tanabe and S. Sugano. On the absorption spectra of complex ions. I. *J. Phys. Soc. Jpn.* **1954**, 9, 753-766.

14. Y. Tanabe and S. Sugano. On the absorption spectra of complex ions. II. *J. Phys. Soc. Jpn.* **1954**, 9, 766-779.

15. A.M. Srivastava and M.G. Brik. Crystal field studies of the Mn^{4+} energy levels in the perovskite $LaAlO_3$. *Opt. Mater.* **2013**, 35, 1544-1548.

16. M.G. Brik, S.J. Camardello, A.M. Srivastava, N.M. Avram and A. Suchocki. Spin-forbidden transitions in the spectra of transition metal ions and nephelauxetic effect. *ECS J. Solid State Sci. Technol.* **2016**, 5, R3067-R3077.

17. K. Ogasawara, F. Alluqmani and H. Nagoshi. Multiplet Energy Level Diagrams for Cr^{3+} and Mn^{4+} in Oxides with O_h Site Symmetry Based on First-Principles Calculations. *ECS J. Solid State Sci. Technol.* **2016**, 5, R3191-R3196.

18. G. Blasse and B.C. Grabmaier. Luminescent Materials. Springer-Verlag, Heidelberg **1994**.

19. F. Seitz. Interpretation of the properties of alkali halide-thallium phosphors. *J. Chem. Phys.*, **1938**, 6, 150-162.

20. A. Ranfagni, D. Mugnai, M. Bacci, G. Viliani and M.P. Fontana. The Optical Properties of Thallium-Like Impurities in Alkali-Halide Crystals. *Adv. Phys.* **1983**, 32, 823-905.

21. M. Fockele, F.J. Ahlers, F. Lohse, J.-M. Spaeth and R.H. Bartram. Optical properties of atomic thallium centres in alkali halides. *J. Phys. C: Solid State Phys.* **1985**, 18, 1963-1974.

22. P.W.M. Jacobs. Alkali halide crystals containing impurity ions with the ns^2 ground-state electronic configuration. *J. Phys. Chem. Solids* **1991**, 52, 35-67.

23. S. Tanimizu. Principal phosphor materials and their optical properties. In W.M. Yen, S. Shionoya and H. Yamamoto Eds., *Phosphor Handbook* 2nd Edition, CRC Press, Boca Raton, USA **2007**, pp.155-166.

24. I.B. Bersuker. The Jahn-Teller Effect. Cambridge University Press, Cambridge 2006.

25. I.B. Bersuker. Pseudo-Jahn-Teller Effect – A Two-State Paradigm in Formation, Deformation, and Transformation of Molecular Systems and Solids. *Chem. Rev.* **2013**, 113, 1351-1390.

26. G. Blasse. Classical Phosphors: A Pandora's Box. *J. Lumin.* **1997**, 72-74, 129-134.

27. E. Nakazawa. Fundamentals of luminescence, In S. Shinoya and W. M. Yen, Eds., *Phosphor Handbook*, CRC Press, New York, NY, USA, **1999**, pp. 11-141.

28. F. Auzel, G. Baldacchini, L. Laversenne and G. Boulon. Radiation trapping and self-quenching analysis in Yb^{3+}, Er^{3+}, and Ho^{3+} doped Y_2O_3. *Opt. Mater.* **2003**, 24, 103-109.

29. C.R. Ronda, Emission and excitation mechanisms of phosphors, In C.R. Ronda, Eds., *Luminescence: From Theory to Applications*, WILEY-VCH Verlag, Weinheim, Germany, **2008**, pp. 1-34.

30. J.J. Joos, D. Poelman and F. Smet. Energy level modeling of lanthanide materials: review and uncertainty analysis. *Phys. Chem. Chem. Phys.* **2015**, 17, 19058-19078.

31. P.A. Tanner. Lanthanide Luminescence in Solids. In P. Hänninen and H. Härmä, Eds., *Lanthanide Luminescence: Photophysical, Analytical and Biological Aspects*, Springer Berlin Heidelberg, **2010**.

32. P. Dorenbos. Thermal quenching of Eu^{2+} 5d - 4f luminescence in inorganic compounds. *J. Phys.: Condens. Matter* **2005**, 17, 8103-8111.

33. M. Ando and Y.A. Ono, Temperature effects in the emission characteristics of CaS:Eu thin-film electroluminescent devices. *J. Cryst. Growth* **1992**, 117, 969-974.

34. N. Kunkel, A. Meijerink and H. Kohlmann. Bright yellow and green Eu(II) luminescence and vibronic fine structures in LiSrH3, LiBaH3 and their corresponding deuterides. *Phys. Chem. Chem. Phys.* **2014**, 16, 4807-4813-

35. G. Blasse, W. Achipper and J.J. Hamelink. On the quenching of the luminescence of the trivalent cerium ion. *Inorg. Chim. Acta* **1991**, 189 77-80.

36. J. Ueda, P. Dorenbos, A.J.J. Bos, A. Meijerink and S. Tanabe. Insight into the Thermal Quenching Mechanism for $Y_3Al_5O_{12}:Ce^{3+}$ through Thermoluminescence Excitation Spectroscopy. *J. Phys. Chem. C* **2015**, 119, 25003-25008.

37. Z. Barandiarán, A. Meijerink and L. Seijo. Configuration coordinate energy level diagrams of intervalence and metal-to-metal charge transfer states of dopant pairs in solids. *Phys. Chem. Chem. Phys.* **2015**, 17, 19874-19884.

38. T. Förster. Zwischenmolekulare Energiewanderung und Fluoreszenz. *Ann. Phys.* **1948**, 437, 55-75.

39. D.L. Dexter. A theory of sensitized luminescence in solids. *J. Chem. Phys.* **1953**, 21, 836-850.

40. C.Z. Hadad and S.O. Vasquez. Energy-transfer processes induced by exchange interactions. *Phys. Rev. B* **1999**, 60, 8586-8594.

41. R.T. Wegh, H. Donker, K.D. Oskam and A. Meijerink. Visible Quantum Cutting in $LiGdF_4:Eu^{3+}$ Through Downconversion. *Science* **1999**, 283, 663-666.

42. F.T. Rabouw and A. Meijerink. Modeling the cooperative energy transfer dynamics of quantum cutting for solar cells. *J. Phys. Chem. C* **2015**, 119 2364-2370.

43. D.R. Gamelin and H.U. Güdel. Design of luminescent inorganic materials: new photophysical processes studied by optical spectroscopy. *Accounts. Chem. Res.* **2000**, 33, 235-242.

44. F. Auzel. Upconversion and anti-Stokes processes with f and d ions in solids. *Chem. Rev.* **2004**, 104, 139-174.

45. J.F. Suijver, Upconversion Phosphors. In C.R. Ronda, Eds., *Luminescence: from theory to applications*, Wiley-VCH Verlag GmbH and Co. KGaA, Weinheim, **2008**, Ch. 6, pp. 137.

46. N. Bloembergen. Solid state infrared quantum counters. *Phys. Rev. Lett.* **1959**, 2, 84-85.

47. V.V. Ovsyakin and P.P. Feofilov. Cooperative sensitization of luminescence in crystals activated with rare earth ions. *JETP Lett. Eng.* **1966**, 4, 317-318.

48. G.M. Salley, R. Valiente and H.U. Güedel. Luminescence upconversion mechanisms in Yb^{3+}-Tb^{3+} systems. *J. Lumin.* **2001**, 94-95, 305-309.

49. G.M. Salley, R. Valiente and H.U. Güedel. Cooperative Yb^{3+}-Tb^{3+} dimer excitations and upconversion in $Cs_3Tb_2Br_9$:Yb^{3+}. *Phys. Rev. B* **2003**, 67, 134111.

50. T. Grzyb, A. Gruszeczka, R.J. Wigluszb and S. Lisa. The effects of down- and up-conversion on dual-mode green luminescence from Yb^{3+}- and Tb^{3+}-doped $LaPO_4$ nanocrystals. *J. Mater. Chem. C* **2013**, 1, 5410-5418.

51. M. Pollnau, D.R. Gamelin, S.R. Luthi, H.U. Güdel and M.P. Hehlen. Power dependence of upconversion luminescence in lanthanide and transition-metal-ion systems. *Phys. Rev. B* **2000**, 61, 3337-3346.

52. J.F. Suyver, A. Aebischer, S. Garcia-Revilla, P. Gerner and H.U. Güdel. Anomalous power dependence of sensitized upconversion luminescence. *Phys. Rev. B* **2005**, 71, 195204.

53. J.F. Suyver, A. Aebischer, D. Biner, P. Gerner, J. Grimm, S. Heer, K.W. Krämer, C. Reinhard and H.U. Güdel. Novel materials doped with trivalent lanthanides and transition metal ions showing near-infrared to visible photon upconversion. *Opt. Mater.* **2005**, 27, 1111-1130.

54. M.F. Joubert. Photon avalanche upconversion in rare earth laser materials. *Opt. Mater.* **1999**, 11, 181-203.

55. Fortunius Licetus, Litheosphorus Sive de Lapide Bononiensi, Università di Bologna, Bologna, 1640.

56. T. Matsuzawa, Y. Aoki, N. Takeuchi, and Y. Murayama. A new long phosphorescent phosphor with high brightness, $SrAl_2O_4$:Eu^{2+},Dy^{3+}. *J. Electrochem. Soc.* **1996**, 143, 2670-2673 (1996).

57. H. Takasaki, S. Tanabe, and T. Hanada. Long-lasting afterglow characteristics of Eu, Dy codoped SrO-Al_2O_3 phosphor. *J. Ceram. Soc. Jpn.* **1996**, 104, 322-326.

58. K. Van den Eeckhout, P.F. Smet and D. Poelman. Persistent luminescence in Eu^{2+}-doped compounds: a review. *Materials* **2010**, 3, 2536-2566.

59. K. Van den Eeckhout, D. Poelman and P.F. Smet Persistent luminescence in non-Eu^{2+}-doped compounds: a review, *Materials* **2013**, 6, 2789-2818.

60. Y. Katayama, H. Kobayashi and S. Tanabe. Deep-red persistent luminescence in Cr^{3+}-doped $LaAlO_3$ perovskite for in vivo imaging. *Appl. Phys. Express* **2015**, 8, 012102.

61. Y. Katayama, H. Kobayashi, J. Ueda, B. Viana and S. Tanabe. Persistent luminescence properties of Cr^{3+}-Sm^{3+} activated $LaAlO_3$ perovskite. *Opt. Mater. Express* **2015**, 6, 1500-1505.

62. F. Liu, W. Yan, Y.J. Chuang, Z. Zhen, J. Xie and Z. Pan. Photostimulated near-infrared persistent luminescence as a new optical read-out from Cr^{3+}-doped $LiGa_5O_8$. *Sci. Rep.* **2013**, 3, 1554.

63. A. Bessière, S. Jacquart, K. Priolkar, A. Lecointre, B. Viana and D. Gourier. $ZnGa_2O_4$:Cr^{3+}: a new red long-lasting phosphor with high brightness. *Opt. Express* **2011**, 19, 10131-10137.

64. Y. Zhuang, J. Ueda and S. Tanabe. Enhancement of Red Persistent Luminescence in Cr^{3+}-Doped $ZnGa_2O_4$ Phosphors by Bi_2O_3 Codoping. *Appl. Phys. Express* **2013**, 6, 052602.

65. Z. Pan, Y.-Y. Lu and F. Liu. Sunlight-activated long-persistent luminescence in the near-infrared from Cr^{3+}-doped zinc gallogermanates. *Nat. Mater.* **2012**, 11, 58-63.

66. M. Allix, S. Chenu, E. Véron, T. Poumeyrol, E.A. Kouadri-Boudjelthia, S. Alahraché, F. Porcher, D. Massiot and F. Fayon. Considerable improvement of long-persistent luminescence in germanium and tin substituted $ZnGa_2O_4$. *Chem. Mater.* **2013**, 25, 1600-1606.

67. Q. Chermont, C. Chanéac, J. Seguin, F. Pellé, S. Maîtrejean, J.-P. Jolivet, D. Gourier, M. Bessodes and D. Scherman. Nanoprobes with near-infrared persistent luminescence for *in vivo* imaging. *Proc. Natl. Acad. Sci. USA* **2007**, 104, 9266-9271.

68. Y. Zhuang, Y. Katayama, J. Ueda and S. Tanabe. A brief review on red to near-infrared persistent luminescence in transition-metal-activated phosphors. *Opt. Mater.* **2014**, 36, 1907-1912.

69. T. Maldiney, A. Bessière, J. Seguin, E. Teston, S.K. Sharma, B. Viana, A.J.J. Bos, P. Dorenbos, M. Bessodes, D. Gourier, D. Scherman and C. Richard. The *in vivo* activation of persistent nanophosphors for optical imaging of vascularization, tumours and grafted cells. *Nat. Mater.* **2014**, 13, 418-426.

70. A. Bessière, S.K. Sharma, N. Basavaraju, K.R. Priolkar, L. Binet, B. Viana, A.J.J. Bos, T. Maldiney, C. Richard, D. Scherman and D. Gourier. Storage of Visible Light for Long-Lasting Phosphorescence in Chromium-Doped Zinc Gallate. *Chem. Mater.* **2014**, 26, 1365-1373.

71. N. Basavaraju, K.R. Priolkar, D. Gourier, S.K. Sharma, A. Bessière and B. Viana. The importance of inversion disorder in the visible light induced persistent luminescence in Cr^{3+} doped AB_2O_4 (A = Zn or Mg and B = Ga or Al). *Phys. Chem. Chem. Phys.* **2015**, 17, 1790-1799.

72. N. Basavaraju, K.R. Priolkar, D. Gourier, A. Bessière and B. Viana. Order and disorder around Cr^{3+} in chromium doped persistent luminescent AB_2O_4 spinels. *Phys. Chem. Chem. Phys.* **2015**, 17, 10993-10999.

73. L. Binet, S.K. Sharma and D. Gourier. Interaction of Cr^{3+} with valence and conduction bands in the long persistent phosphor $ZnGa_2O_4$:Cr^{3+}, studied by ENDOR spectroscopy. *J. Phys.: Condens. Matter* **2016**, 28, 385501.

74. J. Ueda, K. Kuroishi and S. Tanabe. Bright persistent ceramic phosphors of Ce^{3+}-Cr^{3+}-codoped garnet able to store by blue light. *Appl. Phys. Lett.* **2014**, 104, 101904.

75. J. Ueda, P. Dorenbos, A. Bos, K. Kuroishi and S. Tanabe. Control of Electron Transfer between Ce^{3+} and Cr^{3+} in $Y_3Al_{5-x}Ga_xO_{12}$ Host by Conduction Band Engineering. *J. Mater. Chem. C* **2015**, 3, 5642-5651.

76. J. Xu, J. Ueda, Y. Zhuang, B. Viana and S. Tanabe. $Y_3Al_{5-x}Ga_xO_{12}$:Cr^{3+}: A novel red persistent phosphor with high brightness. *Appl. Phys. Express* **2015**, 8, 042602.

77. J. Xu, J. Ueda and S. Tanabe. Design of Deep-Red Persistent Phosphors of $Gd_3Al_{5-x}Ga_xO_{12}$:Cr^{3+} Transparent Ceramics Sensitized by Eu^{3+} as an Electron Trap Using Conduction Band Engineering. *Opt. Mater. Express* **2015**, 5, 963-968.

78. Y. Zhuang, J. Ueda and S. Tanabe. Tunable Trap Depth in $Zn(Ga_{1-x}Al_x)_2O_4$:Cr,Bi Red Persistent Phosphors: Considerations of High-Temperature Persistent Luminescence and Photostimulated Persistent Luminescence. *J. Mater. Chem. C* **2013**, 1, 7849-7855 (2013).

79. H. Lin, J. Xu, Q. Huang, B. Wang, H. Chen, Z. Lin and Y. Wang. Bandgap tailoring via Si doping in inverse-garnet $Mg_3Y_2Ge_3O_{12}:Ce^{3+}$ persistent phosphor potentially applicable in AC-LED. *ACS Appl. Mater. Interfaces* **2015**, 7, 21835-21843.

80. H.L. Luo, A.J.J. Bos and P. Dorenbos. Controlled electron-hole trapping and detrapping process in $GdAlO_3$ by valence band engineering. *J. Phys. Chem. C* **2016**, 120, 5916-5925.

81. P. Dorenbos. Locating lanthanide impurity levels in the forbidden band of host crystals. *J. Lumin.* **2004**, 108, 301-305 (2004).

82. P. Dorenbos. Modeling the Chemical Shift of Lanthanide 4*f* Electron Binding Energies. *Phys. Rev. B* **2012**, 85, 165107.

83. P. Dorenbos. Determining Binding Energies of Valence-Band Electrons in Insulators and Semiconductors via Lanthanide Spectroscopy. *Phys. Rev. B* **2013**, 87, 035118.

84. S.W.S McKeever. Thermoluminescence of solids. Cambridge University Press, 1985.

85. H.F. Brito, J. Hölsä, T. Laamanen, M. Lastusaari, M. Malkamäki and L.C.V. Rodrigues. Persistent luminescence mechanisms: human imagination at work. *Opt. Mater. Express* **2012**, 2, 371-381.

86. P. Kubelka and F. Munk. Ein Beitrag zur Optik der Farbanstriche. *Z. Technische Physik* **1931**, 12, 593-601.

87. J. Tauc, R. Grigorovici and A. Vancu. Optical Properties and Electronic Structure of Amorphous Germanium. *Phys. Status Solidi* **1966**, 15, 627-637.

CHAPTER 3

Bismuth-based Optical Materials: from the Ion to the Host

Abstract Bismuth-based luminescent materials are widely investigated because of their peculiar optical properties, even though many aspects are still under debate, as the impact of the host on Bi ion optical activity. Hence, if, from one hand, many efforts are devoted to the research of new bismuth-based luminescent materials, on the other hand, the comprehension of the fundamental properties for bismuth ions luminescence is still an active research area. In the first part of this chapter, an overview on the luminescent properties of Bi^{3+} and Bi^{2+} ions is reported. Then, the use of bismuth-based compounds as host for luminescent centers (such as lanthanide and transition metal ions) is introduced and the main properties of bismuth oxide polymorphs are briefly reviewed.

3.1 An Overview on Bismuth Luminescence

In this section, the fundamental spectroscopic properties and an account on the literature of Bi^{3+}, Bi^{2+} and Bi-based compounds luminescence are presented.

3.1.1 Bi^{3+} ion: $6s^2$ configuration

As previously introduced in Section 2.2, Bi^{3+} ion belongs to the family of the ns^2 ions. A first attempt to explain the absorption bands of ns^2-ions was provided by Seitz[1] on the basis of an ionic model developed for the interpretation of Tl^+ luminescence in alkali halides. The ground state (GS) of the Bi^{3+} free ion is $^1S_0$ ($6s^2$ configuration), while the excited configuration 6s6p gives rise to a triplet state $^3P_0$, $^3P_1$, $^3P_2$ and a singlet state $^1P_1$ in order of increasing energy. Transitions from the ground state $^1S_0$ to the excited states $^3P_1$, $^3P_2$ and $^1P_1$ are usually denoted as A, B and C, respectively (see Figure 3.1). The allowed electric dipole transition $^1S_0 \longrightarrow {}^1P_1$ (C-band) is the highest in energy and is usually located in the VUV region. $^1S_0 \longrightarrow {}^3P_1$ and $^1S_0 \longrightarrow {}^3P_2$ transitions

(A and B-bands respectively) are spin forbidden; however, A-transition becomes allowed by spin-orbit coupling between $^3P_1$ and $^1P_1$. Finally, the transition from the GS to the lower energy excited state $^3P_0$ is strongly forbidden.

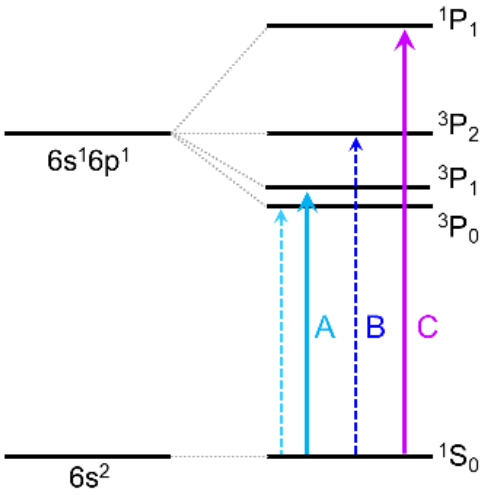

Figure 3.1 Energy level diagram of Bi^{3+} in Seitz model. Dashed arrows represent the forbidden transitions.

Even if this simple model has been successful in the interpretation of the excitation spectra, it resulted inadequate to account for some peculiar behaviours such as the existence of two A-emission bands or the increasing of the B-band with increasing temperature, as in the case of ns^2 ion in alkali halides.[2] Both luminescent behaviours can be well explained by considering the existence of multiple minima in the adiabatic potential energy surfaces of the relaxed excited state induced by the Jahn-Teller effect.[3,4]

The $^3P_0$ level is assumed to act as a metastable trapping state and the small energy difference between $^3P_1$ and $^3P_0$, known as the trap depth, determines a strong temperature dependence of the population ratio between the two states.[4-7] This trap depth varies with the Stokes-shift values. Blasse and van der Steen[8] proposed, as a rule of thumb, that "*smaller the trap depth, larger the Stokes-shift*". However, this effect is still not completely clear, and different interpretations based on excitonic behaviour[9] or on coordination number[8] were proposed.

To give account for the very broad spectral range of Bi^{3+} emission (from UV to red), the off-center position of Bi^{3+} [10] or the influence of the environment described by parameters such as the covalency, site symmetry and coordination number should be considered.[11] The strong influence of the covalency on the excitation band position of ns^2 ions was demonstrated by Duffy *et al.*[12] in glasses. Setlur *et al.*[13] showed the strong dependence of the Bi^{3+} ion-ligand bonds on the $^1S_0 \longrightarrow {}^3P_1$ absorption transition in the case of garnets. Hence, as a result of the increasing covalency of the bonds, a red-shift of the excitation band is expected in virtue of the nephelauxetic effect (Figure 3.2a).

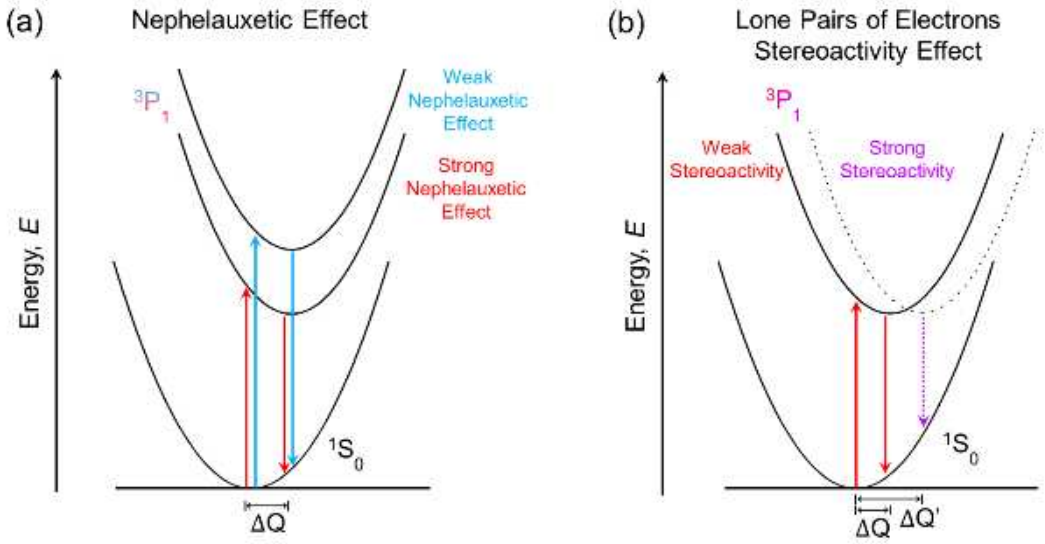

Figure 3.2 (a) Schematic representation of the nephelauxetic effect on the Bi^{3+} excited state. Strong nephelauxetic effect red-shift the excitation band. (b) Schematic effect of the stereoactivity of LPEs on the energy level diagram: the stronger the stereoactivity, the larger the ΔQ shift and, consequently, the Stokes-shift. Full line and dashed line parabola represent the excited state in the presence of weak and strong stereoactivity, respectively.

As discussed in Section 2.2, ns^2 ions are characterized by off-center positions due to the stereochemically active lone pair electrons. In Figure 3.2b the effect of the stereoactivity of LPEs on the excited states is depicted. A strong stereoactivity induces a large shift of the coordinates of the minimum of the excited state with a consequent big Stokes-shift. In the same way, a low symmetry site is expected to induce a larger Stokes-shift than a high symmetry one.
In order to predict the energy position of the A and C bands of Bi^{3+} doped compounds, Wang *et al.* proposed an approach based on the dielectric theory of the chemical bond for complex crystals[11] which considers a modification of the model proposed for the nephelauxetic effect.[14] By defining an environmental factor h_e expressed as:

$$h_e = \sum [f_c(i)\alpha(i)Q(i)^2]^{\frac{1}{2}} \tag{3.1}$$

which depends on the covalency f_c, the bond volume polarizability α and the charge Q (calculated by means of refractive index and crystal structure of the host), they obtained the following empirical relations for the energy of the A and C bands:

$$E_A = 2.972 + 6.206\ exp\left(-\frac{h_e}{0.551}\right) \tag{3.2}$$

$$E_C = 3.236 + 10.924\ exp\left(-\frac{h_e}{0.644}\right). \tag{3.3}$$

Moreover, for the two bands it was also given that:

$$E_C = 3.236 + 2.290(E_A - 2.972)^{0.856}. \tag{3.4}$$

Even if the accuracy in the estimation of the A-band is within ±0.5 eV and for C-band is ±0.6 eV, these relations are a useful tool for the comprehension of the general trends.

In addition to the $6s^2 \longrightarrow 6s^16p^1$ interconfigurational transitions (A, B and C bands), other luminescence peaks are also frequently observed in the spectra of Bi^{3+}-doped phosphors. The so called D-band has a charge transfer character and it is due to the strong interaction of Bi^{3+} ion (in general of all the ns^2 ions) with the host lattice. Hence the D-level absorption can be depicted as the transition from the Bi^{3+} ground state $^1S_0$ to the bottom of the host conduction band and it is described as a trapped exciton state[15] or as a metal-to-metal charge-transfer state.[16]
Boutinaud *et al.*[17,18] deeply investigated the D-band, proposing two empirical equations for the prediction of the D-state excitation energy (considered as MMCT state in the case of host metal cations with d^0 or d^{10} configuration) for the 4-coordinated M^{n+}metals:

$$\mathrm{MMCT}(\mathrm{Bi}^{3+}, \mathrm{cm}^{-1}) = 70000 - 52000\,\frac{\chi_4(\mathrm{M}^{n+})}{d_{corr}} \tag{3.5}$$

whereas, for coordination numbers larger than 4,

$$\mathrm{MMCT}(\mathrm{Bi}^{3+}, \mathrm{cm}^{-1}) = 55000 - 45500\,\frac{\chi_{\mathrm{CN}'>4}(\mathrm{M}^{n+})}{d_{corr}}. \tag{3.6}$$

$\chi_{\mathrm{CN}'}(\mathrm{M}^{n+})$ is the electronegativity (considering the new scale reported by Li and Xue[19]) for the host cations M^{n+} with coordination number CN', and d_{corr} is the shortest distances between the M^{n+} site and the cation site available for Bi^{3+}, corrected to the anion relaxation effect by considering the following formula:[20]

$$d_{corr} = d_{host} + \frac{1}{2}[r(\mathrm{Bi}^{3+}) - r(\mathrm{host})], \tag{3.7}$$

where $r(\mathrm{Bi}^{3+})$ and $r(\mathrm{host})$ are the Bi^{3+} ionic radius and the one of the host cation substituted by Bi^{3+} ion, respectively.

As in the case of the empirical model developed by Wang *et al.*,[11] the error in the estimation of the D-state absorption position is reported to be a quite big value of ±0.37 eV. However, as discussed in Chapter 7, this simple model is a useful tool to build the energy level diagram of Bi^{3+}-activated materials and to discuss the host effect on the luminescence properties of Bi^{3+} ion. In fact, in a simplified view, by considering only the $^1S_0$ ground state of Bi^{3+}, the bottom of the conduction band E_C and the $^3P_1$ excited state of Bi^{3+}, three different situations are possible (as depicted in Figure 3.3):

(a) MMCT energy smaller than A transition: in this situation, absorption and emission from MMCT state is favoured but also A transition can be achieved by photoionization;

(b) MMCT and A transitions with the similar energies: in this case, both the MMCT and $^3P_1$ states should emit with strong temperature dependent ratio;

(c) MMCT energy larger than A transition: this situation promotes the $^3P_1$ state absorption and emission but also MMCT transitions are still possible.

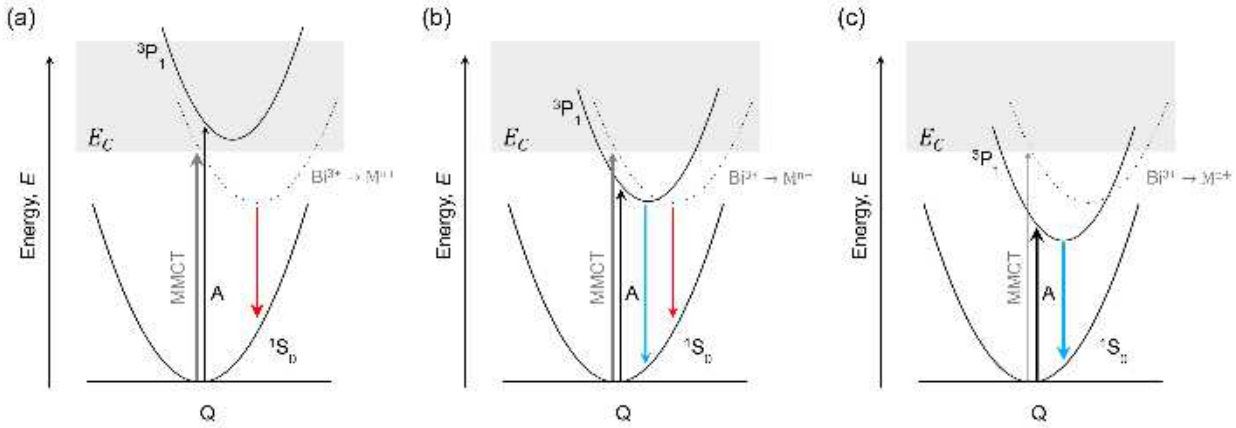

Figure 3.3 Different energy level configurations for Bi^{3+}-doped materials with MMCT state. The black and grey up arrows represent the A and MMCT transitions, respectively. The dashed parabola represents the MMCT state.

The potentialities expressed by Bi^{3+}-activated phosphors have led to deep investigations since long time, aimed to the comprehension of the rules for Bi^{3+} luminescence. Hence, great efforts were devoted to explore many different classes of hosts, such as phosphates,[8,21-24] tungstates,[25-27] antimonates,[6,28-31] alkaline-earth sulphides[32] and fluorides,[33] borates,[34,35] vanadates,[22,36-41] silicates[42] and aluminates and gallates garnets.[13,43-49]

Recently, Bi-activated vanadates has attracted much attention because of the possibility to fine tune the color output in all the visible range.[36-40] In 2016, Kang *et al.*[40] reported the ability of the $(Y,Sc)(Nb,V)O_4:Bi^{3+}$ phosphors to emit in the blue to red range (Figure 3.4 from ref. 40). It is interesting to note that in this case, the color rendering is achieved by means of the bandgap modulation because of the strong effect of the host on the Bi^{3+} performances: whereas the blue emission in $YNbO_4$:Bi is due to band-to-band transition (excited states of Bi^{3+} are higher that the bottom of the CB), yellow, orange and red emissions in YVO_4:Bi and $ScVO_4$:Bi systems arise from the localized Bi^{3+} excited states $^3P_{0,1}$. Moreover, it is noteworthy that the quantum yield of the YVO:Bi system is in the range of 75-92%, depending on the excitation wavenumbers.[22,40]

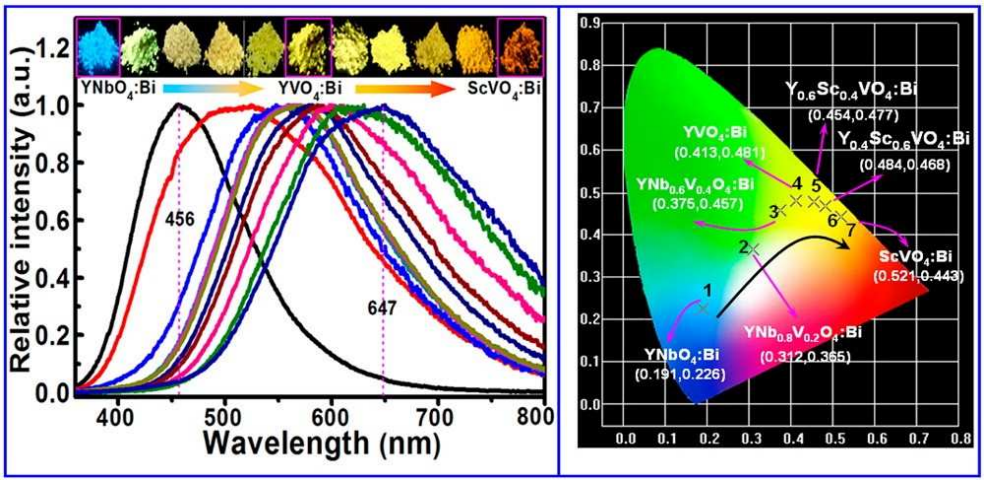

Figure 3.4 Normalized emission spectra of $(Y_{1-y},Sc_y)(Nb_{1-x},V_x)O_4:Bi^{3+}$ phosphors with digital photographs during exposure to UV-C lamp (left) and CIE chromaticity diagram and coordinates (right). From ref. 40.

However, even if some useful empirical rule was recently introduced, as previously discussed,[11,18] to date the interpretation of the luminescent absorption and emission bands of Bi^{3+}-activated phosphors is still a complex matter, and a clear rationalization of the energy level behaviour of Bi^{3+} respect to the different hosts is still a challenge.

Bi^{3+} as sensitizer

In addition to the peculiar emissions showed by Bi^{3+} in different hosts, nowadays Bi^{3+} is one of the most important sensitizer exploited to enhance the PL efficiency of different luminescent centers. In particular, it is mainly used to take advantage of its higher absorption cross-section (for example, with respect to the low absorption cross-section of the forbidden 4f transitions of lanthanides). The studies reported in literature are mainly focused into the energy transfer mechanisms between Bi^{3+} and trivalent lanthanide ions Ln^{3+} to enhance the emissions in the visible range. The most used system consists in the Bi^{3+}-Eu^{3+} pair,[50-53] but also the sensitization of other lanthanide ions was deeply investigated (*i.e.* Bi^{3+}-Sm^{3+},[50,54-56] Bi^{3+}-Dy^{3+},[50,54-56] Bi^{3+}-Ho^{3+},[54-56] Bi^{3+}-Tb^{3+},[50] Bi^{3+}-Yb^{3+} [55]). The parameters described in Section 2.5.1 such as the critical distance are usually investigated to optimize the process.

In Chapter 8, we propose the energy transfer between Bi^{3+} and Er^{3+} in Y_2O_3 nanocrystal as an effective way to enhance not only the emissions in the visible range, but also the telecom emission of Er^{3+} at 1.5 μm.

3.1.2 Bi^{2+} ion: $6s^26p^1$ configuration

Bi^{2+} luminescence has been attributed to the 6p ⟶ 6p parity forbidden transitions between different spin-orbit states in the $6s^26p^1$ electronic configuration.[57-59] Spin-orbit coupling is responsible for the $^2P_{1/2}$ ground state and $^2P_{3/2}$ excited state within the $6s^26p^1$ electronic configuration. Moreover, if the ion is in a low symmetry coordination site, the $^2P_{3/2}$ state splits in two energy levels $^2P_{3/2}(1)$ and $^2P_{3/2}(2)$, enabling the $^2P_{1/2}$ ⟶ $^2P_{3/2}(1)$ excitation and the $^2P_{3/2}(2)$ ⟶ $^2P_{1/2}$ emission (Figure 3.5).

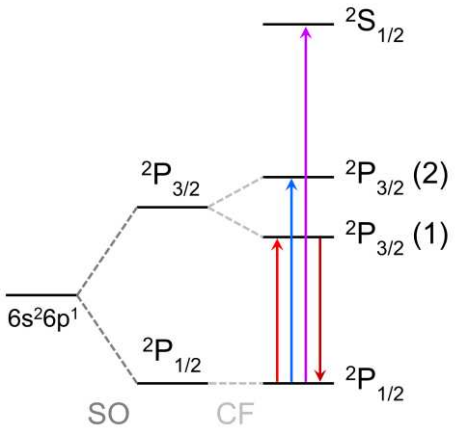

Figure 3.5 Energy level diagram of Bi^{2+} in which the spin-orbit (SO) coupling splits the $6s^26p^1$ and the crystal field (CF) of a low symmetry coordination splits the $^2P_{3/2}$ term.

Recently, the characteristic of Bi^{2+} to emit orange-red light upon excitation in the blue region of the spectrum, attracted the interest of the scientific community with the aim to develop new white illuminating devices charged by blue-LED.[60] The origin of this interesting emission color is due to the strong increase of the spin-orbit coupling with the atomic number, resulting in p-p transitions that fall in the visible-NIR region for heavy elements.

In 1994, it was assumed for the first time by Blasse *et al.*[59] that Bi^{2+} is responsible for the red-orange luminescence of Bi-doped SrB_4O_7. However, since more recent experiments revealed that only very low concentration of Bi^{2+} can be stabilized,[61] the difficulty in stabilizing partially filled p-shell ions has led to limited investigations of intraconfigurational p-p transitions. Only few classes of compounds have been demonstrated to be suitable to stabilize Bi^{2+} such as alkaline-earth-metal sulfates,[62,63] borates,[59-61,64-67] phosphates[68-72] and borophosphates.[73,74] As typical examples of Bi^{2+}-activated phosphors, Figure 3.6 shows the schematic energy level diagrams together with PLE and PL spectra of Bi^{2+}, as reported by Peng *et al.*[65] for $SrB_4O_7:Bi^{2+}$ and $SrB_6O_{10}:Bi^{2+}$.

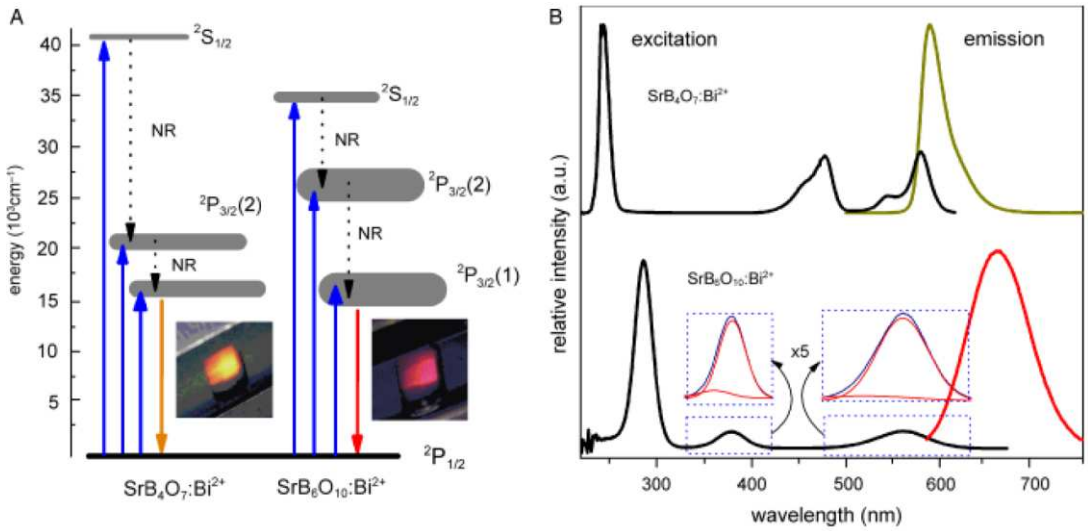

Figure 3.6 (A) Simplified energy level diagrams of $SrB_4O_7:Bi^{2+}$ and $SrB_6O_{10}:Bi^{2+}$, with photographs of the samples. (B) PLE and PL spectra of the systems. From ref. 65.

In Table 3.1, excitations and emission of Bi^{2+}-activated phosphors divided by classes are summarized.

From *ab initio* calculations, Seijo and Barandiarán[75] estimated the excited state energies and the relative absorption oscillator strengths of Bi^{2+} in fields with different symmetries, showing the most favourable ones in terms of high absorption and large splitting of $^2P_{3/2}$ level for red-shifted $^2P_{3/2}(2) \longrightarrow {}^2P_{1/2}$ emission. In particular, the authors have found that the splitting of $^2P_{3/2}$ level is driven not by the symmetry of the actual field, but by its tetragonal D_{4h} and orthorhombic D_{2h} components together with the Bi displacements towards two or four oxygen ligands.

Table 3.1 Excitation and emission wavelengths of Bi^{2+}-activated oxide phosphors with relative references. (s1), (s2) and (s3) represents different lattice sites for Bi^{2+} in the hosts.

Host	**Excitations (nm)**			**Emission (nm)**	**Ref.**
	$^2P_{1/2} \rightarrow {}^2S_{1/2}$	**$^2P_{1/2} \rightarrow {}^2P_{3/2}(2)$**	**$^2P_{1/2} \rightarrow {}^2P_{3/2}(1)$**	**$^2P_{3/2}(1) \rightarrow {}^2P_{1/2}$**	
Sulfates					
$CaSO_4$	255	395	525	580	63
$SrSO_4$	255	452	575	610	62,63
$BaSO_4$	260	452	592	627	62,63
Borates					
SrB_4O_7	245	478	578	588	59,65
SrB_6O_{10}	286	380	560	660	65
BaB_8O_{13}	-	420 (s1) - 368 (s2) - 406 (s3)	-	586 (s1) - 617 (s2) - 670 (s3)	67
α-BaB_4O_7	-	390	-	671	67
$Ba_2B_{10}O_{17}$	-	503 (s1) - 460 (s2)	-	612 (s1) - 663 (s2)	67
Phosphates					
$Ca_2P_2O_7$	281	470	608	653	68
$Sr_2P_2O_7$	261 (s1) - 265 (s2)	428 (s1) - 446 (s2)	628 (s1) - 648 (s2)	667 (s1) - 700 (s2)	69
$Ba_2P_2O_7$	286	384	618	716	68
$Sr_2P_4O_{13}$	250	445	605	658	72
$Ba_2P_4O_{13}$	278	435	620	686	72
Borophosphates					
$CaBPO_5$	231	416	582	630	74
$SrBPO_5$	234	413	616	641	74
$BaBPO_5$	267	430	619	641	74

A peculiar behaviour was reported for Bi^{2+} in $Sr_2P_2O_7$ by Li *et al.*,[71] showing how an unusual high concentration of Bi^{2+} in this host induced an antithermal quenching process with a consequent increase of the quenching temperature.

In addition to the hosts reported in Table 3.1, Cao *et al.*[76] assigned yellow-to-orange emissions at 550 nm and 600 nm of Bi-activated CaF_2 and SrF_2 to Bi^{2+}; however, no absorption to $^2P_{3/2}(1)$ and $^2P_{3/2}(2)$ was detected. Moreover, recently Qin *et al.*[77] showed that the stabilization of Bi^{2+} in $SrSnO_3$ brings to an emission feature peaked in the NIR region at 808 nm, with excitation bands at 298, 528 and 700 nm.

In this contest, the stabilization of Bi^{2+} in perovskite $CaSnO_3$ is presented and discussed in Chapter. 7.

Finally, it is important to mention that, bismuth-activated luminescent materials have also shown other signals with different origin such as Bi^+ near-infrared emissions,[78-85] cluster-related emissions, dimers, trimers and bismuth polycations centers.[86-90] The properties of such kind of luminescent centers are over the scope of this thesis and are reviewed in ref. 91.

3.1.3 Luminescent Bi-based compounds

Besides the luminescence of Bi ions introduced in the host phosphors as activators, Blasse *et al.*[10,92,93] investigated also the luminescence of Bi-based compounds. The most famous luminescent Bi-based compound is $Bi_4Ge_3O_{12}$ (BGE), one of the most important scintillator materials. This compound is characterized by a large Stokes-shift, with a broad emission band centred at about 490 nm and a UV excitation band with a maximum at about 290 nm, linked to the presence of Bi^{3+}.[94] The excitation and emission bands of the Bi-based compounds are typically located in the UV and visible range, respectively, but most do not emit light at room temperature because of concentration quenching effects. Other compounds showing PL emission from Bi^{3+} are reviewed by Barros *et al.*,[95] including compounds such as $Bi_2Al_4O_9$, $Bi_2Ga_4O_9$, $B_{12}TiO_{20}$ and Bi_2WO_6. Recently, Olchowka *et al.*[96] reported a detailed investigation on the luminescence of Sillen X1 series of $ABiO_2X$ (A=Cd, Ca, Sr, Ba, Pb; X=Cl, Br, I) compounds, showing a noteworthy color tunability moving from blue ($BiSrO_2Cl$) to green-yellow ($BiBaO_2Br$).

3.2 Bismuth-based Oxides as Host for Optical Materials

In the last years, bismuth-based oxide materials have attracted great attention because of their promising properties for a wide range of applications such as photocatalysts,[97,98] ferroelectrics,[99,100] fuel cells[101] and multiferroics.[102-104]

The narrow bandgap of bismuth-based oxides compounds prompts the research on this compounds to widen the spectral region accessible for photocatalysis in the visible range, and

many materials were proposed, ranging from bismuth titanates[105] (*e.g.* $Bi_2Ti_2O_7$, $Bi_4Ti_3O_{12}$, $Bi_{12}TiO_{20}$) and silicates[106,107] (*e.g.* Bi_2SiO_5, $Bi_4Si_3O_{12}$) to oxyhalides[108] (general formula $Bi_xO_yA_z$ with A=F, Cl, Br, I) or vanadate.[109,110] Notably, in recent years, the superior properties of $BiVO_4$ has been exploited to develop photoanodes for water splitting.[111-113]

The interest in these materials is driven not only by their low toxicity and costs, but also by the peculiar properties arising from the electronic structure of Bi^{3+}. $6s^2$ lone pairs of electrons (LPEs) characterizing Bi^{3+} can determine non-centrosymmetric crystal structures due to the asymmetric coordination, with consequent interesting properties such as piezoelectricity, second harmonic generation (SHG), pyro- and ferroelectricity.

Walsh *et al.* demonstrated that in Bi_2X_3 series (X=O, S, Se, Te), Bi_2O_3 and Bi_2S_3 display lone pair distortion, while $BiSe_3$ and Bi_2Te_3 do not.[114] They demonstrated[115] that this trend originates from anion-cation interactions where: (i) s^2 electrons of the cation (*e.g.* Bi^{3+}) and p-orbitals of the anion (*e.g.* O^{2-}) interact, forming bonding and anti-bonding orbitals (they are not chemically inert) and (ii) the lone pair asymmetric electron density is induced by the stabilization of the nominally empty cation p-states (Bi^{3+}: $6s^26p^0$), that interact with the anti-bonding orbitals.[115,116]

From the optical point of view, it is clear that this asymmetric electron density can have a significant role on the optical response of the materials, also inducing some unexpected behaviours. In particular, a LPE-induced off-centric displacement of a luminescent center can have strong influence on its emission properties. Hence, the use of bismuth oxide-based materials as host for luminescent centers appears as an attractive topic.

Lira *et al.*[117-119] investigated the optical properties of Er^{3+}-doped $Bi_4Si_3O_{12}$ crystal for optical amplification and laser, while Dy: $Bi_4Si_3O_{12}$ crystal displays promising properties as yellow phosphor for LED application[120] and Dy^{3+}-Eu^{3+} codoping gives perspectives for white light emission devices.[121] Moreover, $Bi_4Ti_3O_{12}$ was exploited as a host for upconverting films[122] and nanoparticles.[123]

In addition to the aforementioned features, another relevant aspect of bismuth-based compounds is the high refractive index. In fact, the refractive index, expressed in term of "local field correction" E_{loc}/E_0, is directly connected to the probabilities of radiative transitions, and for an electric dipole allowed transition it is given that:[124]

$$W = \frac{1}{4\pi\varepsilon_0}\frac{4n\omega_0^3}{3\hbar c_0^3}\left(\frac{E_{loc}}{E_0}\right)^2 |\mu|^2 \tag{3.8}$$

where the local field correction can be approximated as

$$\frac{E_{loc}}{E_0} = \frac{n^2+2}{3}. \tag{3.9}$$

Thus, the spontaneous emission probability increases with the refractive index n.

Bi_2O_3 polymorphs

It is well known that the impact of the crystal structure on the optical properties of the materials could be very strong. Even if the effect is more effective in the case of transition metal or ns^2 ions (as described in Chapter 2), also the performance of lanthanide ions can be strongly affected by crystalline structure in some particular process such as upconversion. A very famous example regards the strong enhancement of upconversion efficiency in $NaYF_4$ induced by the phase transition from cubic to hexagonal phase.[125-127] Recently, Wisser *et al.*[128] showed the effect of the crystal field also by codoping, with an effective on the UC quantum yield of the system.

In this context, by considering the idea to develop bismuth oxide-based phosphors, the polymorphic nature of bismuth oxide can be used to modify and control the optical response of the material.

Bismuth oxide (Bi_2O_3) displays a complex polymorphism existing in six different structures: α, β, δ, γ, ε and ω phases. The monoclinic α-Bi_2O_3 and cubic δ-Bi_2O_3 phases are stable at room and at high temperatures (approximately between 730 °C and 825 °C), respectively.[129] The metastable tetragonal and body-centered cubic phases (β and γ, respectively) are stabilized during the cooling of δ-Bi_2O_3. More recently, an orthorhombic ε-Bi_2O_3 and a triclinic ω-Bi_2O_3 phases were stabilized in specific conditions.[130] Figure 3.7 summarizes the complex temperature dependence stabilization of the different polymorphs.[130]

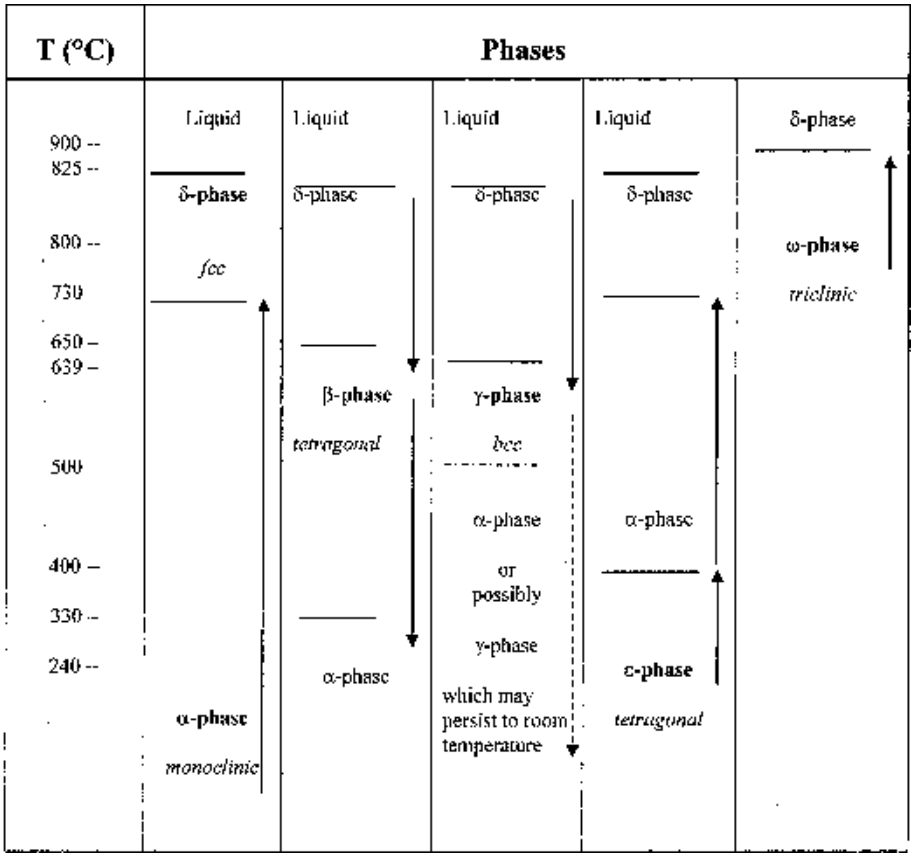

Figure 3.7 Temperature dependence of the stable and metastable polymorphs of Bi_2O_3. From ref. 130.

The unique ionic conductivity properties of the cubic δ-phase has led to a deeply investigation on the relation between the ionic properties and the crystalline structure. δ-Bi_2O_3 consists in a fluorite based structure characterized by an oxygen sublattice with a high fraction of vacancies. Figure 3.8 shows the ideal fluoride structure of the cubic δ-Bi_2O_3 and the possible arrays of vacant sites along different directions. This high content of defects and the promotion of extensive anion disorder induced by the asymmetric electron density around the Bi^{3+} ions are at the basis of the high ion conductivity of δ-Bi_2O_3.[131]

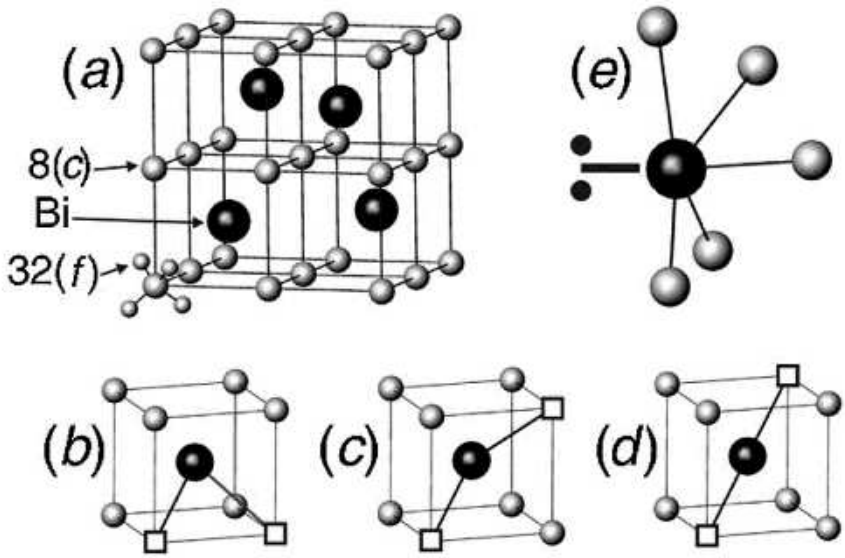

Figure 3.8 Schematic representation of the ideal cubic fluoride structure (a) and the vacancy pairs along the <100>, <110> and <111> directions (b, c and d respectively). (e) Lone pair of electrons characteristic of bismuth oxide compound. From ref. 132.

The main drawback of the δ phase is its stability only above *ca.* 730 °C. Hence, many efforts have been devoted to the stabilization of the δ phase at room temperature, with remarkable results by partially replacing bismuth ions with rare-earth elements such as Er, Dy, Yb and Y.[129,130]

Concerning the anion vacancies of pure δ-Bi_2O_3, three main models were proposed:

1. Sillen model:[133] this model consists in a simple cubic fluorite structure with the 25% oxygen vacancies ordered along the <111> direction;

2. Gattow model:[134] Gattow and Schroder modifies the Sillen model considering the intrinsic vacancies spread over all possible 8c anion sites (assumption of no ordering within oxygen sub-lattice), with a consequent 75% oxygen occupancy at each 8c site;

3. Willis model:[135] this model was originally proposed for CaF_2 phase and, later, was considered for δ-Bi_2O_3; in this case, the occupancy of an additional position (32f) respect to the 8c is considered.

Figure 3.9 displays a schematic representation of the three models.

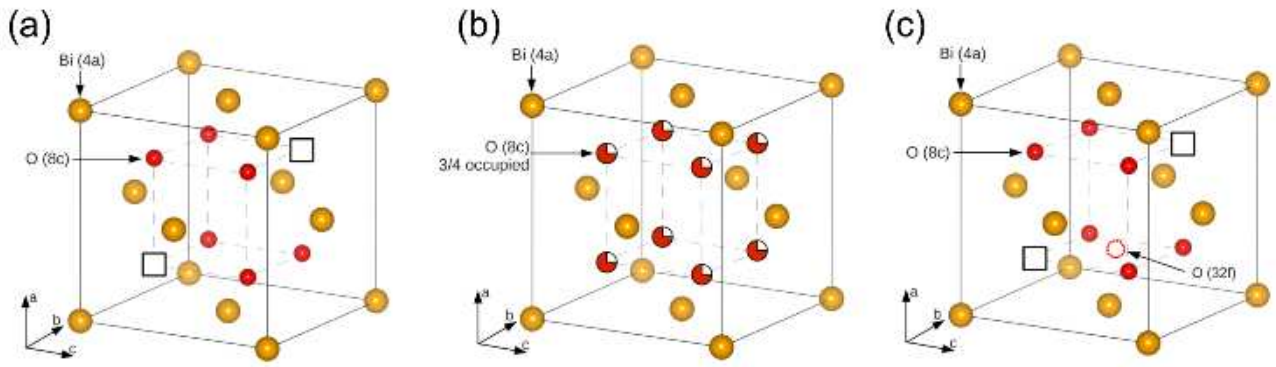

Figure 3.9 Schematic representation of the three models for δ-Bi_2O_3: (a) Sillen model, (b) Gattow model and (c) Willis model.

It is worth underlining how, even if the unique ionic conductivity properties of the δ phase has led to a deep study on the phase stabilization, there is still a large debate on the nature of its crystalline structure, since it is not fully understood.[136]

References

1. F. Seitz. Interpretation of the properties of alkali halide-thallium phosphors. *J. Chem. Phys.*, **1938**, 6, 150-162.
2. A. Ranfagni, D. Mugnai, M. Bacci, G. Viliani and M.P. Fontana. The Optical Properties of Thallium-Like Impurities in Alkali-Halide Crystals. *Adv. Phys.* **1983**, 32, 823-905.
3. A.M. Lemos, M.C. Stauber and J.F. Marion. Structure of the A, B, and C Absorption Bands in KCl:Tl. *Phys. Rev. B* **1970**, 2, 4161-4168.
4. A.C. van der Steen, J.J.A. van Hesteren and A. P. Slok. Luminescence of Bi^{3+} ion in compounds $LiLnO_2$ and $NaLnO_2$ (Ln=Sc, Y, La, Gd, Lu). *J. Electrochem. Soc.* **1981**, 128, 1327-1333.
5. G. Boulon, B. Moine, J. C. Bourcet, R. Reisefeld and Y. Kalisky. Time resolved spectroscopy about $^3P_1$ and $^3P_0$ levels in Bi^{3+} doped germinate glasses. *J. Lumin.* **1979**, 18-19, 924-928.
6. G. Boulon, J.P. Faurie and C. Madej. Préparation, sites de symétrie et photoluminescence de l'ion Bi^{3+} dans les antimoniates de terres rares Y_2BSbO_7 (B=Ga, Lu, Y). *J. Solid State Chem.* **1974**, 10, 167-174.
7. G. Boulon, C.K. Jørgensen and R. Reisfeld. The two luminescent levels of Bi^{3+} in solids. *Chem. Phys. Lett.* **1980**, 75, 24-26.

8. G. Blasse and A. C. van der Steen. Luminescence characteristics of Bi^{3+}-activated oxides. *Solid State Commun.* **1979**, 31, 993-994.

9. R. Moncorgé, B. Jacquier and G. Boulon. Temperature dependent luminescence of $Bi_4Ge_3O_{12}$ - discussion on possible models. *J. Lumin.* **1976**, 14, 337-348.

10. C.W.M. Timmermans and G. Blasse. The luminescence of some oxidic bismuth and lead compounds. *J. Solid State Chem.* **1984**, 52, 222-232.

11. L. Wang, Q. Sun, Q. Liu and J. Shi. Investigation and application of quantitative relationship between sp energy levels of Bi^{3+} ion and host lattice. *J. Solid State Chem.* **2012**, 191, 142-146.

12. J.A. Duffy and M.D. Ingram. Use of Thallium(I), Lead(II), and Bismuth(III) as spectroscopic probes for ionic-covalent interaction in glasses. *J. Chem. Phys.* **1970**, 52, 3752-3754.

13. A.A. Setlur and A.M. Srivastava. The nature of Bi^{3+} luminescence in garnet hosts. *Opt. Mater.* **2006**, 29, 410-415.

14. F. Gao and S. Zhang. Investigation of mechanism of nephelauxetic effect. *J. Phys. Chem. Solids* **1997**, 58, 1991-1994.

15. A.M. Srivastava and W.W. Beers. On the impurity trapped exciton luminescence in $La_2Zr_2O_7:Bi^{3+}$. *J. Lumin.* **1999**, 81, 293-300.

16. G. Blasse. Optical electron transfer between metal ions and its consequences. In *Complex chemistry* (Structure and bonding series) Springer, Berlin **1991**, Vol. 76, pp. 153-187.

17. P. Boutinaud and E. Cavalli. Predicting Metal-to-Metal Charge Transfer in Close-Shell Transition Metal Oxides doped with Bi^{3+} or Pb^{2+}. *Chem. Phys. Lett.* **2011**, 503, 239-243.

18. P. Boutinaud. Revisiting the Spectroscopy of the Bi^{3+} Ion in Oxide Compounds. *Inorg. Chem.* **2013**, 52, 6028-6038.

19. K. Li and D. Xue. Estimation of electronegativity values of elements in different valence states. *J. Phys. Chem. A* **2006**, 110, 11332-11337.

20. A. H. Krumpel, P. Boutinaud, E. Van der Kolk and P. Dorenbos. Charge transfer transitions in the transition metal oxides $ABO_4:Ln^{3+}$ and $APO_4:ln^{3+}$ (A=La, Gd, Y, Lu, Sc; B=V, Nb, Ta; Ln=lanthanide). *J. Lumin.* **2010**, 130, 1357-1365.

21. F.B.M. van Zon, D.C. Koningsberger, E.W.J.L. Oomen and G. Blasse. An EXAFS study of the luminescent Bi^{3+} center in $LaPO_4$-Bi. *J. Solid State Chem.* **1987**, 71, 396-402.

22. E. Cavalli, F. Angiuli, F. Mezzadri, M. Trevisani, M. Bettinelli, P. Boutinaud and M. Brik. Tunable luminescence of Bi^{3+}-doped $YP_xV_{1-x}O4$ ($0 \leq x \leq 1$). *J. Phys.: Condens. Matter.* **2014**, 26, 385503.

23. A.M. Srivastava and S.J. Camardello. Concentration dependence of the Bi^{3+} luminescence in $LnPO_4$ ($Ln=Y^{3+}$, Lu^{3+}). *Opt. Mater.* **2015**, 39, 130-133.

24. V. Babin, K. Chernenko, P. Demchenko, E. Mihokova, M. Nikl, I. Pashuk, T. Shalapska, A. Voloshinovskii and S. Zazubovich. Luminescence and excited state dynamics in Bi^{3+}-doped $LiLaP_4O_{12}$ phosphates. *J. Lumin.* **2016**, 176, 324-330.

25. G. Blasse. Classical phosphors: A Pandora's box. *J. Lumin.* **1997**, 72-74, 129-134.

26. Y. Zorenko, M. Pashkovsky, A. Voloshinovskii, B. Kuklinski and M. Grinberg. The luminescence of $CaWO_4$:Bi single crystal. *J. Lumin.* **2006**, 116, 43-51.

27. F. Kang and M. Peng. A new study on the energy transfer in the color-tunable phosphor $CaWO_4$:Bi. *Dalton Trans.* **2014**, 43, 277-284.

28. C. Pédrini, G. Boulon and F. Gaume-Mahn. Bi^{3+} and Pb^{2+} centres in alkaline-earth antimonate phosphors. *Phys. Status Solidi A* **1973**, 15, K15-K18.

29. A.M. Srivastava and A. Szarowski. On the quenching of Bi^{3+} luminescence in the pyrochlore Gd_2GaSbO_7. *J. Solid State Chem.* **1999**, 146, 494-498.

30. S. Yao, X. Zhou, Y. Huang, Z. Wang, Y. Long and W. Li. Luminescent properties of Bi^{3+}-activated $Ca_2Sb_2O_7$ nano-phosphor prepared by co-precipitation method. *J. Alloys Compd.* **2015**, 653, 345-350.

31. S. Yao, L. Chen, Y. Huang and W. Li. Enhanced luminescence of $CaSb_2O_6$:Bi^{3+} blue phosphors by efficient charge compensation. *Mater. Sci. Semicond. Process.* **2016**, 41, 265-269.

32. H. Donker, N. Yamashita, W.M.A. Smit and G. Blasse. Luminescence decay times of the Sb^{3+}, Pb^{2+}, and Bi^{3+} ions in alkaline-earth sulfides. *Phys. Status Solidi B* **1989**, 156, 537-544.

33. K.P. Oboth, F.J. Lohmeier and F. Fischer. VUV and UV spectroscopy of Pb^{2+} and Bi^{3+} centres in alkaline-earth fluorides. *Phys. Status Solidi B* **1989**, 154, 789-803.

34. A. Wolfert, E.W.J.L. Oomen and G. Blasse. Host lattice dependence of the Bi3+ luminescence in orthoborates $LnBO_3$ (with *Ln* = Sc, Y, La, Gd, or Lu). *J. Solid State Chem.* **1985**, 59, 280-290.

35. G. Blasse. The ultraviolet absorption bands of Bi^{3+} and Eu^{3+} in oxides. *J. Solid State Chem.* **1972**, 4, 52-54.

36. F. Kang, M. Peng, X. Yang, G. Dong, G. Nie, W. Liang, S. Xu and J. Qiu. Broadly tuning Bi^{3+} emission *via* crystal field modulation in solid solution compounds (Y,Lu,Sc)VO_4:Bi for ultraviolet converted white LEDs. *J. Mater. Chem. C* **2014**, 2, 6068-6076.

37. F. Kang, M. Peng, Q. Zhang and J. Qiu. Abnormal Anti-Quenching and Controllable Multi-Transitions of Bi^{3+} Luminescence by Temperature in a Yellow-Emitting $LuVO_4$:Bi^{3+} Phosphor for UV-Converted White LEDs. *Chem. Eur. J.* **2014**, 20, 11522-11530.

38. F. Kang, Y. Zhang, L. Wondraczek, J. Zhu, X. Yang and M. Peng. Processing-dependence and the nature of the blue-shift of Bi^{3+}-related photoemission in $ScVO_4$ at elevated temperatures. *J. Mater. Chem. C* **2014**, 2, 9850-9857.

39. F. Kang, X. Yang, M. Peng, L. Wondraczek, Z. Ma, Q. Zhang and J. Qiu. Red photoluminescence from Bi^{3+} and the influence of the oxygen-vacancy perturbation in $ScVO_4$: A combined experimental and theoretical study. *J. Phys. Chem. C* **2014**, 118, 7515-7522.

40. F. Kang, H. Zhang, L. Wondraczek, X. Yang, Y. Zhang, D.Y. Lei and M. Peng. Band-gap modulation in single Bi^{3+}-doped yttrium-scandium-niobium vanadates for color tuning over the whole visible spectrum. *Chem. Mater.* **2016**, 28, 2692-2703.

41. S. Mahlik, M. Amer and P. Boutinaud. Energy level structure of Bi^{3+} in zircon and scheelite polymorphs of YVO_4. *J. Phys. Chem. C* **2016**, 120, 8261-8265.

42. Z. Sun, M. Wang, Z. Yang, K. Liu and F. Zhu. Crystal structure and luminescence properties of Bi^{3+} activated $Ca_2Y_8(SiO_4)_6O_2$ phosphors under near UV excitation. *J. Solid State Chem.* **2016**, 239, 165-169.

43. D.E. Lacklison, G.B. Scott and J.L. Page. Absorption spectra of Bi^{3+} and Fe^{3+} in $Y_3Ga_5O_{12}$. *Solid State Comm.* **1974**, 14, 861-863.

44. M. Ilmer, B.C. Grabmaier and G. Blasse. Luminescence of Bi^{3+} in gallate garnets. *Chem. Mater.* **1994**, 6, 204-206.

45. M. Nikl, A. Novoselov, E. Mihoková, K. Polák, M. Dusek, B. McClune, A. Yoshikawa and T. Fukuda. Photoluminescence of Bi^{3+} in $Y_3Ga_5O_{12}$ single-crystal host. *J. Phys.: Condens. Matter* **2005**, 17, 3367-3375.

46. Y Zorenko, V. Gorbenko, T. Voznyak, V. Vistovsky, S. Nedilko and M. Nikl. Luminescence of Bi^{3+} ions in $Y_3Ga_5O_{12}$:Bi single crystalline films. *Radiat. Meas.* **2007**, 42, 882-886.

47. V. Babin, V. Gorbenko, A. Krasnikov, A. Makhov, M. Nikl, K. Polak, S. Zazubovich and Y Zorenko. Peculiarities of excited state structure and photoluminescence in Bi^{3+}-doped $Lu_3Al_5O_{12}$ single-crystalline films. *J. Phys.: Condens. Matter* **2009**, 21, 415502.

48. Y. Zorenko, J.A. Mares, R. Kucerkova, V. Gorbenko, V. Savchyn, T. Voznyak, M. Nikl, A. Beitlerova and K. Jurek. Optical, luminescence and scintillation characteristics of Bi-doped LuAG and YAG single crystalline films. *J. Phys. D: Appl. Phys.* **2009**, 42, 075501.

49. A. Yousif, V. Kumar, H.A.A. Seed Ahmed, S. Som, L.L. Noto, O.M. Ntwaeaborwa and H.C. Swart. Effect of Ga^{3+} doping on the photoluminescence properties of $Y_3Al_{5-x}Ga_xO_{12}$:Bi^{3+} phosphor. *ECS J. Solid State Sci. Technol.* **2014**, 3, R222-R227.

50. G. Blasse and A. Bril. Study of energy transfer from Sb^{3+}, Bi^{3+}, Ce^{3+} to Sm^{3+}, Eu^{3+}, Tb^{3+}, Dy^{3+}. *J. Chem. Phys.* **1967**, 47, 1920-1926.

51. S. Yan, J. Zhang, X. Zhang, S. Lu, X. Ren, Z. Nie and X. Wang. Enhanced Red Emission in $CaMoO_4$:Bi^{3+},Eu^{3+}. *J. Chem. Phys. C* **2007**, 111, 13256-13260.

52. F. Kang, Y. Zhang and M. Peng. Controlling the Energy Transfer via Multi Luminescent Centers to Achieve White Light/Tunable Emissions in a Single-Phased X2-Type Y_2SiO_5:Eu^{3+},Bi^{3+} Phosphor For Ultraviolet Converted LEDs. *Inorg. Chem.* **2015**, 54, 1462-1473.

53. A. Escudero, C. Carrillo-Carrión, M.V. Zyuzin, S. Ashraf, R. Hartmann, N.O. Núñez, M. Ocaña and W.J. Parak. Synthesis and Functionalization of Monodisperse Near-ultraviolet and Visible Excitable Multifunctional Eu^{3+}, Bi^{3+}:$REVO_4$ Nanophosphors for Bioimaging and Biosensing Applications. *Nanoscale* **2016**, 8, 12221-12236.

54. D. Chen, Y. Yu, P. Huang, H. Lin, Z. Shan, L. Zeng, A. Yang and Y. Wang. Color-tunable luminescence for Bi^{3+}/Ln^{3+}:YVO_4 (Ln=Eu, Sm, Dy, Ho) nanophosphors excitable by near-ultraviolet light. *Phys. Chem. Chem. Phys.* **2010**, 12, 7775-7778.

55. X.Y. Huang, J.X. Wang, D.C. Yu, S. Ye, Q.Y. Zhang and X.W. Sun. Spectral conversion for solar cell efficiency enhancement using YVO_4:Bi^{3+},Ln^{3+} (Ln=Dy, Er, Ho, Eu, Sm, and Yb) phosphors. *J. Appl. Phys.* **2011**, 109, 113526

56. G. Ju, Y. Hu, L. Chen, X. Wang, Z. Mu, H. Wu and F. Kang. Luminescence properties of Y_2O_3:Bi^{3+}, Ln^{3+} (Ln=Sm, Eu, Dy, Er, Ho)and the sensitization of Ln^{3+} by Bi^{3+}. *J. Lumin.* **2012**, 132, 1853-1859.

57. M. Fockele, F. J. Ahlers, F. Lohse, J.-M. Spaeth and R. H. Bartram. Optical properties of atomic thallium centres in alkali halides. *J. Phys. C: Solid State Phys.* **1985**, 18, 1963-1974.

58. L. F. Mollenauer, N. D. Vieira and L. Szeto. Optical properties of the $Tl^0(1)$ center in KCl. *Phys. Rev. B* **1983**, 27, 5332-5346.

59. G. Blasse, A. Meijerink, M. Nomes and J. Zuidema. Unusual bismuth luminescence in strontium tetraborate (SrB_4O_7:Bi). *J. Phys. Chem. Solids* **1994**, 55, 171-174.

60. M. Peng and L. Wondraczek. Bi^{2+}-doped strontium borates for white-light-emitting diodes. *Opt. Lett.* **2009**, 34, 2885-2887.

61. M. de Jong, A. Meijerink, R.A. Gordon, Z. Barandiarán and L. Seijo. Is Bi^{2+} responsible for the red-orange emission of bismuth-doped SrB_4O_7? *J. Phys. Chem. C* **2014**, 118, 9696-9705.

62. M.A. Hamstra, H.F. Folkerts and G. Blasse. Red bismuth emission in alkaline-earth-metal sulfates. *J. Mater. Chem.* **1994**, 4, 1349-1350.

63. R. Cao, M. Peng and J. Qiu. Photoluminescence of Bi^{2+}-doped $BaSO_4$ as a red phosphor for white LEDs. *Opt. Express* **2012**, 20, A977-A983.

64. Q. Zeng, T. Zhang, Z. Pei and S.U. Qiang. Luminescence of unusual bismuth in barium borates (BaB_8O_{13}:Bi). *J. Mater. Sci. Technol.* **1999**, 15, 281-282.

65. M. Peng and L. Wondraczek. Orange-to-red emission from Bi^{2+} and alkaline earth codoped strontium borate phosphors for white light emitting diodes. *J. Am. Ceram. Soc.* **2010**, 93, 1437-1442.

66. M. de Jong, A. Meijerink, Z. Barandiarán and L. Seijo. Structure and hindered vibration of Bi^{2+} in the red-orange phosphor SrB_4O_7:Bi. *J. Phys. Chem. C* **2014**, 118, 17932-17939.

67. M. de Jong and A. Meijerink. Color tuning of Bi^{2+} luminescence in barium borates. *J. Lumin.* **2016**, 170, 240-247.

68. M. Peng, B. Sprenger, M.A. Schmidt, H.G.L. Schwefel and L. Wondraczek. Broadband NIR photoluminescence from Bi-doped $Ba_2P_2O_7$ crystals: Insights into the nature of NIR-emitting Bismuth centers. *Opt. Express* **2010**, 18, 12852-12863.

69. M. Peng and L. Wondraczek. Photoluminescence of $Sr_2P_2O_7$:Bi^{2+} as a red phosphor for additive light generation. *Opt. Lett.* **2010**, 35, 2544-2546.

70. M. Peng, J. Lei, L. Li, L. Wondraczek, Q. Zhang and J. Qiu. Site-specific reduction of Bi^{3+} to Bi^{2+} in bismuth-doped over-stoichiometric barium phosphates. *J. Mater. Chem. C* **2013**, 1, 5303-5308.

71. L. Li, M. Peng, B. Viana, J. Wang, B. Lei, Y. Liu, Q. Zhang and J. Qiu. Unusual concentration induced antithermal quenching of the Bi^{2+} emission from $Sr_2P_2O_7$:Bi^{2+}. *Inorg. Chem.* **2015**, 54, 6028-6034.

72. R. Cao, Y. Cao, T. Fu, S. Jiang, W. Li, Z. Luo and J. Fu. Synthesis and luminescence properties of novel red-emitting $R_3P_4O_{13}$:Bi^{2+} (R=Sr and Ba) phosphors. *J. Alloys Compd.* **2016**, 661, 77-81.

73. A.M. Srivastava. Luminescence of divalent bismuth in $M^{2+}BPO_5$ (M^{2+}=Ba^{2+}, Sr^{2+} and Ca^{2+}). *J. Lumin.* **1998**, 78, 239-243.

74. M. Peng, N. Da, S. Krolikowski, A. Stiegelschmitt and L. Wondraczek. Luminescence from Bi^{2+}-activated alkali earth borophosphates for white LEDs. *Opt. Express* **2009**, 17, 21169-21178.

75. L. Seijo and Z. Barandiarán. Blue absorption and red emission of Bi^{2+} in solids: strongly spin-orbit coupled 6p levels in low symmetry fields. *Phys. Chem. Chem. Phys.* **2014**, 16, 17305-17314.

76. R. Cao, F. Zhang, C. Liao and J. Qiu. Yellow-to-orange emission from Bi^{2+}-doped RF_2 (R=Ca and Sr) phosphors. *Opt. Express* **2013**, 21, 15728-15733.

77. X. Qin, Y. Li, D. Wu, Y. Wu, R. Chen, Z. Ma, S. Liu and J. Qiu. A novel NIR long phosphorescent phosphor $SrSnO_3$:Bi^{2+}. *RSC Adv.* **2015**, 5, 101347-101352.

78. S. Zhou, N. Jiang, B. Zhu, H. Yang, S. Ye, G. Lakshminarayana, J. Hao and J. Qiu. Multifunctional bismuth-doped nanoporous silica galss: from blue-green, orange, red and white light sources to ultra-broadband infrared amplifiers. *Adv. Funct. Mater.* **2008**, 18, 1407-1413.

79. H.-T. Sun, T. Hasegawa, M. Fujii, F. Shimaoka, Z. Bai, M. Mizuhata, S. Hayashi and S. Deki. Significamt enhanced superbroadband near infrared emission in bismuth/aluminium doped high-silica zeolite derived nanoparticles. *Opt. Express* **2009**, 17, 6239-6244.

80. H.-T. Sun, A. Hosokawa, Y. Miwa, F. Shimaoka, M. Fujii, M. Mizuhata, S. Hayashi and S. Deki. Strong ultra-broadband near-infrared photoluminescence from bismuth-embedded zeolites and their derivatives. *Adv. Mater.* **2009**, 21, 3694-3698.

81. H.-T. Sun, Y. Miwa, F. Shimaoka, M. Fujii, A. Hosokawa, M. Mizuhata, S. Hayashi and S. Deki. Superbroadband near-IR nano-optical source based on bismuth-doped high-silica nanocrystalline zeolites. *Opt. Lett.* **2009**, 34, 1219-1221.

82. H.-T. Sun, M. Fujii, Y. Sakka, Z. Bai, N. Shirahata, L. Zhang, Y. Miwa and H. Gao. Near-infrared photoluminescence and Raman characterization of bismuth-embedded sodalite nanocrystals. *Opt. Lett.* **2010**, 35, 1743-1745.

83. H.-T. Sun, J. Yang, M. Fujii, Y. Sakka, Y. Zhu, T. Asahara, N. Shirahata, M. Li, Z. Bai, J.-G. Li and H. Gao. Highly fluorescent silica-coated bismuth-doped aluminosilicate nanoparticles for near-infrared bioimaging. *Small* **2011**, 7, 199-203.

84. A.N.Romanov, A.A. Veber, Z.T. Fattakhova, D.N. Vtyurina, M.S. Kouznetsov, K.S. Zaramenskikh, I.S. Lisitsky, V.N. Korchak, V.B. Tsvetkov and V.B. Sulimov. Spectral properties and NIR photoluminescence of Bi^{+} impurity in $CsCdCl_3$ ternary cjloride. *J. Lumin.* **2014**, 149, 292-296.

85. A.N.Romanov, A.A. Veber, D.N. Vtyurina, Z.T. Fattakhova, E.V. Haula, D.P. Shashkin, V.B. Sulimov, V.B. Tsvetkov and V.N. Korchak. Near infrared photoluminescence of the univalent bismuth impurity center in leucite and pollucite crystal hosts. *J. Mater. Chem. C* **2015**, 3, 3592-3598.

86. M. Peng, J. Qiu, D. Chen, X. Meng and C. Zhu. Superbroadband 1310 nm emission from bismuth and tantalum codoped germanium oxide glasses. *Opt. Lett.* **2005**, 30, 2433-2435.

87. R. Cao, M. Peng, L. Wondraczek and J. Qiu. Superbroad near-to-mid-infrared luminescence from Bi_5^{3+} in $Bi_5(AlCl_4)_3$. *Opt. Lett.* **2012**, 20, 2562-2571.

88. H.-T. Sun, Y. Sakka, N. Shirahata, J. Matsuhita, K. Deguchi and T. Shimizu. NMR, ESR, and luminescence characterization of bismuth embedded zeolites Y. *J. Phys. Chem. C* **2013**, 117, 6399-6408.

89. T. Wakabayashi, Y. Wada, K. Nakajima, Y. Morisawa, S. Kuma, Y. Miyamoto, N. Sasao, M. Yoshimura, T. Sato and K. Kawaguchi. Low-lying electronic states in bismuth trimer Bi_3 as revealed by laser-induced NIR emission spectroscopy in solid Ne. *J. Phys. Chem. A* **2015**, 119, 2644-2650.

90. S. Gu, B. Zhou, W. Luo, L. Wang, W. Jiang and W. Jiang. Near-infrared broadband photoluminescence of bismuth-doped zeolite-derived silica glass prepared by SPS. *J. Am. Ceram. Soc.* **2016**, 99, 121-127.

91. H.-T. Sun, J. Zhou and J. Qiu. Recent advances in bismuth activated photonic materials. *Prog. Mater. Sci.* **2014**, 64, 1-72.

92. G. Blasse and L. Boon. The luminescence of bismuth molybdates. *Ber. Bunsenges. Phys. Chem.* **1984**, 88, 929-930.

93. H.F. Folkerts, J. Zuidema and G. Blasse. Different types of s^2 ion luminescence in compounds with eulytite structure. *Chem. Phys. Lett.* **1996**, 249, 59-63.

94. M. Itoh, T. Katariri, H. Mitani, M. Fujita and Y. Usuki. Comparative study of excitonic structures and luminescence properties of $Bi_4Ge_3O_{12}$ and $Bi_{12}GeO_{20}$. *Phys. Stat. Sol. B* **2008**, 245, 2733-2736.

95. A. Barros, R. Deloncle, J. Deschamp, P. Boutinaud, G. Chadeyron, R. Mahiou, E. Cavalli and M.G. Brik. Optical properties and electronic band structure of $BiMg_2PO_6$, $BiMg_2VO_6$, $BiMg_2VO_6:Pr^{3+}$ and $BiMg_2VO_6:Eu^{3+}$. *Opt. Matter.* **2014**, 36, 1724-1729.

96. J. Olchowka, H. Kabbour, M. Colmont, M. Adlung, C. Wickleder and O. Mentré. $ABiO_2X$ (A=Cd, Ca, Sr, Ba, Pb; X=halogen) *Sillen* X1 series: polymorphism versus optical properties. *Inorg. Chem.* **2016**, 55, 7582-7592.

97. P. Riente, A. Matas Adams, J. Albero, E. Palomares and M. A. Pericàs. Light-Driven Organocatalysis Using Inexpensive, Nontoxic Bi_2O_3 as the Photocatalyst. *Angew. Chem. Int. Ed.* **2014**, 53, 9613-9616.

98. S. Dong, J. Feng, M. Fan, Y. Pi, L. Hu, X. Han, M. Liu, J. Sun and J. Sun. Recent developments in heterogeneous photocatalytic water treatment using visible light-responsive photocatalysts: a review. *RSC Adv.* **2015**, 5, 14610-14630.

99. B.H. Park, B.S. Kang, S.D. Bu, T.W. Noh, J. Lee and W. Jo. Lanthanum-substituted bismuth titanate for use in non-volatile memories. *Nature* **1999**, 401, 682-684.

100. W.S. Choi, M.F. Chismholm, D.J. Singh, T. Choi, G.E. Jellison Jr. and H.N. Lee. Wide bandgap tunability in complex transition metal oxides by site-specific substitution. *Nat. Commun.* **2012**, 3, 689.

101. S. Sanna, V. Esposito, J.W. Andreasen, J. Hjelm, W. Zhang, T. Kasama, S.B. Simonsen, M. Christensen, S. Linderoth and N. Pryds. Enhancement of chemical stability in confined δ-Bi_2O_3. *Nat. Mater.* **2015**, 14, 500-504.

102. M. Guennou, M. Viret and J. Kreisel. Bismuth-based perovskites as multiferroics. *Comptes Rendus Physique* **2015**, 16, 182-192.

103. A. Chen, H. Zhou, Z. Bi, Y. Zhu, Z. Luo, A. Bayraktaroglu, J. Phillips, E.-M. Choi, J.L. MacManus-Driscoll, S.J. Pennycook, J. Narayan, Q. Jia, X. Zhang and H. Wang. A New Class Of Room-Temperature Multiferroic Thin Films with Bismuth-Based Supercell Structure. *Adv. Mater.* **2013**, 25, 1028-1032.

104. R. Nachache, C. Harnagea, S. Li, L. Cardenas, W. Huang, J. Chakrabartty and F. Rosei. Bandgap tuning of multiferroic oxide solar cells. *Nat. Photonics* **2015**, 9, 61-67.

105. J. Hou, Y. Qu, D. Krsmanovic, C. Ducati, D. Eder and R.V. Kumar. Hierarchical assemblies of bismuth titanate complex architectures and their visible-light photocatalytic activities. *J. Mater. Chem.* **2010**, 20, 2418-2423.

106. P. Zhang, J. Hu and J. Li. Controllable morphology and photocatalytic performance of bismuth silicate nanobelts/nanosheets. *RSC Adv.* **2011**, 1, 1072-1077.

107. D. Liu, J. Wang, M. Zhang, Y. Liu and Y. Zhu. A superior photocatalytic performance of a novel Bi_2SiO_5 flower-like microsphere *via* a phase junction. *Nanoscale* **2014**, 6, 15222-15227.

108. D.S. Bhachu, S.J.A. oniz, S. Sathasivam, D.O. Scanlon, A. Walsh, S.M. Bawaked, M. Mokhtar, A.Y. Obaid, I.P. Parkin, J. Tang and C.J. Carmalt. Bismuth oxyhalides: synthesis, structure and photoelectrochemical activity. *Chem. Sci.* **2016**, 7, 4832-4841.

109. T. Saison, N. Chemin, C. Chanéac, O. Durupthy, L. Mariey, F. Maugé, V. Brezová and J.-P. Jolivet. New insights into $BiVO_4$ properties as visible light photocatalyst. *J. Phys. Chem. C* **2015**, 119, 12967-12977.

110. T. Tachikawa, T. Ochi and Y. Kobori. Crystal-face-dependent charge dynamics on a $BiVO_4$ photocatalyst revealed by single-particle spectroelectrochemistry. *ACS Catal.* **2016**, 6, 2250-2256.

111. F.F. Abdi, L. Han, A.H.M. Smets, M. Zeman, B. Dam and R. van de Krol. Efficient solar water splitting by enhanced charge separation in bismuth vanadate-silicon tandem photoelectrode. *Nat. Commun.* **2013**, 4, 2195.

112. T.W. Kim, Y. Ping, G.A. Galli and K.-S. Choi. Simultaneous enhancements in photon absorption and charge transport of bismuth vanadate photoanodes for solar water splitting. *Nat. Commun.* **2015**, 6, 8769.

113. J. Resasco, H. Zhang, N. Kornienko, N. Becknell, H. Lee, J. Guo, A.L. Briseno and P. Yang. $TiO_2/BiVO_4$ nanowire heterostructure photoanodes based on type II band alignement. *ACS Cent. Sci.* **2016**, 2, 80-88.

114. A. Walsh, G.W. Watson, D.J. Payne, R.G. Edgell, J. Guo, P.-A. Glans, T. Leaemonth and K.E. Smith. Electronic structure of the α and δ phases of Bi_2O_3: A combined *ab initio* and x-ray spectroscopy study. *Phys. Rev. B* **2006**, 73, 235104.

115. A. Walsh, D.J. Payne, R.G. Egdell and G.W. Watson. Stereochemistry of post-transition metal oxides: revision of the classical lone pair model. *Chem. Soc. Rev.* **2011**, 40, 4455-4463.

116. D.J. Payne, R.G. Egdell, A. Walsh, G.W. Watson, J. Guo, P.-A. Glans, T. Leaemonth and K.E. Smith. Electronic origins of structural distortions in post-transition metal oxides: experimental and theoretical evidence for a revision of the lone pair model. *Phys. Rev. Lett.* **2006**, 96, 157403.

117. A.C. Lira, I. Camarillo, E. Camarillo, F. Ramos, M. Flores and U. Caldiño. Spectroscopic characterization of Er^{3+} transitions in $Bi_4Si_3O_{12}$. *J. Phys.: Condens. Matter* **2004**, 16, 5925-5936.

118. A.C. Lira, M.O. Ramírez, J. García Solé and U. Caldiño. Photoluminescence of $Bi_4Si_3O_{12}:Er^{3+}$ crystal excited in the commercial laser diode emission region. *Opt. Mater.* **2007**, 29, 605-609.

119. A.C. Lira, E. Martín-Rodríguez, R. Martínez-Martínez, I. Camarillo, G.H. Muñoz, J. García Solé and U. Caldiño. Spectroscopy of the $Bi_4Si_3O_{12}:Er^{3+}$ glass for optical amplification and laser application. *Opt. Mater.* **2010**, 32, 1266-1273.

120. B. Yang, J. Xu, Y. Zhang, Y. Chu, M. Wang and Y. Wen. A yellow emitting phosphor Dy:$Bi_4Si_3O_{12}$ crystal for LED application. *Opt. Mater.* **2014**, 135, 176-179.

121. Q. Wei, G. Liu, Z. Zhou, J. Wan, J. Wang and Q. Liu. Combinatorial discovery of self-mixing phosphors $Bi_{4(1-x)}Si_3O_{12};RE_{4x}^{3+}$ (RE^{3+}=Dy^{3+}, Eu^{3+}) for direct white light emission. *RSC Adv.* **2015**, 5, 85862-85871.

122. L. Sun, F. Gao and Q. Huang. White upconversion photoluminescence for Er^{3+}-Tm^{3+}-Yb^{3+} tri-codoped bismuth titanate ferroelectric thin films. *J. Alloys Compd.* **2014**, 588, 158-162.

123. T. Wei, T.B. Zhang, Y.J. Ma, Y. F. Xie, C.Z. Zhao, F.M. Yang, H.Y. Xiao and Y. Zhao. Up-conversion photoluminescence and temperature sensing properties of Er^{3+}-doped $Bi_4Ti_3O_{12}$ nanoparticles with good water-resistance performance. *RSC Adv.* **2016**, 6, 7643-7652.

124. J. García Solé, L.E. Bausá and D. Jaque. An introduction to the optical spectroscopy of inorganic solids, Wiley, 2005.

125. K.W. Krämer, D. Biner, G. Frei, H.U. Güdel, M.P. Hehlen and S.R. Lüthi. Hexagonal sodium yttrium fluoride based green and blue emitting upconversion phosphors. *Chem. Mater.* **2004**, 16, 1244-1251.

126. H. Schäfer, P. Ptacek, H. Eickmeier and M. Haase. Synthesis of hexagonal Yb^{3+},Er^{3+}-doped $NaYF_4$ nanocrystals at low temperature. *Adv. Funct. Mater.* **2009**, 19, 3091-3097.

127. S. Jin, L. Zhou, Z. Gu, G. Tian, L. Yan, W. Ren, W. Yin, X. Liu, X. Zhang, Z. Hu and Y. Zhao. A new near infrared photosensitizing nanoplatforms containing blue-emitting up-conversion nanoparticles and hypocrellin A for photodynamic therapy of cancer cells. *Nanoscale* **2013**, 5, 11910-11918.

128. M.D. Wisser, S. Fischer, P.C. Maurer, N.D. Bronstein, S. Chu, A.P. Alivisatos, A. Salleo and J.A. Dionne. Enhancing quantum yield via symmetry distortion in lanthanide-based upconverting nanoparticles. *ACS Photonics* **2016**, 3, 1523-1530.

129. N. M. Sammes, G. A. Tompsett, H. Näfe and F. Aldinger. Bismuth Based Oxide Electrolytes - Sructure and Ionic Conductivity. *J. Eur. Ceram. Soc.* **1999**, 19, 1801-1826.

130. M. Drache, P. Roussel and J.-P. Wignacourt. Structures of Oxide Mobility in Bi-Ln-O Materials: Heritage of Bi_2O_3. *Chem. Rev.* **2007**, 107, 80-96.

131. L. Malavasi, C. A. J. Fisher and M. S. Islam. Oxide-ion proton conducting electrolyte materials for clean energy applications: structural and mechanistic features. *Chem. Soc. Rev.* **2010**, 39, 4370-4387.

132. C.E. Mohn, S. Stølen, S.T. Norberg and S. Hull. Oxide-ion disorder within the high temperature δ phase of Bi_2O_3. *Phys. Rev. Lett.* **2009**, 102, 155502.

133. L.G. Sillen. X-ray studies on bismuth trioxide. *Ark. Kemi. Mineral. Geol.* **1937**, 12A, 1-15.

134. G. Gattow and H. Schroder. Über Wismutoxide. III. Die Kristallstruktur der Hochtemperaturmodifikation von Wismut(III)-oxid (δ-Bi_2O_3). *Z. Anorg. Allg. Chem.* **1962**, 318, 176-189.

135. B.T.M. Willis. The anomalous behaviour of the neutron reflexion of fluorite. *Acta Crys.* **1965**, 18, 75-76.

136. A. Matsumoto, Y. Koyama and I. Tanaka. Structures and energetics of Bi_2O_3 polymorphs in a defective fluorite family derived by systematic first-principles lattice dynamics calculations. *Phys. Rev. B* **2010**, 81, 094117.

CHAPTER 4

Bismuth Oxide-based UCNPs: Tuning the Upconversion Emission by Bandgap Engineering

Abstract In the field of novel applications involving upconverting processes, the determination of new strategies for realizing emission-tunable nanomaterials is a challenge. Here we present the design of Y^{3+} and Er^{3+} codoped bismuth oxide-based upconverting nanoparticles where the active role of the matrix allows for the emission selectivity with chromaticity control. We demonstrate that the possibility to manipulate the bandgap of the bismuth oxide-based host in a range of 0.65 eV consequently leads to an upconversion color emission tunability across a range going from red to yellow-greenish. The resulting fine control of the nanoparticle chromaticity through accurate host bandgap engineering determines a new concept for the development of a new generation of upconverting nanophosphors. Finally, we discuss the effect of Yb^{3+} content on the UC properties of Yb^{3+}-Er^{3+} codoped Bi_2O_3 nanoparticles and we show the great potentialities of Bi_2O_3:Yb^{3+},Ho^{3+} and Bi_2O_3:Yb^{3+},Tm^{3+} systems for application like multiplex encoding.

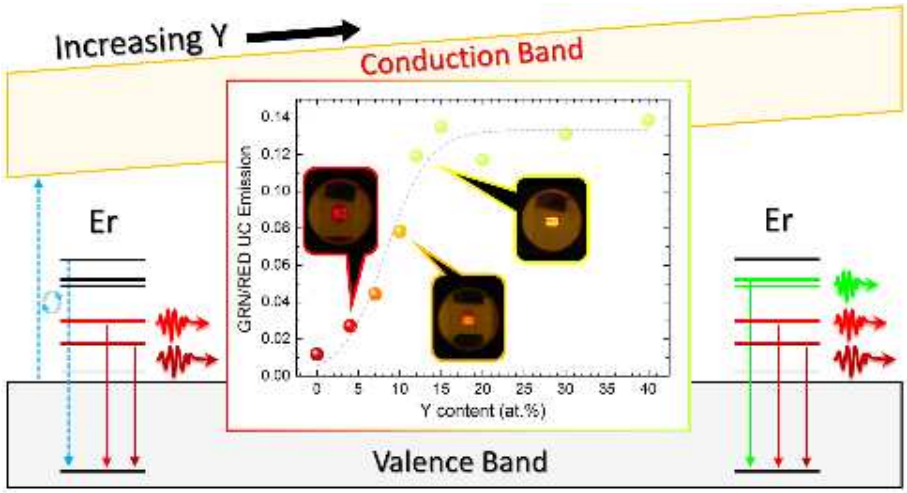

4.1 Introduction

Recently, an increasing interest has been focused on the development of lanthanide (Ln) ion doped unpconverting nanoparticles (UCNPs) for application in the fields of biological imaging and multiplexed assays,[1-5] photovoltaic technologies,[6-8] optical nanothermometers[9-11] and anti-counterfeiting.[12-15] To date, the big impulse in the development of nanophosphors with precise color emission control has led to a wide variety of strategies for UCNP design, like antenna effects,[16] convenient fluorescence resonance energy transfer (FRET) pathways,[17] cross-relaxation processes,[18,19] size/surface effects,[20,21] energy migration-mediated processes,[22,23] or by means of more complex architectures like core-shell structures with finely controlled ion doping[24] or local structure engineering of the host.[25]

Since Ln doped NPs usually exhibit multipeak emission spectra, the challenge is the achievement of UC emission color fine-tuning over a broad spectral range, as well as single-band UC emission with selected chromaticity. Regarding the latter issue, the high red-to-green (R/G) emission ratio observed in fluoride UCNPs doped with Yb^{3+} and Er^{3+} has brought to single-band red emitting UC nanophosphors targeted for bioimaging applications.[26,27] However the search for color output control in UCNPs can not disregard from the study of novel host materials and their manipulation, depending from the host nature and the luminescent dopant concentration.

In the last years, bismuth-based oxide materials have attracted great attention because of their low toxicity,[28,29] low cost and promising properties for a wide range of applications like photocatalysts,[29,30] ferroelectrics,[31,32] fuel cells,[33] multiferroics,[34,35,36] gas sensing,[37] topological insulators[38,39] and in the medicine field.[28] The wide bandgap tunability of bismuth-based materials was exploited for electronic and energy applications,[32,36] but for the best of our knowledge, there is no literature about the use of this property to manipulate the color emission in UCNPs. In this regard, the main limit to the use of bismuth oxide as host for lanthanide ions is its narrow bandgap, which falls in the visible range (2.3-3 eV). However, the anti-Stokes nature of the upconversion process, consisting in the conversion of two low-energy photons into a single photon at higher energy, allows to overcome such a problem.

In this first part of the Chapter, we propose the possibility to control the UC color emission tunability by the bandgap engineering of the bismuth oxide via ion doping. To this purpose, Y^{3+} and Er^{3+} ions were chosen as electronic structure modifier and probe for upconversion processes, respectively. Combining a theoretical and experimental approach, we focused on the assessment of the ion doped Bi_2O_3 electronic configuration, as it represents the key point for UC nanophosphor design. We observed a clear correlation between the progressive opening of the host bandgap, as the Y^{3+} content is increased, and the resulting Er^{3+} UC emission color, characterized by a wide-range tunable chromaticity output, ranging from red to yellow-greenish.

In the final section, we turn our attention on the possibility to realize efficient Bi_2O_3 based UCNPs by Yb^{3+}, Ln^{3+} ($Ln^{3+} = Er^{3+}$, Ho^{3+}, Tm^{3+}) codoping, where Yb plays the dual role of UC sensitizer, in virtue of the large absorption cross section characterizing its $^2F_{7/2} \rightarrow {}^2F_{5/2}$ transition at around 980 nm, and of structural modifier, as Y ion in the case of Y^{3+}, Er^{3+} codoped Bi_2O_3 NPs. In this regards, the latter aspect was addressed for the Yb-Er system, where a series of samples with different Yb content was realized.

In perspectives, the results of this research may be extended by considering either further dopants as modifier of the Bi_2O_3 band structure or different lanthanide ions as UC PL emitters, as well as other Bi-based oxide hosts.

4.2 Sample Preparation

Materials. $Bi(NO_3)_3 \cdot 5H_2O$ (99.99%, Sigma-Aldrich), $Y(NO_3)_3 \cdot 6H2O$ (99.9%, Sigma-Aldrich), $Er(NO_3)_3 \cdot 5H_2O$ (99.9%, Sigma-Aldrich), citric acid (99%, Carlo Erba), ethylene glycol (99.5%, Acros Organics), and HNO_3 60% (Sigma-Aldrich) were used for the preparation of the samples without further purification.

Synthesis. A series of samples made of Bi_2O_3 nanoparticles doped with x at.% of Y (x=0, 4, 7, 10, 12, 15, 20, 30, 40) and 2 at.% of Er, respectively, were prepared by a modified Pechini-type sol-gel process.[40] In a typical synthesis, citric acid, ethylene glycol and the dopant salts are mixed following the reaction:

$$xBi(NO_3)_3 + yY(NO_3)_3 + zEr(NO_3)_3 + HOC(COOH)(CH_2COOH)_2$$
$$+HOCH_2CH_2OH \xrightarrow{HNO_3,H_2O} Bi_xO_3{:}\,Y_y, Er_z$$

where the molar proportions between the salts (x:y:z) were chosen according to the stoichiometry of Bi_2O_3 and the desired dopant concentration. The molar ratio between the salts, the citric acid, and the ethylene glycol was maintained in proportions of 1:3:4.5. The reaction was kept at 120°C for about 12 h and the final samples were obtained after calcination of the products in a muffle kiln at 750 °C in air for 2 h. This temperature was chosen considering the 815 °C melting point of bismuth oxide. The samples were labeled as YxEr2, with x=0, 4, 7, 10, 12, 15, 20, 30, 40, corresponding to the Y atomic percentage.

Moreover, with the same synthetic procedure, a series of Yb^{3+}, Er^{3+} codoped samples labeled as YbxEr2, with x=0, 4, 7, 10, 25, 20 corresponding to the atomic percentage of Yb were synthesized and, with the aim to compare the typical UC systems, a sample codoped with Yb, Ho (10 at.% of Yb and 1 at.% of Ho) and one with Yb, Tm (10 at.% of Yb and 0.2 at.% of Tm) were prepared.

4.3 Y^{3+},Er^{3+} codoped Bi_2O_3 UCNPs

4.3.1 Structural and morphological analysis

Figure 4.1a shows the structural evolution of the system from the tetragonal β-Bi_2O_3 phase (ICSD#41764) to the cubic δ-Bi_2O_3 phase (ICSD#98144) at the increasing of Y^{3+} content. The cell parameters were estimated from Rietveld analysis and the cell volumes of β-phase were divided by two to consider the same number of unit formula and then to compare the volume values of both the phases. The results of the Rietveld refinement method are shown in Table 4.1 and the fit of the Y4Er2 and Y30Er2 samples are displayed in Figure 4.1c and d.

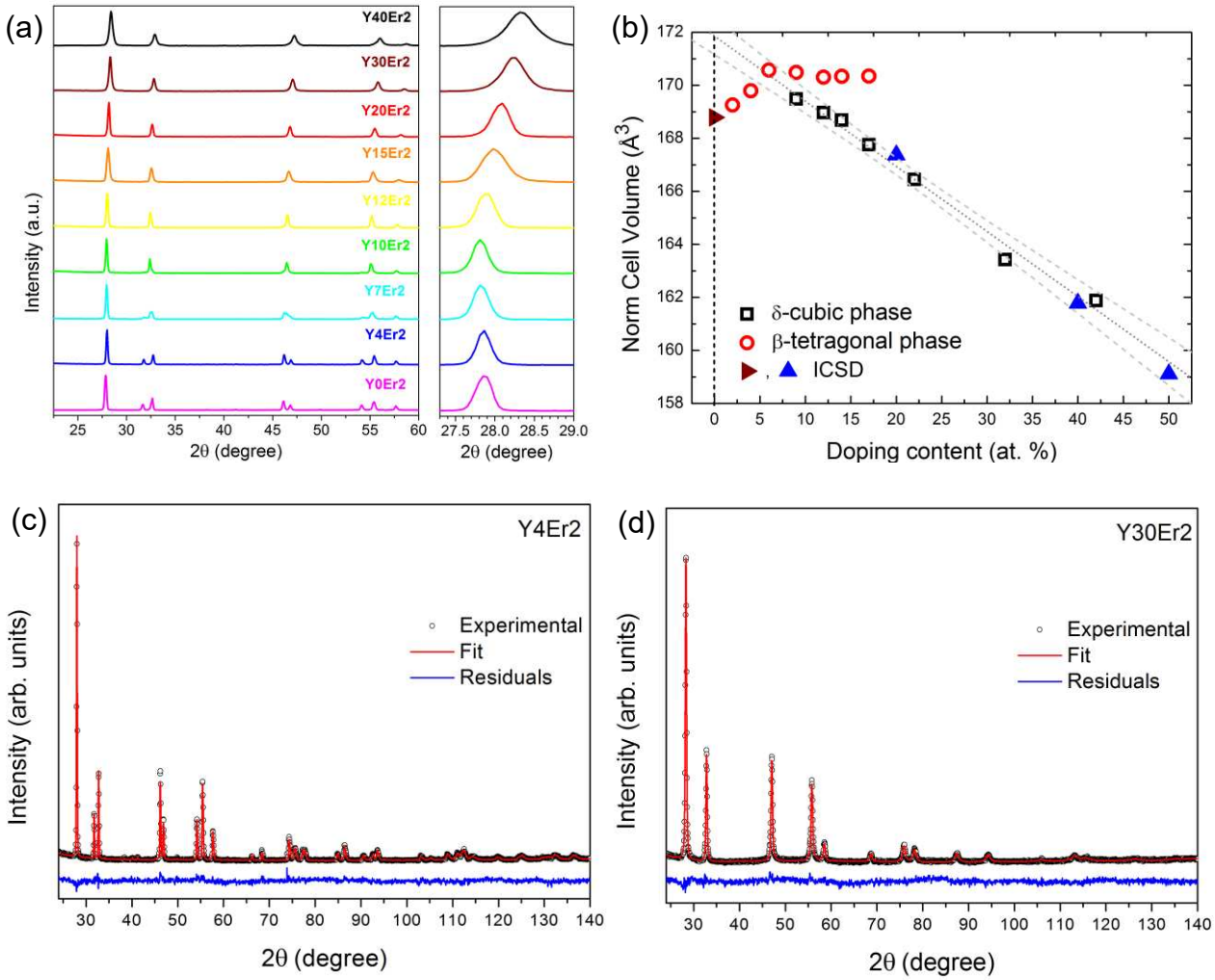

Figure 4.1 (a) XRPD patterns of the synthesized Bi_2O_3-based nanoparticles, with different Y content; in the right panel, zoom of the 27.3-29° region. (b) Trend of phase cell volume *versus* overall doping content (0-40 at.% of Y; 2 at.% of Er); the triangles corresponds to the data from the literature. Rietveld refinement fit performed on the samples Y4Er2 (c) and Y30Er2 (d).

Table 4.1. Summary of the parameters obtained from Rietveld refinement of the samples.

Sample	Cubic phase			Tetragonal phase						
	a	V_{cell}	wt%	a	c	$V_{cell}/2$	wt%	R_p	R_{wp}	GOF
Y0Er2	-	-	-	7.748	5.639	169.25883	100	8.91	11.78	1.59
Y4Er2	-	-	-	7.7684	5.65315	170.57852	100	8.11	10.25	1.45
Y7Er2	5.53403	169.48237	44.82	7.77896	5.63469	170.48354	55.18	8.37	11.05	1.60
Y10Er2	5.52848	168.97278	84.19	7.77605	5.63315	170.30976	15.81	7.34	9.40	1.38
Y12Er2	5.52534	168.68512	86.98	7.77903	5.6299	170.34194	13.02	6.96	8.94	1.30
Y15Er2	5.51516	167.75429	96.75	7.779	5.63	170.34365	3.25	7.13	9.24	1.39
Y20Er2	5.5008	166.44761	100	-	-	-	-	7.07	9.09	1.31
Y30Er2	5.467	163.39812	100	-	-	-	-	6.64	8.77	1.41
Y40Er2	5.45	161.87863	100	-	-	-	-	8.05	11.66	1.84

GOF= goodness of fit

As plotted in Figure 4.1b, for β-phase, after a slight increase up to 4% of Y^{3+}, the cell volume remains constant while for δ-phase an evident decrease in the cell volume as the Y content rises

is noticed. This contraction for the δ phase is due to the difference in the cationic radius of Y^{3+} (1.019 Å) respect to Bi^{3+} (1.17 Å) and it is in good agreement with the value reported in literature (the triangles in Figure 4.1b correspond to the ICSD numbers 52732, 182303, 182305 and 182306).

Concerning the sublattice of the bismuth atoms, it must be pointed out that the structural change from the tetragonal phase ($P421c$ space group) to the cubic phase ($Fm3m$ space group) is a smooth transition consisting in a very small contraction of the c cell-edge and small variation of the Bi/Y atom positions (see the atoms positions reported in Figure 4.2).

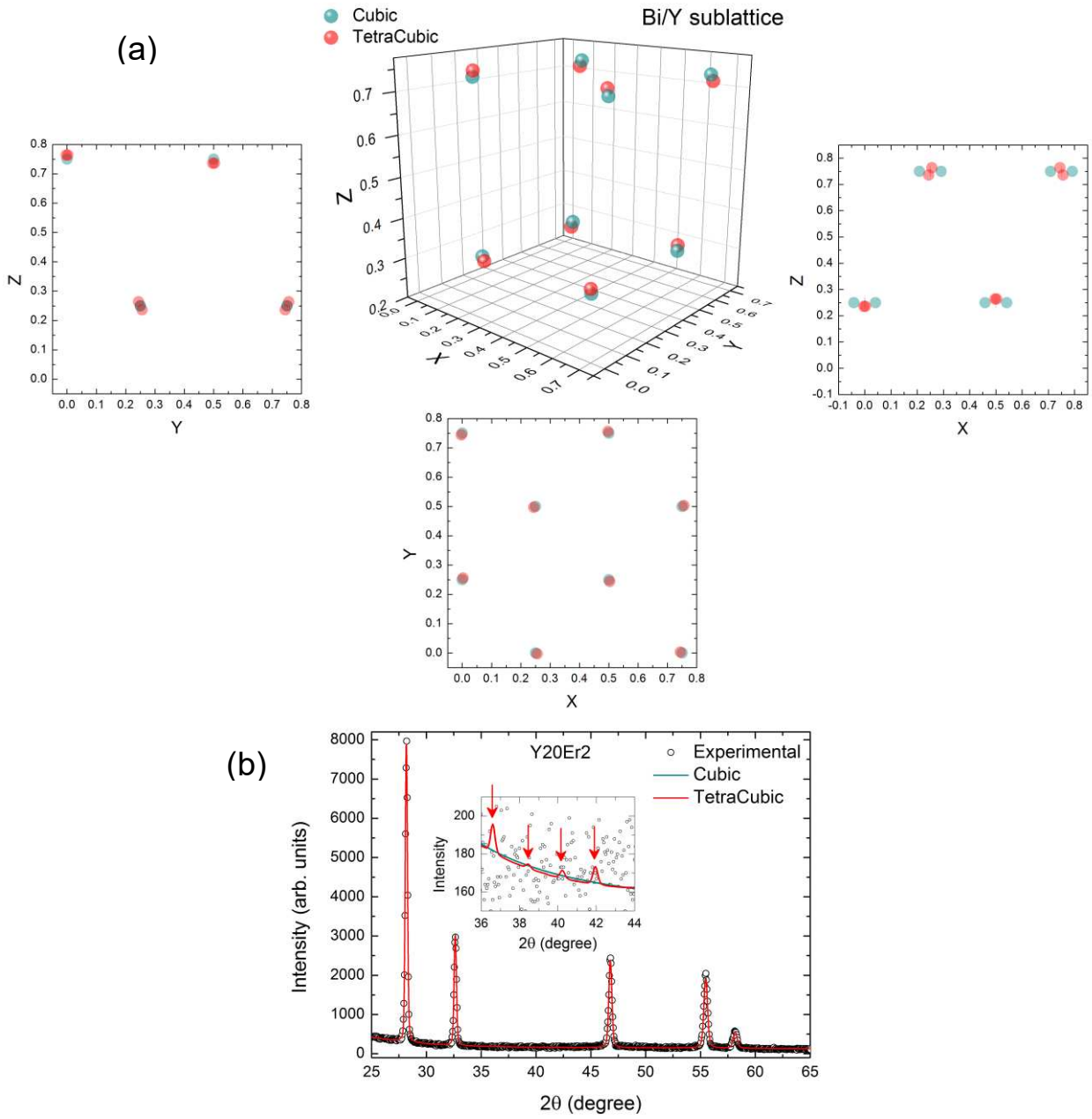

Figure 4.2 (a) 3D plot and projections along the xy, xz and yz plans of the bismuth (Y) sublattice in the cubic δ-Bi_2O_3 cell (green spheres) respect to that one resulting by considering the tetragonal phase with a small contraction of the c cell-edge (red spheres). (b) Rietveld refinement fit performed on the sample Y20Er2 with the two phases. Inset shows very small peaks due to the oxygen in tetragonal phase.

As an evidence of the possibility to consider the cubic phase as a distorted tetragonal phase (with a very small contraction of *c* cell-edge) the perfect match of the fit of the XRPD pattern of Y20Er2 sample performed in the two situations are presented in Figure 4.2b. In fact, the fit of the XRPD spectrum of sample Y20Er2 (cubic phase), can be performed considering a cubic cell (space group *Fm*3*m*) with a=5.5008. However, the same spectrum can be obtained by fitting with a tetragonal cell (space group *P*421*c*) with a=7.7800 and c=5.5003, refining the atomic position with very small variations. In the inset, oxygen related peaks in the tetragonal phases are evidenced, however, the intensity is so small to be within the error and the present analyses are not able to distinguish between the two fit.

FE-SEM images and EDS analysis reported in Figures 4.3a,b and c, respectively, concern Y10Er2 sample. The NPs appear as homogeneous in size, in the range of about 40-50 nm. This observation agrees with the results of the Scherrer analysis, performed on the different samples, which clearly suggests the independence of the average crystallite size from the Y content (see Figure 4.3d). The composition of the samples were checked by EDS analysis, confirming the relative Bi:Y:Er ratios, in agreement with the chemical formula $(Bi_{0.98-x}Y_xEr_{0.02})_2O_3$, with x=0, 0.04, 0.07, 0.10, 0.12, 0.15, 0.20, 0.30 and 0.40.

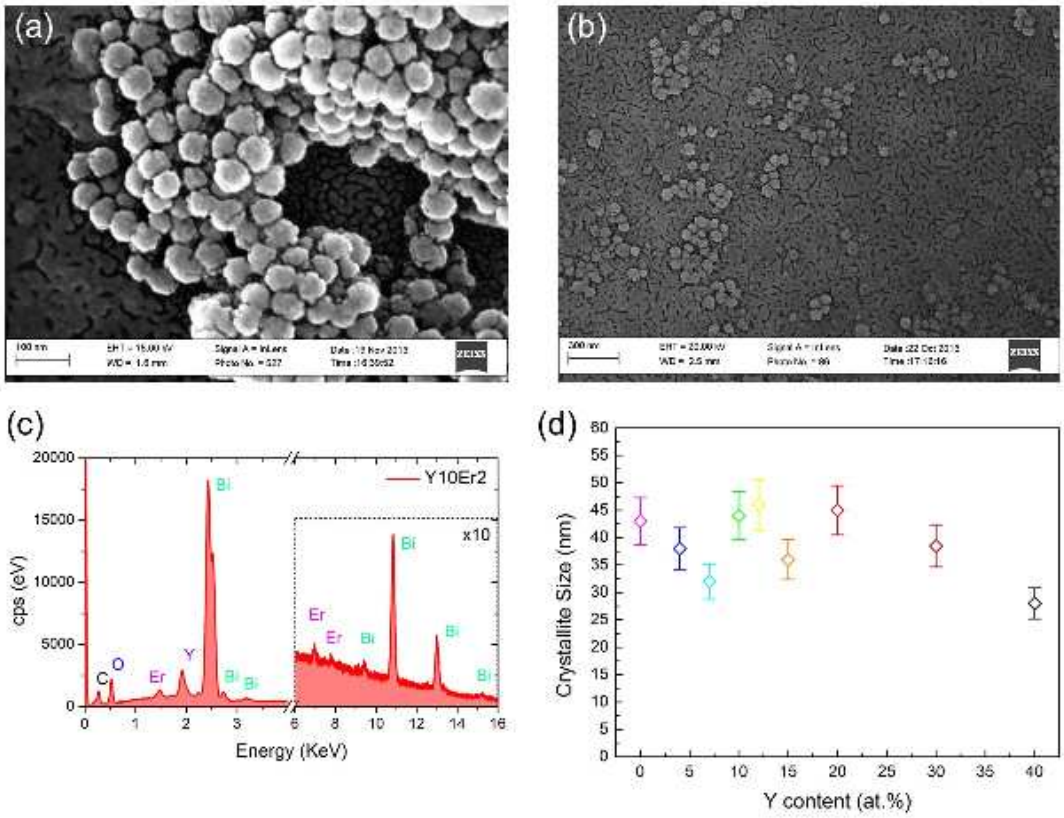

Figure 4.3 (a,b) FE-SEM images and (c) EDS spectrum of the Y10Er2 sample. (d) Average crystallite size estimated by Scherrer analysis as a function of the Y content.

4.3.2 Bandgap engineering

As far as the electronic structure of bismuth oxide concerns, DFT calculations of the DOS for the different polymorphs reveal that the conduction band consists mainly of Bi 6p states,[41,42] while

the valence band is mainly due to O 2p ones. Moreover, metal and non-metal doping may strongly affect the CB and VB edges because of the covalent character of the Bi-O bonding with a consequent big impact in the energy gap of the materials.

Optical diffuse reflectance (*R*) measurements were performed to obtain information about the optical bandgap from the powder samples. The bandgap was estimated from the Tauc plot[43] of the Kubelka-Munk function *F(R)*,[44] considering the direct bandgap semiconductor nature of both the β and δ-Bi_2O_3 phases.[45,46,41] From the plot of $(F(R)\cdot h\nu)^2$ *versus* the energy hν, the bandgap energy E_g is estimated by extrapolating the intercept of the fitted straight line at *F(R)*=0. In Figure 4.4a, we observed a blue shift of the absorption edge of the samples from 2.34 eV up to 2.99 eV as the Y^{3+} content increases. As evidenced in Figure 4.4b, the observed trend clearly indicates the possibility of a direct control of the host optical bandgap by adjusting the Y^{3+} ion doping level, with a consequent tuning in an energy range of 0.65 eV. In this regard, on the other hand, the color of the powder samples turns from yellow-orangish to pale yellow by increasing the Y content (Figure 4.4c).

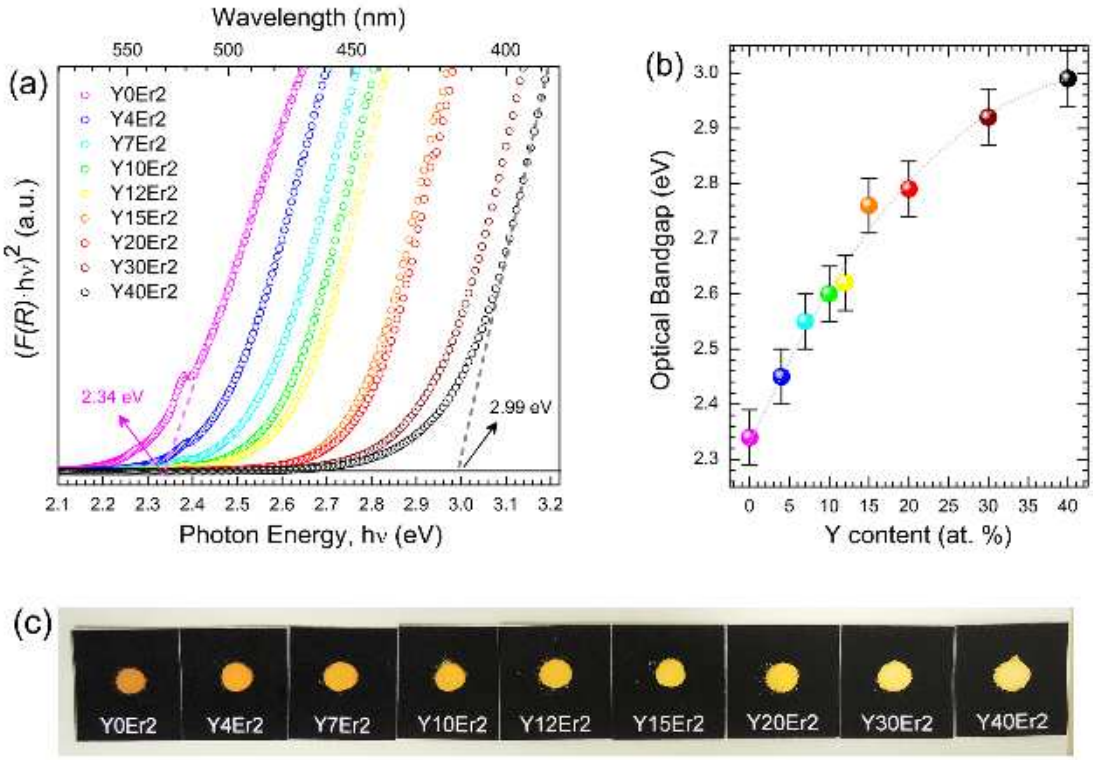

Figure 4.4. (a) Tauc plot of the Kubelka-Munk function *F(R)* for the synthesized samples, (b) trend of optical bandgap values *versus* Y content and (c) pictures of the powder samples.

4.3.3 UC luminescence analysis

The spectrum shown in Figure 4.5a is a typical UC PL spectrum under 980 nm excitation characterizing the Y, Er codoped samples object of this study. The most intense signal comes from the Er^{3+} $^4F_{9/2}\rightarrow{}^4I_{15/2}$ transition, that will be labeled as RED emission in the following,

whereas in the zoom boxes other two remarkable features are evidenced therein: the GRN labeled emission in the green part of the visible spectrum, due to the Er^{3+} $^4S_{3/2} \rightarrow {}^4I_{15/2}$ and $^2H_{11/2} \rightarrow {}^4I_{15/2}$ transitions, and the NIR labeled one at the edge between the visible and the near-IR region, due to the Er^{3+} $^4I_{9/2} \rightarrow {}^4I_{15/2}$ transition. For each of the three emissions, the behavior of the PL intensity as a function of the Y content integrated over the whole wavelength range is reported in Figure 4.5b, where each trend is normalized for the signal related to the Y12Er2 sample; the reason of this normalization will be clarified in the following.

About the dynamics characterizing the observed UC PL emission features, Figure 4.5c reports the time decay curves for the three emissions (labeled as GRN, RED and NIR, respectively) obtained for the Y12Er2 sample under 980 nm pumping. Furthermore, in Figure 4.5d it is possible to appreciate the general trends of the time constant characterizing the UC PL decay of each emission as a function of the Y content, obtained by single-exponential fit procedure; the values obtained are in the order of hundreds of microseconds.

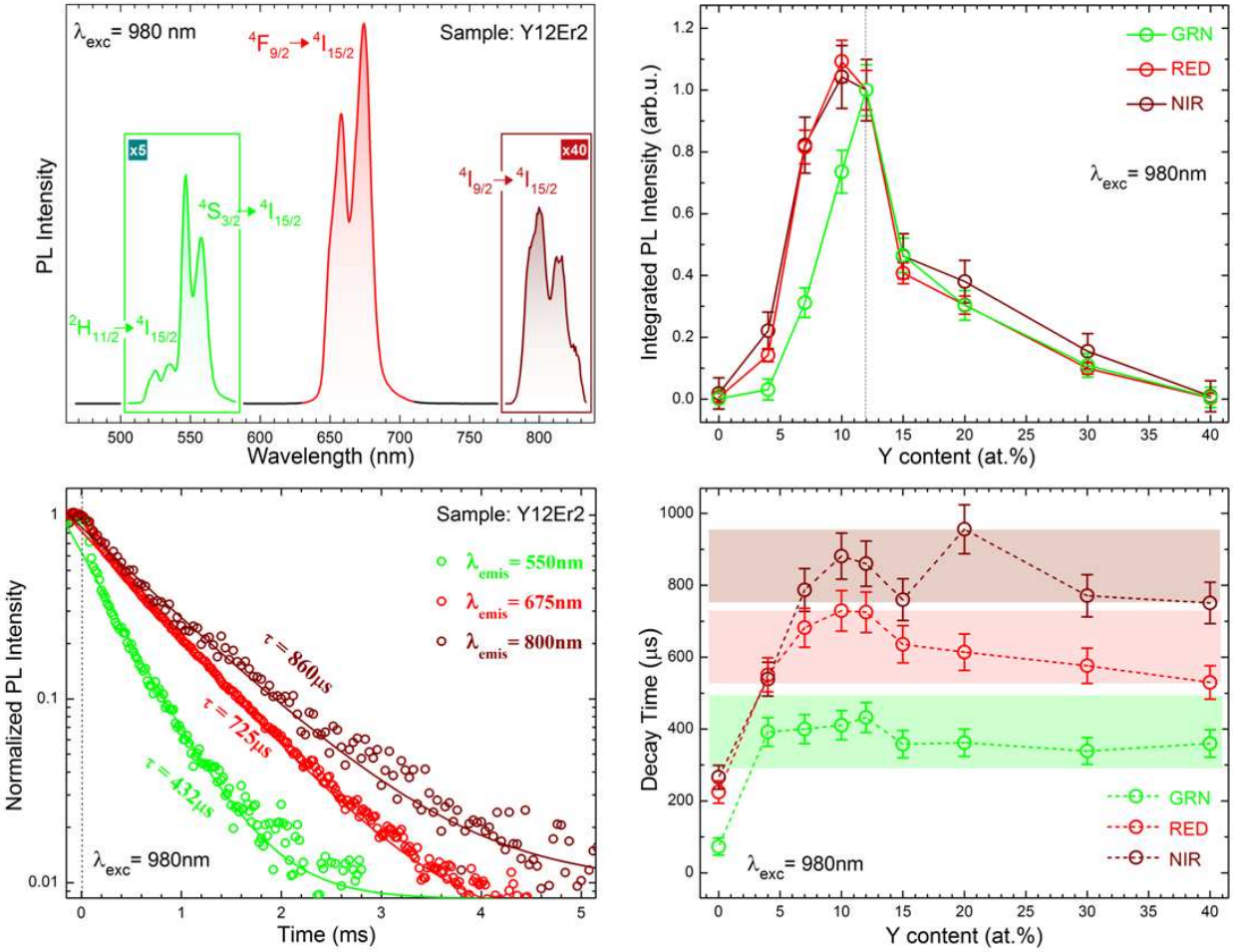

Figure 4.5 (a) UC PL emission spectrum of Y12Er2 sample under 980 nm laser diode exposure. (b) Trend of the integrated PL intensity for the GRN, RED and NIR transitions *versus* Y content. (c) UC PL decay curves collected at wavelengths corresponding to GRN, RED and NIR emission for the Y12Er2 sample, with decay time constant estimates obtained by single-exponential fit procedure. (d) Trend of UC PL decay time constant estimates *versus* Y content.

In regard of the UC process order, the power dependence of UC luminescence intensity for the three transitions was also analyzed (see Figure 4.6). The number *n* of pump photons required to excite the emitting states was estimated from the slope of the plot of the luminescence intensity *versus* the pump power, in double-logarithmic representation. In the considered pumping power range, the measured slopes are close to 2 for all the analyzed PL emissions, suggesting a two-step UC process for the population of the excited levels, as expected from the literature.[47]

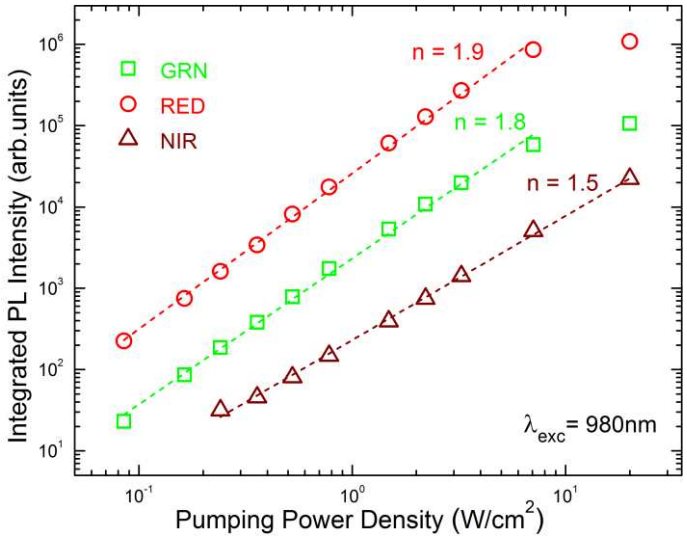

Figure 4.6. Double-log-plot of the integrated UC PL intensity of the GRN, RED and NIR emissions *versus* pumping power density of the 980 nm laser diode excitation source and the corresponding order (n) of the UC process.

As a first comment to the observed UC PL behavior, Figure 4.5b shows that by increasing the Y content up to a doping level of 10-12 at.% the intensity of each emissive features reaches a maximum, although among these a different trend can be noticed. Then, a general reduction characterizes all UC PL signals by further incorporation of Y^{3+} ions.

To give account for this downward trend at high Y doping regime, it is firstly pointed out that the invariance of the estimated time decays reported in Figure 4.5d suggests that the Er^{3+} population is characterized by a constant luminescence yield, since it is determined by the relative rate between the dynamics of radiative and non-radiative relaxation processes. On the other hand, the spectra of the Kubelka-Munk function reported in Figure 4.7 show a general decrease as the Y content is raised for the absorptive features linked to the characteristic Er^{3+} ground state absorption processes. The zoom shown for the region around 980 nm gives account of this in regard to the Er^{3+} $^4I_{15/2} \rightarrow {}^4I_{11/2}$ transition, which is primarily involved when operating in UC mode. Hence the reason of the progressive PL reduction trend can be attributed to a weakening of the absorption process that triggers the overall UC mechanism rather than a general loss in the Er^{3+} luminescence quantum efficiency.

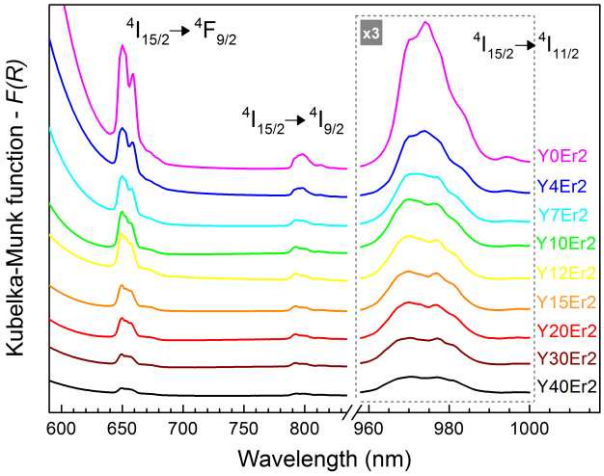

Figure 4.7 Kubelka-Munk function *F(R)* spectra for the synthesized samples; the curves were shifted by a fixed offset and the signals can be compared in intensity; the labelled absorptive features are referred to Er^{3+} ground-to-excited state transitions.

The evidences emerging from Figure 4.7 nonetheless seem in contrast with the strong reduction of UC PL signals at low Y doping regime, as shown in Figure 4.5b. In this context, it is worth paying attention to a further relevant feature, that determines a peculiar behavior from the point of view of the light emission properties for the UC PL signals at low Y doping regime.

The normalization adopted in Figure 4.5b allows to appreciate that the GRN emission intensity remains depressed for Y doping level below 12 at.% with respect to both RED and NIR ones, whose trends well overlap over the whole Y content range here considered. Since Figure 4.5d shows that for all three transitions the time decay constant estimates follow the same trend over the whole Y content range here considered. Since Figure 4.5d shows that for all three transitions the time decay constant estimates follow the same trend over the whole Y content range, a possible GRN PL weakening effect owed to a related quantum efficiency reduction seems to play at least a minor role.

Therefore, to motivate the observed behavior we must take into account the overall process that leads to the activation of the Er^{3+} UC PL emissions. In the following discussion, we refer to the energy level diagrams depicted in Scheme 4.1.

As shown in the left side of the scheme, the 980 nm pumping source firstly promotes $^4I_{15/2} \rightarrow {}^4I_{11/2}$ transition by direct Er^{3+} ground state absorption (GSA) or by energy transfer (ET) from a nearby ion. For the subsequent step, to define the higher-lying energy level transitions involved and the consequent radiative relaxations promoted via UC excitation, here we consider the crossroads between two competitive main mechanisms, labeled as (I) and (II) in Scheme 1.

Under 980 nm radiation, mechanism (I) is linked to the prompt activation of $^4I_{11/2} \rightarrow {}^4F_{7/2}$ transition by Er^{3+} excited state absorption (ESA) or nearby ion-mediated energy transfer upconversion (ETU) processes. Since the photon energy of this transition is usually twice that of the pumping source, the related spectral feature falls in the blue region of the e.m. spectrum, with a peak wavelength around 490 nm. Following non-radiative multiphonon relaxations lead to downward

transitions to the lower energy levels from which the observed GRN, RED, NIR emissions originate.

Scheme 4.1. Scheme of the energy level diagram representing the proposed mechanisms for the generation of the different UC emissions showed by the doped Bi_2O_3 NPs.

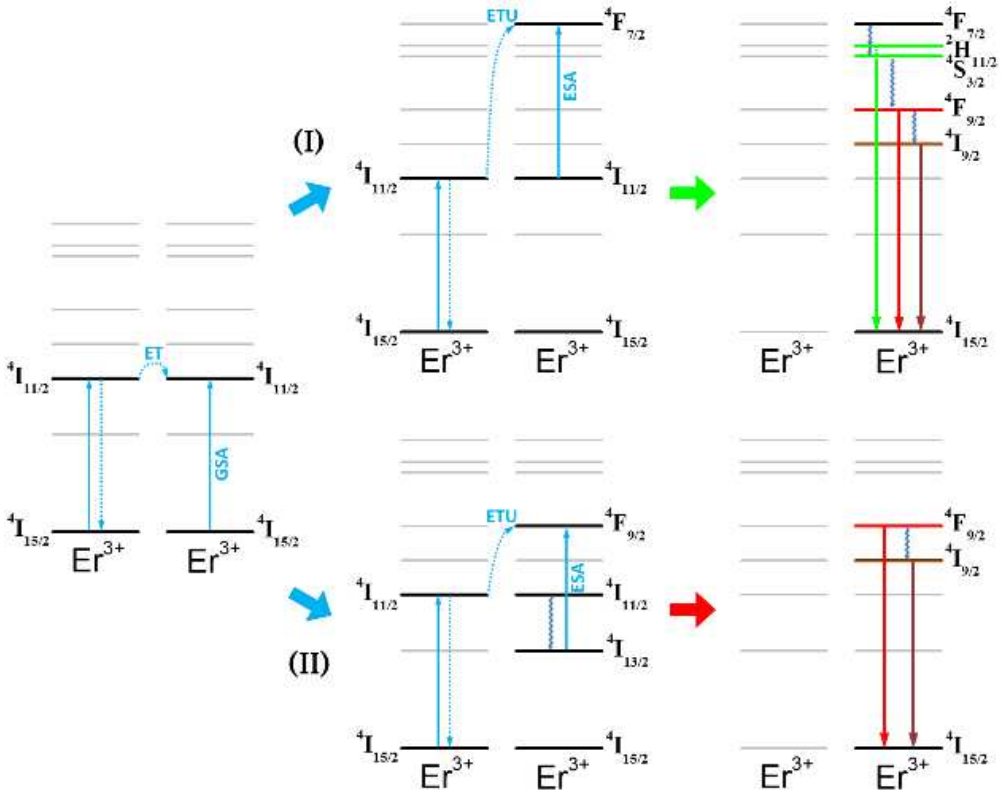

Mechanism (II) is triggered by an early step in which a relaxation to the $^4I_{13/2}$ excited state firstly occurs. Then some 980 nm pump photons are conveyed into ESA or ETU mediated $^4I_{13/2} \rightarrow {}^4F_{9/2}$ absorption. It is worth stressing that from the $^4F_{9/2}$ level only the transition responsible for the RED emission and, after phonon assisted relaxation to the $^4I_{9/2}$ level, the NIR one can take place, whereas an energy shortfall remains for the generation of the GRN emission. This is the crucial point: the reduced intensity of the GRN emission with respect to both the RED and NIR ones has to be caused by a relatively lower efficiency of mechanism (I) with respect to (II) with Y doping level below 12 at.%.

To give account for this claim, we have to consider the results of the optical bandgap estimation presented in Figure 4.4. For Y content ranging up to 10 at.%, the band-to-band energy gap estimation for the doped Bi_2O_3 host is always below 2.6 eV. This photon energy corresponds to a wavelength of about 480 nm, a value that well matches the transition from Er^{3+} ground to $^4F_{7/2}$ excited states (and viceversa). Then we hypothesize that, at low Y doping regime, an Er ion promoted to the $^4F_{7/2}$ excited state through mechanism (I) can relax even through a process based on excitation migration towards the embedding matrix, being this energetically allowed by the relatively narrow energy gap. This alternative, host-mediated path is competitive with all $^4F_{7/2}$ de-

excitation mechanisms and determines the weakening or even the complete suppression for the radiative emissions occurring from the energy levels below.

On the other hand, irrespective of the Y content, mechanism (II) must be unaffected by the host-mediated $^4F_{7/2}$ depletion path, since the Er^{3+} excited levels involved by, and the related transition to the ground state, can not supply the energy to bridge the matrix band gap. In fact, the $^4I_{9/2} \rightarrow {}^4I_{15/2}$ transition determines an energetic jump of about 1.9 eV, even far below the energy gap of the undoped Bi_2O_3 matrix.

4.3.4 VRBE diagram and UC color output

To gain more insight into the proposed scenario, the vacuum referred binding energy (VRBE) diagram was considered to figure out the relative position of the Er^{3+} energy levels respect to the host conduction (CB) and valence (VB) bands. Dorenbos proposed a general method, the chemical shift model,[48-50] to construct the VRBE diagram via lanthanide spectroscopy based on three main parameters: (i) the Coulomb repulsion energy $U(6,A)$; (ii) the vacuum referred binding energy of an electron in the $4f^7$ ground state of Eu^{2+} in the chemical environment A, E_{4f} (7, 2+, A), defined as

$$E_{4f}(7, 2+, A) = -24.92 + \frac{18.05 - U(6, A)}{0.777 - 0.0353U(6, A)}$$

where -24.92 eV is the VRBE for the free ion; (iii) the charge transfer E^{CT}(6, 3+, A) from the valence band to the Eu^{3+} ion. Hence, the energy at the top of the valence band $E_V(A)$ can be defined as $E_V(A)=E_{4f}(7, 2+, A)-E^{CT}(6, 3+, A)$, then the energy at the bottom of the conduction band as $E_C(A)=E_V(A)+E_g(A)$, where $E_g(A)$ is the bandgap energy of the material. Considering the energy of the Eu^{3+}-O^{2-} charge transfer band (CTB) in Bi_2O_3 reported by Dutta,[51] the bandgap energy E_g estimated by the diffuse reflectance analysis and a value of 6.8 eV for the $U(6,A)$, the VRBE diagram of Ln ions in Bi_2O_3 was realized (see Figure 4.8).

It is important to point out that the Er^{3+} ion energy levels involved in the UC processes, and in particular the $^4F_{7/2}$ excited state, lie below the CB edge of the Bi_2O_3 (see Figure 4.8b). Moreover, it is clear that through progressive Y ion incorporation, the system ideally evolves from Bi_2O_3 to Y_2O_3. The data reported by Dorenbos for the VRBE of Y_2O_3 was used,[52] demonstrating a slightly decrease of the VB energy and a significant increase in the CB energy moving from bismuth to yttrium oxides (Figure 4.8a). These data are consistent with the fact that in the oxides, and in particular in M_2O_3 oxides, the VB is mainly formed by O 2p orbitals while the bottom of the CB is composed of M states. Hence, the analysis of the VRBE diagram strongly supports the occurrence of an excitation migration process through an energy transfer involving Er^{3+} excited states and the host band-to-band transitions, instead of a direct injection of the electron in the conduction band of the matrix.

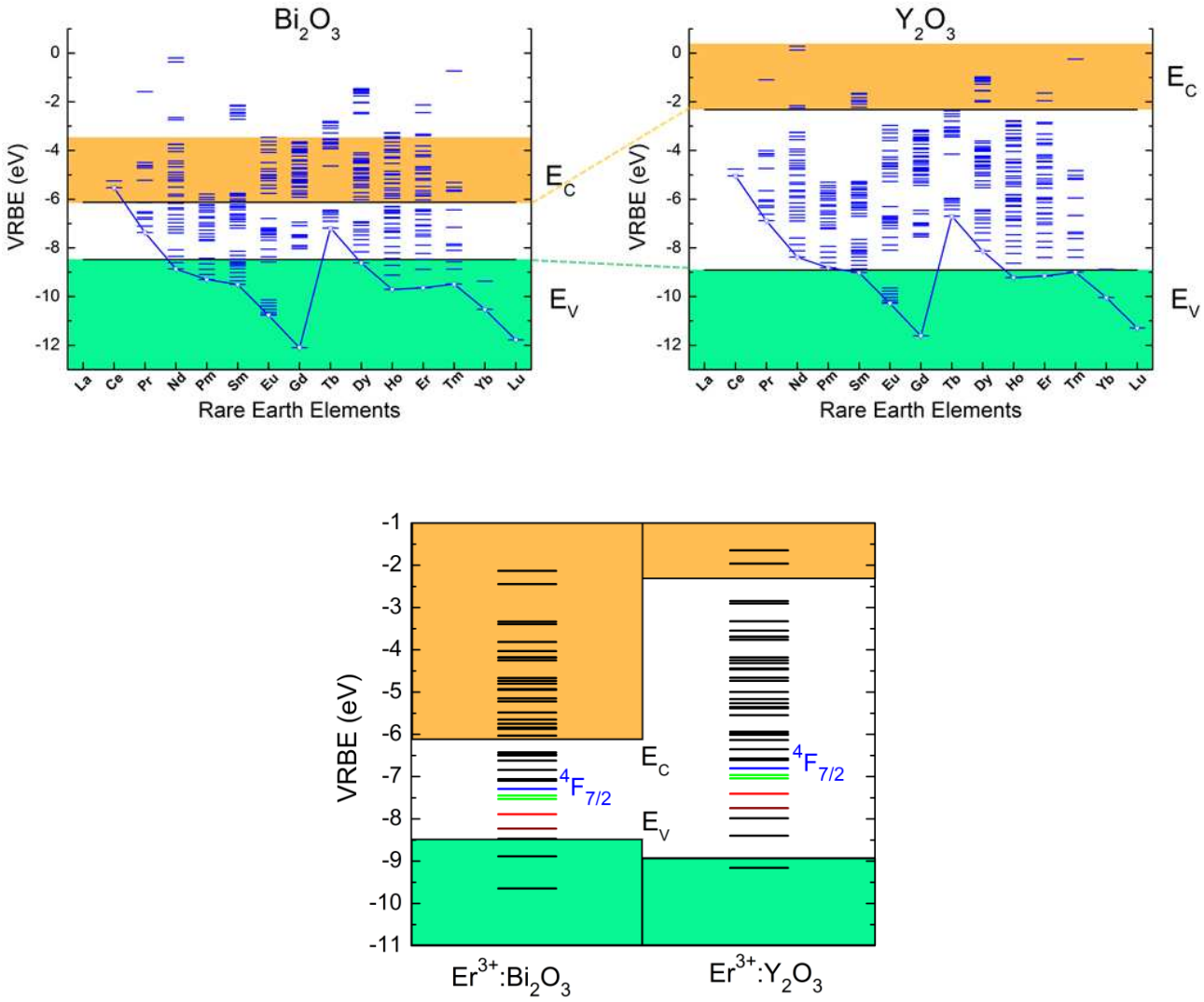

Figure 4.8. Vacuum-referred binding energy (VRBE) diagrams for Er^{3+} energy levels in Bi_2O_3 and Y_2O_3 hosts.

Concerning the color rendering of the light output from the doped NPs, the remarkable result is that the Y content can directly influence the relative intensity ratio between the observed emissions, with possible variation of the chromaticity as determined by the convolution of the different radiative transitions, in particular the GRN and the RED ones. In this regards, the graph in Figure 4.9 reports the trend of the GRN/RED emission intensity ratio, which shows a progressive increase as the Y content scales up to 12 at.%. This determines a consequent color emission tuning from red to orange and then to yellow-greenish, as can be appreciated from the pictures within the graph, related to three specific Y doped samples under 980 nm LED exposure.

In addition to the perspectives opened by the resulting great selectivity of the UC color emission, it is worth considering the suitability for bioimaging of UC nanophosphors deprived of any green component. In fact, at low Y content, Bi_2O_3 NPs are characterized by prominent RED and NIR emissions that both fall in the typical biological optical windows. Moreover, the weakness of the

GRN emission limits the drawback represented by the production of background radiation, responsible of the reduction of the signal-to-noise-ratio.

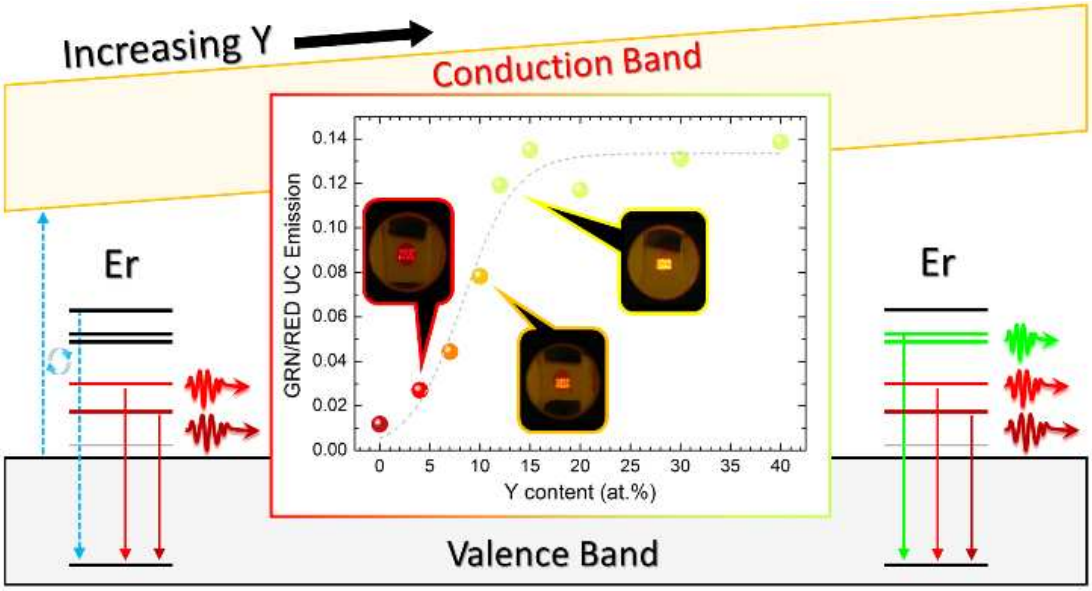

Figure 4.9 Trend of the GRN/RED UC PL emission ratio *versus* Y content, and schematic representation of the main mechanism responsible for the observed color tenability; digital camera images of the Y4Er2, Y10Er2 and Y12Er2 samples under 980 nm laser diode exposure are reported within the graph.

Figure 4.9 includes also a sketch for suggesting how the Er^{3+} 4f state configuration and the variation of the energy gap as depending on the Y content can determine the NPs radiative emission behavior. In this context, this study has demonstrated the possibility of an effective manipulation of the optical properties for a new class of UCNPs, by acting on the host band structure. The observed Bi_2O_3 bandgap engineering, with proper control of the resulting host energy gap, represents an effective method for achieving the chromatic selectivity of the UC emission.

Finally, it can be pointed out that the different nature of the VB (mainly composed by O 2p orbital) respect to the CB (due to the outer electron shells of the metal M) of the oxide materials leads to predict a similar behavior for Bi_2O_3 doped with other trivalent cations (e.g., La^{3+}, Gd^{3+}, Yb^{3+}, Lu^{3+}, Sc^{3+}, In^{3+}).

4.4 Yb^{3+}, Ln^{3+} (Ln=Er, Ho, Tm) codoped Bi_2O_3 UCNPs

4.4.1 Structure and optical bandgap analysis

Figure 4.10 shows the XRPD patterns of the YbxEr2 series. As for the YxEr2 samples reported in Section 4.3, the same structural evolution from the tetragonal β-Bi_2O_3 phase (ICSD#41764) to the cubic δ-Bi_2O_3 phase (ICSD#98144) at the increasing of Yb^{3+} content is achieved. This is in

agreement with the expected behavior due to the similar radii of Y^{3+} (1.019 Å) and Yb^{3+} (0.985 Å). Moreover, as can be appreciated from SEM image of Yb10Er2 sample in Figure 4.10b, also the Yb-Er codoped NPs are generally characterized by an average size of 45±5 nm.

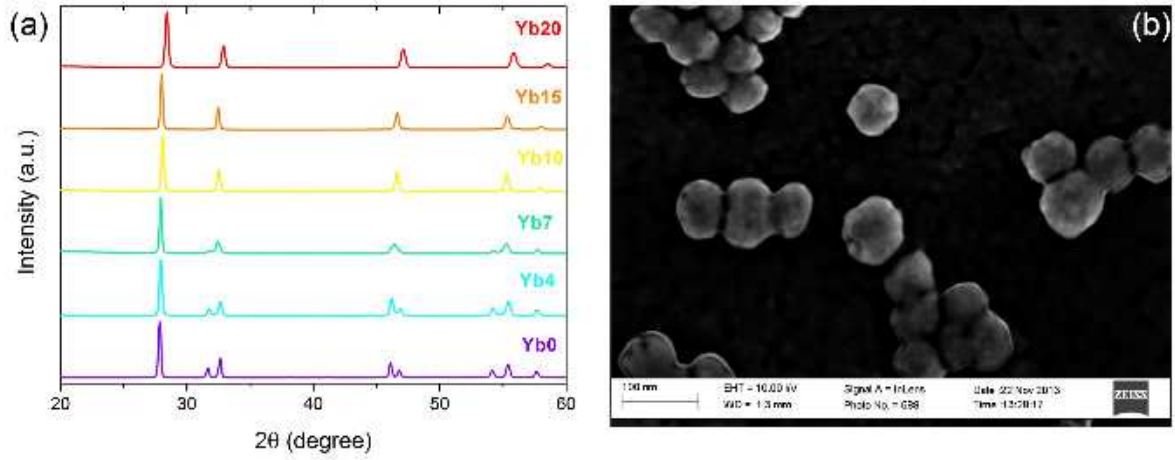

Figure 4.10 (a) XRPD patterns of the YbxEr2 samples and (b) SEM image of Yb10Er2 sample.

As in the case of Y-Er codoped samples, by considering the direct bandgap nature of both the crystalline phases and by means of the Kubelka-Munk function and the Tauc plot, from diffuse reflectance spectral analysis the optical bandgap of the samples was extrapolated from the graph of Figure 4.11a and plotted as a function of the Yb^{3+} content (Figure 4.11b).

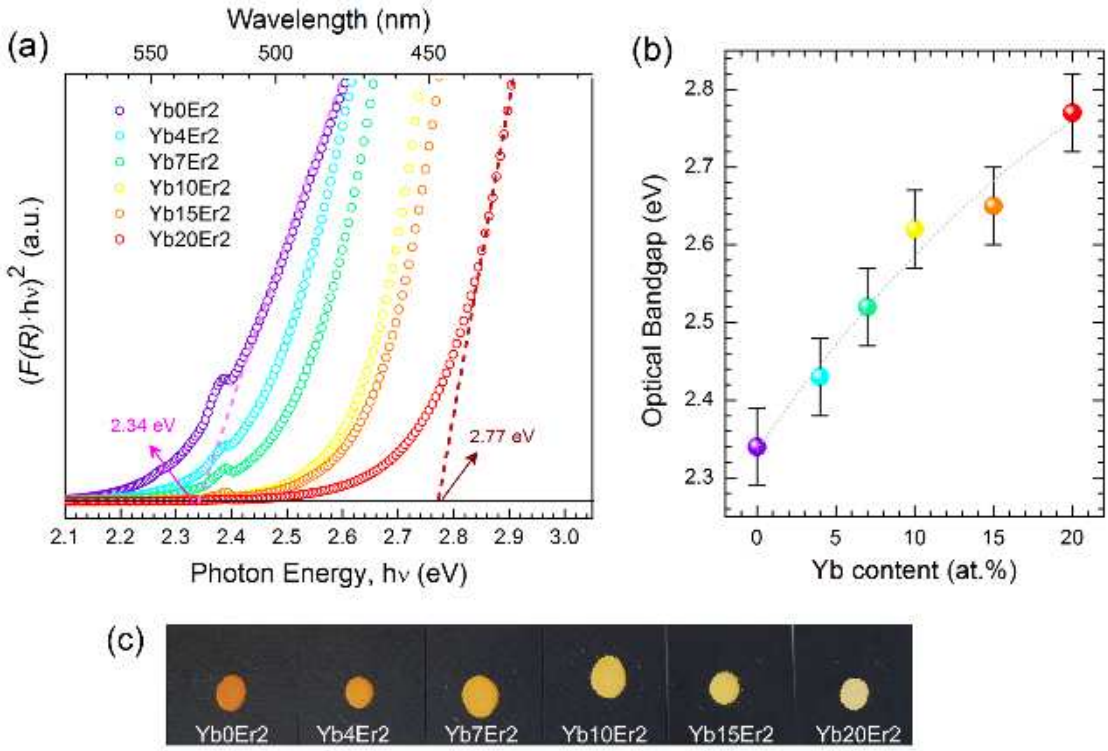

Figure 4.11 (a) Tauc plot of the Kubelka-Munk function *F(R)* for the synthesized samples, (b) trend of optical bandgap values *versus* Yb content and (c) pictures of the powder samples.

It is worth noticing that the variation of the Yb^{3+} doping level determines a wide bandgap energy tunability of 0.43 eV, in good agreement with the trend and the values reported in Figure 4.4b for the system codoped with Y. In addition, the powder color shows a gradual whitening as the Yb content is increased, as expected in virtue of the progressive bandgap widening and the energy gap threshold moving towards the UV wavelength range (Figure 4.11c).

In order to compare the three different Yb-Ln systems, in Figure 4.12 the diffuse reflectance analysis and the relative Tauc plot of the Kubelka-Munk function of Yb10Er2, Yb10Ho1 and Yb10Tm0.2 samples are reported. The spectra are characterized by a strong absorption band peak at 980 nm, due to the Yb^{3+} GSA process. Moreover, the main evidence emerging from the Tauc plot is that the estimated energy gap values scale down moving from Yb10Er2 (2.65 eV), to Yb10Ho1 (2.55 eV) and to Yb10Tm0.2 (2.53eV) samples. In the hypothesis that this trend is linked to the progressive decrease of the whole lanthanide content (Yb+Ln at.%), it seems demonstrated that also Er/Ho/Tm ions have a role as Bi_2O_3 structural modifiers and that a careful doping allows for a precise control of the host bandgap.

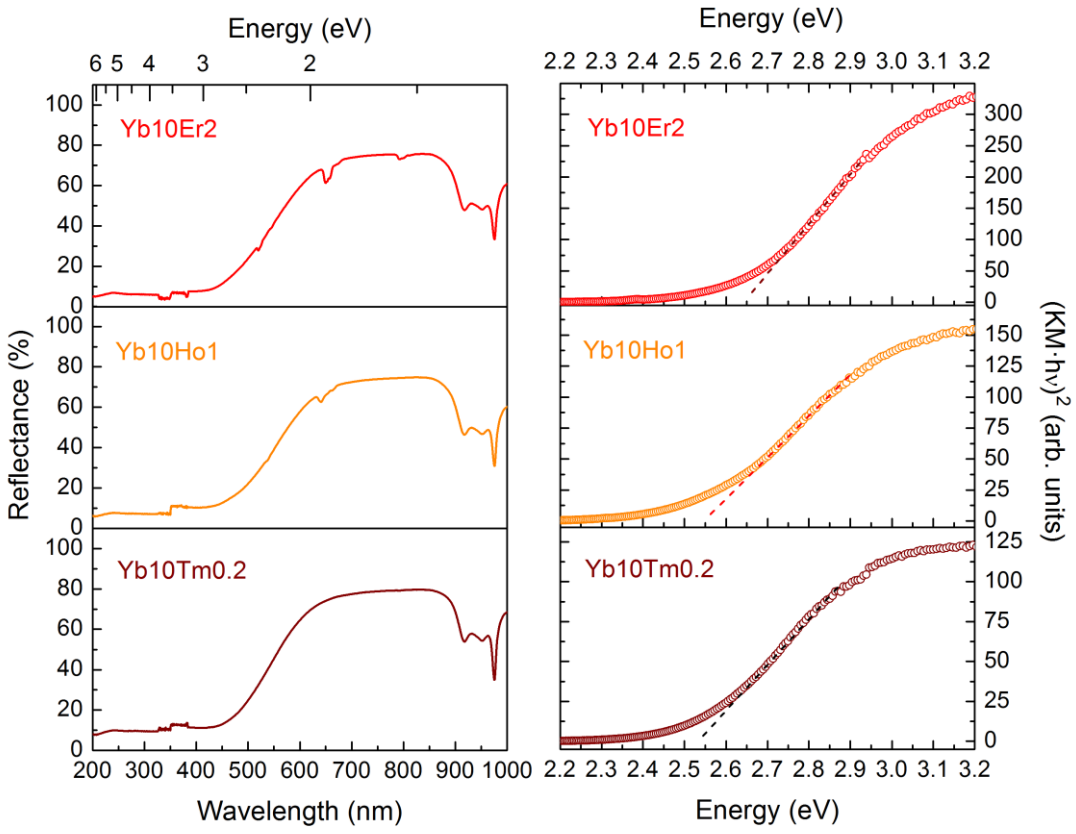

Figure 4.12 Diffuse reflectance spectra and corresponding Tauc plot of the Kubelka-Munk function *F(R)* for the Yb10Er2, Yb10Ho1 and Yb10Tm0.2 samples.

4.4.2 UC properties of Yb^{3+}, Er^{3+} codoped NPs

Figure 4.13a shows the UC emission spectrum of Yb10Er2 sample under 980 nm laser excitation; the dotted line is relative to Y10Er2 sample and its presence is useful to evidence the UC PL enhancement effect driven by the Yb sensitizer.

Even thought for both Yb-Er and Y-Er codoped systems the Er^{3+} spectrum is characterized by three main features, that are the dominant so-called RED emission ($^4F_{9/2}\rightarrow{}^4I_{15/2}$ transition) and the weaker GRN ($^4S_{3/2}\rightarrow{}^4I_{15/2}$ and $^2H_{11/2}\rightarrow{}^4I_{15/2}$ transitions) and NIR ($^4I_{9/2}\rightarrow{}^4I_{15/2}$ transitions) ones, in the case of Yb the RED emission is even more enhanced than both the other two.

This behaviour is characteristic for the whole Yb-Er series, resulting in eye-visible red UC luminescence as a consequence of the near single-band emission at the red wavelengths of the visible spectrum shown by these samples. Moreover, this trend is in agreement to what usually observed for the Yb-Er system in different host, and Yb codoping is a useful strategy to realize single red-emitting phosphor operating in UC mode.[53-56]

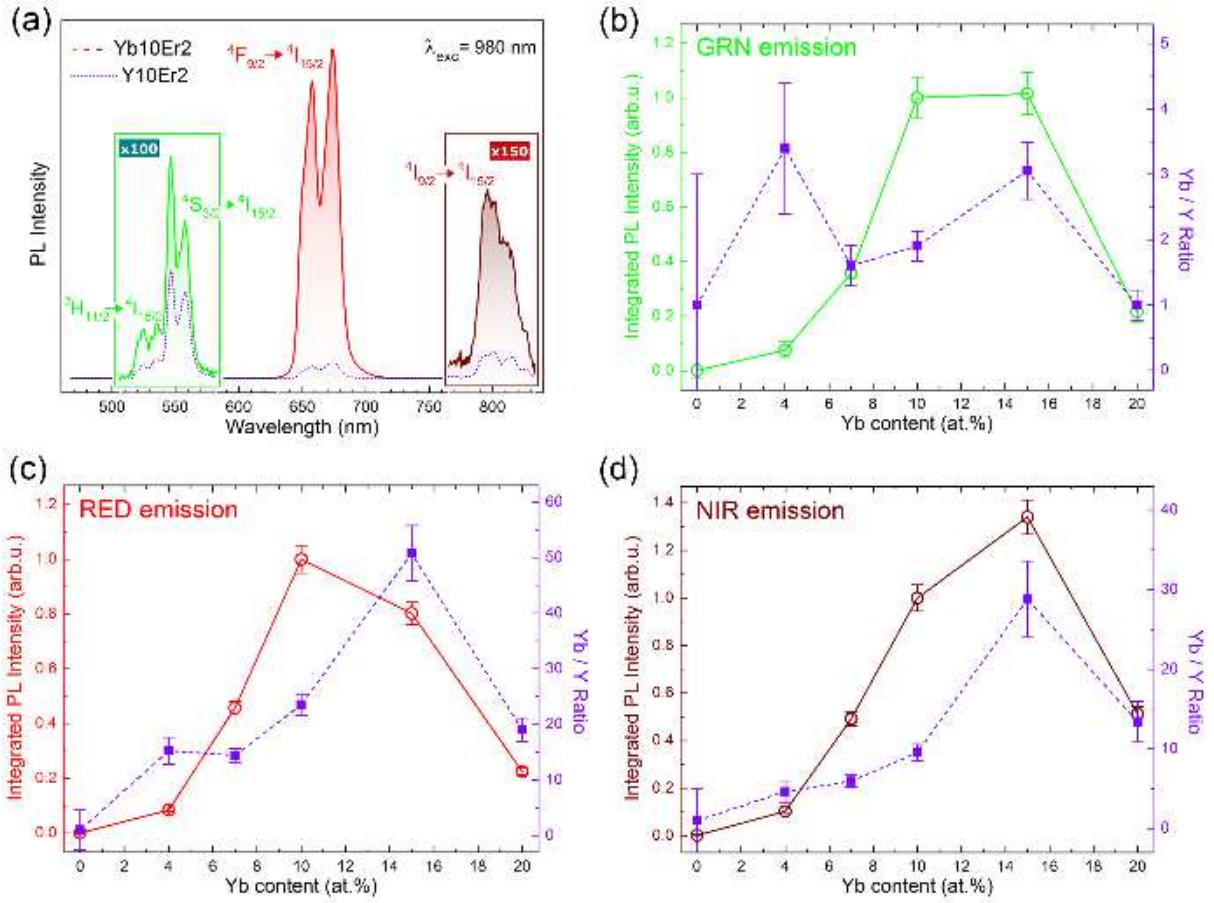

Figure 4.13 (a) UC PL emission spectrum under 980 nm laser diode exposure of Yb10Er2 sample and comparison with Y10Er2 sample (dotted line). Trend of the integrated PL intensity for the Yb-Er system *versus* Yb content (solid line) and trend of the relative ratio between Yb-Er and Y-Er codoped series (dashed line) for (b) GRN, (c) RED and (d) NIR emissions.

In Figure 4.13b,c,d, the influence of Yb content on the UCPL intensity for the different spectral emissions is reported, showing a general increase up to an optimal Yb concentration of 10-15 at.%. This upward trend can be ascribed to (i) the enlarged photon absorption efficiency at 980 nm as the Yb^{3+} density increases and (ii) the bandgap engineering effect previously discussed in the case of Y codoping.

To discriminate between these two effects and, in particular, to give emphasis on the Yb mediated sensitization, we can refer to the violet dashed lines within these graphs, which are related to the trend of the intensity ratio between Yb-Er and Y-Er codoped samples having the same Yb or Y content. Having determined that Y and Yb ions behave in the same way as structure modifier dopant, the effect of the progressive bandgap widening can be ruled out from the observed behaviour.

It is noticed that the UCPL enhances up to some tens of times for the NIR and the RED emissions, reaching for the latter a factor larger than 50 at the optimal Yb concentration, while for the GRN one the increase is notably lower (maximum Yb/Y ratio of 3). Therefore, it is clear that, in presence of the Yb-driven UC process, the advantage in terms of luminescence intensity increase is much more for the RED emission with respect to GRN one.

Going over the optimal Yb doping level, the observed reduction of the overall PL signal is presumably due to concentration quenching of luminescent activators: when in presence of such a large density of surrounding Yb ions, energy migration to these (for instance, through energy backtransfer process) can originate from an Er^{3+} emitter, causing its radiationless relaxation with effective reduction of the luminescent signals in the visible/near-IR range.[57]

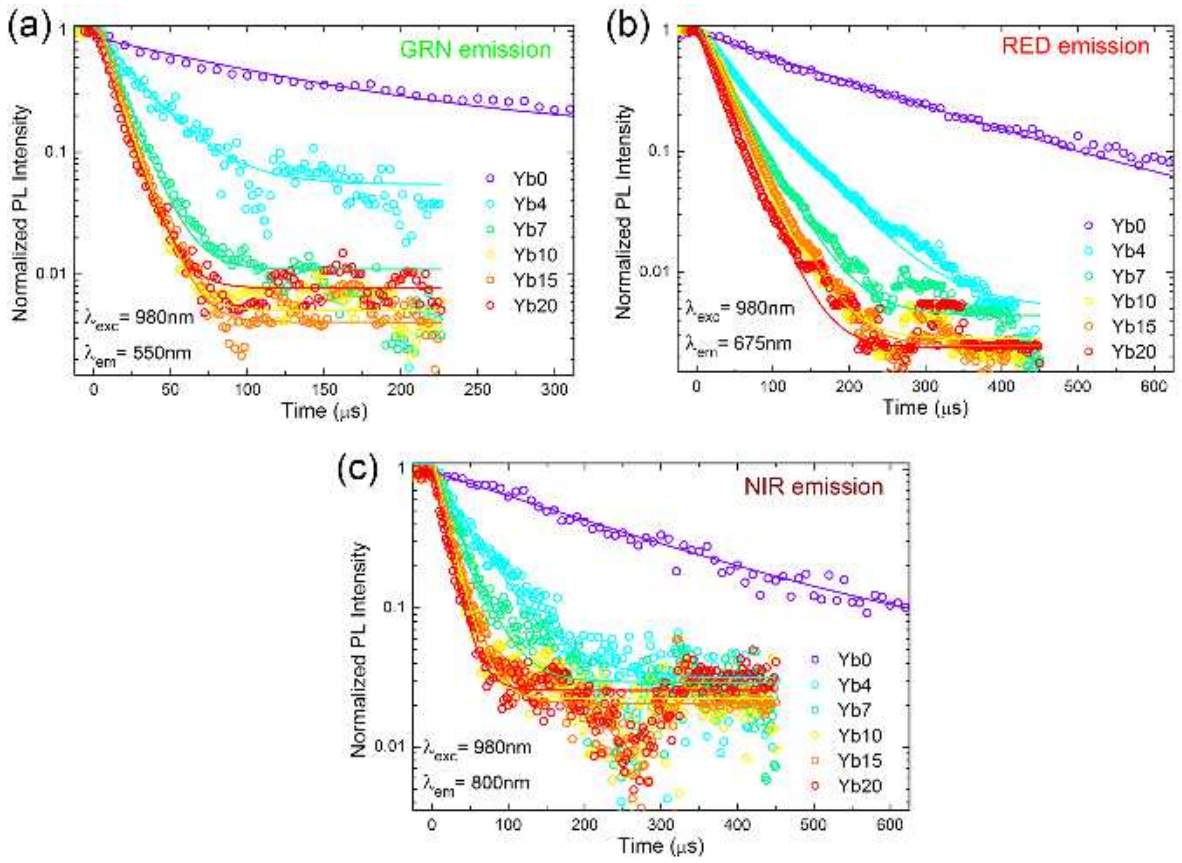

Figure 4.14 UC PL decay curves collected at wavelengths corresponding to (a) GRN, (b) RED and (c) NIR emissions for the Yb-Er codoped samples.

This effect could also explain why the decay traces for the three Er^{3+} emissions become faster as the Yb content increases (see Figure 4.14): with respect to an Yb-free sample, an overall major

impact of non-radiative processes on the Er^{3+} luminescence dynamics can determine the observed lifetime decrease.[58] In this regards, the measured waveforms of Figure 4.14 were described adequately by a single exponential fit, and the resulting lifetime estimates are listed in the following Table 4.2.

Table 4.2 Decay time of GRN, RED and NIR transitions of the YbxEr2 samples estimates by single-exponential fit procedure.

Sample	Decay Time (μs)		
	GRN	RED	NIR
Yb0Er2	73	225	266
Yb4Er2	26.6	55.7	48.3
Yb7Er2	12.9	37.3	28.8
Yb10Er2	10.9	34.8	18.1
Yb15Er2	11.3	37.9	20.8
Yb20Er2	11.4	27.1	16.3

We enter in the merit of the mechanisms bringing to the observed Er^{3+} UCPL behaviour later in this Section.

4.4.3 UC properties of Yb^{3+}, Ho^{3+} and Yb^{3+}, Tm^{3+} codoped NPs

The spectra of Figure 4.15 are respectively referred to the UC PL emission shown by the Yb10Ho1 and the Yb10Tm0.2 samples, under 980 nm LED exposure.

In the case of the Yb-Ho system, the spectrum exhibits the typical features commonly observed for Ho-based UC phosphors in the visible–near-IR range, that span over the green, the red and NIR spectral regions and that are originated from the following transitions: $^5F_4$, $^5S_2 \rightarrow {}^5I_8$ (~550 nm), $^5F_5 \rightarrow {}^5I_8$ (~660 nm) and $^5F_4$, $^5S_2 \rightarrow {}^5I_7$ (~760 nm). The red component is dominant in intensity; thus, at least in the visible range, the UC PL emission appears rather similar to the one shown for the Yb10Er2 sample. But, in virtue of the larger green-to-red intensity ratio, for the Yb10Ho1 the resulting eye-visible color output turns to orange.

Concerning the Yb-Tm system, the spectrum of Figure 4.15b deviates significantly to what can be found in literature for the largest part of Tm-based UC phosphors. In fact, three main features in the visible–near-IR region are usually exhibited: a dominant band around 475 nm, excited-to-ground state $^1G_4 \rightarrow {}^3H_6$ transition, that gives the typical blue color output, a weaker one around 650 nm, linked to the excited-to-excited state $^1G_4 \rightarrow {}^3F_4$ transition, and an intense one around 800 nm, linked to the excited-to-ground state $^3H_4 \rightarrow {}^3H_6$ transition. In the case of our Yb10Tm0.2, none of the main bands can be appreciated in the visible range, leaving the place to a faint, secondary emission around 700 nm originated from to the $^2F_{2,3} \rightarrow {}^3H_6$ transitions, while the 800 nm band emerges as extremely intense. In this regards, it must be pointed out that, by comparing all the UC nanoparticles object of this investigation, the PL signals measured for this Tm^{3+} emission were among the most intense.

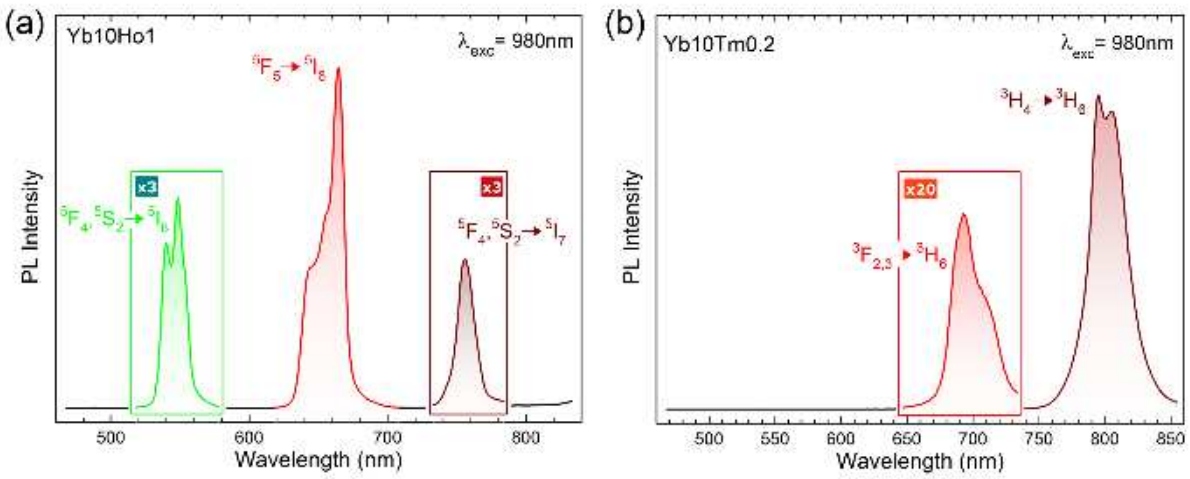

Figure 4.15 UC PL emission spectrum under 980 nm laser diode exposure for (a) Yb10Ho1 and (b) Yb10Tm0.2 samples.

The time decay curves for the UC PL emissions characterizing the Yb10Ho1 and Yb10Tm0.2 samples are shown in Figure 4.16. We observe that the decay profiles can be fitted with a sum of two exponential functions:

$$I(t) = I_0^A e^{-t/\tau_{fast}} + I_0^B e^{-t/\tau_{slow}}$$

From the estimated lifetime values reported in the graphs, it is evidenced the presence of a slow component (τ_{slow}) that are in the typical range for lifetimes characterizing the Ho^{3+}/Tm^{3+} excited states involved in the UC PL emission processes. The origin of the faster decay component (τ_{fast}), presumably related to a non-radiative decay path, that is not yet clarified.

As expected, in the case of Yb, Ho codoped sample the trends for the emissions in the green and in the near-IR well match, since both radiative processes originate from the $^5F_4$, $^5S_2$ manifolds and the observed decay profiles have to reflect the lifetime characterizing this excited state.

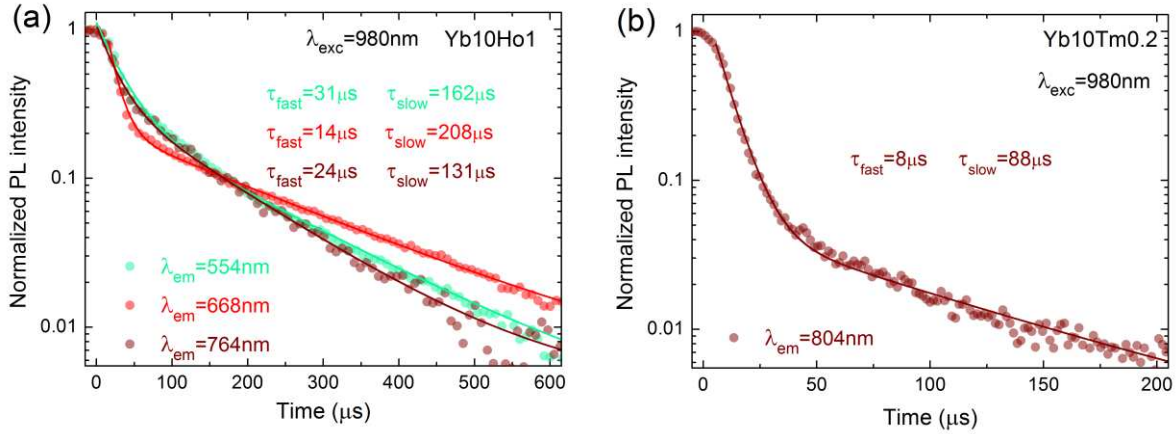

Figure 4.16 UC PL decay curves by 980 nm excitation for (a) Yb10Ho1 sample, with emission signals taken at 554, 668 and 764 nm, and (b) Yb10Tm0.2 sample, with emission signal taken at 804 nm (lifetime analysis for the emission originated from the $^2F_{2,3} \rightarrow {}^3H_6$ transitions not reliable due to the weakness of the signal). The lifetime estimates within the graph were obtained by double-exponential fit procedure and the resulting fitting curves are reported in the graphs as solid lines.

4.4.4 Insight into the UC mechanism

Considering a codoped Bi_2O_3 system with Yb content at 10 at.%, the schematic energy level diagram of Figure 4.17 gives account of the main transitions involved in UC process for the three Yb^{3+}-Ln^{3+} ion pairs, with particular emphasis on the energy transfer mechanisms where Yb^{3+} ions act as donor. It is worth underlining that, since it is well known the typical large cross section characterizing the Yb^{3+} GSA process ($^2F_{7/2} \rightarrow {}^2F_{5/2}$), this transition is considered as the main triggering event for UC activation, whereas ESA/GSA processes for the other Ln^{3+} ions have a very low probability.

In the case of Yb-Er system, the scheme follows what already evidenced in the case of Y-Er codoped samples. Therefore, by 10 at.% Yb doping, the estimated host bandgap energy allows for the $^4F_{7/2}$ state to be active from the point of view of UC process, behaving as such a landing point for the direct two-photon absorption, mainly determined by a double combination of Yb^{3+} GSA ($^2F_{7/2} \rightarrow {}^2F_{5/2}$) and energy transfer to Er^{3+} ion (Er^{3+} $4I_{11/2}$ state involved too).

Despite this, as discussed before, the enhancement of the GRN emission seems quite limited as the Bi_2O_3 bandgap widens (*i.e.* the Yb content increases) with respect to RED and NIR ones. In fact, the scheme of Figure 4.17 reports a peculiar effect already observed for the Yb-Er system in different hosts:[59,60] at high Yb concentration, Er ions undergo an energy backtransfer process (EBT, pink dashed lines in the scheme), whose mechanism can be summarized as $[Er^{3+}]^4S_{3/2} + [Yb^{3+}]^2F_{7/2} \rightarrow [Er^{3+}]^4I_{13/2} + [Yb^{3+}]^2F_{5/2}$, followed by ETU, with consequent Er^{3+} transition in the $^4F_{9/2}$ state from the long-living $^4I_{13/2}$ one and further feeding of RED and NIR radiative relaxations. This result in a slight increase of GRN emission by progressive host bandgap widening, being this

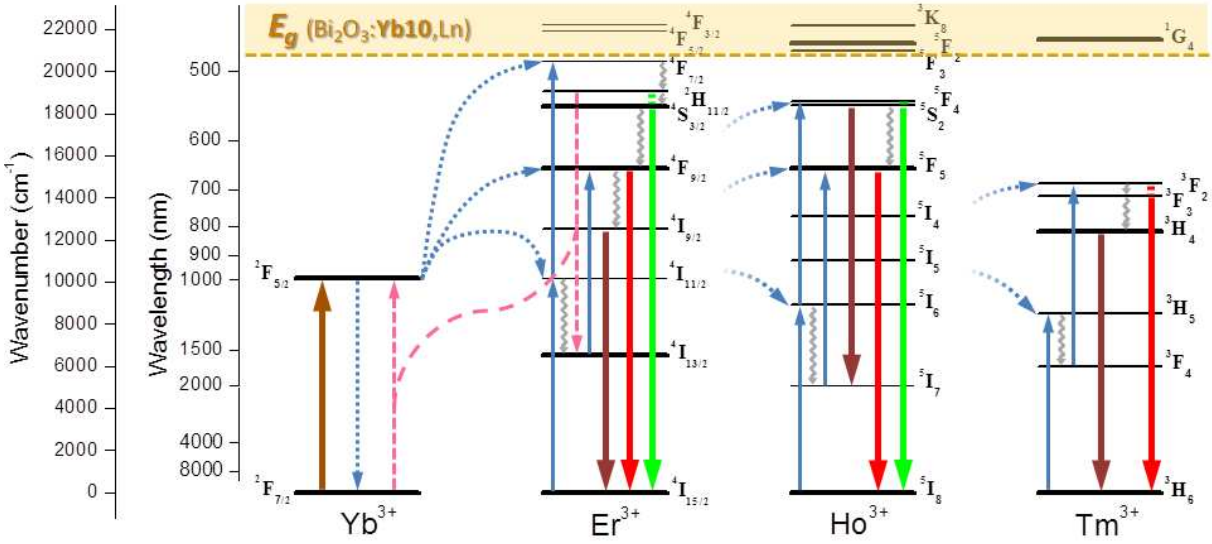

Figure 4.17 Scheme of the energy level diagram representing UC and transition mechanisms originating the luminescence emissions observed for the Yb-Er, Yb-Ho and Yb-Tm systems. The brown upward arrow refers to Yb^{3+} GSA process; solid downward arrows refer to Ln^{3+} radiative relaxations, with colors representing transitions in the red, green and near-IR spectral ranges; blue arrows refer to ET/ETU processes; pink dashed arrows refer to EBT process for the Yb-Er system; grey wavelike arrows refer to multiphonon relaxations. The horizontal dashed orange line marks the energy threshold for Bi_2O_3 band-to-band transition, as estimated in the case of Yb-Ln codoped samples with 10 at.% of Yb.

effect limited by EBT activation, while the intensity of RED and, partially, of NIR UC luminescences are strongly enhanced.

The picture in Figure 4.18a is relative to the Yb10Er2 sample, characterized by red color output.

For the Yb-Ho system, the scheme of Figure 4.17 is helpful to evidence that the direct two-step UC process can directly bring an Ho^{3+} ion from the ground to the $^5F_4$, $^5S_2$ excited states (through the $^5I_6$ manifold), which are well below the threshold energy for bridging the host band gap as well as all the states involved in the transitions that determine the observed UC PL spectrum. From the results of the Kubelka-Munk analysis reported in Section 4.4.1, it is claimed that this condition would be maintained also at very low Yb content. Therefore, we exclude that the Yb-Ho UC mechanism can be influenced by possible excitation migration processes to the host.

The previous considerations are aligned to the fact that, as shown in the picture in Figure 4.18b, the Yb10Ho1 sample shines orange light under 980 nm photoexcitation, like the largest part of YbHo-based UC phosphors.

Furthermore, with the aim to modify the UC PL response of the system, an interesting perspective is to dope the NPs with different structural modifier ions in order to promote the shrinkage of the Bi_2O_3 bandgap like, for instance, with In^{3+} ions.[61] By referring to the case of the Er^{3+} UC response, we envisage that this could lead to limit (or quench) all transitions involving the $^5F_4$, $^5S_2$ states, as those determining the emissions in the green ($^5F_4$, $^5S_2 \rightarrow {}^5I_8$) and in the near-IR ($^5F_4$, $^5S_2 \rightarrow {}^5I_7$) regions. Since the $^5F_5 \rightarrow {}^5I_8$ transition (responsible for the red emission) remains fully activated, this could represent an effective strategy, based again on the host bandgap engineering, to realize a single-band red emitting UC nanophosphor.

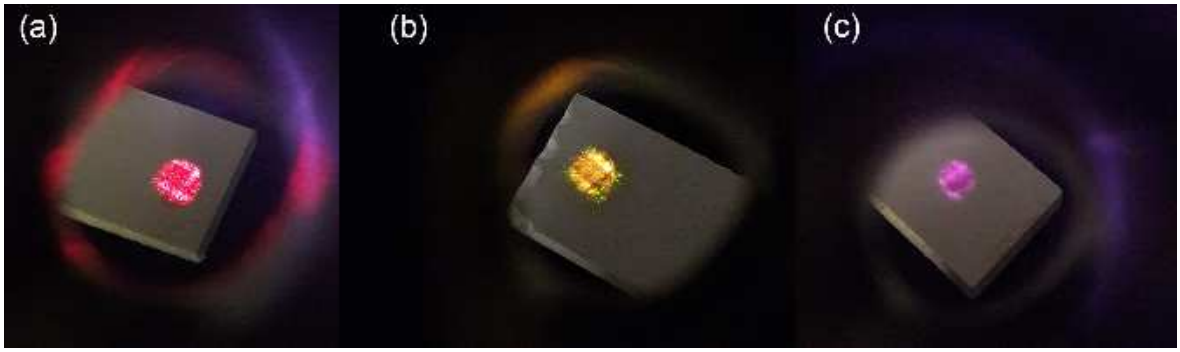

Figure 4.18 Photographs of the Yb-Ln (Ln=Er, Ho, Tm) samples under 980 nm excitation source, collected by using a 900 nm long-cut filter. In the case of Yb10Tm0.2 sample, the CCD camera associates the violet color to the 800 nm emission.

In the case of Yb-Tm system, the scenario emerging from the sketch of Figure 4.17 directly accounts for the peculiar UC PL response exhibited by the Yb10Tm0.2 sample. Basically the $^1G_4$ state is located so high in the energy scheme that the relaxation to the ground state is energetically larger than the Bi_2O_3 band-to-band transition (by taking into account the energy gap estimate obtained by the Kubelka-Munk analysis). Therefore, due to the competitive relaxation

mechanisms determined by excitation migration to the host, it is pointed out that all (radiative) transitions involving the $^1G_4$ state can be limited or fully quenched.

Furthermore, it is worth considering that these transitions are typically three-step UC mechanisms under 980 nm excitation, as typically emerging from the analysis of the pumping power dependence of the UC PL emissions shown by Yb-Tm systems,[62-64] and this is a direct consequence of the fact that at least three photons are needed to populate the $^1G_4$ level. Concerning the Yb10Tm0.2 sample, the emission band around 800 nm, dominating the UC PL spectrum, seems linked to a two-photon process, as inferred from the trend of the signal intensity versus the 980 nm pumping power observed in Figure 4.19c, where the $I_{UCPL} \propto P_{980nm}^{n}$ relationship holds for a n parameter close to 2.

Moreover, this a general behaviour characterizing also the UC PL emission signal relative to both the Yb10Er2 and Yb10Ho1 samples (see Figure 4.19a and b, respectively). This result agrees to the idea that, for the investigated Yb-Ln samples, only two-step processes are allowed, whereas possible interferences caused by transitions across the host bandgap can affect the activation of UC PL ones determined by mechanisms combining three or more photons (n parameter > 2).

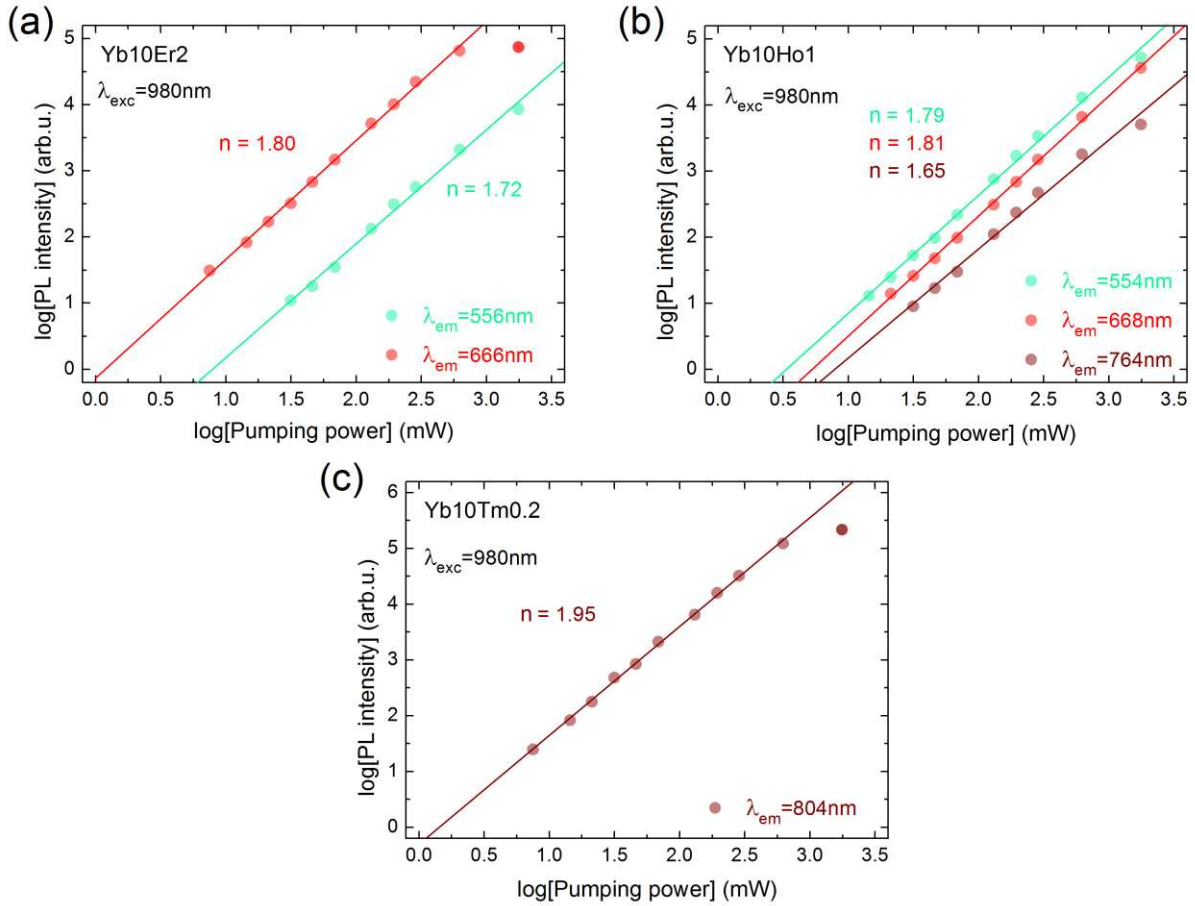

Figure 4.19 Double-log-plot of the integrated UC PL emission intensity *versus* 980 nm pumping power for (a) Yb10Er2, (b) Yb10Ho1 and (c) Yb10Tm0.2 samples (the analysis for the emissions originated from Er^{3+} $^4I_{9/2} \rightarrow {}^4I_{15/2}$ and Tm^{3+} $^2F_{2,3} \rightarrow {}^3H_6$ transitions not reliable due to the weakness of the signal). In each graph, the corresponding order of the UC process is reported as the n parameter obtained by the linear fit of the experimental data.

The efficiency performance of the three Yb-Ln samples doped with 10 at% of Yb was measured by means of the integrating sphere method. A high absorption efficiency of 67±3% for all the three Yb-Ln samples gives account of the effective capability of the system to collect the 980 nm irradiating photons, whereas the quantum yield (QY) is related to the fraction of these that are converted into emitted photons generated through an UC mechanism.

The significant absorption efficiencies were not unexpected on the basis of the pronounced feature originated by Yb^{3+} GSA absorption at 980 nm, characterizing the reflectance spectra of Figure 4.12.

Concerning the QY results (summarized in Table 4.3), it must be underlined that the reported values are remarkable compared to most state-of-the-art of UC phosphors, including those based on fluoride hosts that are known to exhibit the best performances. By referring to the up-to-date list of fluoride-based UC nano-sized phosphors reported by Nadort *et al.* in ref. 65, in Table 4.3 the QY estimates of our Yb-Ln codoped samples are compared to some systems reported in literature. In general, it can be observed that Ln-doped UCNPs hardly reach efficiency of the order of 1%, whereas in the case of core-shell nanostructures values of several % are achieved.

Table 4.3 Absolute QY of various UC nanosystems measured by integrating sphere method.

Material	Size (nm)	QY (%)	I_{ex} (Wcm^{-2})	Ref.
Bi_2O_3:$Yb_{0.2}$,$Er_{0.04}$	40	2.2 ± 0.5	1.3	This work
Bi_2O_3:$Yb_{0.2}$,$Ho_{0.02}$	40	1.7 ± 0.5	1.3	This work
Bi_2O_3:$Yb_{0.2}$,$Tm_{0.004}$	40	2.6 ± 0.5	1.3	This work
$NaYF_4$:$Yb_{0.2}$,$Er_{0.02}$	100	0.30 ± 0.10	150	66
$NaYF_4$:$Yb_{0.2}$,$Er_{0.02}$	30	0.10 ± 0.05	150	66
$NaYF_4$:$Yb_{0.2}$,$Er_{0.02}$	8-10	0.005 ± 0.005	150	66
$NaYF_4$:$Yb_{0.2}$,$Er_{0.02}$@$NaYF_4$	30	0.30 ± 0.10	150	66
$NaLuF_4$:$Gd_{0.24}$,$Yb_{0.2}$,$Tm_{0.01}$	<10	0.47 ± 0.06	17.5	67
$NaYF_4$:$Yb_{0.25}$,$Tm_{0.003}$@$NaYF_4$	42 (30@6)	0.04-3.5	0.02-78	68
$NaYF_4$:$Yb_{0.25}$,$Tm_{0.003}$	33	0.45-0.91	1.3-20	69
$NaYF_4$:$Yb_{0.25}$,$Tm_{0.003}$@$NaYF_4$	43 (33@5)	1.2-2.6	3.8-20	69
$NaYF_4$:$Yb_{0.8}$,$Er_{0.02}$@CaF_2	26	3.2 ± 0.1	10	70
$LiLuF_4$:$Yb_{0.2}Er_{0.01}$	28	0.11	127	71
$LiLuF_4$:$Yb_{0.2}Er_{0.01}$@$LiLuF_4$	40 (28@6)	3.6	127	71
$LiLuF_4$:$Yb_{0.2}Er_{0.01}$@$LiLuF_4$	51 (28@11)	5.0	127	71
$LiLuF_4$:$Yb_{0.2}Tm_{0.005}$	28	0.61	127	71
$LiLuF_4$:$Yb_{0.2}Tm_{0.005}$@$LiLuF_4$	51 (28@6)	6.7	127	71
$LiLuF_4$:$Yb_{0.2}Tm_{0.005}$@$LiLuF_4$	51 (28@11)	7.6	127	71
$NaGdF_4$:$Yb_{0.22}$,$Er_{0.025}$@$NaYF_4$	21 (10.5@5)	0.89 ± 0.05	50	72
$NaYF_4$:$Yb_{0.2}$,$Er_{0.02}$@$NaYF_4$	14 (8@3)	0.49 ± 0.25	100	73

In any case, by considering the nature of our samples that consist of a “simple” bismuth oxide NPs without the need of core/shell architects, we consider the estimates for our samples as a promising starting point and strategies can be developed to further enhance the UC efficiency.

4.5 Conclusion

In summary, we have prepared a new class of UCNPs based on Bi_2O_3 host embedding Y^{3+} and Er^{3+} ions, by means of a modified Pechini-type sol-gel route. Acting on the Y^{3+} doping level, it has been established a novel method for tuning the UC emission chromaticity through the engineering of the host bandgap, as it plays a relevant role in determining the mechanism and the relative efficiency of the Er^{3+} radiative process.

In this regards we propose a scenario where, under IR pumping, transitions across the narrow Bi_2O_3 bandgap determine a channel for the depletion of the higher-lying Er^{3+} excited states via an energy transfer mechanism, causing the switch off of the Er^{3+} visible emissions at the shorter wavelengths. Through Y^{3+} incorporation, the host bandgap widens as the doping level is raised up, determining the full activation of UC PL transitions in the whole visible spectrum. The resulting color output directly derives from a proper balance among the Er^{3+} emission lines into the green and the red spectral regions, allowing for a chromatic selectivity from red to yellow-greenish as the Y content increases.

In addition, the properties of Yb^{3+}-Ln^{3+} (Ln^{3+}=Er^{3+},Ho^{3+},Tm^{3+}) codoped Bi_2O_3 NPs were explored. The same wide bandgap tunability evidenced for Y-Er codoped samples was established by Yb-Er codoping and the active role of the bandgap host was confirmed also in this case. Promising QY values were estimated for the Yb-Ln systems, while a peculiar single near-IR emission characterizes the UC PL spectrum of the Yb10Tm0.2 sample.

As emerging from this research, bandgap engineering of bismuth oxide used as host for Ln ions opens intriguing possibilities for the realization of UCNPs with peculiar properties, envisaging potential application in the field of photonics, bio-labeling, thermal sensing, anti-counterfeiting.

Materials and Methods

Experimental Details. X-Ray Powder Diffraction (XRPD) measurements were performed by means of a Philips diffractometer with a PW 1319 goniometer with Bragg-Brentano geometry, equipped with a focusing graphite monochromator and a proportional counter with a pulse-height discriminator. Nickel-filtered Cu Kα radiation and a step-by-step technique were employed (steps of 0.05° in 2θ), with collection time of 30 s per step. The crystallite size estimation has been performed by Scherrer analysis and the instrumental line broadening has been evaluated by means of LaB_6 SRM660s standard by NIST.

Size and morphology of the nanoparticles and EDS analysis were carried out by a Carl Zeiss Sigma VP Field Emission Scanning Electron Microscope (FE-SEM) equipped with a Bruker Quantax 200 microanalysis detector. The EDS spectra were collected at the same condition (20 KeV) for all the samples.

The diffusive reflective UV-Vis (DRUV-Vis) spectra were collected with a JASCO V-570 UV-vis spectrophotometer equipped with an integrating sphere accessory. Barium sulfate was used as reference.

Photoluminescence measurements were performed by using a CNI MDL-III-980 diode laser as 980 nm photon pumping source, with output power of 2W over a spot of 5×8 mm^2 (power density of 5 W/cm^2).

PL Emission spectra were acquired by means of a QE65 Pro Ocean Optics spectrometer; for measurements at different pumping power, neutral density filters were used to attenuate the pumping radiation. Time resolved PL curves were collected by a R928 Hamamatsu PMT coupled to a CINEL single-grating (600 lines/mm) monochromator; the pumping radiation was modulated by a mechanical chopper, whose frequency (up to 1 KHz) was used as trigger for signal sampling by a Tektronix TDS3032 oscilloscope.

Upconversion and absorption efficiencies were measured by means of an integrating sphere (152 mm diameter, coated with Spectralon), equipped with a calibrated radiometer (ILT 1700, International Light Technologies). A baffle is mounted between the sample and the detector. A 980 nm laser diode was used as excitation source and the irradiance was 1.3 W/cm².

References

1. N.-N. Dong, M. Pedroni, F. Piccinelli, G. Conti, A. Sbarbati, J. E. Ramírez-Hernández, L. Martínez Maestro, M. C. Iglesias-de la Cruz, F. Sanz-Rodriguez, A. Juarranz, F. Chen, F. Vetrone, J. A. Capobianco, J. García Solé, M. Bettinelli, D. Jaque and A. Speghini. NIR-to-NIR Two-Photon Excited $CaF_2:Tm^{3+},Yb^{3+}$ Nanoparticles: Multifunctional Nanoprobes for Highly Penetrating Fluorescence Bio-Imaging. *ACS Nano*, **2011**, 5, 8665-8671.

2. Y. Liu, D. Tu, H. Zhu and X. Chen. Lanthanide-doped luminescent nanoprobes: controlled synthesis, optical spectroscopy, and bioapplications. *Chem. Soc. Rev.*, **2013**, 42, 6924-6958.

3. L. Zhou, R. Wang, C. Yao, X. Li, C. Wang, X. Zhang, C. Xu, A. Zeng, D. Zhao and F. Zhang. Single-band upconversion nanoprobes for multiplexed simultaneous in situ molecular mapping of cancer biomarkers. *Nat. Commun.*, **2015**, 6, 6938.

4. G. Chen, H. Qiu, P. N. Prasad and X. Chen. Upconversion Nanoparticles: Design, Nanochemistry, and Applications in Theranostics. *Chem. Rev.*, **2014**, 114, 5161-5214.

5. A. Gnach, T. Lipinski, A. Bednarkiewicz, J. Rybka and J. A. Capobianco. Upconverting nanoparticles: assessing the toxicity. *Chem. Soc. Rev.*, **2015**, 44, 1561-1584.

6. H.-Q. Wang, M. Batentschuk, A. Osvet, L. Pinna and C. Brabec. Rare-Earth Ion Doped Up-Conversion Materials for Photovoltaic Applications. *Adv. Mater.*, **2011**, 23, 2675-2680.

7. A. Shalav, B. S. Richards and M. A. Green. Luminescent layers for enhanced silicon solar cell performance: Up-conversion. *Sol. Energ. Mat. Sol. C.*, **2007**, 91, 829-842.

8. C. Strümpel, M. McCann, G. Beaucarne, V. Arkhipov, A. Slaoui, V. Švrček, C. del Canizo and I. Tobias. Modifying the solar spectrum to enhance silicon solar cell efficiency – An overview of available materials. *Sol. Energ. Mat. Sol. C.*, **2007**, 91, 238-249.

9. C. D. S. Brites, P. P. Lima, N. J. O. Silva, A. Millán, V. S. Amaral, F. Palacio and L. D. Carlos. Thermometry at the nanoscale. *Nanoscale*, **2012**, 4, 4799-4829.

10. A. Sedlmeier, D. E. Achatz, L. H. Fischer, H. H. Gorris and O. Wolfbeis. Photon upconverting nanoparticles for luminescent sensing of temperature. *Nanoscale*, **2012**, 4, 7090-7096.

11. F. Vetrone, R. Naccache, A. Zamarrón, A. Juarranz de la Fuente, F. Sanz-Rodríguez, L. Martinez Maestro, E. Martín Rodriguez, D. Jaque, J. García Solé and J. A. Capobianco. Temperature Sensing Using Fluorescent Nanothermometers. *ACS Nano*, **2010**, 4, 3254-3258.

12. Y. Zhang, L. Zhang, R. Deng, J. Tian, Y. Zong, D. Jin and X. Liu. Multicolor Barcoding in a Single Upconversion Crystal. *J. Am. Chem. Soc.*, **2014**, 136, 4893-4896.

13. M. You, J. Zhong, Y. Hong, Z. Duan, M. Lin and F. Xu. Inkjet printing of upconversion nanoparticles for anti-counterfeit applications. *Nanoscale*, **2015**, 7, 4423-4431.

14. J. M. Meruga, A. Baride, W. Cross, J. J. Kellar and P. S. May. Red-green-blue printing using luminescence-upconvertion inks. *J. Mater. Chem. C*, **2014**, 2, 2221-2227.

15. Y. Lu, J. Zhao, R. Zhang, Y. Liu, D. Liu, E. M. Goldys, X. Yang, P. Xi, A. Sunna, J. Lu, Y. Shi, R. C. Leif, Y. Huo, J. Shen, J. A. Piper, J. P. Robinson and D. Jin. Tunable Lifetime Multiplexing Using Luminescent Nanocrystals. *Nat. Photonics*, **2014**, 8, 32-36.

16. W. Zou, C. Visser, J. A. Maduro, M. S. Pshenichnikov and J. C. Hummelen. Broadband dye-sentized upconversion of near-infrared light. *Nat. Photonics*, **2012**, 6, 560-564.

17. H. H. Gorris, R. Ali, S. M. Saleh and O. S. Wolfbeis. Tuning the Dual Emission of Photon-Upconverting Nanoparticles for Ratiometric Multiplexed Encoding. *Adv. Mater.*, **2011**, 23, 1652-1655.

18. F. Vetrone, J.-C. Boyer, J. A. Capobianco, A. Speghini and M. Bettinelli. Concentration-Dependent Near-Infrared to Visible Upconversion in Nanocrystalline and Bulk Y_2O_2:Er^{3+}. *Chem. Mater.*, **2003**, 15, 2737-2743.

19. V. Mahalingam, R. Naccache, F. Vetrone and J. A. Capobianco. Preferential suppression of high-energy upconverted emissions of Tm^{3+} by Dy^{3+} ions in Tm^{3+}/Dy^{3+}/Yb^{3+}-doped $LiYF_4$ colloidal nanocrystals. *Chem. Commun.*, **2011**, 47, 3481-3483.

20. H.-X. Mai, Y.-W. Zhang, L.-D. Sun and C.-H. Yan. Highly Efficient Multicolor Up-Conversion Emissions and Their Mechanisms Monodisperse $NaYF_4$:Yb,Er Core and Core/Shell-Structured Nanocrystals. *J. Phys. Chem. C*, **2007**, 111, 13721-13729.

21. F. Wang, J. Wang and X. Liu. Direct Evidence of a Surface Quenching Effect on Size-Dependent Luminescence of Upconversion Nanoparticles. *Angew. Chem. Int. Ed.*, **2010**, 49, 7456-7460.

22. Q. Su, S. Han, X. Xie, H. Zhu, H. Chen, C.-K. Chen, R.-S. Liu, X. Chen, F. Wang and X. Liu. The Effect of Surface Coating on Energy Migration-Mediated Upconversion. *J. Am. Chem. Soc.*, **2012**, 134, 20849-20857.

23. F. Wang, R. Deng, J. Wang, Q. Wang, Y. Han, H. Zhu, X. Chen and X. Liu. Tuning upconversion through energy migration in core-shell nanoparticles. *Nat. Mater.*, **2011**, 10, 968-973.

24. B. Zhou, B. Shi, D. Jin and X. Liu. Controlling upconversion nanocrystals for emerging applications. *Nat. Nanotechnol.*, **2015**, 10, 924-936.

25. H. Dong, L.-D. Sun, Y.-F. Wang, J. Ke, R. Si, J.-W. Xiao, G.-M. Lyu, S. Shi and C.-H. Yan. Efficient Tailoring of Upconversion Selectivity by Engineering the Local Structure of Lanthanides in Na_xREF_{3+x} Nanocrystals. *J. Am. Chem. Soc.*, **2015**, 137, 6569-6576.

26. G. Yi, Y. Peng, and Z. Gao. Strong Red-Emitting near-Infrared-to-Visible Upconversion Fluorescent Nanoparticles. *Chem. Mater.*, **2011**, 23, 2729-2734.

27. J. Wang, F. Wang, C. Wang, Z. Liu, and X. Liu. Single-Band Upconversion Emission in Lanthanide-Doped $KMnF_3$ Nanocrystals. *Angew. Chem.*, **2011**, 50, 10369-10372.

28. G. G. Briand and N. Burford. Bismuth Compounds and Preparations with Biological or Medicinal Relevance. *Chem. Rev.*, **1999**, 99, 2601-2657.

29. P. Riente, A. Matas Adams, J. Albero, E. Palomares and M. A. Pericàs. Light-Driven Organocatalysis Using Inexpensive, Nontoxic Bi_2O_3 as the Photocatalyst. *Angew. Chem. Int. Ed.*, **2014**, 53, 9613-9616.

30. S. Dong, J. Feng, M. Fan, Y. Pi, L. Hu, X. Han, M. Liu, J. Sun and J. Sun. Recent developments in heterogeneous photocatalytic water treatment using visible light-responsive photocatalysts: a review. *RSC Adv.*, **2015**, 5, 14610-14630.

31. B. H. Park, B. S. Kang, S. D. Bu, T. W. Noh, J. Lee and W. Jo. Lanthanum-substituted bismuth titanate for use in non-volatile memories. *Nature*, **1999**, 401, 682-684.

32. W. S. Choi, M. F. Chismholm, D. J. Singh, T. Choi, G. E. Jellison Jr. and H. N. Lee. Wide bandgap tunability in complex transition metal oxides by site-specific substitution. *Nat. Commun.*, **2012**, 3, 689.

33. S. Sanna, V. Esposito, J. W. Andreasen, J. Hjelm, W. Zhang, T. Kasama, S. B. Simonsen, M. Christensen, S. Linderoth and N. Pryds. Enhancement of chemical stability in confined δ-Bi_2O_3. *Nat. Mater.*, **2015**, 14, 500-504.

34. M. Guennou, M. Viret and J. Kreisel. Bismuth-based perovskites as multiferroics. *Comptes Rendus Physique*, **2015**, 16, 182-192.

35. A. Chen, H. Zhou, Z. Bi, Y. Zhu, Z. Luo, A. Bayraktaroglu, J. Phillips, E.-M. Choi, J. L. MacManus-Driscoll, S. J. Pennycook, J. Narayan, Q. Jia, X. Zhang and H. Wang. A New Class Of Room-Temperature Multiferroic Thin Films with Bismuth-Based Supercell Structure. *Adv. Mater.*, **2013**, 25, 1028-1032.

36. R. Nachache, C. Harnagea, S. Li, L. Cardenas, W. Huang, J. Chakrabartty and F. Rosei. Bandgap tuning of multiferroic oxide solar cells. *Nat. Photonics*, **2015**, 9, 61-67.

37. G. Dong, H. Fan, H. Tian, J. Fang and Q. Li. Gas-sensing and electrical properties of perovskite structure p-type barium-substituted bismuth ferrite. *RSC Adv.*, **2015**, 5, 29618-29623.

38. B. Rasche, A. Isaeva, M. Ruck, S. Borisenko, V. Zabolotnyy, B. Büchner, K. Koepernik, C. Ortix, M. Richter and J. van den Brink. Stacked topological insulator built from bismuth-based graphene sheet analogues. *Nat. Mater.*, **2013**, 12, 422-425.

39. G. Autès, A. Isaeva, L. Moreschini, J. C. Johannsen, A. Pisoni, R. Mori, W. Zhang, T. G. Filatova, A. N. Kuznetsov, L. Forró5, W. Van den Broek, Y. Kim, K. Su Kim, A. Lanzara, J. D. Denlinger, E. Rotenberg, A. Bostwick, M. Grioni and O. V. Yazyev. A novel quasi-one-dimensional topological insulator in bismuth iodide β-Bi_4I_4. *Nat. Mater.*, **2016**, 15, 154-159.

40. M. Back, E. Trave, R. Marin, N. Mazzucco, D. Cristofori and P. Riello. Energy transfer in Bi- and Er-codoped Y_2O_3 nanocrystals: An effective system for rare earth fluorescence enhancement. *J. Phys. Chem. C*, **2014**, 118, 30071-30078.

41. H. Cheng, B. Huang, J. Lu, Z. Wang, B. Xu, X. Qin, X. Zhang and Y. Dai. Synergistic Effect of Crystal and Electronic Structures on the Visible-Light-Driven Photocatalytic Performances of Bi_2O_3 Polymorphs. *Phys. Chem. Chem. Phys.*, **2010**, 12, 15468-15475.

42. J. Zhang, W. Dang, X. Yan, M. Li, H. Gao and Z. Ao. Doping Indium in β-Bi_2O_3 to Tune the Electronic Structure and Improve the Photocatalytic Activities: First-Principles Calculations and Experimental Investigation. *Phys. Chem. Chem. Phys.*, **2014**, 16, 23476-23482.

43. J. Tauc, R. Grigorovici and A. Vancu. Optical Properties and Electronic Structure of Amorphous Germanium. *Phys. Status Solidi*, **1966**, 15, 627-637.

44. P. Kubelka and F. Munk. Ein Beitrag zur Optik der Farbanstriche. *Z. Technische Physik*, **1931**, 12, 593-601.

45. Y. Lu, Y. Zhao, J. Zhao, Y. Song, Z. Huang, F. Gao, N. Li and Y. Li. Induced Aqueous Synthesis of Metastable β-Bi_2O_3 Microcrystals for Visible-Light Photocatalyst Study. *Cryst. Growth Des.* **2015**, 15, 1031-1042.

46. H.-Y. Jiang, P. Li, G. Liu, J. Ye and J. Lin. Synthesis and Photocatalytic Properties of Metastable β-Bi_2O_3 Stabilized by Surface-Coordination Effects. *J. Mater. Chem. A*, **2015** 3, 5119-5125.

47. M. Pollnau, D.R. Gamelin, S.R. Lüthi, H.U. Güdel and M.P. Hehlen. Power Dependence of Upconversion Luminescence in Lanthanide and Transition-Metal-Ion Systems. *Phys. Rev. B* **2000**, 61, 3337-3346.

48. P. Dorenbos. Modeling the Chemical Shift of Lanthanide 4*f* Electron Binding Energies. *Phys. Rev. B* **2012**, 85, 165107.

49. P. Dorenbos. Determining Binding Energies of Valence-Band Electrons in Insulators and Semiconductors via Lanthanide Spectroscopy. *Phys. Rev. B* **2013**, 87, 035118.

50. P. Dorenbos. Ce^{3+} 5d-centroid shift and vacuum referred 4f-electron binding energies of all lanthanide impurities in 150 different compounds. *J. Lumin.* **2013**, 135, 93-104.

51. D.P. Dutta, M. Roy and A.K. Tyagi. Dual Function of Rare Earth Doped Nano Bi_2O_3: White Light Emission and Photocatalytic Properties. *Dalton Trans.* **2012**, 41, 10238-10248.

52. E. G. Rogers and P. Dorenbos. Vacuum Referred Binding Energy of the Single 3d, 4d, or 5d Electron in Transition Metal and Lanthanide Impurities in Compounds. *ECS J. Solid State Sci. Technol.* **2014**, 3, R173-R184.

53. J. Wang, F. Wang, C. Wang, Z. Liu and X. Liu. Single-band upconversion emission in lanthanide-doped $KMnF_3$ nanocrystals. *Angew. Chem. Int. Ed.* **2011**, 50, 10369-10372.

54. M. Wu, E.H. Song, Z.T. Chen, S. Ye, J.J. Zhou, S.Q. Xu and Q.Y. Zhang. Single-band red upconversion luminescence of Yb^{3+}-Er^{3+} *via* non-equivalent substitution in perovskite $KMgF_3$ nanocrystals. *J. Mater. Chem. C* **2016**, 4, 1675-1684.

55. G. Tian, Z. Gu, L. Zhou, W. Yin, X. Liu, L. Yan, S. Jin, W. Ren, G. Xing, S. Li and Y. Zhao. Mn^{2+} dopant-controlled synthesis of $NaYF_4$:Yb/Er upconversion nanoparticles for in vivo imaging and drug delivery. *Adv. Mater.* **2012**, 24, 1226-1231.

56. J. Liao, L. Nie, S. Liu, B. Liu and H.-R. Wen. Yb^{3+} concentration dependence of upconversion luminescence in $Y_2Sn_2O_7$:Yb^{3+}/Er^{3+} nanophosphors. *J. Mater. Sci.* **2014**, 49, 6081-6086.

57. L. Tu, X. Liu, F. Wu and H. Zhang. Excitation energy migration dynamics in upconversion nanomaterials. *Chem. Soc. Rev.* **2015**, 44, 1331-1345.

58. A. Li, D. Xu, Y. Zhang, H. Lin, S. Yang, Z. Chen and Y. Shao. Upconversion Luminescence and Energy-Transfer Mechanism of $NaGd(MoO_4)_2$: Yb^{3+}/Er^{3+} Microcrystals. *J. Am. Ceram. Soc.* **2016**, 99, 1657-1663.

59. M.T. Berry and P.S. May. Disputed mechanism for NIR-to red upconversion luminescence in $NaYF_4:Yb^{3+},Er^{3+}$. *J. Phys. Chem. A* **2015**, 119, 9805-9811.

60. J. Zhang, Z. Hao, J. Li, X. Zhang, Y. Luo and G. Pan. Observation of efficient population of the red-emitting state from the green state by non-multiphonon relaxation in Er^{3+}-Yb^{3+} system. *Light Sci. Appl.* **2015**, 4, e239.

61. J. Zhang, W. Dang, X. Yan, M. Li, H. Gao and Z. Ao. Doping indium in β-Bi_2O_3 to tune the electronic structure and improve the photocatalytic activities: first-principles calculations and experimental investigation. *Phys. Chem. Chem. Phys.* **2014**, 16, 23476.

62. H. Zhang, Y. Li, Y. Lin, Y. Huang and X. Duan. Composition tuning the upconversion emission in $NaYF_4$:Yb/Tm hexaplate nanocrystals. *Nanoscale* **2011**, 3, 963-966.

63. J.F. Suyver, J. Grimm, M.K. van Veen, D. Biner, K.W. Krämer and H.U. Güdel. Upconversion spectroscopy and properties of $NaYF_4$ doped with Er^{3+}, Tm^{3+} and/or Yb^{3+}. *J. Lumin.* **2006**, 117, 1-12.

64. A. Yin, Y. Zhang, L. Sun and C. Yan. Colloidal synthesis and blue based multicolour upconversion emissions of size and composition controlled monodisperse hexagonal $NaYF_4$: Yb,Tm nanocrystals. *Nanoscale* **2010**, 2, 953-959.

65. A. Nadort, J. Zhao and E.M. Goldys. Lanthanide upconversion luminescence at the nanoscale: foundamentals and optical properties. *Nanoscale* **2016**, 8, 13099-13130.

66. J.-C. Boyer and F.C. van Veggel. Absolute quantum yield measurements of colloidal $NaYF_4:Er^{3+}$, Yb^{3+} upconverting nanoparticles. *Nanoscale* **2010**, 2, 1417-1419.

67. Q. Liu, Y. Sun, T. Yang, W. Feng, C. Li and F. Li. Sub-10 nm hexagonal lanthanide-doped $NaLuF_4$ upconversion nanocrystals for sensitive bioimaging in vivo. *J. Am. Chem. Soc.* **2011**, 133, 17122-17125.

68. C. T. Xu, P. Svenmarker, H. Liu, X. Wu, M.E. Messing, L.R. Wallenberg and S. Andersson-Engels. High-resolution fluorescence diffuse optical tomography developed with nonlinear upconverting nanoparticles. *ACS Nano* **2012**, 6, 4788-4795.

69. H. Liu, C. T. Xu, D. Lindgren, H. Xie, D. Thomas, C. Gundlach and S. Andersson-Engels. Balancing power density based quantum yield characterization of upconverting nanoparticles for arbitrary excitation intensities. *Nanoscale* **2013**, 5, 4770-4775.

70. A. Punjabi, X. Wu, A. Tokatli-Apollon, M. El-Rifai, H. Lee, Y. Zhang, C. Wang, Z. Liu, E.M. Chan, C. Duan and G. Han. Amplifying the red-emission of upconverting nanoparticles for biocompatible clinically used prodrug-induced photodynamic therapy. *ACS Nano* **2014**, 8, 10621-10630.

71. P. Huang, W. Zheng, S. Zhou, D. Tu, Z. Chen, H. Zhu, R. Li, E. Ma, M. Huang and X. Chen. Lanthanide-doped $LiLuF_4$ upconversion nanoprobes for the detection of disease biomarkers. *Angew. Chem. Int. Ed.* **2014**, 53, 1252-1257.

72. X. Li, R. Wang, F. Zhang and D. Zhao. Engineering homogeneous doping in single nanoparticle to enhance upconversion efficiency. *Nano Lett.* **2014**, 14, 3634-3639.

73. D.J. Gargas, E.M. Chan, A.D. Ostrowski, S. Aloni, M.V.P. Altoe, E.S. Bernard, B. Sanii, J.J. Urban, D.J. Milliron and B.E. Cohen. Engineering bright sub-10-nm upconverting nanocrystals for single-molecule imaging. *Nat. Nanotechnol.* **2014**, 9, 300-305.

CHAPTER 5

Bi_2SiO_5@SiO_2 UCNPs: A Bismuth-Driven Core-Shell Self-Assembly Mechanism

Abstract In this Chapter we investigate the lanthanide-doped Bi_2SiO_5 nanocrystal formation inside mesoporous silica nanoparticles (MSNs). The role of synthesis temperature and of the concentration of bismuth precursor impregnated into the MSNs are discussed, and a mechanism for the formation of Bi_2SiO_5@SiO_2 core-shell nanosystem is proposed. In addition, the easy tunability of the color output of the upconverting system is demonstrated by suitable chosen of the doping lanthanide ions with interesting potentialities in several application fields.

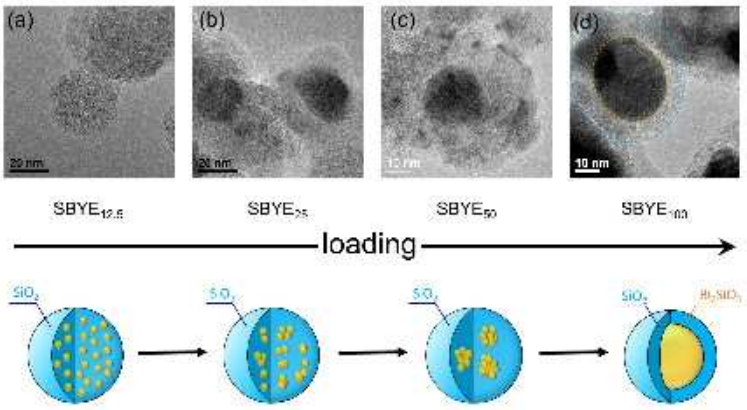

5.1 Introduction

Among silicon oxide (SiO_2) nanostructured materials, mesoporous silica nanoparticles (MSNs) have emerged as one of the most promising nanosystems of the last 20 years, being involved in a wide variety of fields, moving from catalysis[1-5] to cultural heritage,[6,7] from biomedicine[5,8-11] to sensing,[12-14] to name but a few. In particular, MSNs have great potentialities for the use as nanovectors able to combine cancer imaging and therapy by drug delivery.[11] Some characteristics, such as the biocompatibility and high surface-area, make this material very appealing for bio-technological applications. In addition, beside the suitable carrier ability, silica meso-channels are also used as nano-reactors (templates) for the growth of different kinds of nano-sized structures, like metal (*e.g.* Au, Ag, Cu, Pt) or metal oxide NPs (*e.g.* Fe_3O_4, TiO_2).

From another point of view, silica is typically used for realizing shells embedding nanoparticles, with the aim of reducing their activity or their toxicity. SiO_2 coatings promote water dispersion and chemical stability, with the great advantage to allow the functionalization of the outer NP surface irrespective to their nature through the silane chemistry. The synthesis of SiO_2 shells is of particular interest for protecting the surface of metal nanoparticles,[15,16] and for coating quantum dots and inorganic nanocrystals,[17] becoming thus a challenge. As reported by Gnanasammandhan *et al.*[18] the formation of amorphous silica shell on upconverting nanoparticles (UCNPs) is a fundamental step for the synthesis of photodynamic therapy (PDT) systems.[19] Therefore, novel approaches to synthesize core-shell nanosystems are highly desirable.

As previously discussed in Chapter 1 and 3, bismuth based materials are promising candidates for many applications due to their low toxicity and costs,[20-24] in addition to the possibility to use them in multimodal platforms by taking advantage of their suitable features for clinical imaging such as computed X-ray tomography[25,26] (CT), photoacoustic tomography[27] (PAT) and single-photon emission CT[28] (SPECT).

Bismuth oxide easily reacts with silica to form a variety of glasses and crystalline compounds, depending on the preparation method. Bi_2O_3 based glasses find applications mainly in the field of electronics, sensors and solar cells owing to their low melting temperature.[29] The complex nature of the Bi_2O_3-SiO_2 phase diagram is still under investigation, showing many stable and metastable phases that strongly depend on the synthesis parameters.[30-34] The main crystalline arrangements are the sillenite $Bi_{12}SiO_{20}$, the eulytite $Bi_4Si_3O_{12}$ and the metastable Bi_2SiO_5 phases. While the $Bi_{12}SiO_{20}$ phase belongs to the family of so-called sillenite-type structures,[35-39] isomorphous to γ-Bi_2O_3, and it was exploited in many applications due to its photorefractive, piezoelectric, electro-optic, dielectric and photocatalytic properties,[40-47] the $Bi_4Si_3O_{12}$ phase has been widely investigated as scintillator[48-50] and phosphor host.[51-57] The metastable bismuth silicate Bi_2SiO_5 phase has been reported as the next generation lead-free ferroelectric material[58-63] and as a promising photocatalyst.[64-69] Taniguchi *et al.* deeply investigated the ferroelectric properties of Bi_2SiO_5 in correlation to the crystalline structure, showing at the same time the typical distortion induced by $6s^2$ lone pair electrons of Bi^{3+} and a unique twisted silicate chains induced ferroelectric behaviour.[60,61] However, even if Bi_2SiO_5 is characterized by very appealing properties, new synthesis able to stabilize the single phase is a challenge and, for the best of our knowledge, there are no reports about the use of Bi_2SiO_5 as host for luminescent species, like lanthanide ions. Moreover, in view of possible biological applications of Bi_2SiO_5 NPs, it is worth considering that

the relevant bismuth silicate photocatalytic activity could represent a drawback, thus a NP surface coating is desirable.

In this Chapter, by leveraging the mesochannels structure of the porous silica system, the impregnation of MSNs with bismuth precursor is reported as an effective method to stabilized the metastable Bi_2SiO_5 phase. Moreover, a concentration-driven process leading to a core/shell nanosystem formation is discovered. The temperature and concentration effects were investigated and the key role of bismuth in the formation of the glassy silica shell is determined. In addition, by doping with Yb and Ln (Ln=Er, Ho, Tm) ions, a new core/shell upconversion luminescence systems is synthesized, with a remarkable optical tunability in the visible range as resulting from the CIE diagram.

5.2 Sample Preparation

Materials. Tetraethyl orthosilicate (TEOS, 98%, Sigma-Aldrich), cetyltrimethylammonium bromide (CTAB, Sigma-Aldrich), ethanol (99.8%, Fluka), ammonium hydroxide solution (Fluka, 28 wt% in water), $Bi(NO_3)_3 \cdot 5H_2O$ (99.99%, Sigma-Aldrich), $Yb(NO_3)_3 \cdot 5H_2O$ (99.9%, Sigma-Aldrich), $Er(NO_3)_3 \cdot 5H_2O$ (99.9%, Sigma-Aldrich), and HNO_3 65% (J.T. Baker) were used for the preparation of the samples without further purification.

Mesoporous Silica Nanoparticles (MSNs) Synthesis. The mesoporous silica nanoparticles were prepared following the synthesis reported by Quiao *et al.*[70] with slightly modifications. In the typical procedure, distilled water (145.2 mL), EtOH (22.8 mL) and CTAB (5.73 g) were mixed and stirred in a bath oil at 60°C. When the complete dissolution of the surfactant occurred, NH_3 (1.25 mL) was added into the mixture. After 30 minutes, TEOS (14.6 mL) was dropped slowly and the stirring was kept for 2 h at 60°C. Finally, the suspension was cooled at room temperature. The solid product was recovered and washed several times (initially in water and finally in ethanol) with five cycles of centrifugation (30 min at 9000 rpm). The solid powder was dried at 130°C overnight and finally calcined at 500°C for 6 h in order to remove the surfactant. The molar ratio of the reagents for the synthesis was 1TEOS : 0.28NH_3 : 0.24CTAB : 125.7H_2O : 6.1EtOH. The bare sample is labelled as MSNs.

Impregnation Method. The precipitation of lanthanide-doped Bi silicate nanoparticles into the MSN mesopores was conducted by incipient wetness impregnation at room temperature. In the typical procedure, the bare MSNs (0.3 g) were dispersed in a H_2O/HNO_3 solution (5:1, 25 mL), keeping the mixture under stirring. After 30 minutes, the salt precursors of bismuth and ytterbium, and a solution of another one or more selected lanthanides (Ln) were added to the dispersion with a continuous stirring of 1 h. The powders were recovered through the removal of the solvent by means of a rotary evaporator and calcined at a selected temperature, with a heating rate of 1°C min^{-1}, for 2 h. In the following, we refer to the MSN pore occupancy, expressed in vol%, as the fraction of the total pore volume occupied by Bi and Ln precursor salts.

In order to evaluate how the system could be influenced by the thermal treatments, the bismuth/lanthanides concentration and the nature of the selected lanthanides, three series of samples were prepared as described below:

1) In the first series, the samples were calcined at different temperature between 550°C and 750°C range, fixing the nominal fraction of the loaded lanthanide-doped Bi oxide into the MSNs pores. A nominal concentration of 14.52 wt% for the Ln-doped Bi_2O_3 (Ln=Yb,Er) was calculated in order to achieve a pore occupancy of 12.5 vol% by means of the impregnation procedure. The considered Bi:Yb:Er molar ratio was 1:0.1:0.02. The samples are labelled as $SBYE_{12.5}\_T$, where *T* represents the temperature (°C) of calcination (*T*=550, 600, 650, 700, 750), and are listed in Table 5.1.

2) For the second series, different degrees of MSN impregnation with Bi and Ln (Ln=Yb,Er) precursor salts were considered up to the complete volume pore occupancy (impregnation at 12.5, 25, 50 and 100 vol%). As in the case of the previous series, Bi:Yb:Er molar ratio was 1:0.1:0.02. The samples were treated fixing the calcination temperature at 750°C and labelled as $SBYE_x\_750$, where *x*=12.5, 25, 50, 100 vol% refers to the pore occupancy. The samples of $SBYE_x\_750$ series are listed in Table 5.1. A sample loaded at 100 vol% ($SBYE_{100}$) was maintained unheated for in situ temperature dependent SR-XRPD measurement.

3) In the third series, the samples were doped with ytterbium in combination with one or more other lanthanides, among Ho, Tm, and Er. For this study, the impregnation degree was kept at 100 vol% and the thermal treatment fixed at 750°C. The considered Bi:Ln molar ratio was 1:0.12. The samples are referred as SBY*Ln* series, where *Ln*= H, T, E represent Ho, Tm and Er, respectively.

Table 5.1 Molar ratios and calcination temperature of the $SBYE_{12.5}\_T$, $SBYE_X\_750$ and SBY*Ln* series; nominal pore occupancy refers to the fraction of MSN pore volume impregnated by salt precursors.

Sample	*Ln*	*Ln*-doped Bi_2O_3 concentration [wt%]	Pore occupancy [vol%]	Si:(Bi+Ln) molar ratio	Temperature [°C]
			$SBYE_{12.5}\_T$ series		
$SBYE_{12.5}\_550$	Er	14.52	12.5	22.85:1	550
$SBYE_{12.5}\_600$					600
$SBYE_{12.5}\_650$					650
$SBYE_{12.5}\_700$					700
$SBYE_{12.5}\_750$					750
			$SBYE_X\_750$ series		
$SBYE_{12.5}\_750$	Er	14.52	12.5	22.85:1	750
$SBYE_{25}\_750$		25.36	25	11.43:1	
$SBYE_{50}\_750$		40.46	50	5.71:1	
$SBYE_{100}\_750$		57.61	100	2.86:1	
			SBY*Ln* series		
SBYE	Er	57.61	100	2.86:1	750
SBYT	Tm				
SBYH	Ho				
SBYET1	Er+Tm				
SBYET2	Er+Tm				
SBYHT	Ho+Tm				
SBYEHT	Er+Ho+Tm				

5.3 Bismuth-Driven Low Melting Point Effect in MSNs

With the aim to investigate the loading effect of bismuth salt on the mesoporous silica system, and in particular on the variation of the melting temperature, MSNs of about 60 nm, with pores of about 2.4 nm, were prepared following the synthesis method reported by Qiao et al.[70]

SEM analysis on the calcined MSNs evidence nanostructures with spheroidal shape and diameter of about 60-70 nm (Figure 5.1a,b). The presence of both isolated and aggregated nanoparticles is shown in the images of a bare MSN sample, reported in Figure 5.1a,b.

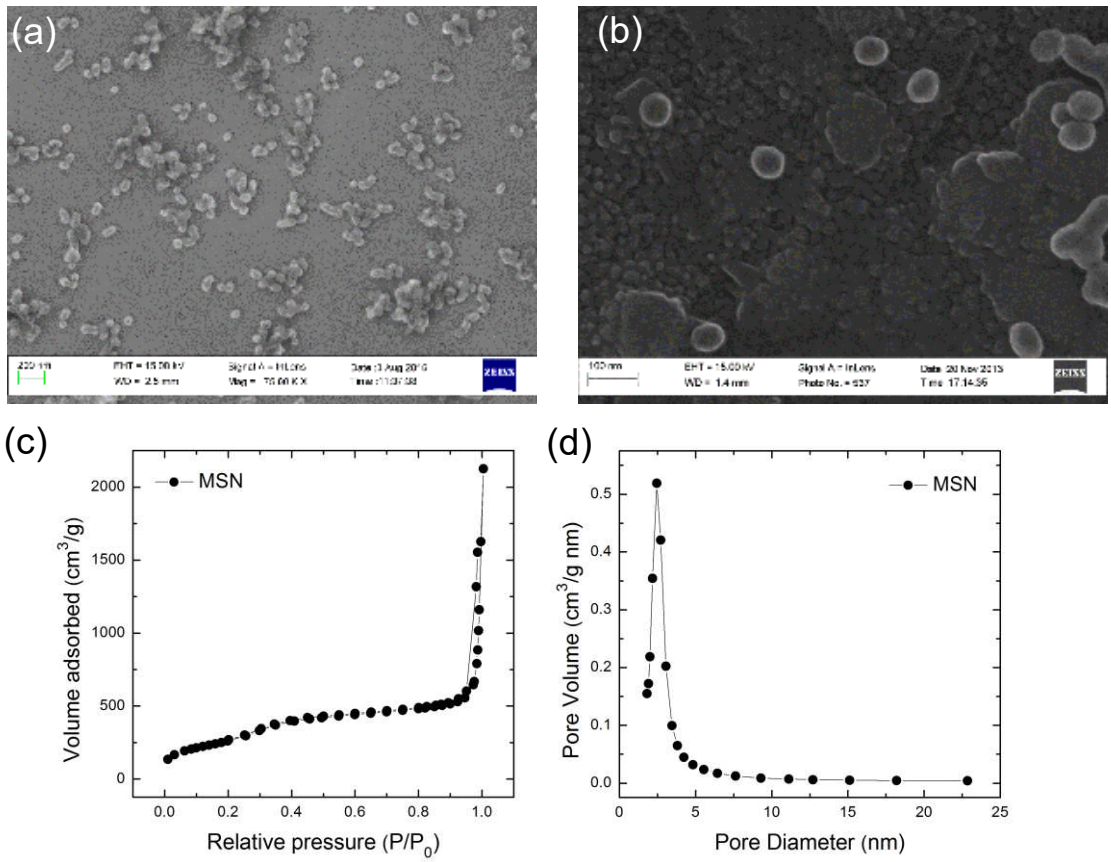

Figure 5.1 (a,b) FE-SEM images of a bare MSN sample. (c) N_2 adsorption/desorption isothermal curves and (d) pore size distribution curve.

The mesoporosity of this sample was assessed by N_2 absorption/desorption measurements, evidencing an isothermal curve (Figure 5.1c) with the typical IV isothermal shape (according to IUPAC classification[71]). Brunauer-Emmett-Teller (BET) method allowed the estimation of a relevant surface area value of 1050 ± 30 m^2/g, while the pore size distribution was determined by Barrett-Joyner-Halenda (BJH) method, showing a narrow pore diameter distribution with a peak maximum centred at 2.4 nm. This value is thus considered as the average pore diameter. In addition, a total pore volume of 1.2 cm^3/g was found, further confirmation of the high mesoporosity of the synthesized MSNs.

To figure out the effect of bismuth-driven melting point decrease for the mesoporous silica system, a series of MSNs impregnated with the same nominal fraction of precursor salts (pore occupancy of 12.5 vol%), followed by thermal treatment in the 550-750 °C range, was prepared (Table 5.1).

Figure 5.2a shows the comparison of the XRPD pattern between the sample annealed at the lower temperature (550 °C) and the bare MSNs. It is evident that the spectral shape suggests the presence of another phase in addition to the typical silica contribute. When the bismuth salt is impregnated into the silica pores, the growth of bismuth oxide is expected upon following annealing in air. However, the process of formation of Bi_2O_3 into the channel of the MSN could be in competition with the reaction of bismuth with silica. As a result, it is difficult to provide the assignment of the crystalline phase stabilized into the mesoporous channels. Moreover, the size of aggregates grown into the meso-channels is expected to be so small (*ca*. 2-3 nm) as to be difficult to determine if the new phase is amorphous or crystalline.

In order to provide a tentative assignment, Rietveld refinement was performed to identify possible features belonging to bismuth-based phases like Bi oxide polymorphs and Bi silicates. Among all of these, reasonable fit results were obtained for cubic δ-Bi_2O_3 phase and, in particular, for $Bi_{12}SiO_{20}$ phase, which provides the best agreement with the experimental measurement (Figure 5.2b). In addition, considering the latter phase, the quantitative determination of the Bi oxide content into the MSNs (16.97 wt%) well agrees, within the error, with the nominal calculation (14.52 wt%).

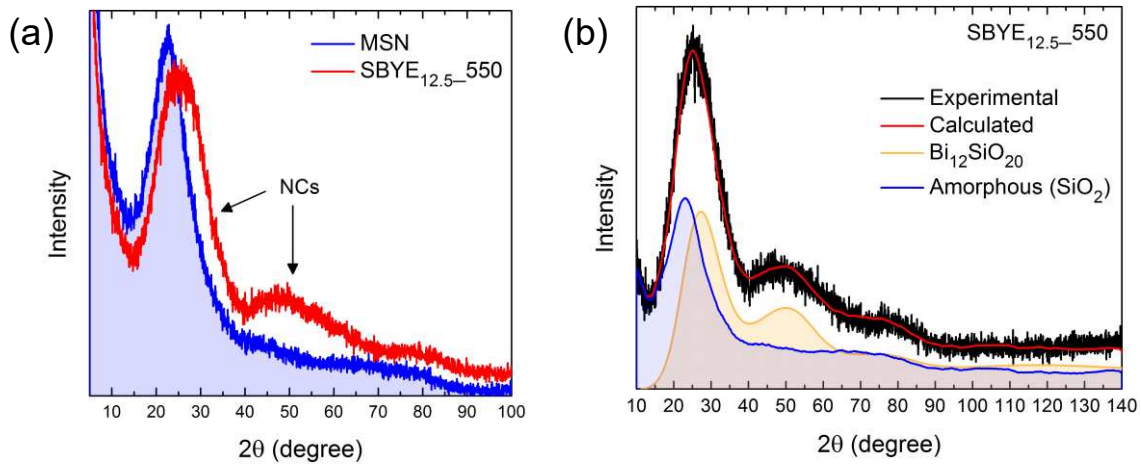

Figure 5.2 (a) Comparison of the XRPD patterns of $SBYE_{12.5}$_550 sample with the bare MSNs and (b) experimental and refined with Rietveld method of $SBYE_{12.5}$_550 sample.

Comparing the XRPD spectra for the impregnated MSNs, heated at the different temperatures, no evident differences are detectable up to 700 °C, while at 750 °C a series of features, even if small, ascribable to the Bi_2SiO_5 phase can be observed in Figure 5.3b.

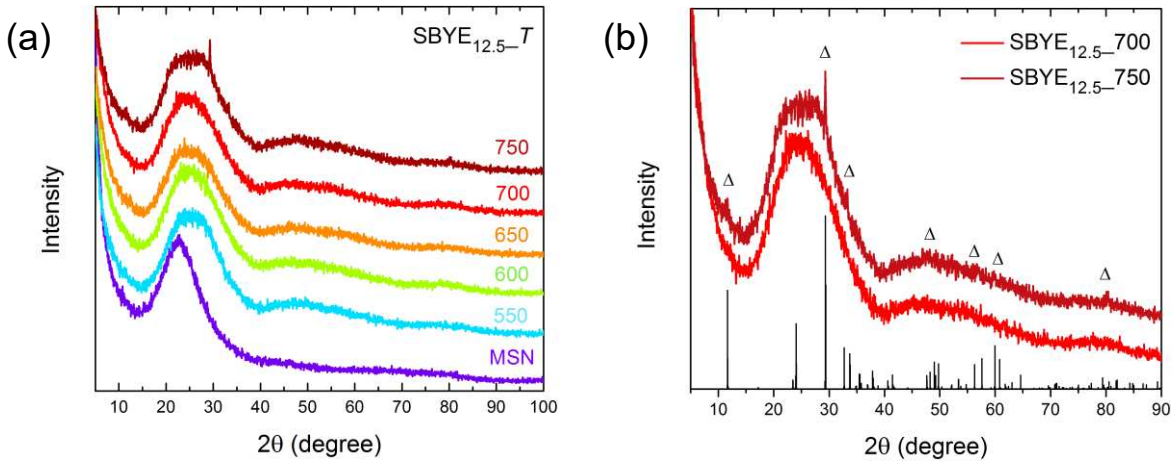

Figure 5.3 (a) XRPD patterns for the samples at different annealing temperature in the 550-750 °C range. (b) Comparison between the samples annealed at 700 and 750 °C with (triangles).

SEM images of the samples reported in Figure 5.4 (550 and 750 °C in Figure 5.4a and b, respectively) prove the same spherical morphology for all the samples irrespective to the annealing temperature. The EDS analysis confirmed the presence of the basic elements (Si, Bi, Yb and Er) in all the samples (Figure 5.4c shows the comparison between 550 and 750 samples). In addition, the semi-quantitative elemental analysis provided, within the errors, the same atomic ratio among the elements supporting the suitability of the adopted sample preparation route in limiting any precursor loss during the different preparation steps (impregnation and post-annealing).

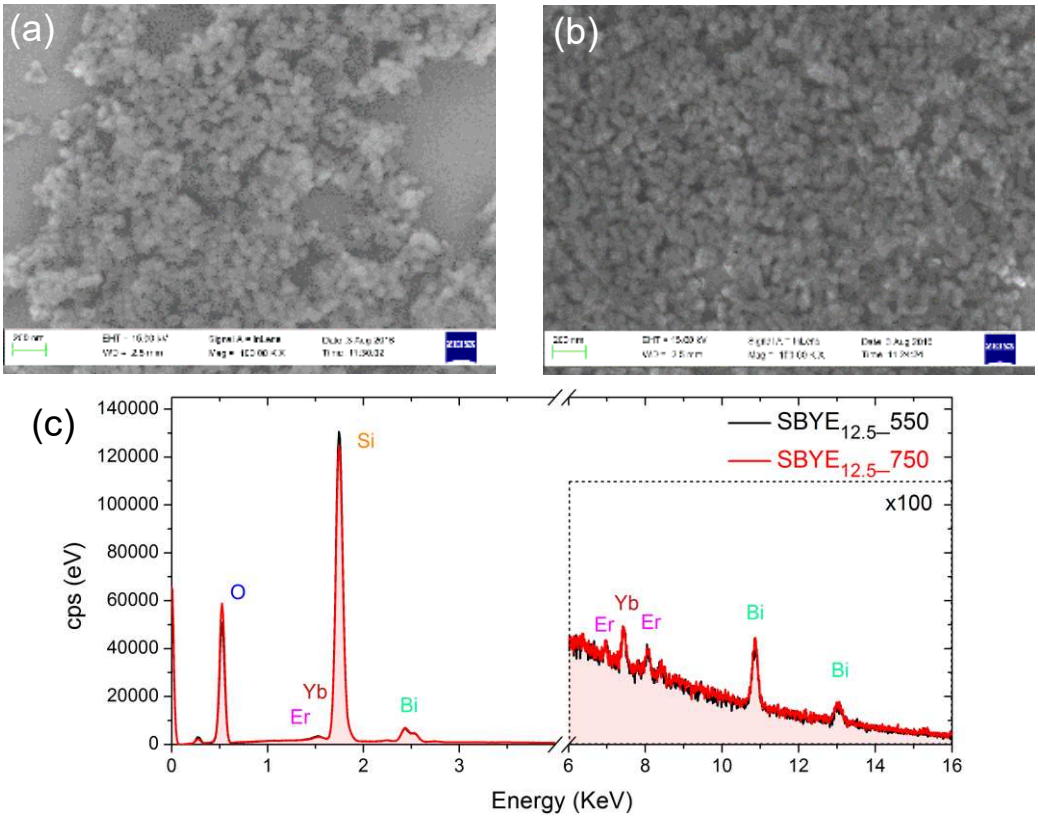

Figure 5.4 SEM images of the $SBYE_{12.5}$_550 sample (a) and of the $SBYE_{12.5}$_750 sample (b). EDS spectra of samples at 550 and 750 °C, with element labels (c).

TEM micrographs of the $SBYE_{12.5}$_750 sample evidence uniform distributed nanoaggregates of about 2-3 nm embedded into the MSN. Selected area electron diffraction (SAED) analysis were performed on the sample. However, both the selected area diffraction pattern collected at low magnification (40k, reported in Figure 5.5e) and nanodiffraction at high magnification (not reported) do not show any diffraction spot. The EDS analysis confirms the presence of Bi into the MSNs and no traces of other elements were found outside the silica nanoparticles, suggesting the effectiveness of the impregnation procedure.

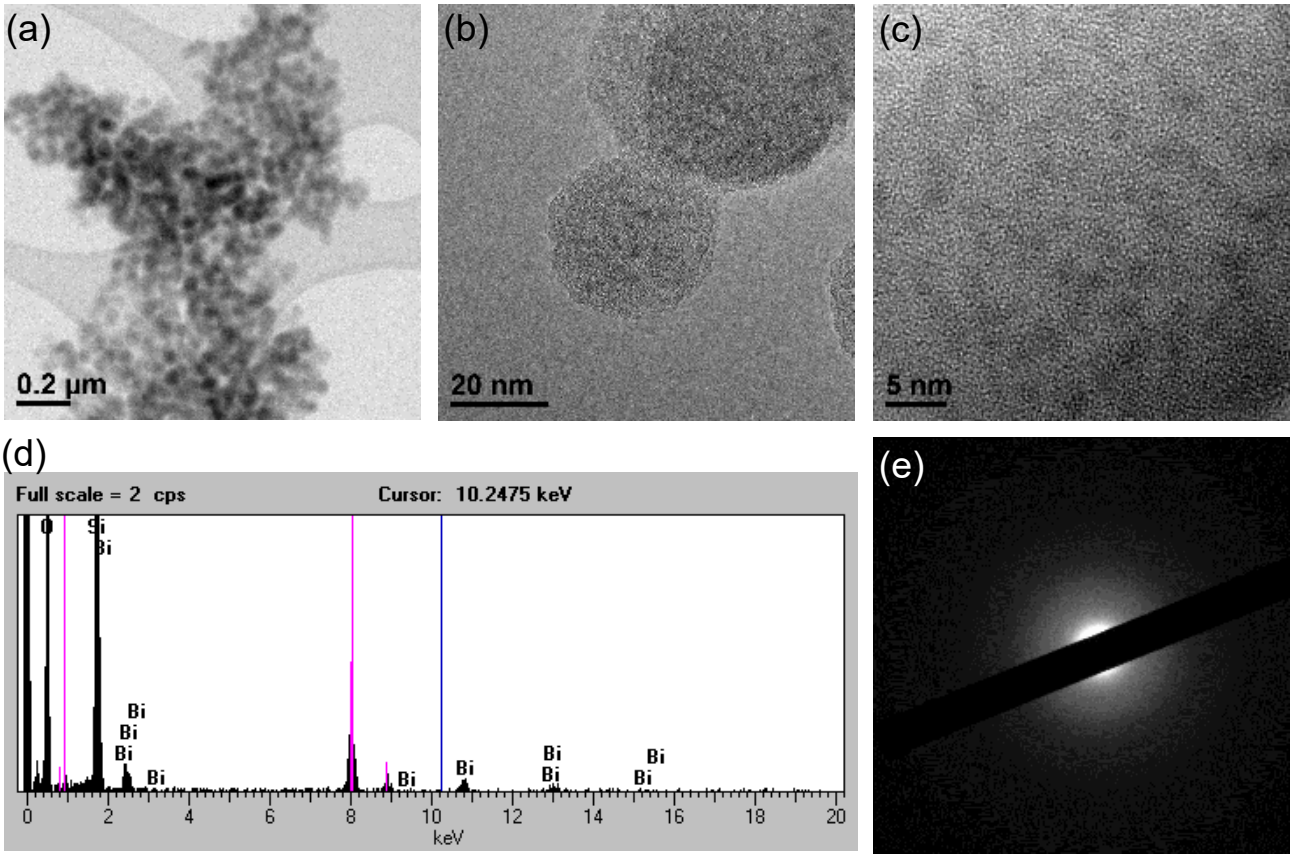

Figure 5.5 (a,b,c) TEM micrographs of the $SBYE_{12.5}$_750 sample at different magnifications, (d) EDS spectrum and (e) SAED pattern of $SBYE_{12.5}$_750 sample.

With the aim to investigate the effect of thermal treatment after the precursors loading on the silica mesoporous structure, N_2 absorption/desorption measurements were carried out. As shown in Figure 5.6a, the same type of isothermal curve is maintained for all the temperature, except at 750 °C. The surface area and the pore size estimated by the by BET and BJH method respectively, evidenced a pretty steady-state condition in the 550-700 °C temperature range, with a significant decrease of the parameters characterizing the mesoporous structure at 750 °C (Figure 5.6c). A first evident change in the mesostructure of the nanoparticles consists in the decrease of the surface area from 1050 m^2/g for the bare MSNs to about 800 m^2/g for the 12.5% loaded samples

heated up to 700 °C, with a corresponding decrease of the pore volume from 1.2 cm^3/g to about 1 cm^3/g. However, moving to the sample annealed at 750 °C, it is clear that the deep decrease of the surface area (135 m^2/g) and the pore volume (0.26 cm^3/g) can not be explained only in terms of a bismuth oxide occupancy of the MSN meso-channels.

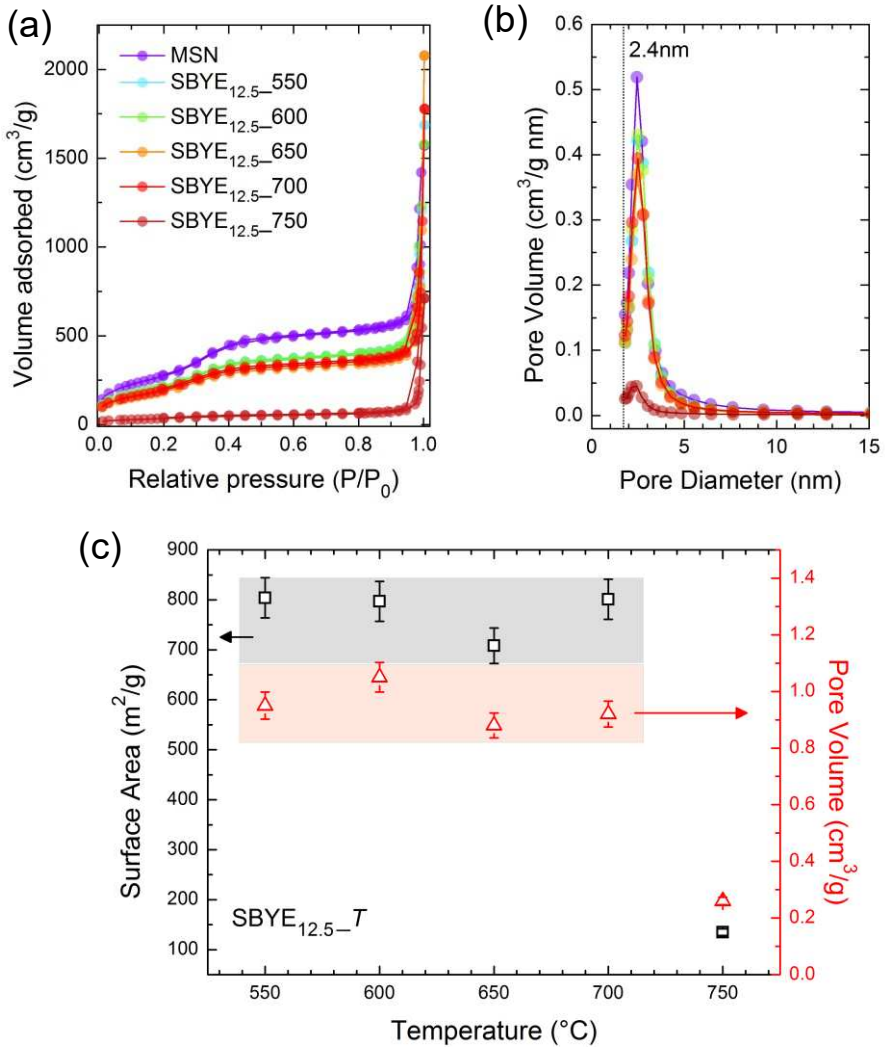

Figure 5.6 (a,b) N_2 adsorption-desorption isotherms and BJH pore size distribution of the $SBYE_{12.5}\_T$ samples. (c) Surface area (left) and pore volume values (right) as a function of temperature for the $SBYE_{12.5}\_T$ samples.

To assess the role of bismuth, in a further experiment, bare MSNs were annealed at 800 °C for 2 hours, showing a negligible reduction for both the surface area and the pore volume (950 m^2/g and 1.1 cm^3/g). Hence, bismuth seems to play a key role in the collapse of the mesoporous architecture. Once the decomposition of bismuth nitrate is complete, bismuth oxide is expected to be stabilized into the channels. Even if it is difficult to assign the phase from electron diffraction analysis, TEM images of the sample annealed at 750 °C (Figure 5.5) evidences nanoaggregates homogeneously dispersed inside the MSNs. Rietveld refinement of the XRPD patterns suggests the stabilization of $Bi_{12}SiO_{20}$ phase into the silica channels (Figure 5.2), and the presence of a small fraction of Bi_2SiO_5 phase is evidenced at 750°C, in correspondence to the porosity collapse.

It is worth stressing that the melting temperature of the materials changes at the nanoscale. As for other fundamental properties, the melting point depends on the nanostructure size, reaching lower and lower temperature as the size decrease. As a first approximation, the size-dependent melting point T_m roughly follows a $1/D$ behaviour:[72]

$$T_m = T_0\left(1 - \frac{X}{D}\right)$$

where T_0 is the melting point of the bulk, D is the nanoparticle diameter and X depends from the model considered.

It is well known (in particular for metal) that the melting point depression at the nanoscale is related to the increasing relative amount of surfaces with low-bound atoms in the neighbourhood. Guenther *et al.*[72] demonstrate the decreasing of the melting point with the diameter of bismuth oxide nanoparticles, showing a melting temperature T_m of about 210 °C for nanoparticles with diameter of 6.7 nm. Even if the situation is rather different because of the silica matrix surrounding the nanoparticles, a decrease of the melting temperature due to the particles size is expected. Therefore, at 750 °C different processes can be related to the loss of the mesoporous structure: if from one hand, bismuth precursor decomposition leads to the formation of $Bi_{12}SiO_{20}$ aggregates, from the other hand, these nanostructures could melt inside the meso-channels, reacting with silica in virtue of Bi attitude to act as a low melting point agent, with consequent porosity collapse. Moreover, it is important to remember that the mesoporous silica matrix can be considered as a viscous and elastic fluid at $T \approx T_g$.[73] As the temperature increases, the viscosity of the silica enhances with the loss of the elastic character.[74]

In conclusion, as suggested by Figure 5.6c, for the investigated system a specific temperature can be recognized in the 700-750 °C range, which determines a threshold for the bismuth-driven melting transition.

Now we turn our attention to the results of the spectroscopic analysis underwent by the investigated samples. Figure 5.7 shows the comparison of the infrared spectra between mesoporous silica and $SBYE_{12.5}$_550 sample.

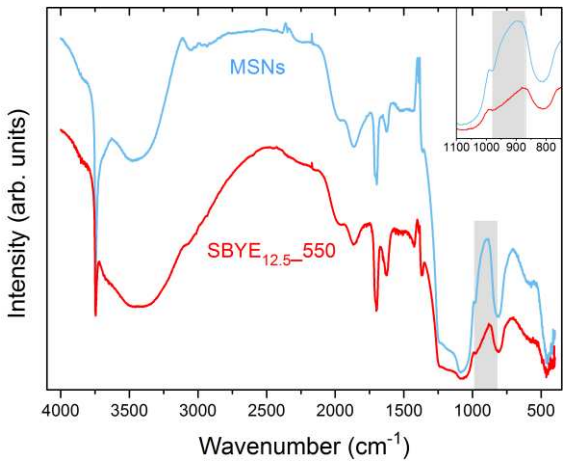

Figure 5.7 FTIR spectra of MSNs and SBYE2_550 sample. Magnification of the 1100-750 cm^{-1} region is reported in inset.

Mesoporous silica exhibits the typical absorption band of siloxane (Si-O-Si) bonding at 1200 cm^{-1}, the silanol -OH band at 3743 cm^{-1} and other peaks due to adsorbed or hydrogen-bonded water molecules in the 3700-3000 cm^{-1} range.[75] Peaks in the 800-1000 cm^{-1} range are expected for Bi-O-Bi and Bi-O-Si bonds;[76,77] in this regard, differences among the two samples are evidenced by the inset of Figure 5.7. However, specific bond recognition was not accomplished due to the lack of clear spectral features. Furthermore, at higher temperatures, any further changes in the FTIR spectrum were not observed (spectra not shown).

From the optical point of view, the diffuse reflectance spectra show the typical absorption features related to Er^{3+} ion transitions in the visible range, for all the samples, and a step-like edge going towards the UV, due to matrix absorption, which results clearly red-shifted in the case of the sample treated at the highest temperature. The difference in this absorption edge reflects the modification on the energy gap of the material, that can be estimated as the intercept at $F(R)=0$ of the straight region of the Kubelka-Munk function. A bandgap energy of 4.3 eV is calculated for all the samples up to 700 °C, while a smaller value of 4.2 eV is estimated at 750 °C. Both of these estimates are not consistent with the typical bandgap energy of bismuth oxide polymorphs (2.3-3 eV), $Bi_{12}SiO_{20}$ (2.95-3.2 eV[46,78]) or Bi_2SiO_5 (2.71-3.8 eV[64,68,79,80]). As an hypothesis, we argue that these values could reflect a quantum size effect in the smaller Bi silicate-based aggregates (size of ~2 nm) trapped in the meso-channels, resulting in a typical bandgap widening and consequent blueshift of the energy gap threshold with respect to the bulk system. Furthermore, since the bandgap energy variation occurs with sample heating at 750°C, as in the case of the pore structure collapse, it seems that this temperature determines such a turning point for a deep modification of the material structure.

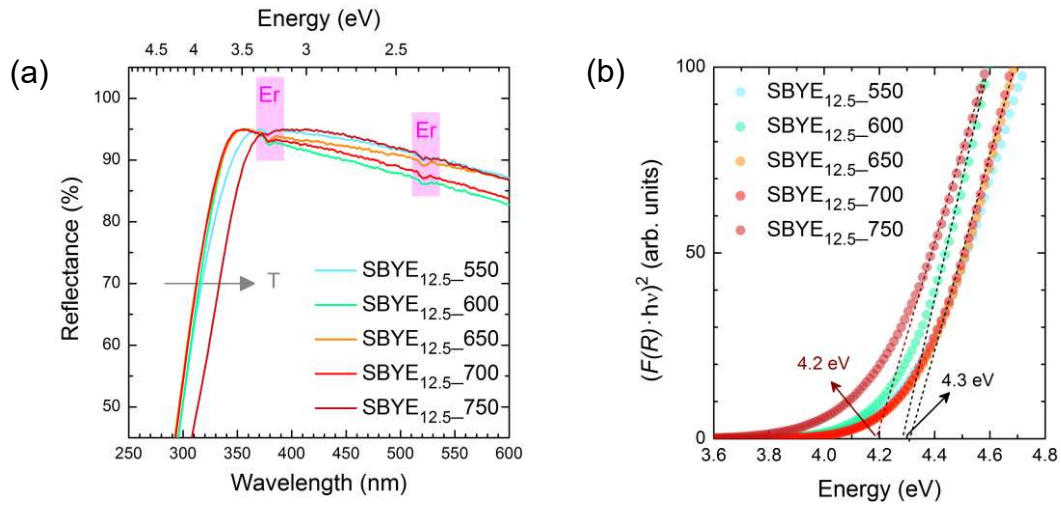

Figure 5.8 Diffuse reflectance spectra (a) and Kubelka-Munk function $F(R)$ (b) for the SBYE_*T* samples. (c) Comparison between the UCPL spectra of the samples annealed at 550 and 750 °C.

5.4 Crystalline Thermal Evolution

In order to monitor the local structural evolution as a function of temperature, a sample fully impregnated by Bi and Ln salt precursors (sample $SBYE_{100}$, pore occupancy of 100 vol%) was analyzed by *in situ* temperature dependent synchrotron radiation X-ray powder diffraction (SR-

XRPD). The structural evolution of the system was followed by increasing the temperature up to 1000 °C. At low temperature (100-450 °C range) only very weak peaks due to bismuth nitrates were detected (not shown). From 500 °C, the *in situ* SR-XRPD analysis in Figure 5.9 reveals the growth of a crystalline phase, recognized as the orthorhombic Bi_2SiO_5 ($Cmc21$ space group, ICSD#30995), whose structural features increase in intensity up 750 °C, and then progressively decrease with complete disappearing of the crystalline phase and amorphisation of the sample at 900 °C.

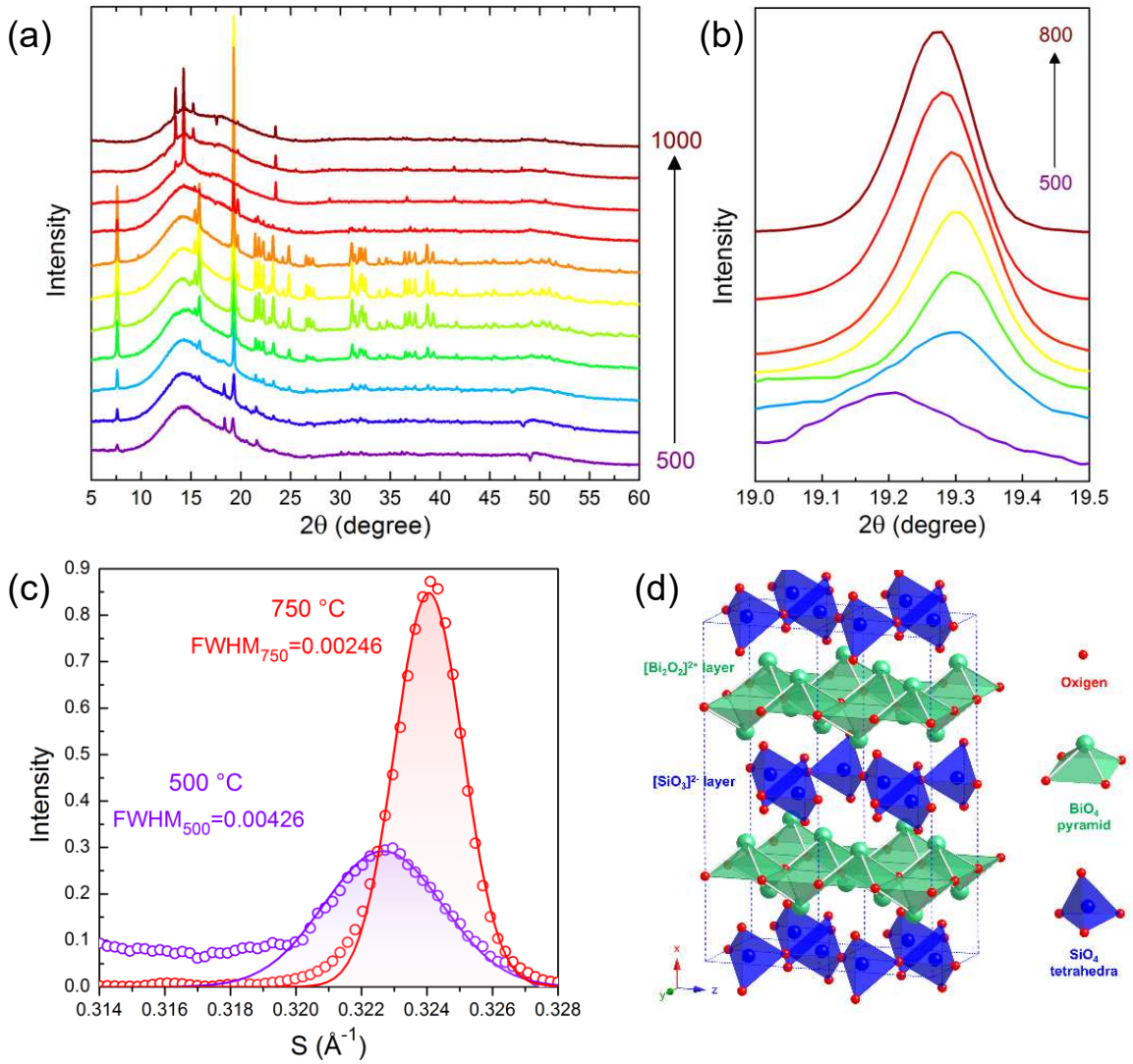

Figure 5.9 (a,b) *In situ* temperature dependent synchrotron X-ray powder diffraction patterns (λ=1.03333 Å) of $SBYE_{100}$ sample in the range of 500-1000 °C and magnification of the (311) reflection peak. (c) Comparison between the (311) reflection peak broadening as a function of S ($2\sin(\theta)/\lambda$) at 500 and 750 °C. (d) Crystalline structure of Bi_2SiO_5 with the typical coordination site for bismuth and silicon.

In regard to the occurring stabilization of the orthorhombic Bi_2SiO_5 phase during the heating process, it is worth considering that this is a metastable phase hardly stabilized by solid state reaction (only by means of very long cooling from the melt[60]). In this view, the meso-channels of MSNs are suggested to work as nanoreactors allowing the direct stabilization of the metastable phase after the thermal treatment at 750 °C for 2 hours, without any further cooling process.

Figure 5.9b shows the temperature dependence of the (311) reflection peak of the Bi_2SiO_5 phase in the 500-800 °C range. In order to emphasize the difference in the crystallite dimension at 500 and 750 °C, Figure 5.9c evidences the full weight at half maximum (FWHM) of the peak at about 19.25°. The two values estimated by means of the Scherrer equation of about 22 nm and 38 nm at 500 and 750 °C, respectively, confirm the increase of the crystallite size with the temperature.

In order to follow the decomposition/crystallization path respect to the structural evolution displayed by the *in situ* temperature dependent SR-XRPD investigation, thermogravimetric analysis (TG-DSC) was carried out on the unheated $SBYE_{100}$ sample (Figure 5.10). TG-DSC measurements support the structural observations providing a thermal process in which the decomposition features showed up to 500 °C are consistent with: (i) water removal (endothermic peak at 100.4 °C); (ii) dehydration and decomposition of $Bi(OH)_3$ and bismuth nitrates[81-83] (faint peak at about 220°C and peak at 327.4 °C); (iii) phase transition of Bi_2O_3 [82,83] (peak at 472.3 °C) with a total weight loss of about 14%.

A further element emerging from the TG-DSC analysis, which certainly deserves a deeper investigation in future, is the clear observation of a glass transition at a temperature T_g of 549.2 °C (see inset of Figure 5.10), then in correspondence with Bi_2SiO_5 phase stabilization evidenced by the synchrotron analysis. The activation of this specific transition suggests that the system should be characterized by a certain mobility, responsible of the typical processes occurring in glassy networks, like diffusion and percolation. In addition, a small exothermic peak at 611.9 °C is also revealed, that could be related to the precipitation of a crystalline phase.

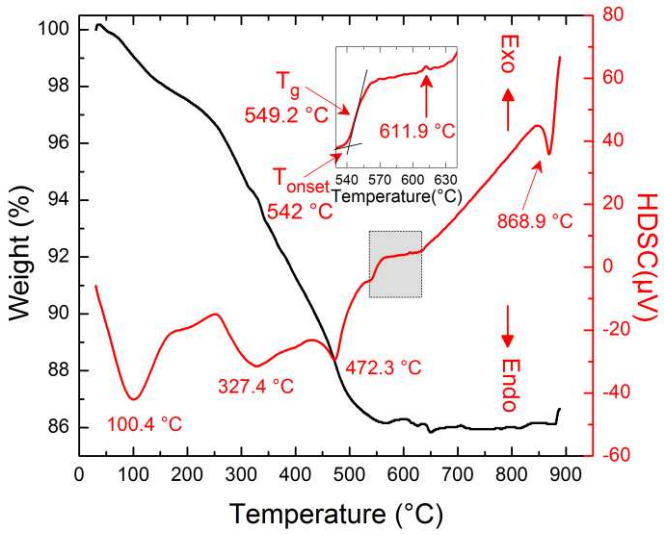

Figure 5.10 Thermogravimetric (TG) and differential scanning calorimetry (DSC) curves of the $SBYE_{100}$ sample, with heating rate of 10 °C/min.

5.5 Morphological and Structural Behaviour: Bismuth Loading Effect

Further considerations about the effect of Bi incorporation into the MSNs can be achieved by considering a series of four MSN samples impregnated with different degree of precursor salt loading (pore occupancy of 12.5, 25, 50 and 100 vol%, respectively), and then annealed at 750

°C, suggested as the ideal temperature for the Bi silicate stabilization from the previous analysis carried out on $SBYE_{100}$ sample.

Figure 5.11a shows the XRPD patterns of the samples as a function of precursor content. As for the bare MSNs, at lower impregnation degree we observe a broaden amorphous-like feature, that can be attributed to both silica and small $Bi_{12}SiO_{20}$ nanoaggregates formation after pore loading (see Figure 5.11b), that progressively disappear by increasing the precursor salt content, leaving the place to a series of crystalline peaks, marking the precipitation of the crystalline Bi_2SiO_5 phase.

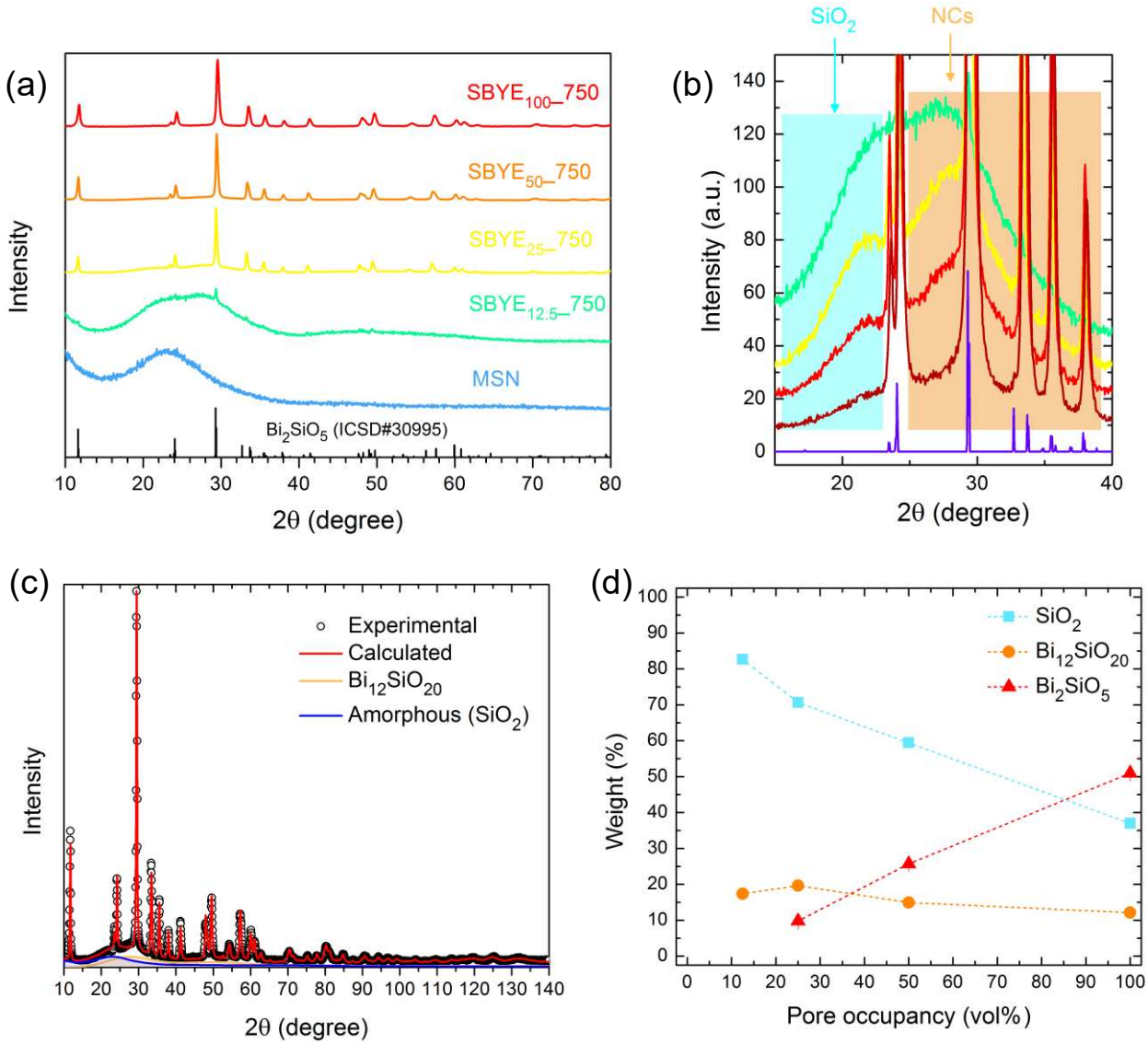

Figure 5.11 (a) XRPD patterns of the $SBYE_x$_750 series, with x=12.5, 25, 50, 100. (b) Zoom of the XRPD to evidence the decrease of the SiO_2 and $Bi_{12}SiO_{20}$ phases contents with increasing the bismuth salt loading. (c) Rietveld refinement fit performed on the sample $SBYE_{50}$_750. (d) Weight percentages of the phases from Rietveld refinement *versus* bismuth precursor loading content calculated as percentages of volume occupied by the salt on the total MSN volume accessible.

Rietveld refinement was performed by considering only the amorphous silica phase, $Bi_{12}SiO_{20}$ nanoaggregates and the Bi_2SiO_5 phase, since no other phases were detected. Figure 5.11c shows

the fit performed on $SBYE_{50}$ (as an example) and the results of the quantitative analysis performed by means of Rietveld refinement[84] are summarized in Table 5.4. As graphically reported in Figure 5.11d, the observed tendency of a progressive reduction of the features attributed to silica and $Bi_{12}SiO_{20}$ is confirmed, leaving the place to the Bi_2SiO_5 phase whose signal increases up to 50 wt%. This trend is in line with the claimed high reactivity between silica and bismuth.

Table 5.4 Summary of the parameters obtained from Rietveld refinement of the samples.

Sample	SiO_2	$Bi_{12}SiO_{20}$	Bi_2SiO_5					R_p	R_{wp}	GOF [a]
	wt%	wt%	wt%	a	b	c	V_{cell}			
$SBYE_{12.5}$	82.67	17.33	-	-	-	-	-	6.67	9.04	0.20
$SBYE_{25}$	70.63	19.62	9.75	15.20107	5.3901	5.38153	440.93704	7.55	9.84	0.61
$SBYE_{50}$	59.40	14.92	25.68	15.1747	5.38118	5.35685	437.42862	9.23	12.04	0.74
$SBYE_{100}$	36.96	12.10	50.94	15.17925	5.37093	5.35708	436.74516	10.04	13.67	0.77

[a] GOF=goodness of fit

From the Rietveld quantitative parameters reported in Table 5.4, it was attempted to deduce the amounts of SiO_2 and Bi_2O_3 that should have reacted for determining the resulting composition of each sample. Table 5.5 provides a comparison between these estimates and the nominal weight percentages adopted during the different syntheses: the agreement is remarkable, indicating the reliability of the method in preparing samples with a refined control of the composition.

Table 5.5 Comparison of the nominal and experimental (from Rietveld refinement) weight percentages of SiO_2 and Bi_2O_3 of the samples.

Sample	nominal		experimental	
	SiO_2 (wt%)	Bi_2O_3 (wt%)	SiO_2 (wt%)	Bi_2O_3 (wt%)
$SBYE_{12.5}$	85.48	14.52	83.03	16.97
$SBYE_{25}$	74.64	25.36	72.15	27.85
$SBYE_{50}$	59.34	40.46	62.64	37.36
$SBYE_{100}$	42.39	58.61	43.03	56.97

To assess the MSN porosity evolution as a function of the impregnation degree, N_2 adsorption-desorption analyses were performed. The analyses suggest that, in addition to the stabilization of an increasing fraction of Bi_2SiO_5, the rise of bismuth loading leads to an abrupt collapse of the mesoporous structure.

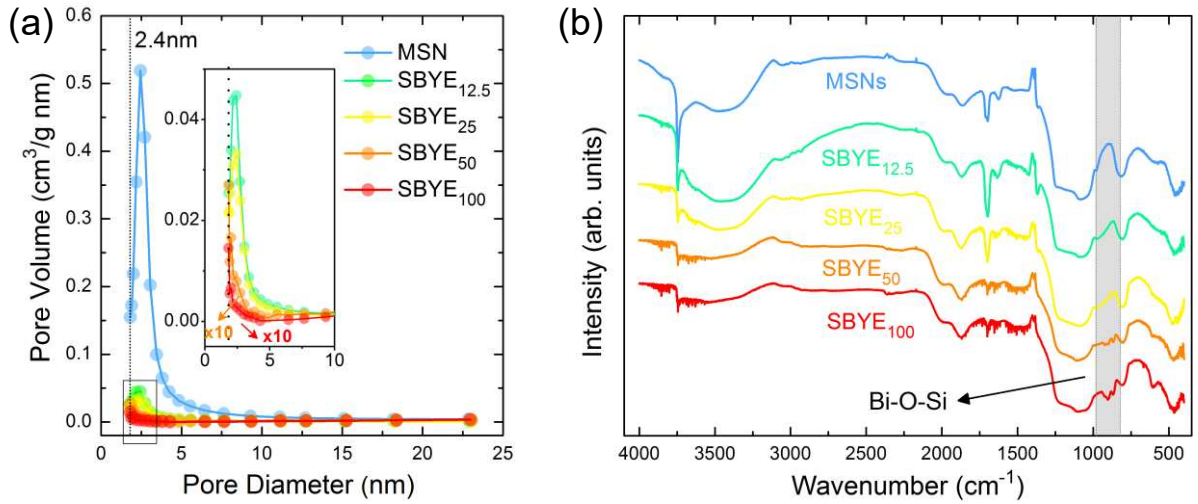

Figure 5.12 BJH pore size distribution (a) and FTIR spectra for the samples at different loadings (b).

As aforementioned in Section 5.2, for the $SBYE_{12.5}$ sample heated at 750 °C the mesoporous character of the host is lost. In the same way, the BET and BJH methods evidenced this trend as the precursor content increased, as implied by the strong decrease of the surface area and pore volume values (see Figure 5.12a and Table 5.5).

Table 5.6 BET specific surface area $S.A._{BET}$ and total pore volume V_p of the MSN and $SBYE_x$ samples.

Sample	$S.A._{BET}$ **(m^2g^{-1})**	V_p **(cm^3g^{-1})**
MSN	1050	1.2
$SBYE_{12.5}$	135	0.26
$SBYE_{25}$	109	0.21
$SBYE_{50}$	18	0.07
$SBYE_{100}$	14	0.06

In particular, as suggested by the BJH pore size distribution trend observed in Fig.5.12a, from the values reported in Table 5.6 it is pointed out that the porosity collapse takes place with 50% of pore volume loading. FTIR spectra in Figure 5.12b also confirms the formation of bismuth silicate phases in the samples due to the characteristic Bi-O-Si vibration.

Representative High-Resolution Transmission Electron Microscopy (HRTEM) images of the samples are reported in Figure 5.13. These images highlight the tendency of the system to evolve from an initial network of well-dispersed, small primary aggregates inside the mesoporous silica channel ($SBYE_{12.5}$_750), to a distribution of Bi silicate-based, larger nanocrystals, that gradually grow until the stabilization of a core-shell system at the highest loading content ($SBYE_{100}$_750). In the following we clarify the crucial aspect.

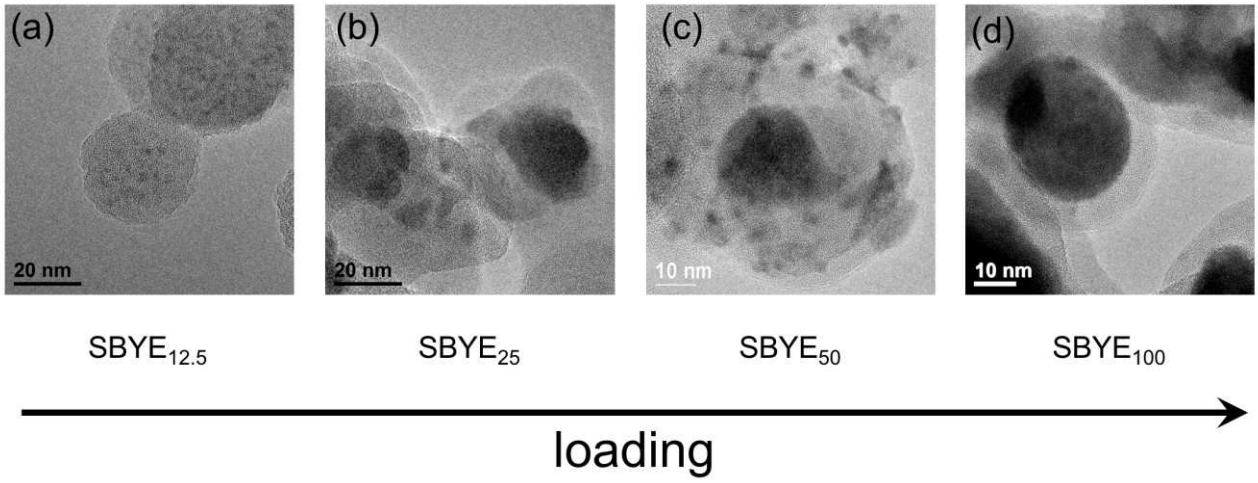

Figure 5.13 TEM images of the nanoparticles at the increasing of the bismuth content, showing the morphological evolution to a core/shell structure.

The process leading to this spontaneous core-shell assembly seems to be determined by the concentration of the precursor into the meso-channels, with the tendency of the primary aggregates to move inside the channels and to react each other, originating larger nanostructures with manifest crystalline character. Figure 5.14 reports some images of the self-assembled core-shell nanosystems at different magnifications and the nano-beam electron diffraction (NBD) analysis on the particle core for the $SBYE_{100}$_750 sample.

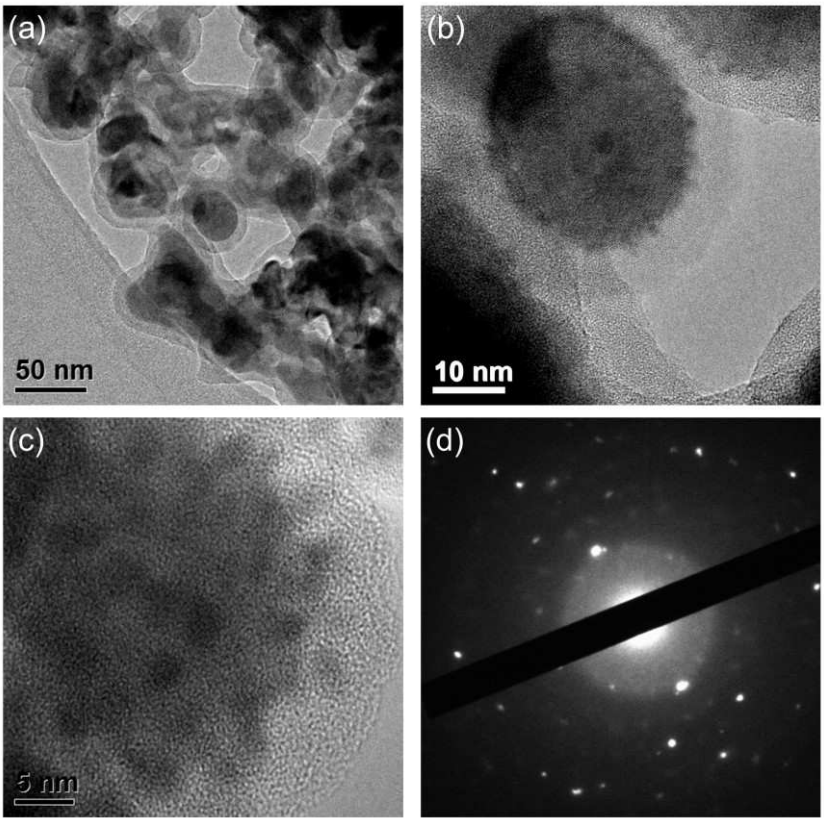

Figure 5.14 (a,b,c) TEM and HR-TEM images of the $SBYE_{100}$_750 sample at different magnifications and (d) Selected Area Electron Diffraction (SAED) conducted on (c).

As previously suggested, in conditions of full pore impregnation, the evolution to the core-shell assembly system is strongly promoted. Figure 5.14a shows that the nanostructures deriving from the reaction of the MSN constituents and the precursor salts are surrounded by an amorphous shell with an estimated thickness of about 4-7 nm. The magnifications provided by the HR-TEM image of Figure 5.14b and c evidences that this shell consists of compact, non-porous silica. Hence, the formation of the core-shell structures occurs in combination with the total loss of the MSN porosity with a process that leads to the densification of the silica framework. Moreover, from these images it is pointed out that the core seems to consist in both an extended crystalline region, with a defined plane structure (difficult to appreciate due to the low quality of the here-reported reproduction of the TEM images) and occupying the larger part of the core itself, and/or an assembly of small (size ≤ 5 nm) crystalline NPs. In Figure 5.14d, nano-beam electron diffraction (NBD) SAED analysis performed on the core region confirms the stabilization of the Bi_2SiO_5 phase. Finally, it is worth mentioning that the dimensions of the ellipsoidal core of the particle visible in Figure 5.14b are estimated to be 35 nm and 28 nm for the major and minor axes, respectively, thus in good agreement with the crystallite dimension value of 38 nm resulting from the *in situ* SR-XRPD analysis on the $SBYE_{100}$ sample heated at 750°C, reported in Section 5.3.

5.6 Core-Shell Self-Assembly Process: A Tentative Mechanism

To date, the details of the formation mechanism of metal oxide nanoparticles (M_xO_y) in the mesoporous silica channels are not known.[85-87] However, it is reasonable that it occurs via an initial formation of generic metal hydroxide $M(OH)_z$, decomposing into the metal oxide during the thermal treatment. This hypothesis is supported by the thermogravimetric analyses together with the temperature dependent *in situ* SR-XRPD analyses that show the concomitance of the degradation of the bismuth nitrates with the consequent stabilization of bismuth oxide-based phases. It must be underlined that, in the present study, the comprehension of the process responsible of the aggregate formation into the MSN channels is complicated by the high reactivity between Bi and Si oxide. On the basis of the structural and morphological analysis presented above, a possible mechanism leading to the formation of the core-shell structure is provided in the following.

At low impregnation level ($SBYE_{12.5}$ samples), the reported HR-TEM images clearly evidence the formation of small, nm-size aggregates (size ~2 nm) inside the mesoporous channels of the MSNs, whose crystalline or amorphous character can not be fully ascertained. By means of Rietveld analysis, the nanostructures stabilized at 550 °C are reasonably assigned to the $Bi_{12}SiO_{20}$ phase (in agreement with the quantitative analysis) suggesting the prompt reactivity between Bi precursor and the silica structure, already at low temperature. Increasing the temperature, the stabilization of a Bi_2SiO_5 phase is observed, with the concomitant collapse of the silica mesoporosity.

As schematically reported in Figure 5.15, we propose a scenario where the primary $Bi_{12}SiO_{20}$ aggregates, segregated into the silica mesochannels (that act as both nanoreactors and sources of silicon), fuse together to form, at first, bigger nanocrystals with size as larger as the precursor salt

content increases, then extended crystalline regions, whose composition progressively turns to Bi_2SiO_5 (as evidenced by TEM images of Figure 5.13).

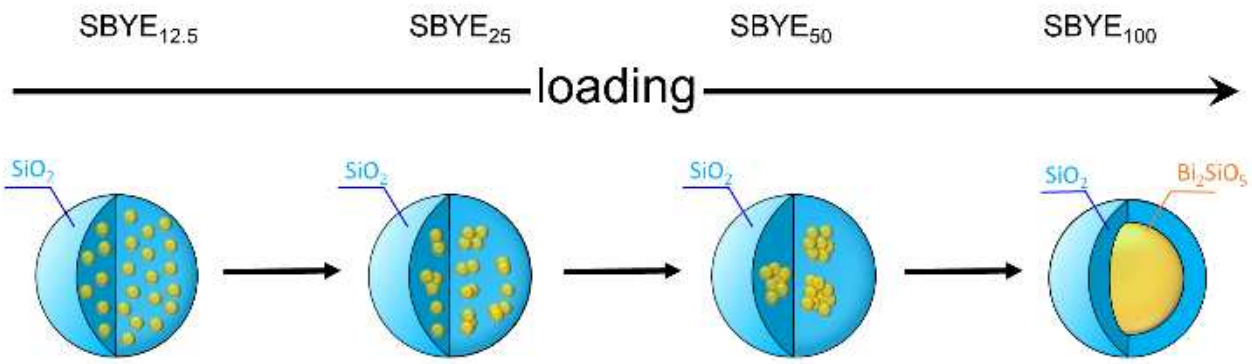

Figure 5.15 Sketch of the core/shell self-assembly process as a function of the bismuth precursor loading into the MSNs.

Both Bi loading content and heating temperature play a key role in determining the evolution of the mechanism leading from the impregnated MSNs to the precipitation of the Bi silicate phases, and in general their increase (with a suggested optimal temperature of 750°C) brings to a full stabilization of the core-shell assembly. In this regard, a clear picture of this is given by TEM images of $SBYE_{100}$_750 sample reported in Figure 5.14.

Depending on the temperature, upon heating the primary aggregates move towards the center of the silica particles, promoting the formation of the Bi silicate-based core region. At the same time, the depletion of the outer layer determines the formation of a silica shell that undergoes a densification process, then turning from porous to glassy, also in virtue of the Bi-induced low melting point effect. Furthermore, referring to the glass transition at T_g=550 °C evidenced by the TG-DSC analysis, it is well known that around the T_g temperature high constituent mobility takes place, with enhanced ion diffusion and percolation processes. Also the mobility into the mesochannels result increased, validating the idea of primary aggregates that progressively move, originating the Bi silicate-based core region. In addition, as previously discussed in Section 5.3, silica may be considered as a viscoelastic fluid at $T \approx T_g$,[73] and a further increase of the temperature can induce an increase of the viscosity of the silica matrix, which loses its elastic character.[74] As a consequence, in the case of the investigated system, porous-to-glass transition involving the outer shell of the silica particle can occur. Finally, it is worth considering that one of the most used route for the preparation of silica NPs and shells is the Stöber method and derived synthesis processes, that usually provides porous materials.[88-90] Therefore, the possibility to achieve the formation of glassy shells covering the investigated NPs is a peculiar result of this research that must be emphasized.

5.7 Optical Analysis and Ln UC PL Emission

At first, we report about the optical properties of the SBYE$_X$_750 series in order to evidence the impact of the precursor loading level on the Ln UC PL properties. Figure 5.16a shows the diffuse reflectance analysis of the samples as a function of the loading content. In the reflectance spectra, at higher pore occupancy the absorption peaks of the lanthanide ions (Yb^{3+} and Er^{3+}) are clearly detectable. By considering the direct bandgap nature of Bi_2SiO_5, described by first-principles calculations of the band structure by Kuwabara *et al.*,[91] Park *et al.*[92] and Zhang *et al.*,[66] the bandgap energy of the samples was estimated plotting the $(F(R) \cdot h\nu)^2$ *versus* $h\nu$ (Figure 5.16b). We obtained an energy value of 3.8 eV for the samples loaded at 25, 50 and 100 vol%, in the range of the typical values reported for Bi silicates, while for the SBYE$_{12.5}$_750 sample a bandgap of 4.2 eV was calculated, as already reported in Section 5.3.

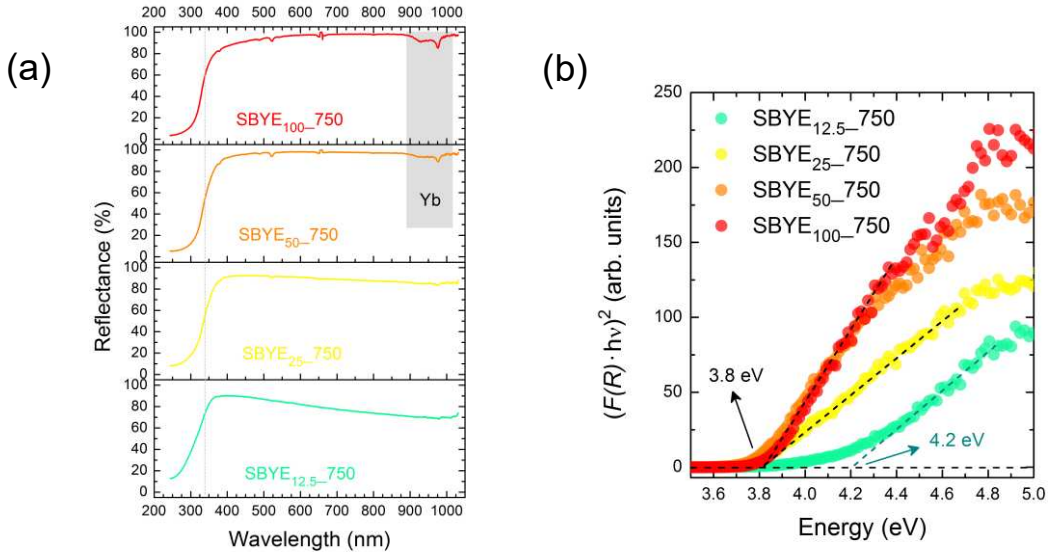

Figure 5.16 Diffuse reflectance spectra (a) and bandgap estimation for the SBYE$_X$_750 series (b).

Figure 5.17a shows the upconversion luminescence spectra in the visible range, collected upon laser diode excitation at 980 nm. We can recognize two main features related to Er^{3+} $^4S_{3/2} \rightarrow {}^4I_{15/2}$ and $^2H_{11/2} \rightarrow {}^4I_{15/2}$ transitions, in the green region of the e.m. spectrum, and $^4F_{9/2} \rightarrow {}^4I_{15/2}$ transition, in the red one.

It is well known that the emission spectral shape reflects the structural environment surrounding the luminescent center. For the high-loaded samples, the presence of quite sharp structures can be linked to the presence of a crystalline site (or more) accommodating the lanthanide ions. As evidenced by SBYE$_{12.5}$_750 sample, in the case of moderate loading a broadening of the emission features can suggest an amorphous-like environment. Figure 5.17b evidences the different spectral shape between SBYE$_{12.5}$_750 and SBYE$_{100}$_750 samples. In addition to this, also a variation in the relative ratio between the emissions falling in the green and in the red is observed.

By considering the two extreme MSN impregnation conditions, these differences in the UC PL emission spectra are in agreement with the distinct behaviour observed from the structural and morphological point of view. In fact, if at low loading level the Ln ions are hosted in a matrix that consists in an amorphous silica matrix, embedding Bi doped aggregates so small that the crystalline character is lacking, at high loading level, the Ln ions are in presence of a stabilized core-shell structure, with a crystalline Bi_2SiO_5 core.

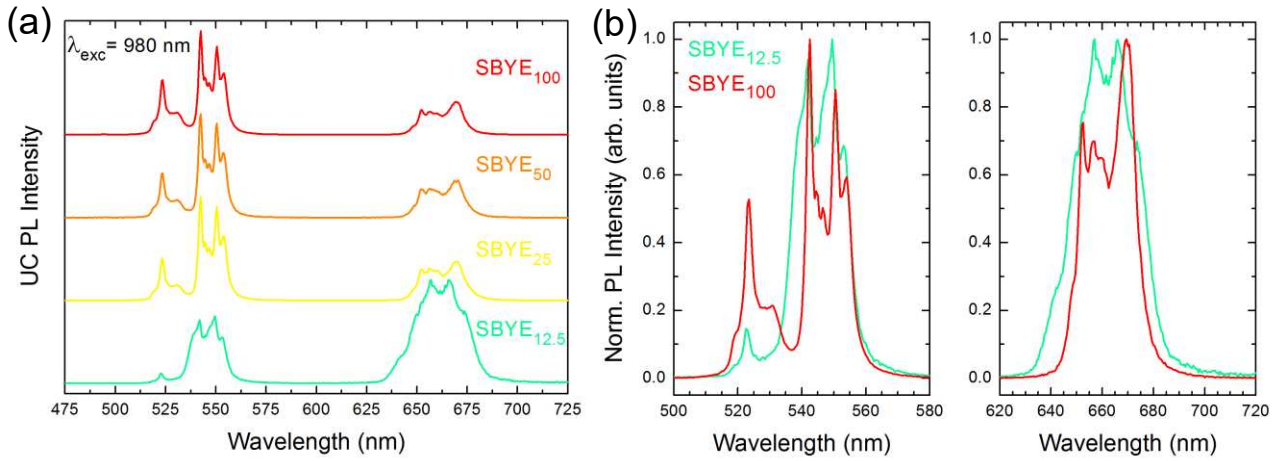

Figure 5.17 (a) UC PL emission spectra as a function of loading into MSNs and (b,c) comparison of the green and red emission shapes at the lower and highest loading.

With the aim to explore the suitability of the investigated material for the realization of a new class of UC nanophosphors, the emission properties and the resulting color output tunability was investigated by doping, through impregnation method, a series of MSN samples with different combination of lanthanide ions typically used for the generating upconverting systems (Yb^{3+} and one or more among Er^{3+}, Ho^{3+} and Tm^{3+} ions). Figure 5.18a and b show, respectively, the UC PL spectra for the synthesized samples (preparation reported in Section 5.2) and the relative colour output as resulting from the reported pictures and CIE diagram. In regard to the assignment of the Ln transitions originating the observed PL features, one can refer to Chapter 4. About the pictures shown in Figure 5.18b, it is worth noticing the bright emission originating from the 980 nm irradiated samples and, in view of the realization of a white-emitting LED, the remarkable result obtained with the reported example of triple Ln doped SBYETH sample.

Table 5.7 summarizes the CIE colour coordinates (x,y) of the samples under 980 nm excitation.

Table 5.7 CIE Colour Coordinates (*x*,*y*) for the samples under 980 nm excitation.

Sample	CIE(*x*,*y*)
SBYE	(0.31,0.68)
SBYH	(0.65,0.34)
SBYT	(0.25,0.13)
SBYET1	(0.26,0.26)
SBYET2	(0.27,0.43)
SBYTH	(0.39,0.20)
SBYETH	(0.41,0.32)

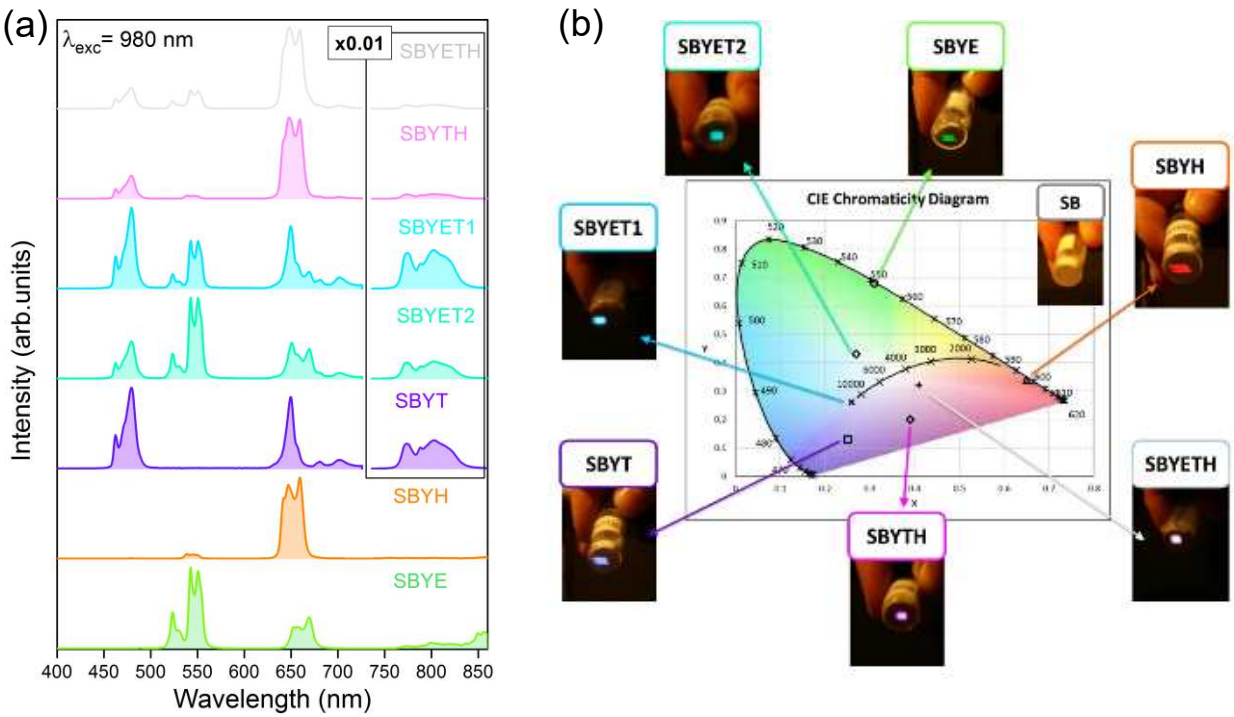

Figure 5.18 (a) UC PL spectra and (b) relative photographs under 980 nm irradiation with CIE diagram for all the samples.

As a final consideration, we underline that a remarkable advantage of silica based nanosystems is the availability of several techniques for surface functionalization, based on the well-developed silane chemistry. Moreover, the easy control of the color output by acting on the UC properties of the systems, the low toxicity of materials and the stability of the silicates, allow to consider this system as a promising candidate in different application fields, like anti-counterfeiting, bioimaging, lightening, optical storage and lasing.

5.8 Conclusions

In this Chapter, we have discussed the synthesis of Ln doped Bi silicate based UC nanophosphors obtained through MSN impregnation. The main purpose of this research was to investigate of the impact of both thermal treatment temperature and Bi loading on the overall properties of the synthesized material. We have shown a clear structural and morphological evolution of the impregnated MSNs, demonstrating (i) the stabilization of the metastable Bi_2SiO_5 phase in virtue of the presence of MSN mesochannels acting as nanoreactors, and (ii) the unexpected resulting formation of a peculiar core-shell nanosystem composed by a crystalline Bi_2SiO_5 core and a glassy silica shell. In particular, the key role of bismuth in the core-shell self-assembly process formation was assessed and a tentative mechanism of formation was proposed. Moreover, the incorporation of lanthanide ions promotes the activation of PL emission under near-IR excitation. The UC PL properties were investigated, showing the possibility to a refined control of the UC output emission in the whole CIE diagram by careful selection of the luminescent doping species and of the relative concentration.

The Bi-driven sealing effect on the MSN pores, leading to the formation of a glassy shell, can be linked to the low silica melting point effect promoted by bismuth doping, and it can be considered an effective method to develop a new class of nanosystems where an active phase (*e.g.* phosphors, pigments, magnetic materials, UV filters), embedded in the NP core, is completely isolated from the environment by means of dense, shielding shell, avoiding undesirable reactions with surrounding medium, like photocatalytic processes or aging mechanisms, as examples. In addition, the low toxicity and low cost of bismuth-based compounds, together with the easy functionalization of the nanomaterial ensured by its silicon nature, allow to consider the new systems very promising in a wide range of applications such as bioimaging, anti-counterfeiting and lightening.

Materials and Methods

Experimental Details. X-Ray Powder Diffraction (XRPD) measurements were performed by means of a Philips diffractometer with a PW 1319 goniometer with Bragg-Brentano geometry, equipped with a focusing graphite monochromator and a proportional counter with a pulse-height discriminator. Nickel-filtered Cu Kα radiation and a step-by-step technique were employed (steps of 0.05° in 2θ), with collection time of 30 s per step. The crystallite size estimation has been performed by Scherrer analysis and the instrumental line broadening has been evaluated by means of LaB_6 SRM660s standard by NIST. The temperature dependent *in situ* Synchrotron Radiation X-ray powder diffraction (SR-XRPD) measurements were collected at the MSX line of ELETTRA Synchrotron Light Laboratories of Trieste, using a quartz glass capillary as sample holder.[93] Nitrogen adsorption-desorption isotherms were measured at liquid nitrogen temperature using a Micrometrics ASAP 2010 system. Each sample has been degassed at 130 °C overnight before the measurements. The Brunauer-Emmett-Teller (BET) equation was used to calculate the specific surface area from adsorption data and the Barrett-Joyner-Halenda (BJH) model was used to estimate the pore-size distribution from the adsorption branches of the isotherms. IR spectra were recorded with a NEXUS-FT-IR instrument implementing a Nicolet AVATAR diffusive reflectance accessory. The thermogravimetric analyses (TG-DSC) were performed in air from 30 to 900 °C with a heating rate of 20 °C min^{-1}. Size and morphology of the nanoparticles and EDS analysis were carried out by a Carl Zeiss Sigma VP Field Emission Scanning Electron Microscope (FE-SEM) equipped with a Bruker Quantax 200 microanalysis detector. The EDS spectra were collected at the same condition (20 KeV) for all the samples. In addition, TEM images were taken at 300 kV with a JEOL3010 instrument with an ultrahigh resolution (UHR) pole-piece (0.17 nm point resolution), equipped with a Gatan slow scan CCD camera (model 794). The powders were dispersed in isopropyl alcohol by means of sonication and then deposited onto a holey carbon film-coated copper grid.

The diffusive reflective UV-Vis (DRUV-Vis) spectra were collected with a JASCO V-570 UV-vis spectrophotometer equipped with an integrating sphere accessory. Barium sulfate was used as reference. Photoluminescence measurements were performed by using a CNI MDL-III-980 diode laser as 980 nm photon pumping source, with output power of 2W over a spot of 5×8 mm^2 (power density of 5 W/cm^2). PL Emission spectra were acquired by means of a QE65 Pro Ocean Optics spectrometer.

References

1. F. Hoffmann, M. Cornelius, J. Morell and M. Fröba. Silica-based mesoporous organic-inorganic hybrid materials. *Angew. Chem. Int. Ed.* **2006**, 45, 3216-3251.

2. S.H. Joo, J.Y. Park, C.-K. Tsung, Y. Yamada, P. Yang and G.A. Somorjai. Thermally stable Pt/mesoporous silica core/shell nanocatalysts for high-temperature reactions. *Nat. Mater.* **2009**, 8, 126-131.

3. C. Rudolf, F. Abi-Ghaida, B. Dragoi, A. Ungureanu, A. Mehdi and E. Dumitriu. An efficient route to prepare highly dispersed metallic copper nanoparticles on ordered mesoporous silica with outstanding activity for hydrogenation reactions. *Catal. Sci. Technol.* **2015**, 5, 3735-3745.

4. D. Shen, L. Chen, J. Yang, R. Zhang, Y. Wei, X. Li, W. Li, Z. Sun, H. Zhu, A.M. Abdullah, A. Al-Enizi, A.A. Elzatahry, F. Zhang and D. Zhao. Ultradispersed palladium nanoparticles in three-dimensional dendritic mesoporous silica nanospheres: towards active and stable heterogeneous catalysts. *ACS Appl. Mater. Interfaces* **2015**, 7, 17450-17459.

5. Y. Chen and J. Shi. Chemistry of mesoporous organosilica in nanotechnology: molecularly organic-inorganic hybridisation into frameworks. *Adv. Mater.* **2016**, 28, 3235-3272.

6. P. Baglioni, E. Carretti and D. Chelazzi. Nanomaterials in art conservation. *Nat. Nanothechnol.* **2015**, 10, 287-290.

7. P. Baglioni and D. Chelazzi. Nanoscience for the conservation of works and art. The Royal Society of Chemistry, **2013**.

8. Q. He and J. Shi. Mesoporous silica nanoparticle based nano drug delivery systems: synthesis, controlled drug release and delivery, pharmacokinetics and biocompatibility. *J. Mater. Chem.* **2011**, 21, 5845-5855.

9. Z. Li, J.C. Barnes, A. Bosoy, J.F. Stoddart and J.I. Zink. Mesoporous silica nanoparticles in biomedical applications. *Chem. Soc. Rev.* **2012**, 41, 2590-2605.

10. N. Hao, L. Li and F. Tang. Shape matters when engineering mesoporous silica-based nanomedicines. *Biomater. Sci.* **2016**, 4, 575-591.

11. M. Bouchoucha, M.-F. Côté, R. C.-Gaudreault, M.-A. Fortin and F. Kleitz. Size-controlled functionalized mesoporous silica nanoparticles for tunable drug release and enhanced anti-tumoral activity. *Chem. Mater.* **2016**, 28, 4243-4258 .

12. I.I. Slowing, B.G. Trewyn, S. Giri and V.S.-Y. Lin. Mesoporous silica nanoparticles for drug delivery and biosensing applications. *Adv. Funct. Mater.* **2007**, 17, 1225-1236.

13. B.J. Melde, B.J. Johnson and P.T. Charles. Mesoporous silicate materials in sensing. *Sensors* **2008**, 8, 5202-5228.

14. J. Lei, L. Wang and J. Zhang. Ratiometric pH sensor based on mesoporous silica nanoparticles and Förster resonance energy transfer. *Chem. Comm.* **2010**, 46, 8445-8447.

15. K.W. Shah, T. Sreethawong, S.-H. Liu, S.-Y. Zhang, L.S. Tan and M.-Y. Han. Aqueous route to facile, efficient and functional silica coating of metal nanoparticles at room temperature. *Nanoscale* **2014**, 6, 11273-11281.

16. G.A. Sotiriou, T. Sannomiya, A. Teleki, F. Krumeich, J. Vörös and S.E. Pratsinis. Non-toxic dry-coated nanosilver for plasmonic biosensors. *Adv. Funct. Mater.* **2010**, 20, 4250-4257.

17. B.D. Anderson, W.-C. Wu and J.B. Tracy. Silica overcoating of CdSe/CdS core/shell quantum dot nanorods with controlled morphologies. *Chem. Mater.* **2016**, 28, 4945-4952.

18. M.K. Gnanasammandhan, N.M. Idris, A. Bansal, K. Huang and Y. Zhang. Near-IR photoactivation using mesoporous silica-coated $NaYF_4$:Yb,Er/Tm upconversion nanoparticles. *Nat. Protoc.* **2016**, 11, 688-713.

19. J.-N. Liu, W.-B. Bu and J.-L. Shi. Silica coated upconversion nanoparticles: A versatile platform for the development of efficient theranostics. *Acc. Chem. Res.* **2015**, 48, 1797-1805.

20. R. Mohan. Green bismuth. *Nat. Chem.* **2010**, 2, 336.

21. A.B. Seabra and N. Durán. Nanotoxicology of metal oxide nanoparticles. *Metals* **2015**, 5, 934-975.

22. H. Suzuki and Y. Matano. Organobismuth Chemistry. Ed. 1, Elsevier, Amsterdam, **2001**.

23. G.G. Briand and N. Burford. Bismuth compounds and preparations with biological or medicinal relevance. *Chem. Rev.* **1999**, *99*, 2601.

24. P. Riente, A. Matas Adams, J. Albero, E. Palomares and M.A. Pericàs. Light-driven organocatalysis using inexpensive, nontoxic Bi_2O_3 as the photocatalyst. *Angew. Chem. Int. Ed.* **2014**, *53*, 9613.

25. O. Rabin, J.M. Perez, J. Grimm, G. Wojtkiewciz and R. Weissleder. An X-ray computed tomography imaging agent based on long-circulating bismuth sulphide nanoparticles. *Nat. Mater.* **2006**, 5, 118-122.

26. K. Ai, Y. Liu, J. Liu, Q. Yuan, Y. He and L. Lu. Large-scale synthesis of Bi_2S_3 nanodots as a contrast agent for in vivo X-ray computed tomography imaging. *Adv. Mater.* **2011**, 23, 4886-4891.

27. X. Zheng, J. Shi, Y. Bu, G. Tian, X. Zhang, W. Yin, B. Gao, Z. Yang, Z. Hu, X. Liu, L. Yan, Z. Gu and Y. Zhao. Silica-coated bismuth sulphide nanorods as multimodal contrast agents for a non-invasive visualization of the gastrointestinal tract. *Nanoscale* **2015**, 7, 12581-12591.

28. J. de Swart, H.S. Chan, M.C. Goorden, A. Morgenstern, F. Bruchertseifer, F.J. Beekman, M. de Jong and M.W. Konijnenberg. Utilizing high-energy γ-photons for high-resolution ^{213}Bi SPECT in mice. *J. Nucl. Med.* **2016**, 57, 486-492.

29. T. Maeder. Review of Bi_2O_3 based glasses for electronics and related applications. *Int. Mater. Rev.* **2013**, 58, 3-40.

30. Y.T. Fei, S.J. Fan, R.Y. Sun, J.Y. Xu and M. Ishii. Crystallizing behaviour of Bi_2O_3-SiO_2 system. *J. Mater. Sci. Lett.* **2000**, 19, 893-895.

31. F. Yiting, F. Shiji, S. Renying and M. Ishii. Study on phase diagram of Bi_2O_3-SiO_2 system for Bridgman growth of $Bi_4Si_3O_{12}$ single crystal. *Prog. Cryst. Growth Charact. Mater.* **2000**, 40, 183-188.

32. V.P. Zhereb and V.M. Skorikov. Metastable states in bismuth-containing oxide systems. *Inorg. Mater.* **2003**, 39, S121-S145.

33. H.W. Guo, X.F. Wang and D.N. Gao. Non-isothermal crystallization kinetics and phase transformation of Bi2O3-SiO2 glass-ceramics. *Sci. Sinter.* **2011**, 43, 352-362.

34. M. Todea, R.V.F. Turcu, M. Vasilescu, D.L. Trandafir and S. Simon. Structural characterization of heavy metal SiO_2-Bi_2O_3 glasses and glass-ceramics. *J. Non-Cryst. Solids* **2016**, 432, 271-276.

35. L.G. Sillén. X-ray studies on bismuth trioxide. *Ark. Kemi. Mineral. Geol.* **1937**, 12A, 1-15.

36. B. Aurivillius and L.G. Sillén. Polymorphy of Bi_2O_3. *Nature* **1945**, 155, 305-306.

37. G. Gattow and H. Schroder. Über Wismutoxide. III. Die Kristallstruktur der Hochtemperaturmodifikation von Wismut(III)-oxid (δ-Bi_2O_3). *Z. Anorg. Allg. Chem.* **1962**, 318, 176-189.

38. M. Weber, M. Schlesinger and M. Mehring. Evaluation of synthetic methods for bismuth(III) oxide polymorphs: formation of binary versus ternary oxides. *Cryst. Growth Des.* **2016**, 16, 5678-5688.

39. Y. Wang, R. He, M. Yang, T. Wen, H. Zhao, J. Liang, Z. Lin, Y. Wang, G. Li and J. Lin. Hydrothermal growths, optical features and first-principles calculations of sillenite-type crystals comprising discrete MO_4 tetrahedra. *Cryst. Eng. Comm.* **2012**, 14, 1063-1068.

40. K. Nakagawa, N. Kajita, J. Chen and T. Minemoto. Measurement of the electrogyratory coefficient in photorefractive $Bi_{12}SiO_{20}$ crystal. *J. Appl. Phys.* **1991**, 69, 954.

41. J. Ricardo, M. Muramatsu, F. Palácios, M.R.R. Gesualdi, J.L. Valin and M.A. Prieto Lopez. Digital holographic microscopy with photorefractive sillenite $Bi_{12}SiO_{20}$ crystals. *Opt. Lasers Eng.* **2013**, 51, 949-952.

42. I. Biaggio, R.W. Hellwarth and J.P. Partanen. Band mobility of photoexcited electrons in $Bi_{12}SiO_{20}$. *Phys. Rev. Lett.* **1997**, 78, 891-894.

43. P. Myrthili, T. Kanagasekaran, G. Bhagavannarayana and R. Gopalakrishnan. Studies on crystal growth, optical and electrical characterization of pure and Dy-doped bismuth silicate single crystals. *J. Cryst. Growth* **2012**, 338, 222-227.

44. A.C. Lira, U. Caldiño, M.O. Ramírez, J.A. Sanz-García and L.E. Bausá. Site-selective spectroscopy of Er^{3+} ions in the $Bi_{12}SiO_{20}$ piezoelectric crystal. *J. Phys.: Condens. Matter* **2001**, 13, 11067-11076.

45. Y. Hu and D.C. Sinclair. Relaxor-like dielectric behaviour in stoichiometric sillenite $Bi_{12}SiO_{20}$. *Chem. Mater.* **2013**, 25, 48-54.

46. D. Hou, X. Hu, Y. Wen, B. Shan, P. Hu, X. Xiong, Y. Qiao and Y. Huang. Electrospun sillenite $Bi_{12}MO_{20}$ (M=Ti, Ge, Si) nanofibers: general synthesis, band structure, and photocatalytic activity. *Phys. Chem. Chem. Phys.* **2013**, 15, 20698-20705.

47. Q. Han, J. Zhang, X. Wang and J. Zhu. Preparing $Bi_{12}SiO_{20}$ crystals at low temperature through nontopotactic solid-state transformation and improving its photocatalytic activity by etching. *J. Mater. Chem. A* **2015**, 3, 7413-7421.

48. M. Kobayashi, M. Ishii, K. Harada and I. Yamaga. Bismuth silicate $Bi_4Si_3O_{12}$, a faster scintillator than bismuth germinate $Bi_4Ge_3O_{12}$. *Nucl. Instr. Meth. Phys. Res.* **1996**, 372, 45-50.

49. X. Jiayue, Y. Bobo and Z. Yan. Development of doped $Bi_4Si_3O_{12}$ crystals for scintillation, laser and LED applications. *Mater. Focus* **2015**, 4, 20-27.

50. F. Yiting, S. Renying, F. Shiji and X. Jiayue. Vertical Bridgman growth and scintillation properties of doped $Bi_4Si_3O_{12}$ crystals. *Cryst. Res. Technol.* **1999**, 34, 1149-1156.

51. A.C. Lira, I. Camarillo, E. Camarillo, F. Ramos, M. Flores and U. Caldiño. Spectroscopic characterization of Er^{3+} transitions in $Bi_4Si_3O_{12}$. *J. Phys.: Condens. Matter* **2004**, 16, 5925-5936.

52. A.C. Lira, M.O. Ramírez, J. García Solé and U. Caldiño. Photoluminescence of $Bi_4Si_3O_{12}$:Er^{3+} crystal excited in the commercial laser diode emission region. *Opt. Mater.* **2007**, 29, 605-609.

53. A.C. Lira, E. Martín-Rodríguez, R. Martínez-Martínez, I. Camarillo, G.H. Muñoz, J. García Solé and U. Caldiño. Spectroscopy of the $Bi_4Si_3O_{12}$:Er^{3+} glass for optical amplification and laser application. *Opt. Mater.* **2010**, 32, 1266-1273.

54. B. Yang, J. Xu, Y. Zhang, Y. Chu, M. Wang and Y. Wen. A yellow emitting phosphor Dy:$Bi_4Si_3O_{12}$ crystal for LED application. *Opt. Mater.* **2014**, 135, 176-179.

55. Q. Wei, G. Liu, Z. Zhou, J. Wan, J. Wang and Q. Liu. Combinatorial discovery of self-mixing phosphors $Bi_{4(1-x)}Si_3O_{12}$;RE_{4x}^{3+} (RE^{3+}=Dy^{3+}, Eu^{3+}) for direct white light emission. *RSC Adv.* **2015**, 5, 85862-85871.

56. L. Sun, F. Gao and Q. Huang. White upconversion photoluminescence for Er^{3+}-Tm^{3+}-Yb^{3+} tri-codoped bismuth titanate ferroelectric thin films. *J. Alloys Compd.* **2014**, 588, 158-162.

57. T. Wei, T.B. Zhang, Y.J. Ma, Y. F. Xie, C.Z. Zhao, F.M. Yang, H.Y. Xiao and Y. Zhao. Up-conversion photoluminescence and temperature sensing properties of Er^{3+}-doped $Bi_4Ti_3O_{12}$ nanoparticles with good water-resistance performance. *RSC Adv.* **2016**, 6, 7643-7652.

58. M. Yamaguchi, K. Hiraki, T. Nagatomo and Y. Masuda. Preparation and properties of Bi_2SiO_5/Si structures. *Jpn. J. Appl. Phys.* **2000**, 39, 5512-5516.

59. M. Yamagushi, K. Hiraki, T. Homma, T. Nagatomo and Y. Masuda. Fabrication and properties of Bi_2SiO_5 thin films for MFIS structures. *IEEE Int. Symp. Appl. Ferroelectrics* **2001**, 629-632.

60. H. Taniguchi, A. Kuwabara, J. Kim, Y. Kim, H. Moriwake, S. Kim, T. Hoshiyama, T. Koyama, S. Mori, M. Takata, H. Hosono, Y. Inaguma and M. Itoh. Ferroelectricity driven by twisting of silicate tetrahedral chains. *Angew. Chem. Int. Ed.* **2013**, 52, 8088-8092.

61. Y. Kim, J. Kim, A. Fujiwara, H. Taniguchi, S. Kim, H. Tanaka, K. Sugimoto, K. Kato, M. Itoh, H. Hosono and M. Takata. Hierarchical dielectric orders in layered ferroelectrics Bi_2SiO_5. *IUCrJ* **2014**, 1, 160-164.

62. H. Taniguchi, T. Nakane, T. Nagai, C. Moriyoshi, Y. Kuroiwa, A. Kuwabara, M. Mizumaki, K. Nitta, R. Okazaki and I. Terasaki. Heterovalent Pb-substitution of ferroelectric bismuth silicate Bi_2SiO_5. *J. Mater. Chem. C* **2016**, 4, 3168-3174.

63. D. Seol, H. Taniguchi, J.-Y. Hwang, M. Itoh, H. Shin, S.W. Kim and Y. Kim. Strong anisotropy of ferroelectricity in lead-free bismuth silicate. *Nanoscale* **2015**, 7, 11561-11565.

64. R. Chen, J. Bi, L. Wu, W. Wang, Z. Li and X. Fu. Template-free hydrothermal synthesis and photocatalytic performances of novel Bi_2SiO_5 nanosheets. *Inorg. Chem.* **2009**, 48, 9072-9076.

65. X.-J. Dai, Y.-S. Luo, S.-Y. Fu, W.-Q. Chen and Y. Lu. Facile hydrothermal synthesis of 3D hierarchical Bi_2SiO_5 nanoflowers and their luminescent properties. *Solid State Sci.* **2010**, 12, 637-642.

66. L. Zhang, W. Wang, S. Sun, J. Xu, M. Shang and J. Ren. Hybrid Bi_2SiO_5 mesoporous microspheres with light response for environment decontamination. *Appl. Catal. B: Environ.* **2010**, 100, 97-101.

67. J. Duan, Y. Liu, X. Pan, Y. Zhang, J. Yu, K. Nakajim and H. Taniguchi. High photodegradation efficiency of Rhodamine B catalysed by bismuth silicate nanoparticles. *Catal. Commun.* **2013**, 39, 65-69.

68. W. Wei and J. Xie. Synthetic bismuth silicate nanostructures: photocatalysts grown from silica aerogels precursors. *J. Mater. Res.* **2013**, 28, 1658-1668.

69. D. Liu, J. Wang, M. Zhang, Y. Liu and Y. Zhu. A superior photocatalytic performance of a novel Bi_2SiO_5 flower-like microsphere *via* a phase junction. *Nanoscale* **2014**, 6, 15222-15227.

70. Z.-A. Qiao, L. Zhang, M. Guo, Y. Liu and Q. Huo. Synthesis of mesoporous silica nanoparticles via controlled hydrolysis and condensation of silicon alkoxide. *Chem. Mater.* **2009**, 21, 3823-3829.

71. F. Rouquerol, J. Rouquerol and K. Sing. Adsorption by powder & porous solids. Principles, methodology and applications. Academic Press, London, (1999) Ch. 1, pp 19.

72. G. Guenther, R. Theissmann and O. Guillon. Size-dependent phase transformations in bismuth oxide nanoparticles. II. Melting and stability diagram. *J. Phys. Chem. C* **2014**, 118, 27020-27027.

73. J.C. Dyre. *Colloquium*: The glass transition and elastic models of glass-forming liquids. *Rev. Mod. Phys.* **2006**, 78, 953-971.

74. M.I. Ojovan. Viscosity and glass transition in amorphous oxides. *Adv. Condens. Matter Phys.* **2008**, 2008, 1-23.

75. R. P. W. Scott. Silica gel and bonded phases. Their production, properties and use in LC. Wiley Science, New York, 1993.

76. X. Feng, X. Qi, J. Li, L. Yang, M. Qiu, J. Yin, F. Lu and J. Zhong. Preparation, structure and photo-catalytic performances of hybrid Bi_2SiO_5 modified Si nanowire arrays. *Appl. Surf. Sci.* **2011**, 257, 5571-5575.

77. S. Simon and M. Todea. Spectroscopic study on iron doped silica-bismuthate glasses and glass ceramics. *J. Non-Cryst. Solids* **2006**, 352, 2947-2951.

78. R. Oberschmid. Absorption centers of $Bi_{12}GeO_{20}$ and $Bi_{12}SiO_{20}$ crystals. *Phys. Stat. Sol. (a)* **1985**, 89, 263-270.

79. G. Cheng, J. Xiong, H. Yang, Z. Lu and R. Chen. Facile solvothermal synthesis of uniform sponge-like Bi2SiO5 hierarchical nanostructure and its application in Cr(VI) removal. *Mater. Lett.* **2012**, 77, 25-28.

80. A. Kuwabara, H. Taniguchi, H. Moriwake and M. Itoh. First-principles calculations of ferroelectric inosilicate Bi_2SiO_5. *AMTC* **2016**, 4, 69.

81. A.N. Christensen, T.R. Jensen, N.V.Y. Scarlett, I.C. Madsen, J.C. Hanson and A. Altomare. *In-situ* X-ray powder diffraction studies of hydrothermal and thermal decomposotion reactions of basic bismuth(III) nitrates in the temperature range 20-650 °C. *Dalton Trans.* **2003**, 16, 3278-3282.

82. Z. Bai, X. Ba, R. Jia, B. Liu, Z. Xiao and X. Zhang. Preparation and characterization of bismuth silicate nanopowders. *Front. Chem. China* **2007**, 2, 131-134.

83. A. Pullanchiyodan and K.P. Surendran. Formulation of sol-gel bismuth silicate dielectric ink for flexible electronics applications. *Ind. Eng. Chem. Res.* **2016**, 55, 7108-7115.

84. P. Riello. Quantitative analysis of amorphous fraction in the study of the microstructure of semi-crystalline materials. In E.J. Mittemeijer and P. Scardi Eds. *Diffraction Analysis of the Microstructure of Materials*. Springer Berlin Heidelberg, 2004, pp. 167-184.

85. M.A. Ballem, F. Söderlind, P. Nordblad, P.-O. Käll and M. Odén. Growth of Gd_2O_3 nanoparticles inside mesoporous silica frameworks. *Micropor. Mesopor. Mater.* **2013**, 168, 221-224.

86. C. Huo, J. Ouyang and H. Yang. CuO nanoparticles encapsulated inside Al-MCM-41 mesoporous materials via direct synthetic route. *Sci. Rep.* **2014**, 4, 3682.

87. A. Parma, I. Freris, P.Riello, D. Cristofori, C. de Julián Fernández, V. Amendola, M. Meneghetti and A. Benedetti. *J. Mater. Chem.* **2012**, 22, 19276-19288.

88. S. Li, Q. Wan, Z. Qin, Y. Fu and Y. Gu. Understanding Stöber silica's pore characteristics measured by gas adsorption. *Langmuir* **2015**, 31, 824-832.

89. S. Li, Q. Wan, Z. Qin, Y. Fu and Y. Gu. Unraveling the mystery of Stöber silica's microporosity. *Langmuir* **2016**, 32, 9180-9187.

90. S.R. Parnell, A.L. Washington, A.J. Parnell, A. Walsh, R.M. Dalgliesh, F. Li, W.A. Hamilton, S. Prevost, J.P.A. Fairclough and R. Pynn. Porosity of silica Stöber particles determined by spin-echo small angle neutron scattering. *Soft Matter* **2016**, 12, 4709-4714.

91. A Kuwabara, H. Taniguchi, H. Moriwake and M. Itoh. First-principles calculations of ferroelectric inosilicate Bi_2SiO_5. *AMTC5* **4**, 69 (2016)

92. J. Park, B.G. Kim, S. Mori and T. Oguchi. Tetrahedral tilting and ferroelectricity in Bi_2AO_5 (A=Si, Ge) from first principles calculations. *J. Solid State Chem.* **2016**, 235, 68-75.

93. P. Riello, A. Lausi, J. Macleaod, J.R. Plaisier, G. Zeraushek and P. Fornasiero. In situ reaction furnace for real-time XRD studies. *J. Synchrotron Rad.* **2013**, 20, 194-196.

CHAPTER 6

Cr^{3+}-doped $Bi_2Ga_4O_9$: Ratiometric Optical Thermometer Based on Dual NIR Emission

Abstract Detailed spectroscopic analysis of the electronic configuration of Cr^{3+} in $Bi_2Ga_4O_9$ is reported. The material exhibits unique luminescent properties arising from the crystal field experienced by Cr^{3+}, with simultaneous strong sharp and broadband near-infrared emissions from the ^2E and $^4T_2$ excited states, in a wide range of temperature. The system displays dual near-infrared emission with attractive maximum thermal sensitivity of $0.7\%\cdot K^{-1}$ in the physiological temperature range. Moreover, the possibility to absorb and emit in the first biological window, allows to consider the system as a new promising candidate for ratiometric fluorescent thermal sensing in biotechnological applications.

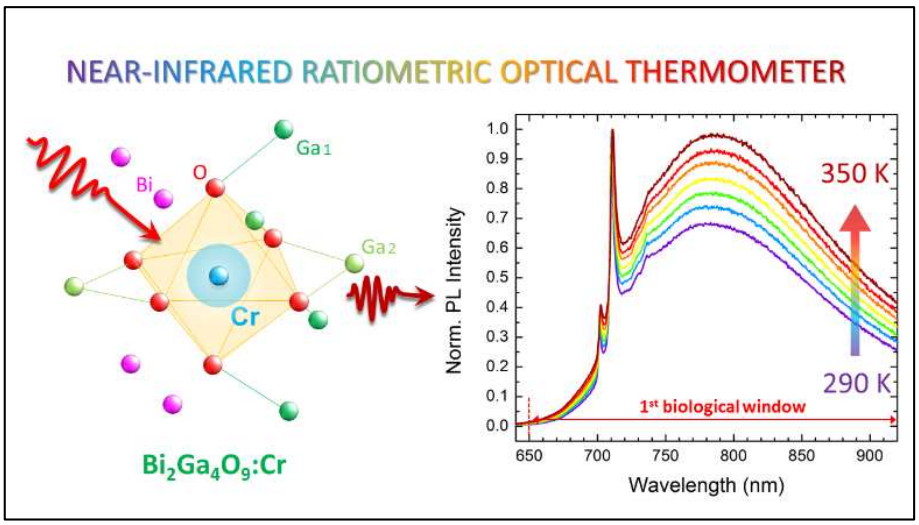

6.1 Introduction

Temperature is a fundamental thermodynamic parameter that plays a critical role in controlling many biological and technological processes. Ratiometric optical thermometry based on fluorescence intensity ratio (FIR) method is recently emerged as useful noninvasive technique with unique advantages ranging from high spatial resolution and detection sensitivity to rapid response, opening new possibilities for the comprehension of the rules governing the processes in biological fluids and fast objects.[1-5] Hence, the design of new materials with suitable luminescent properties for ratiometric optical thermal sensing has become an active research area.

As reported by E.J. McLaurin *et al.*,[2] dual-emitting thermal sensors may be categorized in three main types by the strength of the electronic coupling governing population transfer between the two emissive excited states: (i) decoupled, (ii) moderately coupled and (iii) strongly coupled. In the case of decoupled luminescent excited states, nonspecific environmental factors may change differently the PL behaviour of the two luminophores, strongly limiting the accuracy of the measurements. Similarly, even if electronically coupled, in a donor-acceptor pair the concentration dependence of the luminescence output via energy transfer may affect the thermal response. On the other hand, systems characterized by two excited states in thermal equilibrium (strongly thermodynamically coupled) are highly selective for temperature because, in the case of environmental factors affecting the overall quantum yield, the same Boltzmann PL intensity distribution is ensured by fast population renormalization.[2] In this view, an ideal FIR technique-based ratiometric optical thermometer for biological applications consists of a single-doped material with two thermally-coupled excited states that may be excited and emit in the biological optical windows, where both tissue absorption and scattering are minimized.[6-9]

Among the great variety of luminescent materials proposed in the last decade as optical thermometers, lanthanide-based systems have been extensively explored[10] considering Yb-Er upconverting nanoparticles,[11-13] Eu single-doped[14] and Tb-Eu pair-based systems,[15-18] or Dy,[19,20] Pr and Tb doped materials.[21] However, among the single-doped materials, up to now, only Nd^{3+} doped systems[22-26] seem to meet the requirements to both absorb and emit in the biological window.

The possibility to tune and control the position and the relative intensity of the sharp $^2E \rightarrow {}^4A_2$ and the broadband $^4T_2 \rightarrow {}^4A_2$ transitions in the Cr^{3+}-doped materials, designing the host properties, lead to a great interest in the scientific community. The discovery of the first laser (the ruby laser) in 1960 by T.H. Maiman,[27] gave a big boost in the development of Cr^{3+}-based materials and, more recently, a renewed interest in the design of Cr^{3+}-based luminescent materials originated from the crucial role of chromium in persistent luminescent materials, working as an electron trap and/or luminescent centre.[28-34] Owing to the peculiar near-infrared (NIR) emissions coming from the $3d^3$ electronic configuration of Cr^{3+}, many efforts were devoted to the design of chromium-based thermal sensors. However, single-transition Cr^{3+}-based materials have been mainly considered[35-41] allowing the study of the thermal response by means of temperature dependence of lifetimes, with strong limitation from the practical point of view.

In this Chapter, we report a spectroscopic investigation on Cr^{3+}-doped $Bi_2Ga_4O_9$ mullite system, demonstrating its potentialities as rational optical thermal sensor arising from the peculiar crystal

field experienced by Cr^{3+} in this host. The reliability of the description of electronic configuration of Cr^{3+} in $Bi_2Ga_4O_9$ is supported by the consistency between the experimental and theoretical results. This new self-referencing thermometer is the first example of FIR technique based Cr^{3+}-single-doped thermal sensor. The variation of the luminescent intensity ratio from the $^4T_2$ and ^2E states allowed absolute measurements in the 77-450 K temperature range, with a relative temperature sensitivity up to $0.7\%\cdot K^{-1}$ in the physiological temperature range. Moreover, for the best of our knowledge, this is the first non-lanthanide based material used as ratiometric luminescent thermometer characterized by the possibility to both absorb and emit in the first optical window of biological tissue.

6.2 Sample Preparation

Un-doped $Bi_2Ga_4O_9$ (BG) and Cr^{3+}-doped $Bi_2Ga_{3.97}O_9:Cr_{0.03}$ (BG-Cr) samples were prepared by solid-state reaction method. The chemical reagents Bi_2O_3 (4N), Ga_2O_3 (4N) and Cr_2O_3 (4N) were used as starting materials, grounded in an alumina mortar to form homogeneous fine powder mixtures and pressed into pellets (0.6 g, ϕ 15 mm) with a uniaxial loading of 50 MPa in a stainless steel mold. Then, the pellets were fired at 950 °C for 6 h in air atmosphere.

6.3 Structural Analysis

The XRD pattern of the un-doped BG and Cr-doped BG-Cr samples in Figure 6.1a evidences the stabilization of a single crystalline phase, corresponding to the orthorhombic $Bi_2Ga_4O_9$ phase (space group *Pbam*, JCPDS 01-072-1833). This phase belongs to the family of mullite-type structures and is characterized by octahedral GaO_6 chains linked by tetrahedral Ga_2O_7 dimers and by highly asymmetric BiO_3 groups (Figure 6.1b). Moreover, in this compound the Bi $6s^2$ lone pair electrons (LP) are stereochemically active.[42]

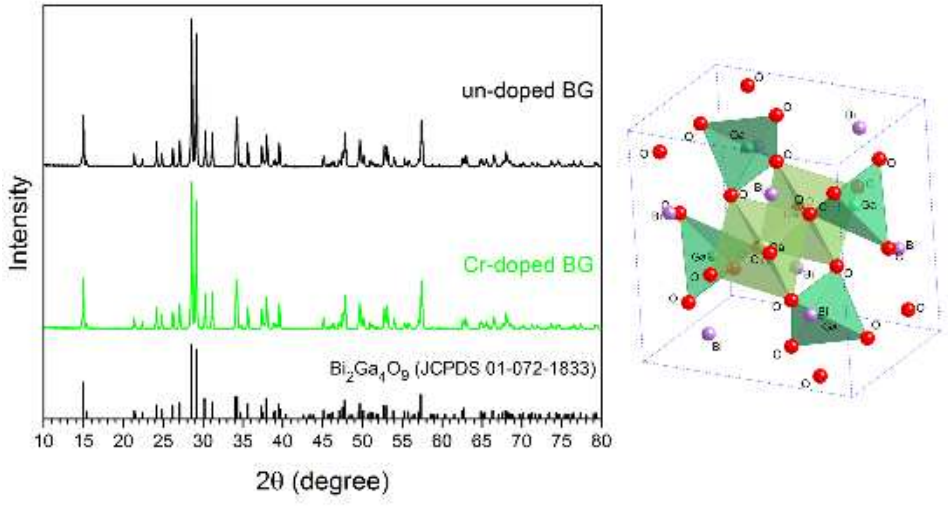

Figure 6.1 X-ray diffraction spectra of BG and BG-Cr samples and crystalline mullite-type structure of $Bi_2Ga_4O_9$.

6.4 Optical Properties and Crystal Field Analysis: Tanabe-Sugano Diagram

It is well known that the electronic states due to the 3*d* electrons of the outer shell of the transition metal ions are strongly affected by the nearest environment. In particular, when a transition metal ion, like Cr^{3+}, is incorporated in an octahedral site (O_h crystal field), the energy level splitting can be expressed by the Tanabe-Sugano diagram[43] and the energy level configuration can uniquely be described by considering three key spectroscopic parameters: the crystal field strength *Dq* and the two Racah parameters *B* and *C*.

In order to reliably estimate the parameters describing the Cr^{3+} properties in this host (e.g. Racah parameters *B* and *C*, 10*Dq* and *Dq*/*B*) and thus analyze the crystal field effect designing the Tanabe-Sugano diagram for Cr^{3+} ion in the octahedral site, we consider the conversion of the spectra to the energy scale, converting the emission spectrum from photon flux per constant wavelength interval to photon flux per constant energy interval by means of the conversion formula $\frac{d\phi(E)}{dE} \propto \frac{d\phi(\lambda)}{d\lambda}\lambda^2$.[44]

Figure 6.2a shows the diffuse reflectance spectra of BG and BG-Cr samples. The introduction of Cr^{3+} in the octahedral Ga^{3+} site is responsible for the change of colour from slight yellow (un-doped sample BG) to green (Cr-doped sample) as observed in the pictures of Figure 6.2a. The spectrum of BG-Cr is composed of two main absorption bands in the visible range due to the allowed transitions of Cr^{3+} (mainly $^4A_2 \rightarrow {}^4T_2$ and $^4A_2 \rightarrow {}^4T_1$). Moreover, the strong absorptions from the $^4A_2 \rightarrow {}^2E$ *R*-lines are also detected. From the diffuse reflectance analysis, considering the Kubelka-Munk function[45] and the Tauc plot,[46] an optical bandgap of 2.83±0.04 eV is estimated for BG (see Figure 6.2b), in agreement with the theoretical value of 2.86 eV reported in literature.[47]

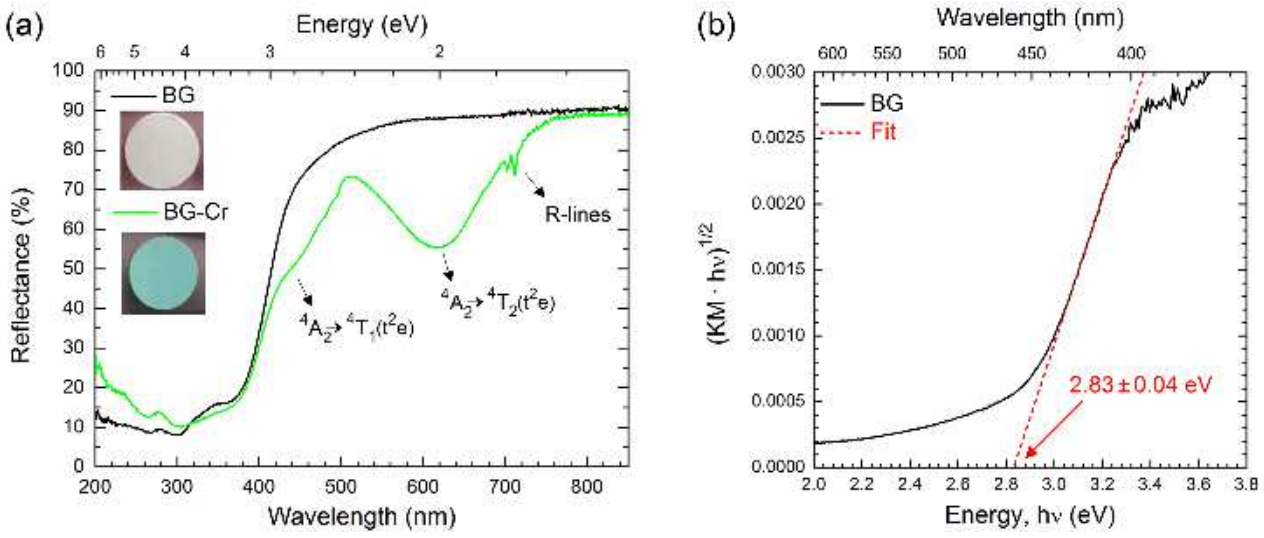

Figure 6.2 Diffuse reflectance spectra of BG and BG-Cr samples with pictures of the samples (a) and bandgap estimation of $Bi_2Ga_4O_9$ from the Tauc plot of the Kubelka-Munk function (b).

Figure 6.3a displays the photoluminescence emission and excitation spectra of the Cr^{3+} doped sample. The excitation spectrum consists of three main peaks due to the spin-allowed Cr^{3+} *d-d* intra-transitions. The $^4A_2 \rightarrow {}^4T_2(t^2e)$ absorption peak centred at about 625 nm is in good agreement with the peak collected from the diffuse reflectance while the peaks due to the $^4A_2 \rightarrow {}^4T_1(te^2)$ and $^4A_2 \rightarrow {}^4T_1(t^2e)$ absorptions at about 340 nm and 445 nm, respectively, are not clearly detectable in the reflectance spectrum because of the overlap with the absorption edge of the host. The PL emission spectrum is composed by two sharp luminescence lines due to the spin-forbidden $^2E \rightarrow {}^4A_2$ transitions (*R*-lines) at 702 and 710 nm and a broad luminescence band centred at about 800 nm due to the spin-allowed electronic transition from the excited state $^4T_{2g}$ (^4F) to the ground state $^4A_{2g}$ (^4F). The simultaneous presence of both the narrow line emissions from the ^2E_g and the broadband emission from the $^4T_{2g}$ excited state at RT is consistent with a situation of thermal equilibrium between these two states, suggesting an intermediate crystal field splitting. It is notable that the strong broad emission from the $^4T_{2g}$ (^4F) excited state lies in the middle of the first NIR window (the biological window, 650-950 nm) and that the material can be also excited in the same window, proving to be a promising system for the bio-field. Moreover, the emission range well matches the highest sensitivity part of the typical silicon photomultiplier response curve, a critical aspect for the practical use of the NIR emitting materials. In Figure 6.3b the comparison of the emission spectrum of Cr^{3+}-doped BG with ruby is reported to point out the unusual broadening of the $^4T_2 \rightarrow {}^4A_2$ transition.

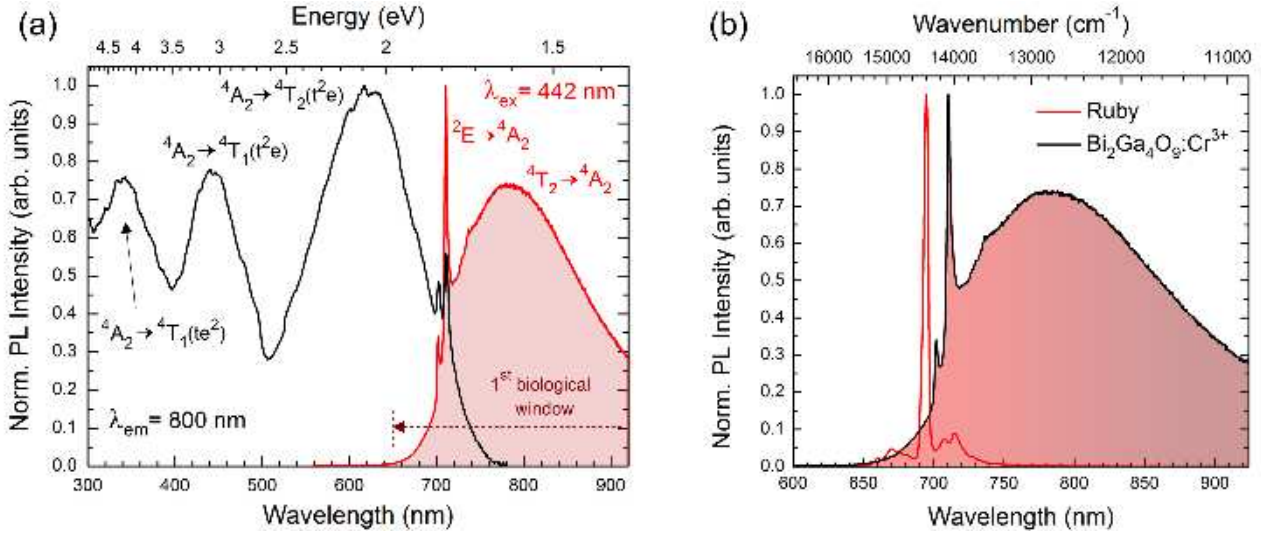

Figure 6.3 (a) PL and PLE spectra of Cr^{3+} doped $Bi_2Ga_4O_9$ at RT, exciting at 442 nm and collecting at 800 nm respectively. (b) Comparison between Cr^{3+}-doped BG and ruby emissions.

10 *Dq*, *B* and *C* parameters can by directly estimated from the position of the excitation and emission bands.[48] As previously discussed, the corrected values for the discussion of the parameters were extrapolated from the energy scale spectra. The energies of the absorption peaks for $^4T_1(t^2e)$, $^4T_2(t^2e)$ and ^2E were estimated to be 22422 cm^{-1}, 15748 cm^{-1} and 14065 cm^{-1} respectively, while the broad emission band due to the $^4T_2(t^2e) \rightarrow {}^4A_2$ transition is centred at 12495 cm^{-1}. *Dq* parameter is directly obtained from the peak energy of the $^4A_2 \rightarrow {}^4T_2$ transition:

$$Dq = \frac{E\left({}^4A_2 \rightarrow {}^4T_2\right)}{10} \tag{6.1}$$

while B and C Racah parameters can be estimated by the following equations:

$$\frac{B}{Dq} = \frac{\left(\Delta E_{4T}/Dq\right)^2 - 10\left(\Delta E_{4T}/Dq\right)}{15\left(\Delta E_{4T}/Dq - 8\right)} \tag{6.2}$$

$$C \cong \frac{E\left({}^2E\right)}{3.05} - \frac{7.90B}{3.05} + \frac{1.8}{3.08}\left(\frac{B^2}{Dq}\right) \tag{6.3}$$

where $\Delta E_{4T} = E\left({}^4T_{1g}\right) - E\left({}^4T_{2g}\right)$, the difference in energy between the $^4T_1$ and $^4T_2$ states. Considering the value of Dq (1574.8 cm^{-1}) and ΔE_{4T} (6674 cm^{-1}) and substituting in the formulas, B, C and Dq/B were estimated to be 681 cm^{-1}, 3019 cm^{-1}, and 2.31 cm^{-1} respectively. As reported in Figure 6.4, the value of Dq/B is in agreement with the previous considerations of intermediate crystal field for Cr^{3+} in $Bi_2Ga_4O_9$. It is important to remember that the value estimated for Dq/B is an average value representative of the crystal field strength for the cation. In fact, in a real system, the crystal field strength consists of a distribution of values reflecting the fluctuation of the cation-anion distance induced by the lattice vibrations, defects and by local variations of the structure.

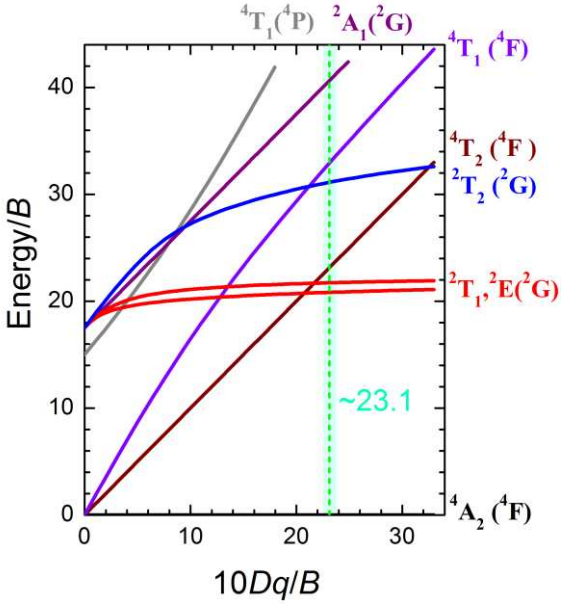

Figure 6.4 (a) Tanabe-Sugano diagram for d^3 ion in octahedral site symmetry with Dq/B (green dashed vertical line) for Cr^{3+} in BG host.

It is interesting to underline that Dq/B and B values of Cr^{3+} in BG are among the lowest and the highest values, respectively, compare to other gallate-based materials (see Table 6.1). These values reflect the particular crystal field surrounding of Cr^{3+} ion in this material. To figure out this behaviour, an insight into the parameters affecting the outer d orbitals is needed. Trueba *et al.*[49] demonstrated that the dominant contribution to the $10Dq$ value comes from the effective small admixture of the antibonding $e_g(\sim x^2\text{-}y^2, z^2)$ orbital with the deep ligands' *s*-orbitals. Instead, the

dominant covalency with valence ligands' *p*-orbitals is responsible for the reduction of Racah parameters. In fact, when a TM ion is introduced into a crystalline solid, the formation of chemical bonds with ligands induces a delocalization of the outer d orbitals (nephelauxetic effect) leading to a d-shell inter-electron repulsion decrease and thus a reduction of the Racah parameters *B* and *C*.

Table 6.1 Cristal field splitting (*Dq*), Racah parameters (*B* and *C*), *Dq*/*B* and energy of the ^{2}E level for Cr^{3+} ion in various gallate-based host.

Compound	*Dq* (cm^{-1})	*B* (cm^{-1})	*C* (cm^{-1})	*Dq*/*B*	E(^{2}E) (cm^{-1})	Ref.
$Ca_3Ga_2Ge_4O_{14}$	1575	761	2811	2.07	14289	50
Ga_2O_3	1667	529	3413	3.15	14286	51
$LaGaO_3$	1914	589	3077	3.25	13713	52
$LaSr_2Ga_{11}O_{20}$	1662	734	2984	2.26	14300	53
$La_{2.32}Lu_{2.61}Ga_{3.07}O_{12}$	1503	412	3751	3.65	14450	54
$La_3Ga_5SiO_{14}$	1695	680	3443	2.49	15366	55
$La_3GaGe_5O_{16}$	1745	654	3124	2.67	14286	56
$La_3Ga_{5.5}Nb_{0.5}O_{14}$	1550	620	3099	2.50	13904	57
$LiGa_5O_{12}$	1694	565	3233	3.00	13982	58
$Y_3Ga_5O_{12}$	1613	651	3214	2.48	14472	59
$ZnGa_2O_4$	1840	553	3461	3.33	14569	60
$Bi_2Ga_4O_9$	1575	681	3019	2.31	14065	This work

To investigate the relationship between the energies of the lowest energy spin-forbidden transition ($^2E_g \rightarrow {}^4A_{2g}$ for d^3 configuration like Cr^{3+}) and covalence of the "metal-ligand" chemical bonds, Brik and co-workers[61] introduced a new parameter, $\beta_1 = \sqrt{\left(\frac{B}{B_0}\right)^2 + \left(\frac{C}{C_0}\right)^2}$, where *B*, *C* and B_0, C_0 are the Racah parameters in crystal and free state, respectively (B_0=918 cm^{-1} and C_0=3850 cm^{-1}). The plot of ^2E_g energy *versus* β_1 for a set of gallate-based hosts shown in Figure 6.5 confirms the reliability of the results for Cr^{3+}-doped $Bi_2Ga_4O_9$. (Table 6.1 summarizes the parameters for the different gallate-based hosts and the references).

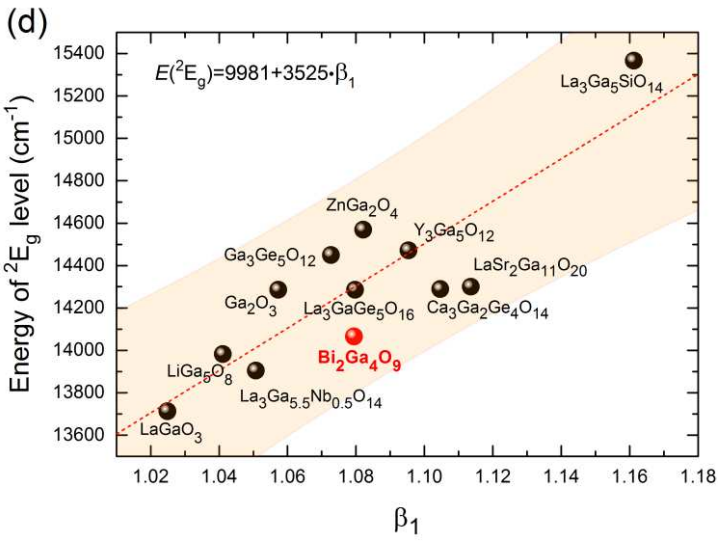

Figure 6.5 Dependence of the ^{2}E level energy on the nephelauxetic ratio β_1 for various gallate-based materials.

6.5 PL Temperature Dependence: Thermal Quenching Process

With the dual aims of analysing the thermal response of Cr^{3+}-doped BG system and investigating in detail the electronic configuration and the parameters describing the coupling with the phonon lattice, the temperature dependent PL emission spectra were analyzed. The spectra reported in Figure 6.6a show the strong thermal quenching of the system at the increasing of the temperature. In order to emphasize the temperature dependence of the emission spectral shape, the PL spectra were normalized to the *R*-line, labelled as R_1 (Figure 6.6b). The trend evidences a strong increase of the broad emission from $^4T_2$ respect to the spin-forbidden *R*-line emission at the increase of the temperature, suggesting a thermally activated process between the excited states.

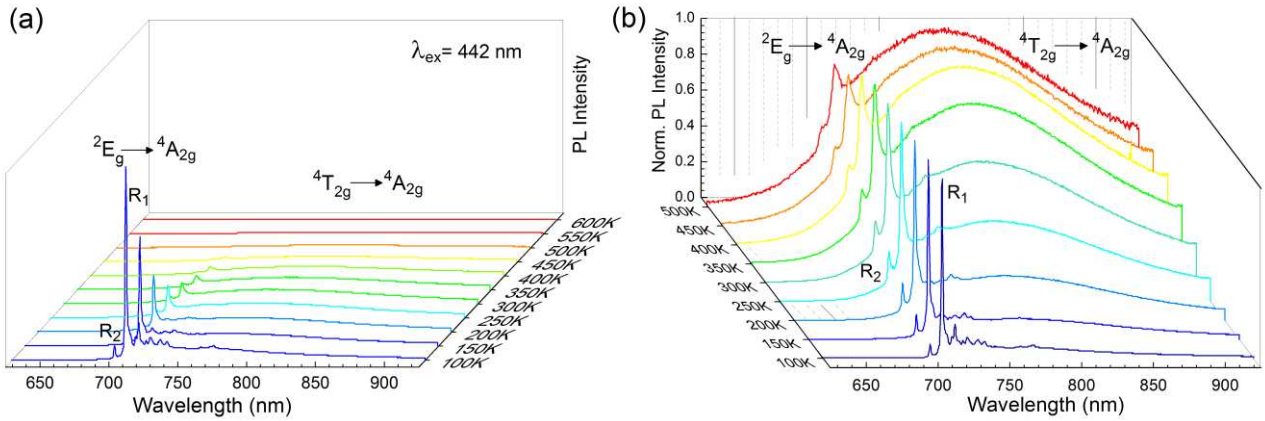

Figure 6.6 Temperature dependence of PL spectra (a) and temperature dependence of PL emission spectra, normalized to the ^2E *R*-line (b).

The intrinsic anharmonic phonon behaviour of $Bi_2Ga_4O_9$ [62] does not allow a clear interpretation of the vibronic progressions in the low temperature spectra. In fact, the coupling of the electronic transitions with different vibrational modes induces the overlap of the vibrationally excited state progressions resulting in a phonon sideband of difficult interpretation. To analyze the temperature dependence of the excited states ^2E and $^4T_2$ individually, the spectra were deconvoluted. The peaks were deconvoluted with Gaussian functions and all the transitions from the ^2E excited state (the sharp emissions from the zero phonon line and from the phonon sideband) were deconvoluted with the same full width at half maximum FWHM, at each temperature. Figure 6.7 shows the deconvolution of the spectra at 100 and 450 K as example.

Figure 6.7c shows the temperature dependence of the integrated PL intensity, derived from the deconvolution of the spectra, for both $^2E \rightarrow {}^4A_2$ and $^4T_2 \rightarrow {}^4A_2$ transitions. From the trend of the $^4T_2$ integrated PL intensity, the quenching temperature T_{50} (temperature at which the intensity become the 50% of that one at low temperature) is estimated to be 450 K. The activation energy for the thermal quenching process is calculated according to the single barrier model:

$$I(T) = \frac{I_0}{1 + (\Gamma_0/\Gamma_v)exp(-E/kT)} \tag{6.4}$$

where I is the PL intensity, Γ_v the radiative rate, Γ_0 the attempt rate of the non-radiative process, E the activation energy, k the Boltzmann constant and T the temperature. The activation energy for the thermal quenching process of the $^4T_2$ excited state $\Delta E_{^4T_2}$ is estimated to be 3431 cm^{-1}. In contrast, the trend of the ^2E excited state evidences a continuous decrease with increasing temperature but, at low temperature, it does not reach a plateau, suggesting the existence of a quenching process at very low temperature.

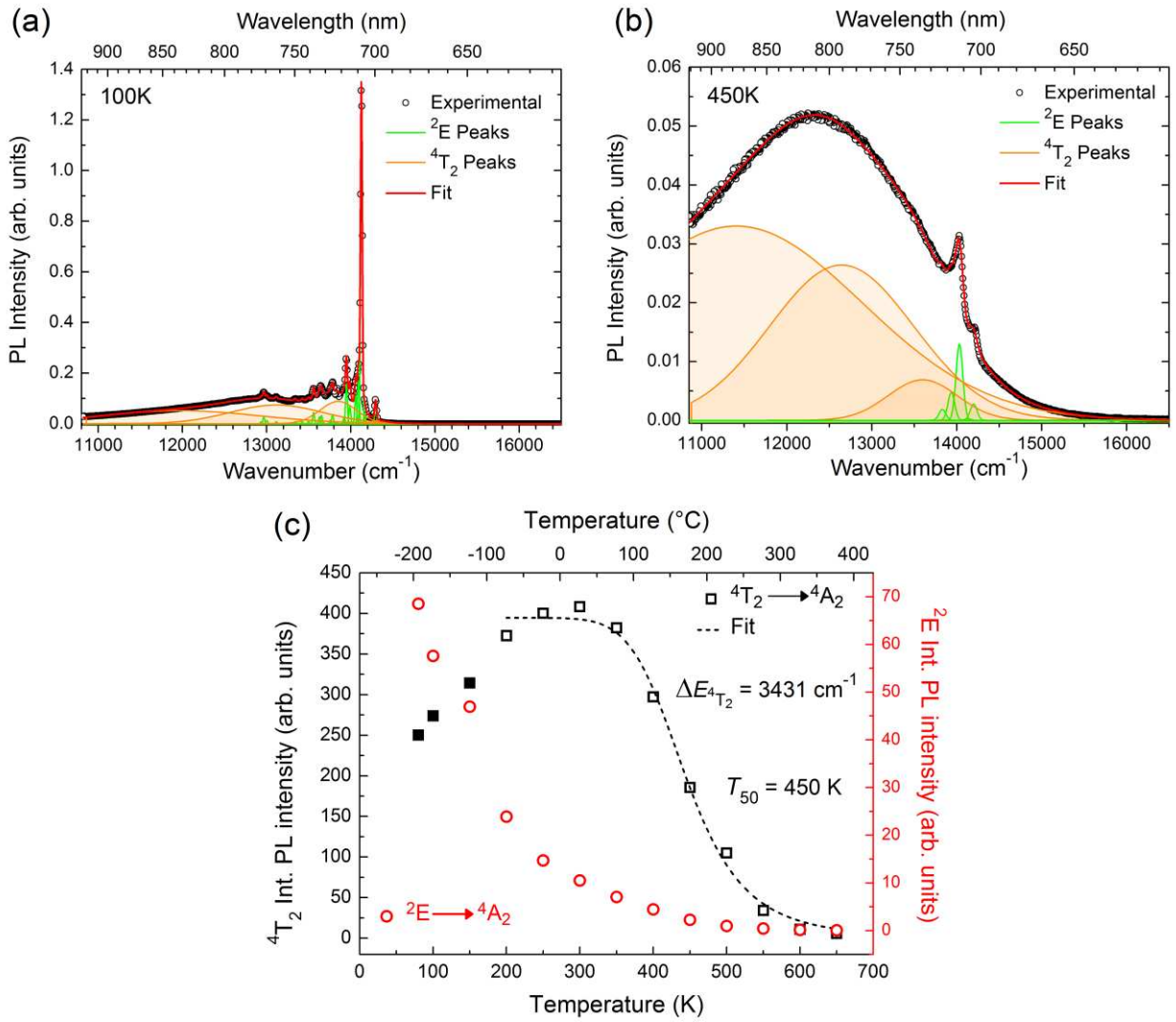

Figure 6.7 (a,b) Deconvolution of the PL spectra collected at 100 and 450 K. (c) Temperature dependence of integrated PL intensities of the transitions from ^2E (red circles) and $^4T_2$ (black squares), and fit (black dashed curve) for the thermal quenching process of the $^4T_2$ luminescent emission.

In order to investigate the nature of the two sharp lines at about 699 nm and 710 nm (labelled as R_2 and R_1 respectively), by following the Boltzmann equation:

$$\frac{I_{R_2}}{I_{R_1}} \propto exp\left(-\frac{\Delta E}{kT}\right) \tag{6.5}$$

the logarithm of the integrated intensity ratio of the two peaks *versus* 1/T was plotted (Figure 6.8a). The good linearity confirms the thermal equilibrium between R_1 and R_2 and thus demonstrates/suggests that the replacing of Cr^{3+} into the octahedral site of Ga^{3+} leads to the splitting of ^2E state into two *R*-lines because of low symmetry site. Comparing ΔE calculated from the spectra of Figure 6.8b (ΔE~ 170 cm^{-1}) with that one estimated from the Arrhenius plot (ΔE~ 122 cm^{-1}) we can observe a good agreement between these values. The discrepancy of the value can be explained by the disorder on the octahedral sites. Moreover, the typical observed split of ^2E (*e.g.* in ruby[63]) consists of about 29 cm^{-1} thus it is notable how Bi $6s^2$ lone electron pair may play a key role in the distortion of the Cr^{3+} site inducing such a large unusual splitting.

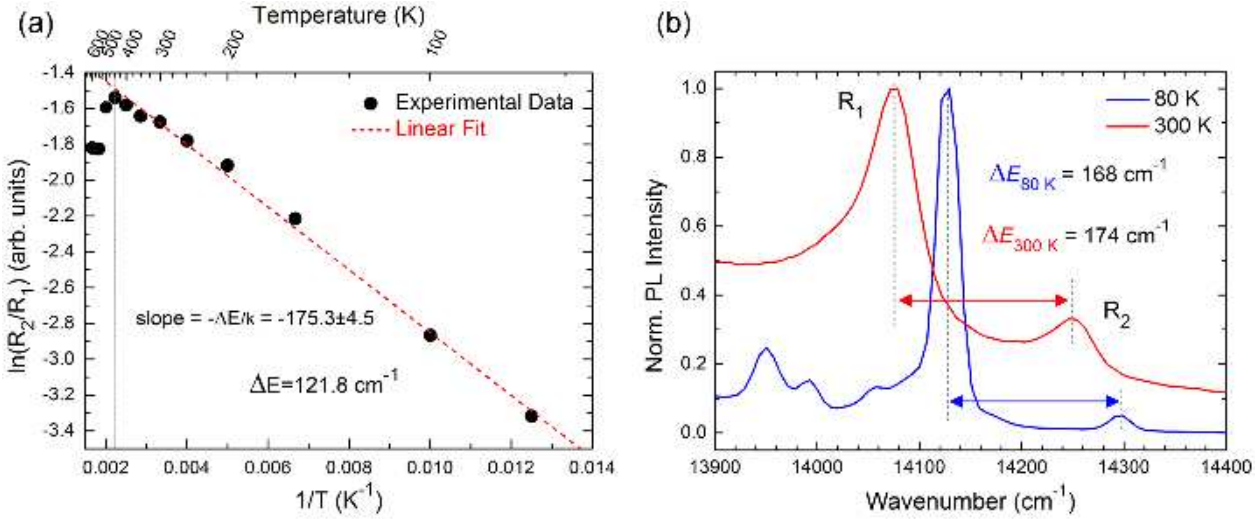

Figure 6.8 (a) Arrhenius plot for the two *R*-lines (R_1 and R_2) and (b) comparison between the *R*-line splitting of Cr^{3+} in the PL spectra at 80 K and 300 K.

6.6 Low Temperature Analysis: ZPLs, Vibrational Energy ħω and Huang-Rhys Parameters S

The PLE spectrum collected at 77 K and the high resolution spectra of the area labelled as A and B are shown in Figure 6.9. As in the excitation spectrum at room temperature (Figure 2b), the excitation spectrum at 77 K shows the typical absorption bands from $^4A_2$ to the $^4T_1(t^2e)$, $^4T_1(te^2)$ and $^4T_2(t^2e)$ excited states, and the strong absorptions of the *R*-lines. Furthermore, in order to investigate in detail the new absorption peaks revealed at low temperature in the regions A and B, high resolution spectra were collected. The high-resolution spectrum at 77 K of the $^4A_2 \rightarrow {}^4T_1(te^2)$ absorption peak (region A) evidences a first peak at about 20290 cm^{-1} that can be ascribed to the $^4T_1$ zero phonon line (ZPL) and a first vibronic transition at 20900 cm^{-1}. Hence, we estimated a vibrational energy ħω of the excited state $^4T_1$ of about 610 cm^{-1}. Besides the sharp lines at 14108 cm^{-1} and 14282 cm^{-1} ascribed to the R_1 and R_2 *R*-lines (zero phonon lines), the high resolution spectrum of the region B has disclosed two weak peaks at 13950 cm^{-1} and 14560 cm^{-1}.

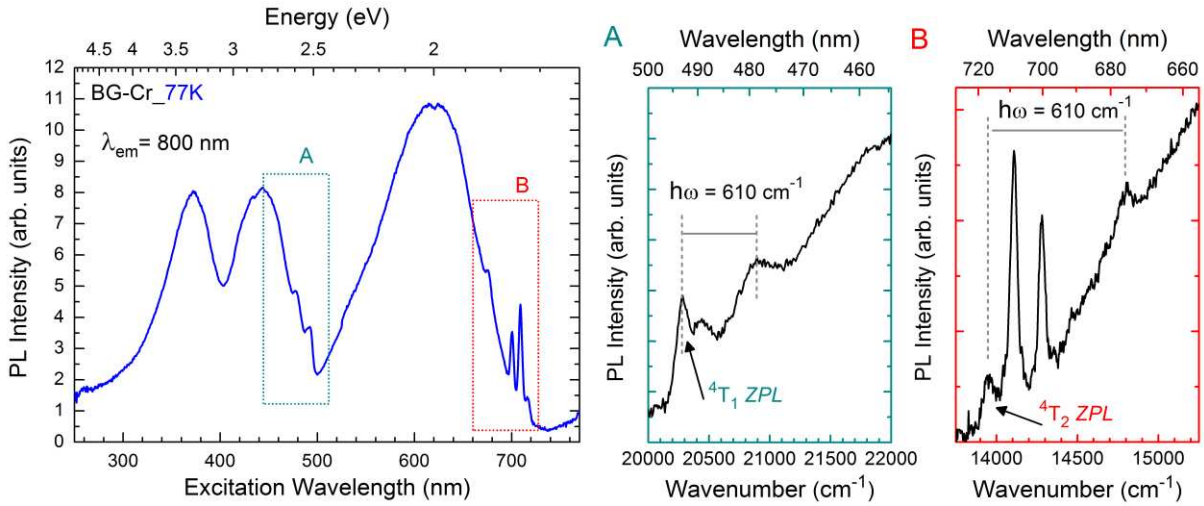

Figure 6.9 (a) PLE spectrum collecting at 800 nm at 77 K and magnification of the (A) $^4T_1$ zero phonon line and first vibrational state, and (B) ^2E and $^4T_2$ absorption peaks, both in the energy scale.

In order to estimate the theoretical position of the ZPL of $^4T_2$, the related Stokes shift E_{Stokes} was evaluated. As underlined by de Jong *et al.*,[64] a comparison with the theory requires the correction of the experimental spectra by dividing a factor E^3 before the analysis. Considering this correction, a Stokes shift of 3500 cm^{-1} was calculated (Figure 6.10), thus the ZPL of $^4T_2$ can be estimated as $E(^4T_2)_{ZPL} = E_{em}(^4T_2) + E_{Stokes}/2$, leading to a theoretical value of 13850 cm^{-1}. Taking into account the error in the estimation of peak maximum for emission and excitation spectra, we can consider the theoretical value in agreement with the peak at 13950 cm^{-1}. Moreover, in view of this result, the peak at 14560 cm^{-1}can be assign to the first vibronic transition of $^4T_2$ and the distance from the zero phonon line gives a vibrational energy ħω of 610 cm^{-1}, the same value estimated for the vibrational energy of the $^4T_1$ excited state.

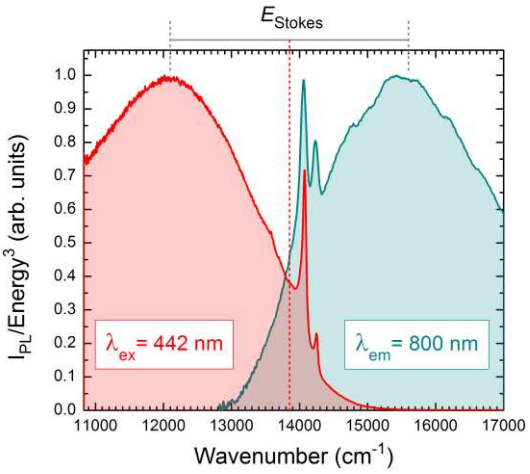

Figure 6.10 Specular corrected energy scale PL and PLE spectra of Cr^{3+} doped BG for the calculation of the Stokes shift of $^4T_2$.

In addition to the vibrational energy ħω, the effect of the lattice vibration on the transitions behaviour is described by the Huang-Rhys parameter *S* that points out the strength of the electron-phonon coupling. Considering the vibrational energy ħω (610 cm^{-1}) and the Stokes shift energy E_{Stokes} (3500 cm^{-1}) estimated, the electron-phonon coupling constant *S* of $^4T_1$ and $^4T_2$ was estimated by the following equations:[48]

$$S_{^4T_1} = \frac{E(^4T_1) - E(^4T_1)_{ZPL}}{\hbar\omega} \cong 3.44 \tag{6.6}$$

$$S_{^4T_2} = \frac{E_{Stokes}}{\hbar\omega} \cong 2.87 \tag{6.7}$$

while the Huang-Rhys parameter for ^2E was evaluated from the equation $I_{ZPL} = I_0 e^{-S}$, as:

$$S_{^2E} = ln\left(\frac{I_0}{I_{ZPL}}\right) \cong 0.6 \tag{6.8}$$

where I_{ZPL} and I_0 are the integrated area of the ZPL and the total emission lines (ZPL and multiphonon transitions) of the spectrum, respectively. For what concern ^2E, taking into account the errors in the calculations, Figure 6.11 demonstrates the temperature independent behaviour of *S* parameter.

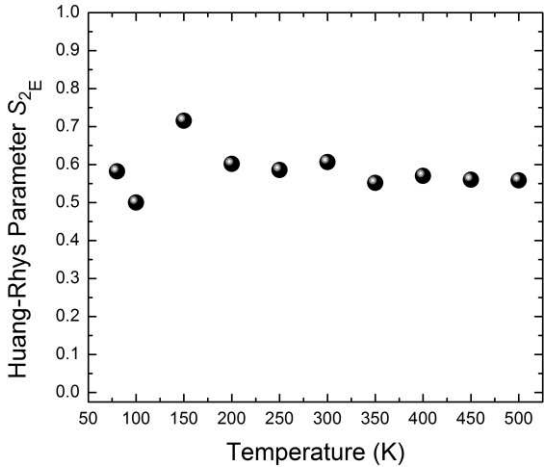

Figure 6.11 Temperature dependence of the Huang-Rhys parameter *S* for the ^2E excited state.

The resulting values for the different excited states are in agreement with the expected range of values. In fact, when the electron-phonon coupling strength is weak (typically *S*<1) an intense ZPL is expected in the spectrum (as for the ^2E, with *S*=0.6), while, when the coupling is strong, the ZPL cannot be separate by the RT spectral structure (as for $^4T_1$ and $^4T_2$, with *S*=3.44 and 2.87, respectively).

6.7 Temperature Dependence of Decay and Rise Curves

Figure 6.12a and b show the temperature dependent decay and rise curves of ^2E_g and $^4T_{2g}$ emissions of Cr^{3+}, respectively. The curves were collected monitoring the emissions at 710 nm and 780 nm upon pulsed excitation at 466 nm.

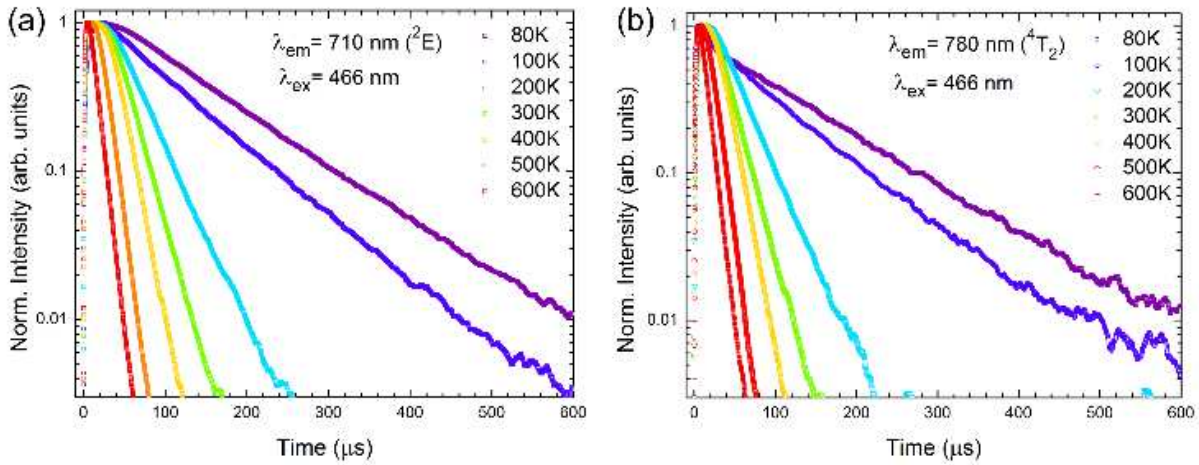

Figure 6.12 Logarithmic scale of decay curves monitoring the emission of Cr^{3+} at 710 nm (a) and 780 nm (b) by excitation at 466 nm.

Each time-resolved curve was fitted by the following double exponential function:

$$I = I_0\left[-exp(-t/\tau_{rise}) + exp\left(-t/\tau_{decay}\right)\right] \tag{6.9}$$

where τ_{rise} and τ_{decay} represent the rise time and decay time, respectively. The resulting values of decay and rise time are reported in Figure 6.13a and b, respectively.

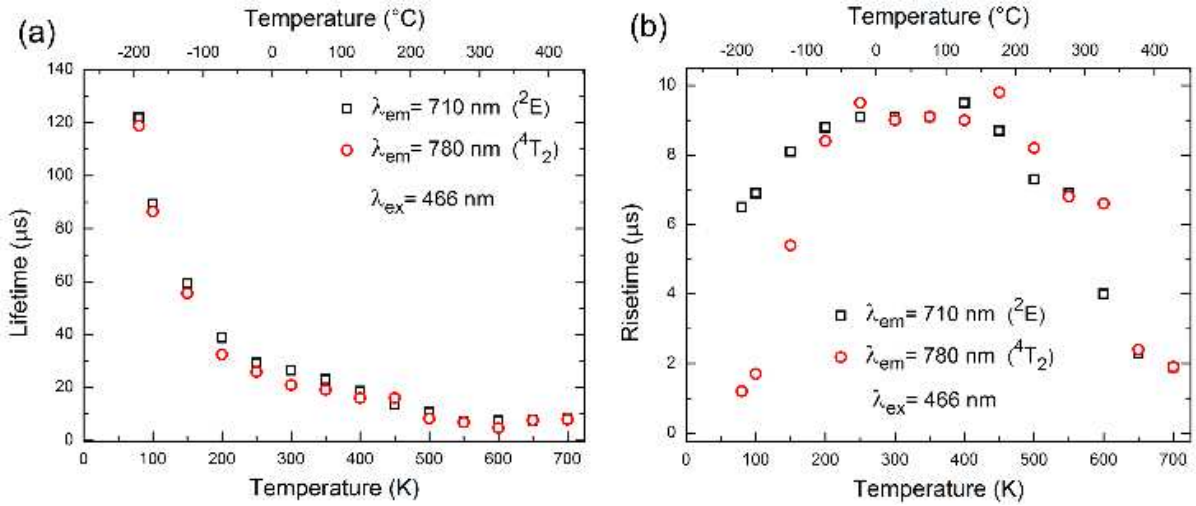

Figure 6.13 Temperature dependence of lifetime (a) and risetime (b) for $^2E \rightarrow {}^4A_2$ and $^4T_2 \rightarrow {}^4A_2$ transitions. The values for ^2E and $^4T_2$ are represented as red circles and black squares respectively.

The temperature dependence of the decay time for the ^2E state results equivalent to that one of the $^4T_2$ state. In principle, it is expected that the two excited states should be characterized by quite different decay times, being in the order of ms or μs scale, reflecting the different nature between the spin-forbidden transition from ^2E state and the spin-allowed one from $^4T_2$ state, respectively. Instead, in the present case the decay time decreases with the same behaviour for both the emissions at increasing temperatures, suggesting a strong connection between the two states. The similar values of decay time at each temperature strongly supports the idea of a mixing of the ^2E

and $^4T_2$ excited states. The same situation ca be configured also by analysing the temperature trend shown by the rise time estimates referred to the PL emissions at 710 nm and 780 nm.

6.8 Configurational Coordinate Diagram and Thermal Sensing

The configurational coordinate diagram (CCD) was designed by considering the absorption energies of the small-offset state ^2E at 14065 cm^{-1}, the broad absorption bands with larger-offset states $^4T_2$ and $^4T_1$ near 15748 and 22422 cm^{-1} and considering the relative zero-phonon lines for $^4T_1$ and $^4T_2$ estimated at 20290 and 13850 cm^{-1}, respectively. Moreover, in order to properly describe the CCD for Cr^{3+}, the effect of the lattice vibration on the transitions behaviour was introduced, considering the Huang-Rhys parameters *S* previously calculated for each excited states. In fact, the Huang-Rhys parameter points out the strength of electron-phonon coupling and the shift of the minima of the adiabatic potentials (the parabolas of the CCD) giving a more accurate description. The following equation was used to describe the parabolic potential curve of the generic excited state ES:

$$E_{ES} = E_{ZPL,ES} + S_{ES}\hbar\omega_{ES}\left(\frac{x}{\Delta Q_{e,ES}} - 1\right)^2 \tag{6.10}$$

where E_{ZPL} is the zero phonon line energy, *S* the Huang-Rhys parameter, $\hbar\omega$ the vibrational energy and ΔQ_e the offset position. The diagram depicted by considering the effect of the lattice vibration (Figure 6.14) explains the thermally activated quenching process of the $^4T_2$ in terms of nonradiative relaxation process from the $^4T_2$ potential curve to the $^4A_2$ ground potential curve through the crossing point in the configurational coordinate diagram. Moreover, the design of the detailed CCD makes light also on the strong quenching of ^2E at low temperature that seems to be related to the particular electronic configuration of Cr^{3+} in $Bi_2Ga_4O_9$.

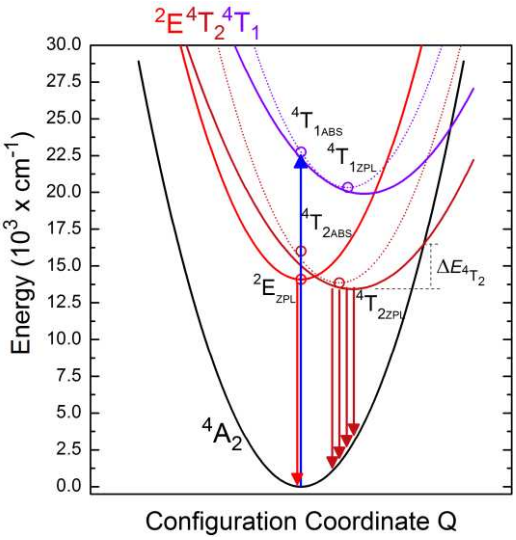

Figure 6.14 Configurational coordinate diagram (open circles corresponds to the ZPLs and absorption peaks of the excited states). Straight arrows designate radiative processes. The diagram is drawn to match the actual energies measured for the ZPLs and the emission and excitation maxima. ΔE^4_{T2} is the activation energy of the thermal quenching process.

Considering the multiplet energy level diagram as a function of Cr-O bond length proposed by Ogasawara *et al.*[65] and the average value of about 1.99 Å for the length bond in the octahedral site of Ga^{3+} in $Bi_2Ga_4O_9$, we confirmed the consistency of our estimations. In fact, for a Cr-O length bond of about 1.99 Å, the theoretical calculation of the multiplet energies predicts the intersection between ^2E and $^4T_2$ states, in good agreement with our experimental results. However, a precise analysis of the energy levels configuration obtained from these theoretical calculations shows a scenario in which the energy of ^2E_g state is slightly lower than the $^4T_{2g}$ energy, in contradiction with our previous detailed CCD design. This discrepancy can be bridged by considering the difference of bond length of Cr-O compared with Ga-O in the same site. In fact, the difference of electronegativity between Cr^{3+} and O^{2-} and between Ga^{3+} and O^{2-} (1.78 and 1.63, respectively[59]) give reason for a more ionic character of Cr^{3+}-O^{2-} bonds respect to Ga^{3+}-O^{2-}. Consequently, the average Cr^{3+}-O^{2-} distances are slightly longer than Ga^{3+}-O^{2-}, confirming a perfect agreement between experimental and theoretical calculations.

To assess the potential of this system as a thermometer, its photoluminescence was investigated in 80-600 K range (Figure 6.6). The linearity of the Arrhenius plot showed in Figure 6.15a evidences the thermal equilibrium between the $^4T_2$ and ^2E states in the 150-500 K range, with ΔE =390 cm^{-1}, in good agreement with the value estimated by the CCD design.

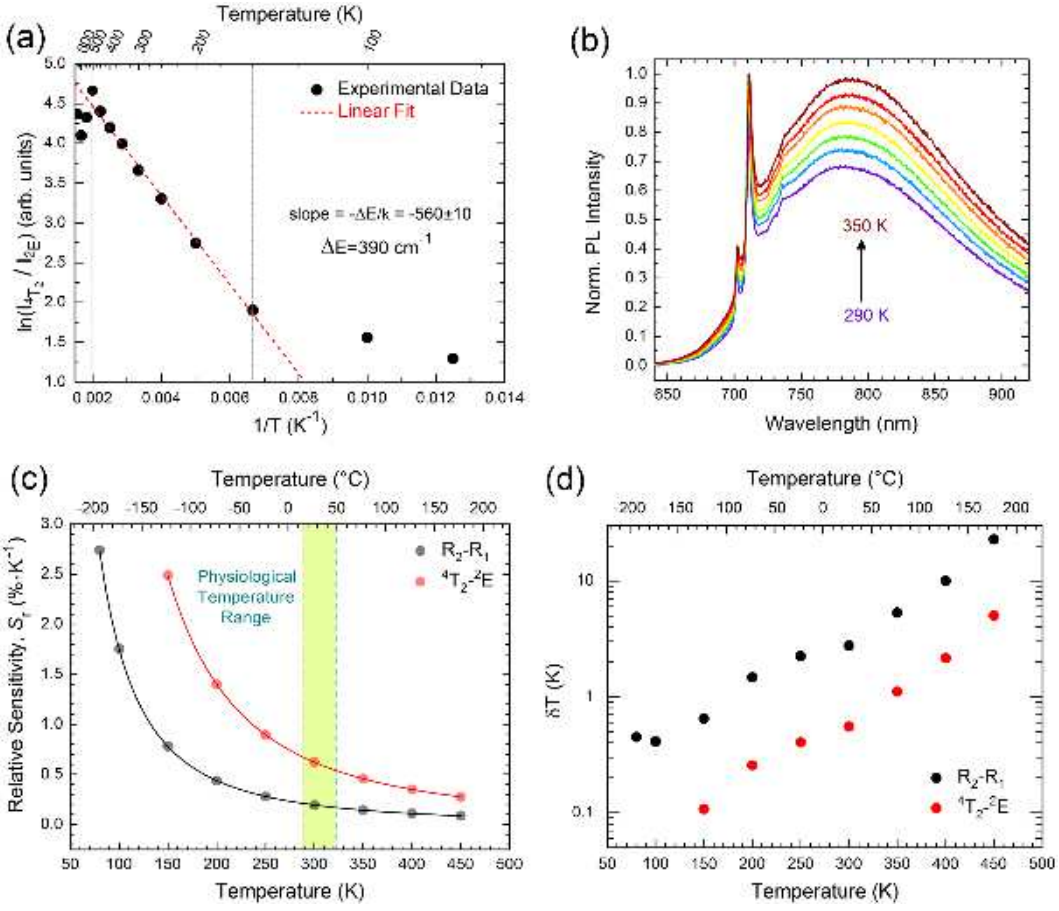

Figure 6.15 (a) Plot of $\ln(I^4_{T2}/ I^2_E)$ *versus* 1/T to calibrate the thermometer. (b) Temperature dependence of PL emission spectra in the 290-350 K range, normalized to the ^2E *R*-line. (c) Relative sensitivity of the thermometers based on the R_2-R_1 and $^4T_2$-^2E couples in the corresponding temperature regions of the linearity for the Boltzmann law. (d) Temperature uncertainty (in log scale) estimated using Eq. 6.12.

The absolute temperature is inferred by considering the experimental parameters Δ_R and $\Delta_{T\text{-}E}$, defined as the integrated intensity ratio of the R_2 and R_1 peaks and of $^4T_2 \rightarrow {}^4A_2$ and $^2E \rightarrow {}^4A_2$ transitions, respectively. In this particular case, the variation with temperature of the intensity ratio of the R_2 and R_1 peaks and of $^4T_2 \rightarrow {}^4A_2$ and $^2E \rightarrow {}^4A_2$ transitions are both demonstrated to follow the Boltzmann thermal distribution (Figure 6.8a and Figure 6.15a, respectively), ensuring the temperature measurement reliability.

To compare the thermometric performance of different thermometers irrespective to their nature, we considered the figure of merit described by the relative sensitivity S_r, defined as:[1]

$$S_r = \frac{1}{\Delta}\frac{\partial \Delta}{\partial T} \tag{6.11}$$

Figure 6.15c depicts the temperature dependence of the relative sensitivity for the two pairs of thermally coupled excited states in Cr^{3+}-doped $Bi_2Ga_4O_9$. In general, the relative sensitivity of the $^4T_2$-^2E pair is higher than that of the R_2-R_1 one, as expected by the difference in the ΔE values. It is notable that the $^4T_2$-^2E pair shows a maximum value of S_r of 0.70 ± 0.02 %·K^{-1} in the physiological temperature range. Figure 6.15b points out the great sensitivity of $Bi_2Ga_4O_9$:Cr^{3+} system to the temperature in the physiological range. Moreover, R_2-R_1 pair exhibits a promising maximum value of 2.74 ± 0.06 %·K^{-1} at 80 K, the lowest temperature explored in this study.

The results confirm the possibility to use such material as ratiometric luminescent thermometer. Moreover, it is worth mentioning that the system is characterized by two excited states couples, both in thermal equilibrium in a wide range of temperature (150-500 K and 80-500 K for $^4T_2$-^2E and R_2-R_1 couples, respectively).

Considering the terms defining the relative sensitivity S_r and the thermometric parameter Δ, the estimate of the temperature uncertainty δT can be achieved by the following relationship[17,22]

$$\delta T = \frac{1}{S_r}\frac{\delta \Delta}{\Delta}, \tag{6.12}$$

where the term $\frac{\delta \Delta}{\Delta}$ contains the factor $\delta\Delta$, that is the uncertainty in the determination of Δ.

The parameter δT depends on the thermometer performance, quantified by S_r, as well as on the experimental set-up for the luminescence detection, since $\frac{\delta \Delta}{\Delta}$ is directly linked to the measurements of the thermometer emission intensities and the relative uncertainties.

In general, for each specific detector a maximum signal-to-noise ratio (SNR) is provided, giving the lowest uncertainty limit. Since the detector usually operates in less favourable conditions, for two luminescent transitions with intensities of I_A and I_B, respectively, whose relative ratio determines the thermometric parameter

$$\Delta = \frac{I_A}{I_B}, \tag{6.13}$$

the estimate of $\frac{\delta \Delta}{\Delta}$ can be obtained considering the uncertainty affecting the intensity measurements:[66]

$$\frac{\delta\Delta}{\Delta} = \sqrt{\left(\frac{\delta I_A}{I_A}\right)^2 + \left(\frac{\delta I_B}{I_B}\right)^2} \,. \tag{6.14}$$

For each transition, we can assume that

$$\frac{\delta I}{I} = \frac{\delta_{BL}}{\langle I \rangle}, \tag{6.15}$$

where δ_{BL} is the uncertainty determined by the readout fluctuations of the baseline and $\langle I \rangle$ is the average intensity given by

$$\langle I \rangle = \frac{\int_{E_0}^{E_1} I(E)\,\mathrm{d}E}{E_1 - E_0}, \tag{6.16}$$

that, for each transition, is evaluated over the whole emission spectral region ($E_0 \leq E \leq E_1$).

Finally, by substituting the estimated value of S_r and $\frac{\delta\Delta}{\Delta}$ in Eq. 6.12, the quantification of the temperature uncertainty δT is achieved.

Figure 6.15d shows the temperature uncertainty for the two thermometers as a function of temperature, suggesting that, if the $^4T_2$-^2E pair can be used in almost all the temperature window explored, the R_2-R_1 based thermometer may ensure an adequate reliability at low temperatures.

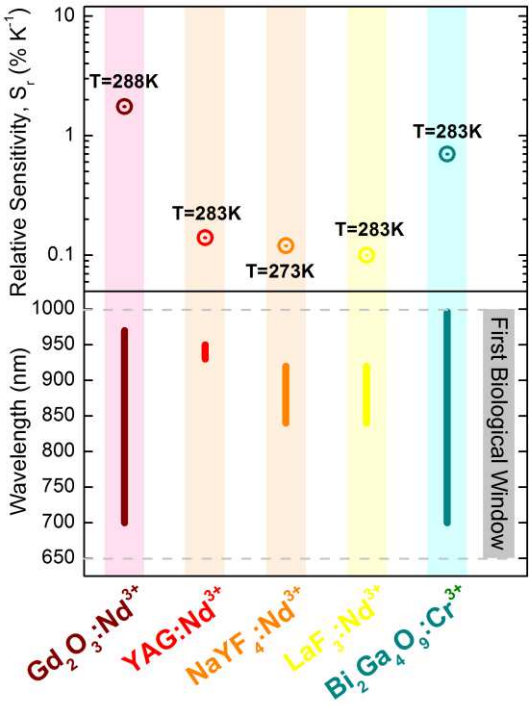

Figure 6.16 Maximum relative sensitivity at the physiological temperatures (logarithmic scale) and emission spectral range of $Bi_2Ga_4O_9$:Cr^{3+}, compared to other single-doped ratiometric luminescent thermometers emitting in the first biological window: Gd_2O_3:Nd^{3+},[22] YAG:Nd^{3+},[25] $NaYF_4$:Nd^{3+} [26] and LaF_3:Nd^{3+} [24].

By comparing the relative sensitivity of the investigated system with some typical single-doped materials exhibiting dual emission in the first biological window, reported in literature (Figure 6.16), it is pointed out that the $Bi_2Ga_4O_9:Cr^{3+}$ system can be considered as a promising candidate for ratiometric thermometry in biological field.

6.9 Conclusions

In this Chapter, we have proposed Cr^{3+}-doped $Bi_2Ga_4O_9$ as a new ratiometric luminescent thermometer. Specifically, we have focused on the spectroscopic analysis of the system pointing out the peculiar crystal field experienced by Cr^{3+}. As a result, the system displays the simultaneous emission from the $^2E \rightarrow {}^4A_2$ and $^4T_2 \rightarrow {}^4A_2$ transitions, both falling in the first optical window. For an accurate description of the Cr^{3+} electronic configuration, detailed experimental analysis were compared with models and theoretical works reported in literature, ensuring the reliability of the measurements. Finally, we have investigated the temperature dependence of the luminescent response, evidencing two pairs of thermally coupled excited states in a wide range of temperature. In addition, a maximum relative sensitivity of 0.70 ± 0.02 %·K^{-1} was achieved in the physiological temperature range and the relative temperature uncertainties were estimated. Our observations suggest Cr^{3+}-doped $Bi_2Ga_4O_9$ as a new promising candidate for luminescent ratiometric thermal sensing in biological applications.

Materials and Methods

Experimental Details. The crystal phase was identified by XRD measurement (Shimadzu, Kyoto, Japan; XRD6000). The diffuse reflectance spectra were collected by a spectrophotometer (Shimadzu, UV3600) equipped with an integrating sphere.

The photoluminescence excitation (PLE) spectra were collected exciting with a 300 W Xe lamp (Asahi Spectra, MAX-302) equipped with a monochromator (Nikon, G250) and detecting by Si photodiode (PD) detector (Electro-Optical System Inc., S-025-H) equipped with a monochromator (Shimadzu, 675 grooves/mm). Photoluminescence (PL) spectra were measured exciting the samples with a 442 nm laser diode (NDHB510APA-E, Nichia Co. Ltd.) and the spectra were collected by a CCD spectrometer (Ocean Optics, QE65Pro) connected with an optical fiber. All the PL spectra were calibrated by using a standard halogen lamp (Labsphere, SCL-600).
Low temperature PLE spectrum (80 K), temperature dependence of PL and of decay curves (80-700 K range) were investigated setting the sample in a cryostat (Helitran LT3, Advanced Research Systems).

The luminescence decay measurements were carried out at varied temperatures from 80 K to 700 K using the cryostat and a precise temperature controlled heater. The sample was excited by using a 466 nm dye (Exciton, LD466) laser pumped with a nitrogen laser pulse excitation. The decay curves of fluorescence at 710 nm and 780 nm were detected by a PMT (Hamamtsu, R1104) equipped with a monochromator (Shimadzu, 675 grooves/mm) and averaged on a digital oscilloscope (Yokogawa, DL1620).

References

1. C.D.S. Brites, P.P. Lima,N.J.O. Silva, A. Millán, V.S. Amaral, F. Palacio and L.D. Carlos. Thermometry at the Nanoscale. *Nanoscale* **2012**, 4, 4799-4829.
2. E.J. McLaurin, L.R. Bradshaw and D.R. Gamelin. Dual-Emitting Nanoscale Temperature Sensors. *Chem. Mater.* **2013**, 25, 1283-1292.
3. L.H. Fischer, G.H. Harms and O.S. Wolfbeis. Upconverting Nanoparticles for Nanoscale Thermometry. *Angew. Chem. Int. Ed.* **2011**, 50, 4546-4551.
4. D. Jaque and F. Vetrone. Luminescence Nanothermometry. *Nanoscale* **2012**, 4, 4301-4326.
5. E.C. Ximendes, W.Q. Santos, U. Rocha, U.K. Kagola, F. Sanz-Rodríguez, N. Fernández, A.S. Gouveia-Neto, D. Bravo, A.M. Domingo, B. del Rosal, C.D.S. Brites, L.D. Carlos, D. Jaque and C. Jacinto. Unveiling in Vivo Subcutaneous Thermal Dynamics by Infrared Luminescent Nanothermometers. *Nano Lett.* **2016**, 1695-1703.
6. A.N. Bashkatov, E.A. Genina, V.I. Kochubey and V.V. Tuchin. Optical Properties of Human Skin, Subcutaneous and Mucous Tissues in the Wavelength Range from 400 to 2000 nm. *J. Phys. D: Appl. Phys.* **2005**, 38, 2543-2555.
7. A.M. Smith, M.C. Mancini and S. Nie. Second Window for in vivo Imaging. *Nat. Nanotechnol.* **2009**, 4, 710-711.
8. E. Hemmer, A. Benayas, F. Légaré and F. Vetrone. Exploiting the Biological Windows: Current Perspectives on Fluorescent Bioprobes Emitting above 1000 nm. *Nanoscale Horiz.* **2016**, 1, 168-184.
9. D. Jaque, C. Richard, B. Viana, K. Soga, X. Liu and J. García Solé. Inorganic Nanoparticles for Optical Bioimaging. *Adv. Opt. Photon.* **2016**, 8, 1-103.
10. X. Wang, Q. Liu, Y. Bu, C.-S. Liu, T. Liu and X. Yan. Optical Temperature Sensing of Rare-Earth ion doped Phosphors. *RSC Adv.* **2015**, 5, 86219-86236.
11. F. Vetrone, R. Naccache, A. Zamarrón, A.J. de la Fuente, F. Sanz-Rodríguez, L. Martinez Maestro, E. Martin Rodriguez, D. Jaque, J. García Solé and J.A. Capobianco. Temperature Sensing Using Fluorescent Nanothermometers. *ACS Nano* **2010**, 4, 3254-3258.
12. E. Hemmer, M. Quintanilla, F. Légaré and F. Vetrone. Temperature-Induced Energy Transfer in Dye-Conjugated Upconverting Nanoparticles: A New Candidate for Nanothermometry. *Chem. Mater.* **2015**, 27, 235-244.
13. T.V. Gavrilović, D.J. Jovanović, V. Lojpur and M.D. Dramićanin. Multifunctional Eu^{3+}- and Er^{3+}/Yb^{3+}-doped $GdVO_4$ Nanoparticles Synthesized by Reverse Micelle Method. *Sci. Rep.* **2014**, 4, 4209.
14. A.S. Souza, L.A.O. Nunes, I.G.N. Silva, F.A.M. Oliveira, L.L. da Luz, H.F. Brito, M.C.F.C. Felinto, R.A.S. Ferreira, S.A. Júnior, L.D. Carlos and O. Malta. L. Highly-Sensitive Eu^{3+} Ratiometric Thermometers Based on Excited State Absorption with Predictable Calibration. *Nanoscale* **2016**, 8, 5327-5333.

15. C.D.S. Brites, P.P. Lima, N.J.O. Silva, A. Millán, V.S. Amaral, F. Palacio and L.D. Carlos. A Luminescent Molecular Thermometer for Long-Term Absolute Temperature Measurements at the Nanoscale. *Adv. Mater.* **2010**, 22, 4499-4504.

16. X. Liu, S. Akerboom, M. de Jong, I. Mutikainen, S. Tanase, A. Meijerink and E. Bouwman. Mixed-Lanthanoid Metal-Organic Framework for Ratiometric Cryogenic Temperature Sensing. *Inorg. Chem.* **2015**, 54, 11323-11329.

17. Z. Wang, D. Ananias, A. Carné-Sánchez, C.D.S. Brites, I. Imaz, D. Maspoch, J. Rocha and L.D. Carlos. Lanthanide-Organic Framework Nanothermometers Prepared by Spray-Drying. *Adv. Func. Mater.* **2015**, 25, 2824-2830.

18. D. Ananias, F.A. Almeida Paz, D.S. Yufit, L.D. Carlos and J. Rocha. Photoluminescent Thermometer Based on a Phase-Transition Lanthanide Silicate with Unusual Structural Disorder. *J. Am. Chem. Soc.* **2015**, 137, 3051-3058.

19. Z. Boruc, M. Kaczkan, B. Fetlinski, S. Turczynski and M. Malinowski. Blue Emissions in Dy^{3+} doped $Y_4Al_2O_9$ Crystals for Temperature Sensing. *Opt. Lett.* **2012**, 37, 5214-5216.

20. Z.M. Cao, S.S. Zhou, G.C. Jiang, Y.H. Chen, C.K. Duan and M. Yin. Temperature Dependent Luminescence of Dy^{3+} doped $BaYF_5$ Nanoparticles for Optical Thermometry. *Curr. Appl. Phys.* **2014**, 14, 1067-1071.

21. Y. Gao, F. Huang, H. Lin, J. Zhou, J. Xu and Y. Wang. A Novel Optical Thermometry Strategy Based on Diverse Thermal Response from Two Intervalence Charge Transfer States. *Adv. Funct. Mater.* **2016**, 26, 3139-3145.

22. S. Balabhadra, M.L. Debasu, C.D.S. Brites, L.A.O. Nunes, O.L. Malta, J. Rocha, M. Bettinelli and L.D. Carlos. Boosting the Sensitivity of Nd^{3+}-based Luminescent Nanothermometers. *Nanoscale* **2015**, 7 17261-17267.

23. E. Carrasco, B. del Rosal, F. Sanz-Rodríguez, A.J. De la Fuente, P. Haro Gonzalez, U. Rocha, K.U. Kumar, C. Jacinto, J. García Solé and D. Jaque. Intratumoral Thermal Reading During Photo Thermal Therapy by Multifunctional Fluorescent Nanoparticles. *Adv. Funct. Mater.* **2015**, 25, 615-626.

24. U. Rocha, C.J. da Silva, W.F. Silva, I. Guedes, A. Benayas, L. Martinez Maestro, M. Acosta Elias, V. Bovero, F.C.J.M. van Veggel, J.A. García Solé and D. Jaque. Subtissue Thermal Sensing based in Neodymium-doped LaF_3 Nanoparticles. *ACS Nano* **2013**, 7, 1188-1199.

25. A. Benayas, B. de Rosal, A. Pérez-Delgado, K. Santacruz-Gómez, D. Jaque, G.A. Hirata and F. Vetrone. Nd:YAG Near-Infrared Luminescent Nanothermometers. *Adv. Optical Mater.* **2015**, 3, 687-694.

26. D. Wawrzynczyk, A. Benarkiewcicz, M. Nyk, W. Strek and M Samoc. Neodymium(III) doped Fluoride Nanoparticles as Non-Contact Optical Temperature Sensors. *Nanoscale* **2012**, 4, 6959-6961.

27. T.H. Maiman. Stimulated Optical Radiation in Ruby. *Nature* **1960**, 187, 493-494.

28. Y. Zhuang, Y. Katayama, J. Ueda and S, Tanabe. A Brief Review on Red to Near-Infrared Persistent Luminescence in Transition-Metal-Activated Phosphors. *Opt. Mater.* **2014**, 36, 1907-1912.

29. A. Bessière, S. Jacquart, K. Priolkar, A. Lecointre, B. Viana and D Gourier. $ZnGa_2O_4:Cr^{3+}$: a New Red Long-Lasting Phosphor with High Brightness. *Opt. Express* **2011**, 19, 10131-10137.

30. J. Ueda, K. Kuroishi and S. Tanabe. Yellow Persistent Luminescence in Ce^{3+}-Cr^{3+}-codoped Gadolinium Aluminium Gallium Garnet Transparent Ceramics After Blue-Light Excitation. *Appl. Phys. Express* **2014**, 7, 062201.

31. Z. Pan, Y.-Y. Lu and F. Liu. Sunlight-Activated Long-Persistent Luminescence in the Near-Infrared from Cr^{3+}-doped Zinc Gallogermanates. *Nat. Mater.* **2012**, 11, 58-63.

32. T. Maldiney, A. Bessière, J. Seguin, E. Teston, S.K. Sharma, B. Viana, A.J.J. Bos, P. Dorenbos, M. Bessodes, D. Gourier, D. Scherman and C. Richard. The *in vivo* Activation of Persistent Nanophosphors for Optical Imaging of Vascularization, Tumours and Grafted Cells. *Nat. Mater.* **2014**, 13, 418-426.

33. Y. Katayama, H. Kobayashi and S. Tanabe. Deep-Red Persistent Luminescence in Cr^{3+}-doped $LaAlO_3$ Perovskite Phosphor for in vivo Imaging. *Appl. Phys. Express* **2015**, 8, 012102.

34. J. Xu, J. Ueda and S. Tanabe. Design of Deep-Red Persistent Phosphors of $Gd_3Al_{5-x}Ga_xO_{12}$:Cr^{3+} Transparent Ceramics Sensitized by Eu^{3+} as an Electron Trap Using Conduction Band Engineering. *Opt. Mater. Express* **2015**, 5, 963-968.

35. S.K. Sharma, E. Glais, M. Pellerin, C. Chaneac and B. Viana. Temperature Sensing Using a Cr:$ZnGa_2O_4$ New Phosphor. *Proc. SPIE* **2016**, 9749, 974922.

36. D. Chen, Z. Wan and Y. Zhou. Optical Spectroscopy of Cr^{3+}-doped Transparent Nano-Glass Ceramics for Lifetime-based Temperature Sensing. *Opt. Lett.* **2015**, 40, 3607-3610.

37. D. Chen, Z. Wan, Y. Zhou and Z. Ji. Cr^{3+}-doped Gallium-based Transparent Bulk Glass Ceramics for Optical Temperature Sensing. *J. Eur. Ceram. Soc.* **2015**, 35, 4211-4216.

38. Z. Zhang, K.T.V. Grattan and A.W. Palmer. Temperature Dependences of Fluorescence Lifetimes in Cr^{3+}-doped Insulating Crystals. *Phys. Rev. B* **1993**, 48, 7772-7778.

39. Z. Zhang, K.T.V. Grattan and A.W. Palmer. Temperature Dependence of the YAG:Cr^{3+} Fluorescence Lifetime Over the Range 77 to 900 K. *Phys. Rev. B* **1995**, 51, 2656-2660.

40. F. Anghel, C. Iliescu, K.T.V. Grattan, A.W. Palmer and Z.Y. Zhang. Fluorescent-based Lifetime Measurement Thermometer for the Use at Subroom Temperatures (200-300 K). *Rev. Sci. Instrum.* **1995**, 66, 2611-2614.

41. S.M. Borisov, K. Gatterer, B. Bitschnau and I. Klimant. Preparation and Characterization of Chromium(III)-Activated Yttrium Aluminum Borate: A New Thermographic Phosphor for Optical Sensing and Imaging at Ambient Temperatures. *J. Phys. Chem. C* **2010**, 114, 9118-9124.

42. A. Beran, E. Libowitzky, M. Burianek, M. Mühlberg, C. Pecharromán and H. Schneider. Infrared and Raman Spectroscopy of Mullite-Type $Bi_2Ga_4O_9$. *Cryst. Res. Technol.* **2008**, 43, 1230-1239.

43. Y. Tanabe and S. Sugano. On the Absorption Spectra of Complex Ions II. *J. Phys. Soc. Japan* **1954**, 9, 766-779.

44. E. Ejder. Methods of Representing Emission, Excitation, and Photoconductivity Spectra. *J. Opt. Soc. Am.* **1969**, 59, 223-224.

45. P. Kubelka and F. Munk. Ein Beitrag zur Optik der Farbanstriche. *Z. Technische Physik* **1931**, 12, 593-601.

46. J. Tauc, R. Grigorovici and A. Vancu. Optical Properties and Electronic Structure of Amorphous Germanium. *Phys. Status Solidi* **1966**, 15, 627-637.

47. E. Zahedi, B. Xiao and M. Shayestefar. First-Principles Investigations of the Structure, Electronic, and Optical Properties of Mullite-Type Orthorhombic $Bi_2M_4O_9$ ($M = Al^{3+}$, Ga^{3+}). *Inorg. Chem.* **2016**, 55, 4824-4835.

48. B. Henderson and G.F. Imbusch. *Optical Spectroscopy of Inorganic Solids*. Oxford University Press: Oxford, 1989.

49. A. Trueba, P. Garcia-Fernandez, J.M. García-Lastra, J.A. Aramburu, M.T. Barriuso, and M. Moreno. Spectrochemical Series and the Dependence of Racah and 10*Dq* Parameters on the Metal-Ligand Distance: Microscopic Origin. *J. Phys. Chem. A* **2011**, 115, 1423-1432.

50. Z.B. Perekalina, T.F. Veremeichik, K.A. Kaldybaev and A.D. Tynaev. Spectroscopy studies of pure and chromium-doped calcium gallogermanate crystals, $Ca_3Ga_2Ge_4O_{14}$. *Crystal. Rep.*, **2000**, 45, 304-306.

51. Y.H. Wang, K. Xu, D.R. Li, H. Zhao and Z.F. Hu. Persistent luminescence and photocatalytic properties of $Ga_2O_3:Cr^{3+},Zn^{2+}$ phosphors. *Opt. Mater.*, **2014**, 36, 1798-1801.

52. W. Ryba-Romanowski, S. Gołab, G. Dominiak-Dzik, I. Sokòlska and M. Berkowski. Optical study of chromium doped $LaGaO_3$ single crystal. *J. Alloys Compds.*, **1999**, 284, 22-26.

53. A. Luci, T. Castrignano, U.M. Grassano, M. Casalboni and A.A. Kaminskii. Optical properties of $LaSrGa_{11}O_{20}$ crystals containing Cr^{3+}. *Phys. Rev. B*, **1995**, 51, 1490-1494.

54. M. Grinberg, B. Kuklínski, K. Wísniewski, C. Koepke, T. Łukasiewicz, J. Kisielewski, M. ´Swirkowicz and A. Suchocki. Spectroscopy of lanthanum lutetium gallium garnet crystals doped with chromium. *J. Opt. Soc. Am. B*, **2003**, 20, 577-584.

55. M. Casalboni, A. Luci, U.M. Grassano, B.V. Mill and A.A. Kaminskii. Optical spectroscopy of $La_3Ga_5SiO_{14}$ crystals. *Phys. Rev. B*, **1994**, 49, 3781-3790.

56. J. Zhou and Z.G. Xia. Synthesis and Near-Infrared luminescence of $La_3GaGe_5O_{16}:Cr^{3+}$ phosphors. *RSC Advances*, **2014**, 4, 46313-46318.

57. Y. Li, S. Ye and Q. Zhang. Ultra-Broadband Near-Infrared Luminescence of Ordered-Disordered Multi-Sited Cr^{3+} in $La_3Ga_{5.5}Nb_{0.5}O_{14}:Cr^{3+}$. *J. Mater. Chem. C*, **2014**, 2, 4636-4641.

58. V. Singh, R.V.S.S.N. Ravikumar, G. Sivaramaiah, J.L. Rao and S.H. Kim. Investigations of the Optical and EPR Properties of $LiGa_5O_8:Cr^{3+}$ Phosphor. *Mater. Res. Bull.*, **2015**, 61, 183-188.

59. P.J. Derén, A. Watras, A. Gągor and R. Pązik. Weak crystal field in Yttrium Gallium Garnet (YGG) submicrocrystals doped with Cr^{3+}. *Cryst. Growth Des.*, **2012**, 12, 4752-4757.

60. M.G. Brik, N.M. Avram and C.N. Avram. Comparative crystal field calculations of the Cr^{3+} energy level schemes in $ZnAl_2S_4$ and $ZnGa_2O_4$. *J. Mater. Sci.: Mater. Electron.*, **2009**, 20, S30-S32.

61. M.G. Brik, S.J. Camardello, A.M. Srivastava, N.M. Avram and A. Suchocki. Spin-Forbidden Transitions in the Spectra of Transition Metal Ions and Nephelauxetic Effect. *ECS J. Solid State Sci. Technol.* **2016**, 5, R3067-R3077.

62. M. Mangir Murshed and T.M. Gesing. Anisotropic Thermal Expansion and Anharmonic Phonon Behaviour of Mullite-Type $Bi_2Ga_4O_9$. *Mater. Res. Bull.* **2013**, 48, 3284-3291.

63. G.F. Imbusch and W.M. Yen. In *Laser, Spectroscopy, and New Ideas*; W. M. Yen and M.D. Levenson, Eds; Springer-Verlag, Berlin, **1987**; Part III, pp. 248-267.

64. M. de Jong, L. Seijo, A. Meijerink, and F.T. Rabouw. Resolving the Ambiguity in the Relation Between Stokes Shift and Huang-Rhys Parameter. *Phys. Chem. Chem. Phys.* **2015**, 17, 16959-16969.

65. K. Ogasawara, F. Alluqmani and F. Nagoshi. Multiplet Energy Level Diagrams for Cr^{3+} and Mn^{4+} in Oxides with O_h Site Symmetry Based on First-Principles Calculations. *ECS J. Solid State Sci. Technol.* **2016**, 5, R3191-R3196.

66. C.D.S. Brites, A. Millán and L.D. Carlos. Chapter 281 - Lanthanide in luminescent thermometry. In *Handbook on the Physics and Chemistry of Rare* Earths; J.-C. Bünzli and V.K. Pecharsky, Eds.; Elzevier, **2016**; vol 49, pp.339-427.

CHAPTER 7

Bismuth-activated $CaSnO_3$: A Novel Persistent Phosphor

Abstract Novel bismuth-activated phosphors are highly desirable due to their low toxicity, low cost and promising optical properties. Here we demonstrated the simultaneous stabilization of Bi^{3+} and Bi^{2+} ions in $CaSnO_3$, discussing the energy transfer between the two luminescent centers and the persistent luminescence performance. The luminescence behaviour is compared to other Bi-activated Ca*B*O_3 perovskites, discussing the factors responsible for the metal-to-metal charge transfer character of the transitions. Temperature dependence of PL emissions, combined with empirical models are exploited to design the energy level diagram of the luminescent center respect to the conduction band and valence band energies of the host. The persistent luminescence performances of the material are analyzed and a tentative mechanism at the basis of the process is proposed. Moreover, the effect of the codoping with Tb^{3+} or with Cr^{3+} ions are investigated. Our results suggest that low-cost and low-toxic Bi-doped $CaSnO_3$ perovskite could be a promising candidate for developing persistent luminescent materials operating in the visible and in the NIR emission regions.

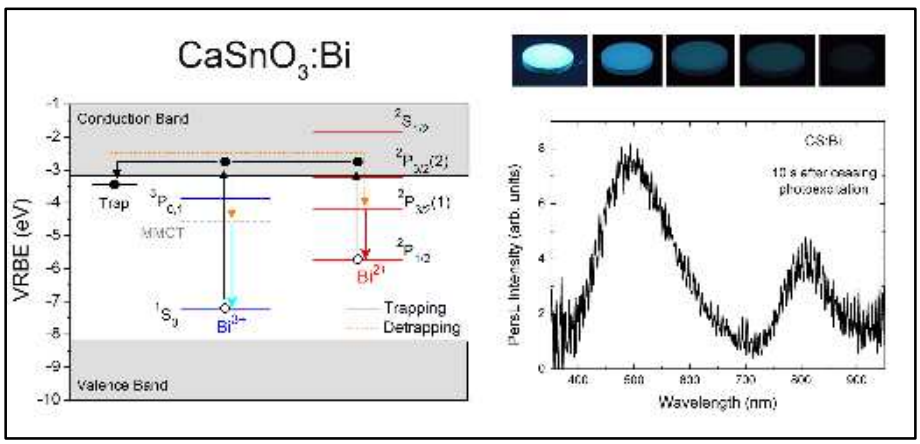

7.1 Introduction

Bismuth-activated luminescent materials have attracted increasing attention in recent years owing to their potentialities in a wide range of photonic applications such as new non-Ln phosphors, broadband amplifiers and fiber lasers.[1-3] These interesting properties of Bi-activated luminescent materials arise from the easy involvement in chemical bonds of the p-orbitals allowing, in principle, to a wide tunability of emissions. In particular, over the intriguing optical properties arising from the peculiar electronic configurations of bismuth ions, such as Bi^{3+} and Bi^{2+}, bismuth-based compounds emerge due to their relatively low cost, large availability, stability and rather low toxicity,[4-7] becoming particularly appealing also for biological applications.

Despite extensive efforts dedicated to the understanding of the optical properties of Bi^{3+} ion in solids,[8-12] many fascinating aspects are still debates.[13] The $^1S_0$ ground state of Bi^{3+} free ion has a $6s^2$ electronic configuration while the $6s^16p^1$ configuration gives rise to the triplets $^3P_0$, $^3P_1$, $^3P_2$ and singlet $^1P_1$ excited states. Transitions from the $^1S_0$ ground state to the excited states $^3P_1$, $^3P_2$ and $^1P_1$ are usually denoted as A, B and C, respectively. If the allowed C-transition is usually located in the VUV region, $^1S_0 \longrightarrow {}^3P_2$ transitions (B-bands) is spin forbidden, while the $^1S_0 \longrightarrow {}^3P_1$ transition (A-band) becomes allowed by spin-orbit coupling between $^3P_1$ and $^1P_1$. Finally, the transition from the GS to the lower energy excited state $^3P_0$ is strongly forbidden. Fast and parity allowed $6s^2 \longleftrightarrow 6s^16p^1$ inter-configurational transitions may lead to efficient excitations and emissions in Bi^{3+}-activated materials. However, many different luminescent signals ascribed to Bi-related structures are also frequently present and sometimes difficult to assign.[13,14] The so called D-state is of particular interest and it is usually considered to be originated from an impurity trapped exciton (TE) state[15] or describe as metal-to-metal charge transfer (MMCT) state.[16]

The recent interest in the development of Bi^{2+}-activated phosphors arises from their appealing ability to absorb the blue light and emit in the orange/red to near-infrared (NIR) region, with attractive perspectives in white-LED illumination devices charged by blue-LED.[17] From the pioneering works of Blasse *et al.* in 1994,[18,19] other Bi^{2+}-doped materials were discovered in the last two decades, showing a strong dependence of the absorption and emission on the selected crystal field host.[20] The stabilization of such unstable ion was achieved only by reducing atmosphere in particular hosts, such as borates,[19-22] sulfates[18,23] and phosphates.[24-26] Hence, the stabilization of Bi^{2+} in mild conditions and in new host compounds is an important challenge.

Bi-activated phosphors have strong potentiality also as persistent phosphors because of the great tunability of emissions over a wide range of wavelengths in the visible spectrum (Bi^{3+}) and in the red to NIR region (Bi^{2+}), with a strong absorption and high quantum efficiency. However, to date, even if bismuth codoping is reported as an effective method to enhance the persistent performances in different hosts,[27-30] only few studies on Bi-doped persistent luminescence materials in which bismuth ions act as luminescent centers have been reported.[31-36] Moreover, Bi^{2+}-activated phosphors with persistent luminescence in the NIR region are highly demanded, being considered as the next generation materials for bio-imaging probes.

In this Chapter, we have investigated the luminescent properties of Bi-activated $CaSnO_3$, discussing the metal-to-metal charge transfer band nature respect to other Ca*B*O3 perovskites (*B*=Ti, Zr) and analyzing the temperature dependence of the luminescence. In addition, the

persistent luminescent behaviour of the system is characterized and the effect of Tb and Cr codoping is investigated, showing an interesting enhancement of the Bi^{2+} emission at 800 nm induced by Cr^{4+} ion.

7.2 Sample Preparation

Un-doped $CaSnO_3$ (CS), Bi-doped $Ca_{0.995}SnO_3:Bi_{0.005}$ (CS:Bi), Bi,Tb-codoped $Ca_{0.9925}SnO_3:Bi_{0.005}Tb_{0.0025}$ (CS:Tb-Bi) and Bi,Cr-codoped $Ca_{0.9925}SnO_3:Bi_{0.005}Cr_{0.0025}$ (CS:Cr-Bi) samples were prepared by conventional solid-state reaction method. The chemical reagents SnO_2 (4N), $CaCO_3$ (4N), Bi_2O_3 (4N), Tb_2O_3 (4N) and Cr_2O_3 (4N) were used as starting materials, grounded in an alumina mortar to form homogeneous fine powder mixtures of the desire composition. The mixture was calcined at 800 °C for 3 h, cooled, grounded again and pressed into pellets (0.45 g, ϕ 15 mm) with a uniaxial loading of 50 MPa in a stainless steel mold. Then, the pellets were fired at 1200 °C for 4 h in air atmosphere.

7.3 Structural and Optical Properties

XRPD diffraction patterns of the samples show the single phase stabilisation of $CaSnO_3$ perovskite structure for all the samples (Figure 7.1). No other peaks are detected, confirming the goodness of the synthesis and the successful introduction of the doping cations into the perovskite structure. Alkaline-earth stannates of formula $ASnO_3$ (A=Ca, Sr, Ba) belong to perovskite structure class. $BaSnO_3$ has the ideal cubic perovskite structure composed by corner-sharing SnO_6 octahedra with Ba^{2+} ions into the cubo-octahedral cavities, while $CaSnO_3$ and $SrSnO_3$ are both distorted by cubic symmetry due to an octahedral tilting distortion with a consequent change in the oxygen and A-site cation environments. Such a distortion (very common in perovskite[37,38]), in the case of calcium and strontium stannate, results in an orthorhombic crystal structure (*Pnma* symmetry). Figure 7.1b shows the crystal structure of the orthorhombic $CaSnO_3$ perovskite.

Diffuse reflectance spectra of un-doped calcium stannate and Bi-doped $CaSnO_3$ are reported in Figure 7.1c, showing a clear absorption peak with a maximum at 305 nm. Recently, Yangthaisong[39] proposed an indirect bandgap semiconductor nature for orthorhombic $CaSnO_3$ by first principles calculations, in contrast with previous predictions of a direct-gap nature for this perovskite,[40,41] evidencing a still unclear situation regarding the semiconductor's nature. Figure 7.1d displays Tauc plots[42] of the Kubelka-Munk function[43] ($F(R)$) for both direct and indirect transitions. The $(F(R)\cdot h\nu)^2$ *versus* $h\nu$ plot yields a direct bandgap of 4.70 ± 0.05 eV, while the indirect bandgap extrapolated by $(F(R)\cdot h\nu)^{1/2}$ *versus* $h\nu$ plot is estimated to be 4.39 ± 0.05 eV, in agreement with previous estimations reported in literature.[44,45]

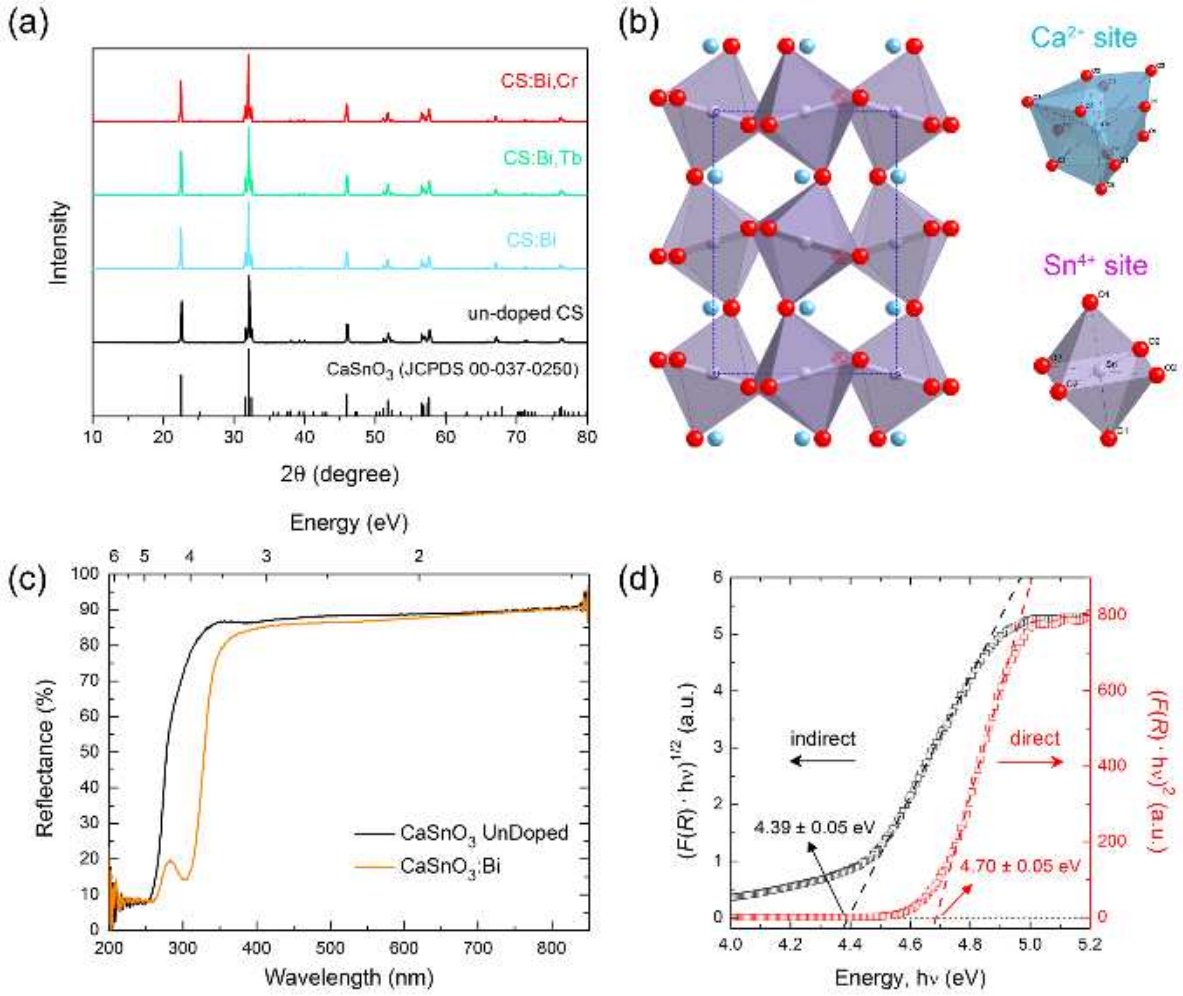

Figure 7.1 (a) XRPD patterns of the samples. (b) Crystalline structure of the perovskite $CaSnO_3$ and Ca^{2+} and Sn^{4+} sites. (c) Diffuse reflectance spectra of the CS and CS:Bi samples and (d) Tauc plot of Kubelka-Munk function $F(R)$ as a function of energy hν for CS obtained from optical reflectivity analysis. Assuming indirect and direct transitions, absorption edges at 4.39 eV and 4.70 eV are observed, respectively.

Figure 7.2a shows the PL and PLE spectra of CS:Bi exciting at 310 nm and collecting at 460 nm, respectively. The PLE spectrum is composed by two bands, with maximum peaks at 258 nm and 307 nm, respectively. The peak at higher energy (4.79 eV) can be assigned to the host exciton absorption, in perfect agreement with the diffuse reflectance analysis (see Figure 7.2b) and the bandgap energy estimation. The strong absorption by host exciton indicates efficient energy transfer process from the host to the activators.

By considering (i) the large Stokes shift (1.33 eV) between the absorption peak at 307 nm and the emission peaked at 460 nm, (ii) the low emission energy respect to the typical UV emissions of Bi^{3+}-activated oxide materials and (iii) the large Full Width at Half Maximum (FWHM) of 0.66 eV, we assign this peak to the D-state, in agreement with the observations of Srivastava.[46]

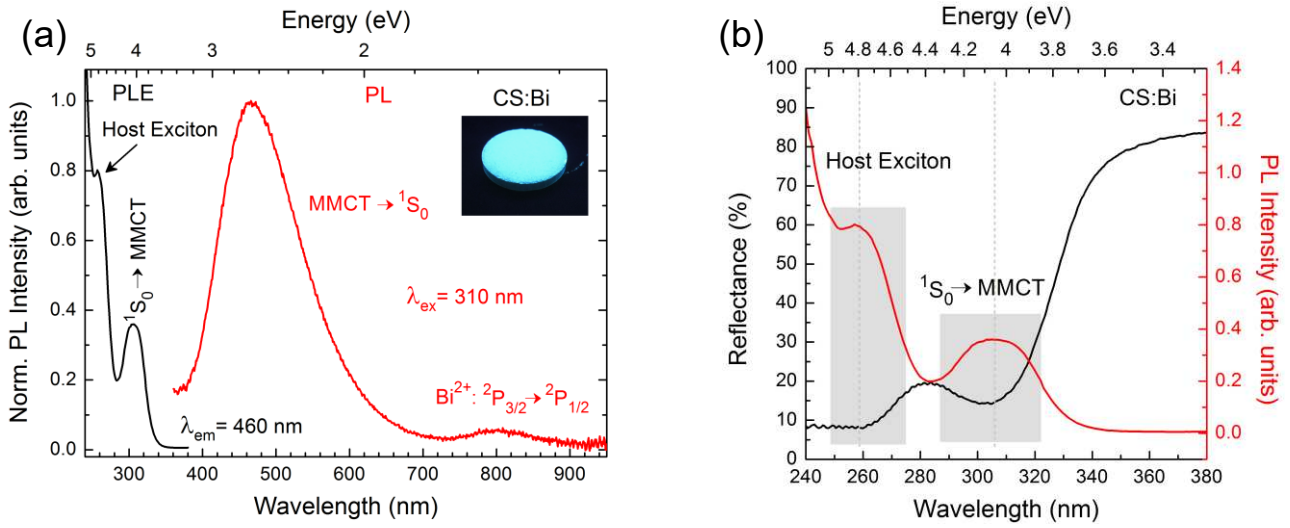

Figure 7.2 (a) PL and PLE spectra of Bi-doped CaSnO3 sample, collected exciting at 310 nm and collecting the emission at 460 nm, respectively. The picture is collected exciting the sample under the UV lamp. (b) PLE (λ_{em}=460 nm) and diffuse reflectance spectra comparison.

It is important to underline that, in addition to the MMCT emission, under 310 nm excitation, the CS:Bi sample exhibits a weak photoluminescent band centred at 800 nm that can be ascribed to $^2P_{3/2}$ (1) ⟶ $^2P_{1/2}$ transition of Bi^{2+} ion. In order to corroborate the goodness of this assignment, PLE spectrum was collected following the emission at 800 nm (Figure 7.3a). The spectrum shows the typical Bi^{2+} absorption peaks due to the $^2P_{1/2}$ ⟶ $^2S_{1/2}$ and $^2P_{1/2}$ ⟶ $^2P_{3/2}$ (2) at about 318 nm and 500 nm, respectively (the scheme of energy levels of Bi^{2+} is reported in Figure 7.3b). It is worth mentioning that the stabilization of Bi^{2+} ions was achieved by substituting Ca^{2+} ions, without the need of reducing atmosphere. A Bi-activated $CaSnO_3$ sample synthesized in inert condition was prepared, showing the same luminescent properties of the sample treated in air atmosphere.

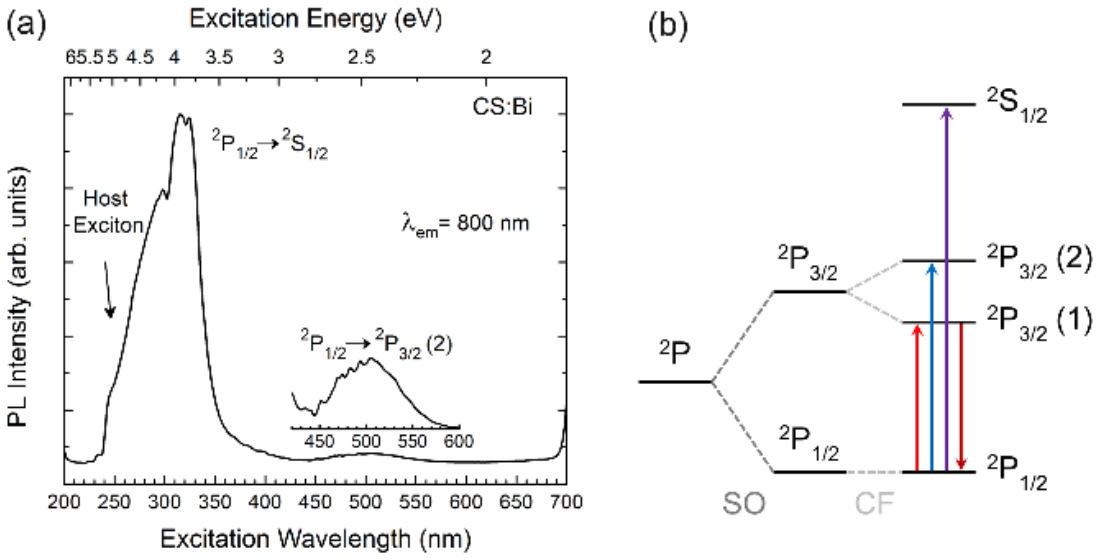

Figure 7.3 (a) PLE spectrum of Bi^{2+} in CS collecting at 800 nm and (b) energy level diagram of the $6s^26p^1$ electronic configuration with spin-orbit (SO) coupling and crystal field (CF) splitting.

7.4 Temperature Dependent PL and PLE

The temperature dependent PL emission spectra were analyzed in the temperature range of 80-600 K. Figure 7.4a shows an evident decrease of the emission at 460 nm from the MMCT state at increasing temperature, while the emission at about 800 nm ascribed to the $^2P_{3/2}$ (1) ⟶ $^2P_{1/2}$ transition of Bi^{2+} ion increases with the temperature. In addition, in agreement with the emission spectrum collected at 10 K showed in ref 42, a weak peak due to the $^3P_{0,1}$ ⟶ $^1S_0$ transition of Bi^{3+} ion was detected at low temperature (Figure 7.4b).

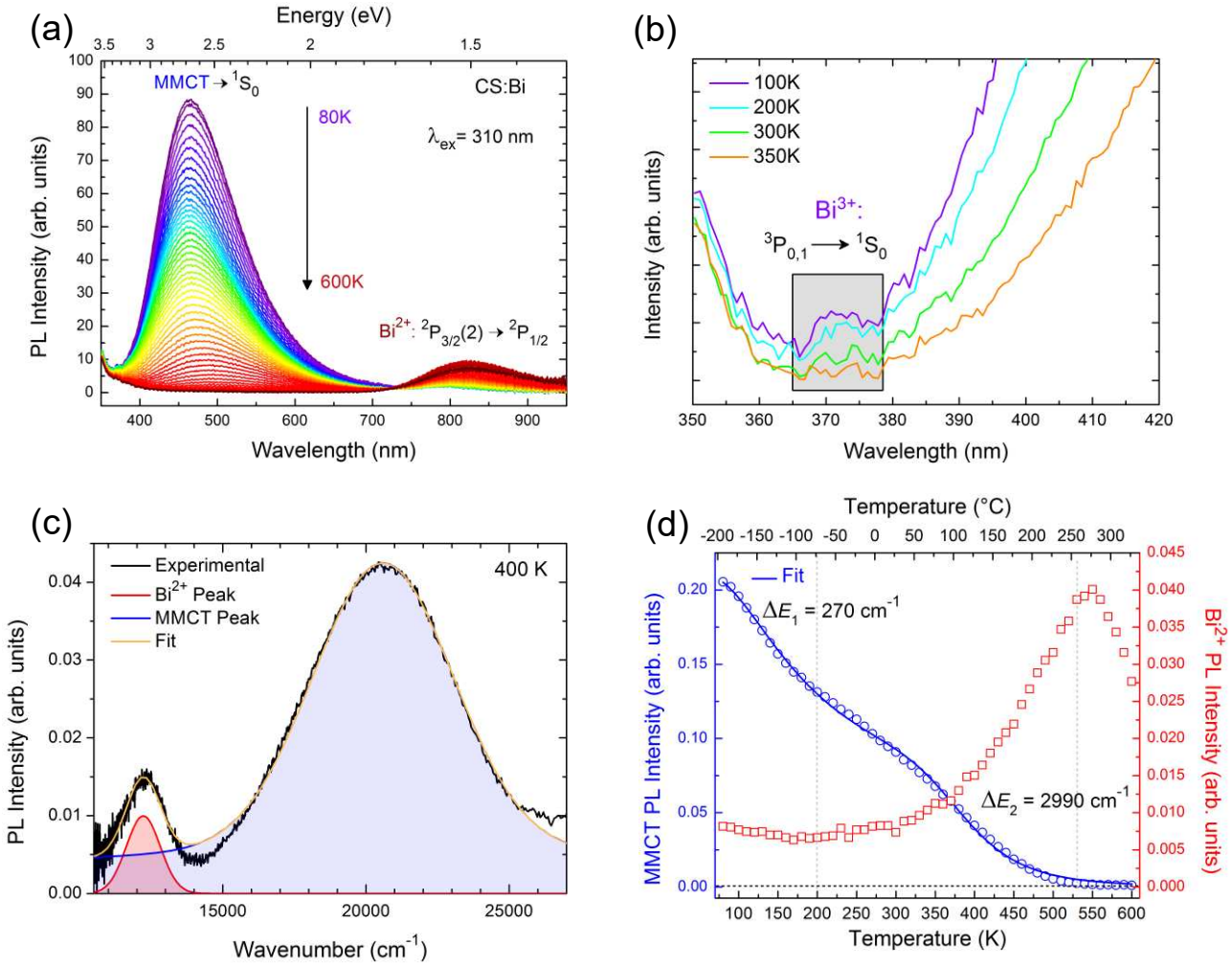

Figure 7.4 (a) Temperature dependence of PL emission of CS:Bi sample in the 80-600 K temperature range. (b) Magnification of the PL spectra at 100, 200, 300 and 350 K with Bi^{3+} emission peak at 100 and 200 K. (c) Deconvolution of the PL spectrum collected at 400 K. (d) Temperature dependence of integrated PL intensities of the transitions from MMCT state (blue circles) and $^2P_{3/2}$(2) (red squares), and fit (blue curve) for the thermal quenching processes of the luminescent emission for the MMCT state.

In order to properly describe the temperature dependence of the system, the energy scale spectra (converted by considering the Jacobian transformation) were deconvoluted. Figure 7.4c shows, as example, the deconvolution of the PL spectrum at 400 K. The plot of the integrated area intensities of the two transitions as a function of temperature, reported in Figure 7.4d, can not be reproduced

by means of the simple crossover quenching process described by Struck and Fonger model.[47] This indicates that several processes contribute to the luminescence quenching and two different regions can be distinguished: (i) up to about 200 K, a first decrease process for the blue emission seems to have no influence on the NIR emission of Bi^{2+}, which remains constant, while (ii) at higher temperature, the decrease of the MMCT emission corresponds to an increase of NIR emission from Bi^{2+} excited state, at increasing temperature. The two different processes can be well described by considering the following equation:

$$I(T) = \frac{I(0)}{1 + C_1 exp(-\Delta E_1/k_B T) + C_2 exp(-\Delta E_2/k_B T)} \quad (7.1)$$

The solid line in Figure 7.4d represents the best fit of the data (open circles) evidencing the suitability of the model expressed by the equation. The fit allowed to estimate the activation energies ΔE_1 (270±10 cm^{-1}) and ΔE_2 (2990±120 cm^{-1}) of the quenching processes evidenced for the MMCT emission.

Figure 7.5a shows the temperature dependence of the PLE spectra, following the blue emission at 460 nm in a temperature range of 100-600 K.

As underline in the normalized view of the temperature dependence trend of PLE (Figure 7.5b), a clear red-shift in the absorption peaks is shown with the increasing of the temperature. The trend is consistent with the PL emission behaviour of the MMCT emission. Moreover, no other peaks were detected.

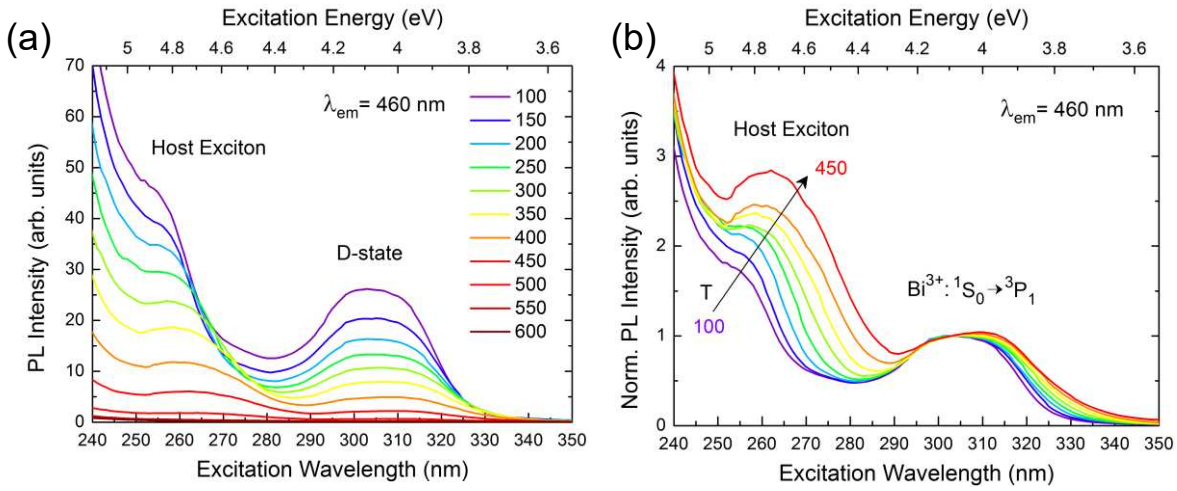

Figure 7.5 (a) Temperature dependence of PLE spectra of CS:Bi monitoring 460 nm emission and (b) temperature dependence of PLE trend normalized to the D-state absorption peak.

7.5 Persistent Luminescence Performances and Thermoluminescence

In addition to the steady-state photoluminescence, CS:Bi shows persistent luminescence properties. Figure 7.6 shows the photographs of the sample under UV lamp and at different times after the ceasing of the exciting source, the persistent luminescence (PersL) spectrum and the

persistent luminescence decay curve collected at 470 nm. In the persistent luminescence spectrum of CS:Bi collected 10 s after the ceasing of the charging process, persistent luminescence from both the MMCT-state transition and $^2P_{3/2}$ (1) ⟶ $^2P_{1/2}$ transition of Bi^{2+} were observed (Figure 7.6b).

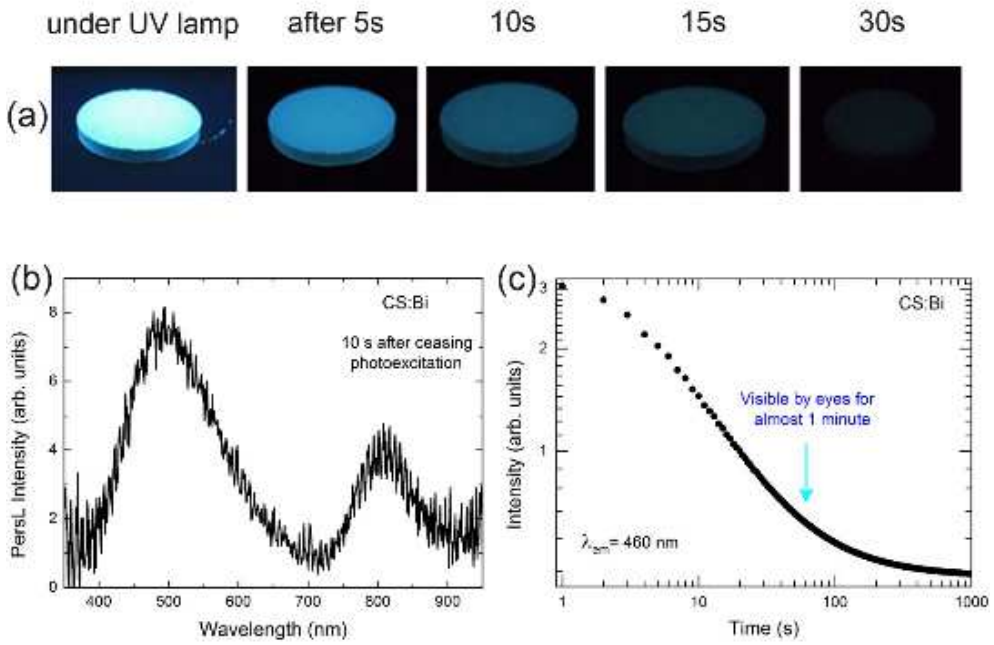

Figure 7.6 (a) Photographs under and after switching off the UV lamp at different times, (b) PersL spectrum 10 s after the ceasing of the excitation source and (c) PersL decay curves of the CS:Bi sample.

It is interesting to note that the relative intensity of the two emissions is different respect to the steady-state photoluminescence, with a relative increase of the peak due to the Bi^{2+} respect to the MMCT transition. Even if the nature of a stable charge transfer state, able to become a persistent luminescence center, is actually not clear (charge transfer states are usually transient states), other persistent luminescent materials such as $CaTiO_3:Pr^{3+}$ involve charge transfer states in the persistent mechanism.[48,49] However, to the best of our knowledge, this is the first example of persistent luminescence from a MMCT-state. The intensity of the persistence luminescence is not strong enough to allow the measure of the persistent luminescence decay curve by means of luminance, however the persistent emission can be watched by eyes for about one minute and the decay curve (reported in double logarithmic scale) evidences the typical shape of persistent materials.

The comparison of the steady-state photoluminescence spectrum with the PersL spectrum (Figure 7.7) evidences a significant red-shift of the emission from 460 nm to about 500 nm, while the emission from Bi^{2+} at about 800 nm remains unchanged.

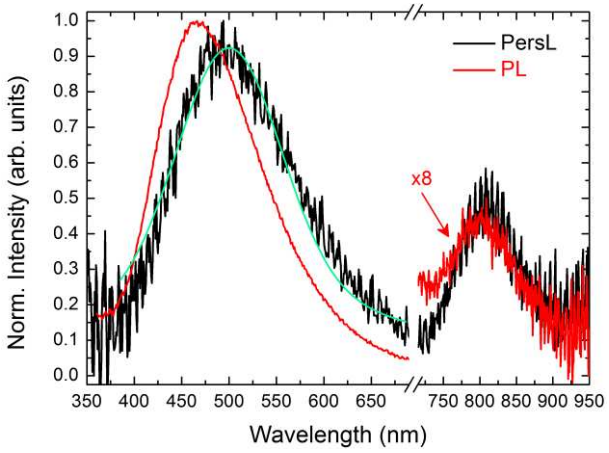

Figure 7.7 Comparison of the persistent luminescence (PersL) with the steady-state photoluminescence (PL) spectra. Green peak represents the result of the MMCT emission peak fit.

A red-shift of PersL spectra respect to the steady-state one was reported in other materials such as $M Al_2Si_2O_8:Eu^{2+}$ (M=Ca, Sr, Ba),[50] $Ca_2Ge_7O_{16}:Nd^{3+}$,[51] $Ca_2Si_5N_8:Eu^{2+}$ [52,53] and $Ca_2SiS_4:Eu^{2+}$, Nd^{3+}.[54] Li *et al.*[52] imputed the red-shift in $Ca_2Si_5N_8:Eu^{2+}$ system to the presence of two different crystallographic Ca-sites, while Clabau *et al.*[50] suggested the perturbation induced by an oxygen vacancy in the proximity to the crystal site of the alkaline-earth as the origin of the red-shift in aluminosilicates. In $CaSnO_3$, from the structural point of view, only one site is accessible for Ca^{2+}, then site of substitution for Bi. However, the exact nature of the different behaviour characterizing persistence and steady-state emission in not clear yet.

In order to investigate the trap distribution responsible for the persistence luminescence of the material, the thermoluminescence (TL) glow curve of the CS:Bi sample was collected. The TL curve shown in Figure 7.8, exhibits a peak at 136 K. To estimate the mean energy of the trap depth E_T, the simple formula reported by Urbach[55] was used:

$$E_T = \frac{T_m}{500} \tag{7.2}$$

leading to a trap depth of 0.27 eV. This shallow traps explain the short persistent luminescence of the material.

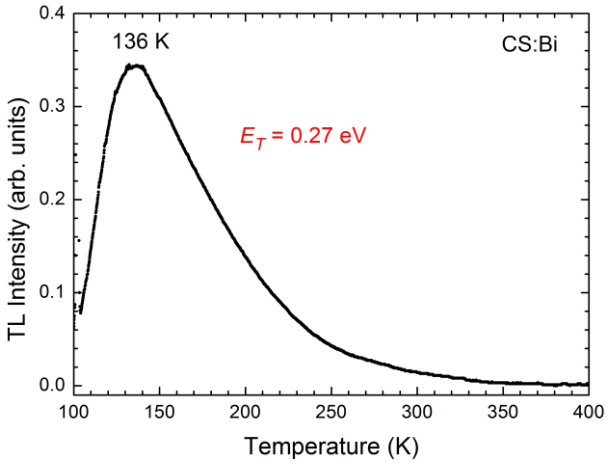

Figure 7.8 Thermoluminescence (TL) glow curve of the CS:Bi sample collecting at 460 nm.

Even if the nature of the trap level is unknown, it is interesting to note that the TL glow curve is completely different from that one previously reported for other persistent systems in which $CaSnO_3$ is used as host.[56,57] Liang *et al.* reported a single TL peak at about 370 K for $CaSnO_3:Tb^{3+}$ persistent system,[56] while two TL peaks at about 325 and 350 K were reported for Sm^{3+}-doped $CaSnO_3$ persistent phosphor.[57] All this trap levels were assigned to defects generated by the introduction of the trivalent lanthanide ions to replace the divalent Ca^{2+}. Hence, in our system, the trap level seems to be associated to bismuth ions or bismuth induced defects of a different nature.

7.6 Vacuum Referred Binding Energies of MMCT and Bi^{2+} in $CaSnO_3$

By a detailed analysis of experimental data reported in literature, Boutinaud *et al.*[13] proposed a model to predict the energy of MMCT transitions in oxide compound containing Bi^{3+}. For a M^{n+} with coordination numbers larger than 4 (as in the case of Sn^{4+}), the following empirical equations was proposed:

$$\mathrm{MMCT}(\mathrm{Bi}^{3+}, \mathrm{cm}^{-1}) = 55000 - 45500\ \frac{\chi_{\mathrm{CN}'}(\mathrm{M}^{n+})}{d_{corr}}. \tag{7.3}$$

$\chi_{\mathrm{CN}'}(\mathrm{M}^{n+})$ is the electronegativity (considering the new scale reported by Li and Xue[58]) for the host cations M^{n+} with coordination number CN' and d_{corr} is the shortest distances between the M^{n+} site and the cation site available for Bi^{3+} (Ca^{2+} in this work), corrected to the anion relaxation effect by considering the following formula:[59]

$$d_{corr} = d_{host} + \frac{1}{2}[r(\mathrm{Bi}^{3+}) - r(\mathrm{host})] \tag{7.4}$$

where $r(\mathrm{Bi}^{3+})$ is the Bi^{3+} ionic radius and $r(\mathrm{host})$ is the ionic radius of the host cation substituted by Bi^{3+} ion. With this model, the absorption into the MMCT state (D-state) is predicted to occur at about 316 nm, confirming the assumption of a MMCT-state nature ($Bi^{3+}+Sn^{4+} \longrightarrow Bi^{5+}+Sn^{2+}$) of the peak observed in the excitation spectrum of CS:Bi. In addition, the luminescence from the MMCT-state gives rise to the broadband Stokes-shifted emission. It is important to note that the charge transfer mechanism considered herein between Bi^{3+} and Sn^{4+} results in a two electrons process. In addition, from the structural point of view, the distorted orthorhombic perovskite structure is characterized by a short distance between the Sn^{4+} ion site and the Bi^{3+} substituting site of Ca^{2+} ion, promoting the process.

With the aim to compare the bismuth luminescence in different $A^{2+}B^{4+}O_3$-type orthorhombic perovskite structures and try to spread light on the metal-to-metal charge transfer state behaviour of Bi in such compounds, $CaTiO_3$:Bi and $CaZrO_3$:Bi samples were synthesized. Both the samples showed orthorhombic *Pnma* perovskite structure and no other peaks were detected, ensuring the goodness of the synthesis (not shown).

Figure 7.9a shows the typical luminescent features of the $CaBO_3$:Bi systems (*B*=Ti, Sn, Zr). The photoluminescence analyses are in agreement with the optical behaviour reported in literature.[14,46,60]

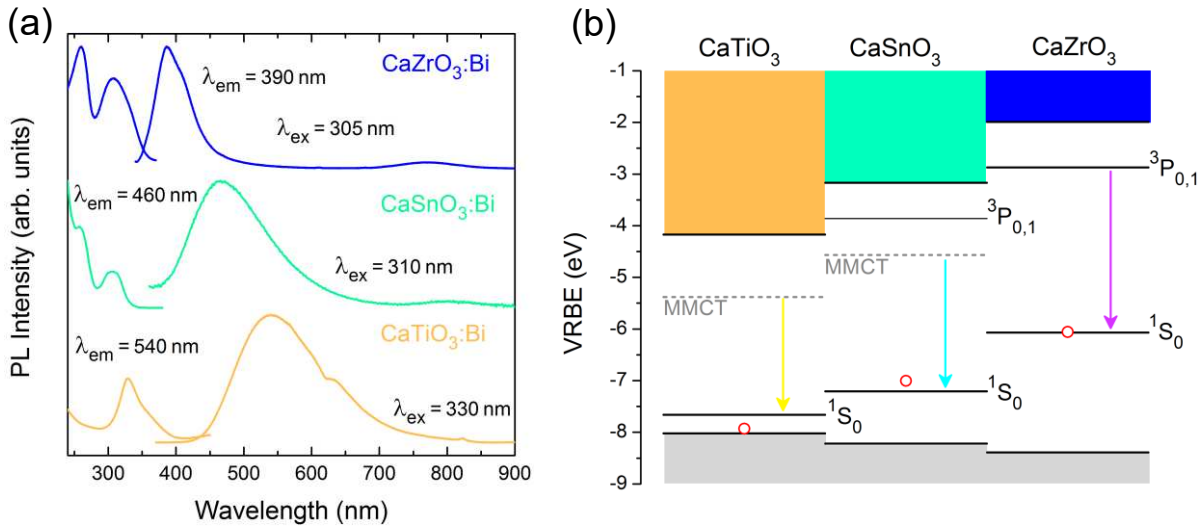

Figure 7.9 (a) PL and PLE spectra for Ca*B*O_3:Bi systems (*B*=Zr, Sn, Ti) and vacuum referred binding energy (VRBE) diagram constructed by experimental and theoretical data. The red circles represent the $^1S_0$ ground state energy estimated from the theoretical values calculated for the MMCT-state absorption using Equ. 7.3.[13]

By considering the equation proposed by Boutinaud *et al.*[13] and the same definition of corrected distances d_{corr} and values of electronegativity *EN* previously reported, the theoretical MMCT states energies were calculated and compared with experimental ones, as summarised in Table 7.1. It is important to point out that for a reliable calculation of the peak position, the spectra were considered in energy scale after suitable transformation. A certain discrepancy between the values in $CaTiO_3$ and $CaZrO_3$ is evidenced; however, for both the compounds, the discrepancy is within the accuracy of ±0.37 eV for the prediction of the MMCT energies,[13] with a good consistency between experimental and theoretical analyses.

Table 7.1 Experimental and calculated energy values of MMCT state, VB and CB for the Ca*B*O_3 perovskites doped with bismuth.

Perovskite	EN[a]	d_{corr}[b] (Å)	$MMCT_{Theor}$[c] (eV)	$MMCT_{Exp}$ (eV)	E_V[d] (eV)	E_C[d] (eV)
$CaZrO_3$:Bi	1.61	3.3	4.07	4.08	-8.39	-1.99
$CaSnO_3$:Bi	1.706	3.225	3.84	4.04	-8.22	-3.17
$CaTiO_3$:Bi	1.73	3.19	3.76	3.50	-8.02	-4.07

[a] electronegativity values from ref. 54; [b] calculated from Equ. 7.4; [c] calculated from Equ. 7.3; [d] VB and CB energies of $CaZrO_3$ from ref. 61 and of $CaSnO_3$ and $CaTiO_3$ from ref. 62.

The photoluminescence emissions display a clear red-shift trend of the emission band moving from $CaZrO_3$ to $CaSnO_3$ and $CaTiO_3$. As reported in Table 7.1, this red-shift trend seems to be related to the EN of the B^{4+} cation and the d_{corr} distance, with an increase of the emission wavelength (decrease of the energy) at the increasing EN and the consequent decreasing distances between Bi^{3+} site and B^{4+} in the structures. The electronegativity of B^{4+} ion directly influences also the band structure of the $CaBO_3$ perovskites.

To provide a detailed explanation about the effect of the different B^{4+} cation choice on the optical properties of Bi^{3+} for $CaBO_3$ perovskite family, the Dorenbos and Rogers approach,[63] together with the empirical model proposed by Boutinaud and Cavalli,[13,14] were considered. The energies of the top of the valence band (VB) and the bottom of the conduction band (CB) used in the construction of VRBE diagram of Figure 7.9b are summarised in Table 7.1. The energy of the MMCT state represents the gap between the Bi^{3+} ground state $^1S_0$ and the bottom of the conduction band, allowing the location of the Bi^{3+} ground state in the VRBE diagram ($^1S_0$ ground state from the theoretical and experimental MMCT-state absorption are described as a red circle and a line, respectively). Moreover, where visible by experiments, the first excited state $^3P_1$ can also be recognised. The VRBE diagrams of the Bi^{3+} respect to the MMCT-state for the three perovskites are depicted in Figure 7.3b. As previously discussed, MMCT states are characterized by large Stokes shift and FWHM, indicating such kind of character for $CaSnO_3$ and $CaTiO_3$, as shown in Figure 7.9a, while $CaZrO_3$ emission can be ascribed to the first excited state $^3P_1$ of Bi^{3+}. According to the energies of the emission bands of $CaTiO_3$:Bi and $CaSnO_3$:Bi systems, the bottom of the MMCT-state can be depicted in the diagram (dashed grey line). From this analysis, in regard to the band structure of the $CaBO_3$:Bi systems (B=Ti,Sn,Zr), it can be inferred that the EN and d_{corr} values of $CaZrO_3$ system seem to be the highest and lowest threshold values, respectively, for the stabilization of the MMCT state with an energy lower than the first Bi^{3+} excited state. Even if this analysis is limited to the orthorhombic perovskite with $CaBO_3$ structure, this is an important starting point for the development of new strategies for the design of Bi-based materials.

With the aim to disclose the mechanism of the persistent luminescence of Bi-activated $CaSnO_3$ and to qualitatively describe the temperature dependence of the luminescence of the material, the vacuum referred binding energy (VRBE) diagram with the energy levels of both Bi^{3+} and Bi^{2+} ions was built (see Figure 7.10). As previously discussed, the absolute values for the bottom of the conduction band (-3.17) and the top of the valence band (-8.22 eV) of $CaSnO_3$ are taken from ref. 62. Moreover, the MMCT absorption band at 4.04 eV allows to allocate the Bi^{3+} ground state $^1S_0$ at -7.21 eV, and consequently, from the PL spectra, the energy level of the emitting MMCT state and of the $^1P_{0,1}$ excited state can be estimated at -4.57 eV and -3.86 eV, respectively (as inferred in Figure 7.9b).

The PL spectrum in Figure 7.2a shown the simultaneous emission from the MMCT state with the Bi^{2+} emission band originating from the $^2P_{3/2}(1)$ excited state. Similar to that recently reported by Awater and Dorenbos[64] for Bi^{2+} in $Li_2BaP_2O_7$, $^2P_{3/2}(1)$ excited state is expected at an energy below the CB and, in particular, to take into account the emission collected at high temperatures, $^2P_{3/2}(1)$ is estimated to be located at least 1 eV below the bottom of the conduction band. In this way, by considering the emission at 800 nm and based on the excitation energies in Figure 7.3, the ground state $^2P_{1/2}$ and the excited states $^2P_{3/2}(1)$, $^2P_{3/2}(2)$ and $^2S_{1/2}$ are located at -5.72, -4.17, -3.24 and -1.82 eV, respectively.

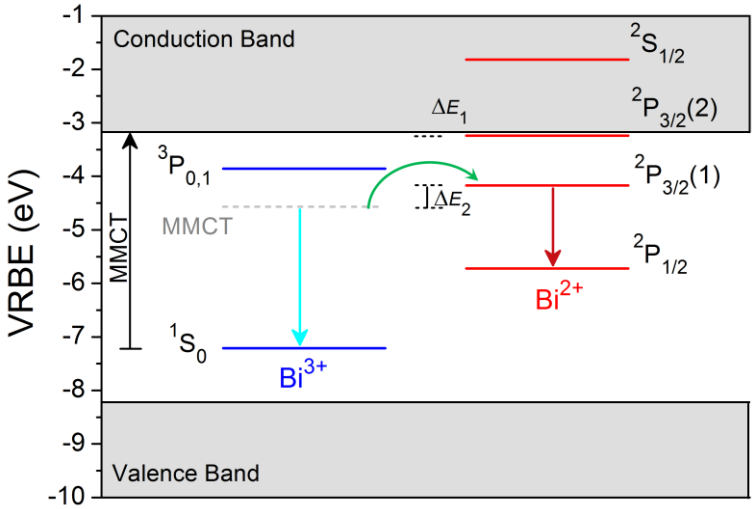

Figure 7.10 Vacuum referred binding energy scheme of Bi^{3+} and Bi^{2+} respect to the energy of the bottom of the CB and the top of the VB of $CaSnO_3$ host.

Concerning the VRBE diagram depicted in Figure 7.10, it is interesting to consider the PL temperature dependence behaviour described in Section 7.4. The trend of the PL area as a function of the temperature for the MMCT state describes a situation in which two distinguished quenching processes take place. The first process is characterized by a small activation energy ΔE_1 of 270±10 cm^{-1} (0.033 eV) in concomitance with a slight decrease of the Bi^{2+} emission. The analysis was conducted by exciting at 310 nm, bringing the electrons of both the Bi^{3+} and the Bi^{2+} ground state into the CB through which the electrons can move to the excited state of both the ions. The activation energy of this first process at low temperature is consistent, within the errors, with the energy difference between the $^2P_{3/2}(2)$ excited state and the bottom of the CB (gap of 0.07 eV), explaining the decrease of the Bi^{2+} emission as a feeding process to the CB. At higher temperatures, a second thermal process is linked to the decrease of the MMCT emission band with the increase of the Bi^{2+} emission at 800 nm. These simultaneous behaviours for the two emission bands suggests a potential interaction between Bi^{3+} and Bi^{2+} ions and a different pathway respect to the other thermal process occurring through the CB. Hence, by considering the VRBE diagram, an excellent agreement between the MMCT state and $^2P_{3/2}(1)$ energy gap (0.4 eV), and the activation energy ΔE_2 of 2990±120 cm^{-1} (0.37 eV) characterizing this second thermal process, was found. This assumption suggests a thermally activated energy transfer process from the MMCT state to the $^2P_{3/2}(1)$ excited state of Bi^{2+} and it is consistent with the results of all the reported analyses.

It is worth mentioning that for both the quenching processes, the activation energies show the same small mismatch of about 0.04 eV with respect to the VRBE diagram energy levels previously depicted, suggesting a slightly downshifted position of 0.04 eV for the energy levels of Bi^{2+}. In this view, the potentiality of a comprehensive analysis that consider both experimental temperature dependent PL behaviour and the theoretical VRBE diagram design is demonstrated.

TL analysis reported in Figure 7.8 has evidenced a trap distribution with a depth around 0.27 eV below the bottom of the CB. By considering an electron trap level characterized by such trap depth, the VRBE diagram depicted in Figure 7.11 allows to describe the possible persistent

luminescence mechanism for $CaSnO_3$:Bi system, in which trapping and detrapping processes (solid black arrows and dashed orange arrows, respectively) consist in an electron transfer process between luminescence centers and trapping *via* the conduction band. This mechanism accounts for the simultaneous PersL emissions originating from both the excited states.

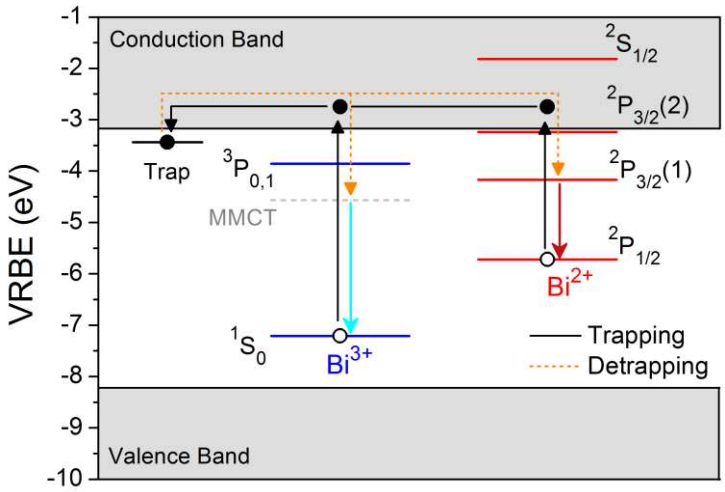

Figure 7.11 Persistent luminescence process for Bi-activated $CaSnO_3$ by VRBE diagram. Solid black and dashed orange arrows represent the trapping and releasing processes, respectively.

7.7 Tb^{3+} and Cr^{3+} co-doping Effect on Bi-activated $CaSnO_3$

In addition to the Bi-single-doped sample, Bi-Tb and Bi-Cr codoped samples were synthesized. The XRPD patterns confirm the single phase stabilization for both the samples (Figure 7.1a). The diffuse reflectance spectrum of the Bi-Tb codoped sample reported in Figure 7.12 shows the same behaviour of the single doped sample reported in Figure 7.1c, without evidence of Tb^{3+} absorption.

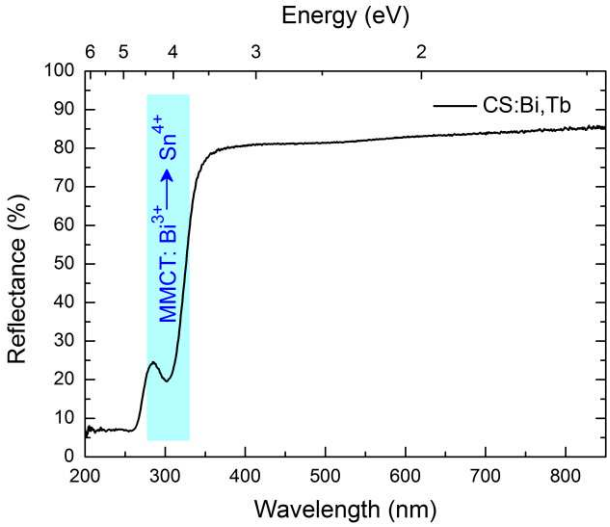

Figure 7.12 Diffuse reflectance spectrum of CS:Bi,Tb sample.

However, once excited, the sample shows the simultaneous emission from the MMCT state and from Tb^{3+} excited states (Figure 7.13). The PLE spectrum is composed by two absorption peaks

due to the host absorption and MMCT state ($Bi^{3+} \longrightarrow Sn^{4+}$) at the same energies of the Bi-single-doped sample, without other absorption peaks. Hence, the PLE spectrum suggests an energy transfer from the charge transfer state to Tb^{3+} leading to the simultaneous emission from both the MMCT-state and the Tb^{3+}, excited states. The picture of the sample under the UV lamp shown in the inset of Figure 7.13, displays a similar color output with respect to the CS:Bi sample, apart for a slightly green character due to the Tb^{3+} emissions.

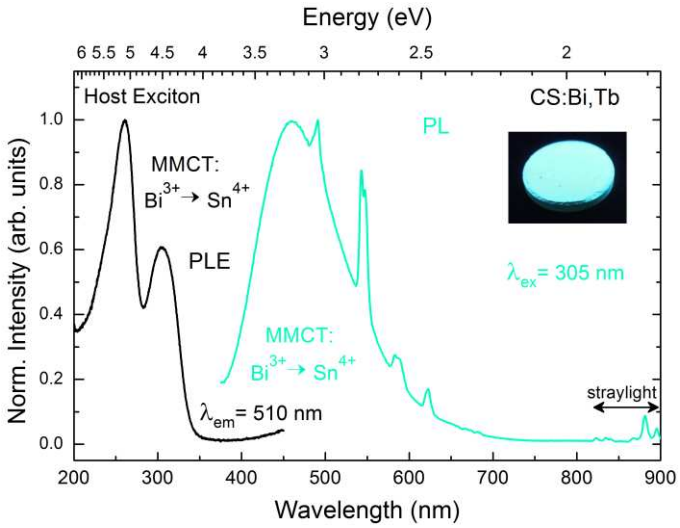

Figure 7.13 PL and PLE spectra of the Bi,Tb codoped $CaSnO_3$ sample exciting at 305 nm and collecting at 510 nm, respectively.

In contrast with the PL color output, dominated by the MMCT emission band, in the PersL spectra the relative intensity of the MMCT state with respect to the Tb^{3+} related transitions progressively changes, with a greener character due to the typical Tb^{3+} f-f transitions. This trend can be explained by the different pathway in the two distinct regimes. Figure 7.14 shows the PersL spectra collected at different times and various photographs of the sample under and after the ceasing of the UV lamp. In addition, as a comparison, Figure 7.15 evidences the same intensity ratio between Tb^{3+} and Bi-related peaks after 10 and 60 s, suggesting the same PersL mechanism.

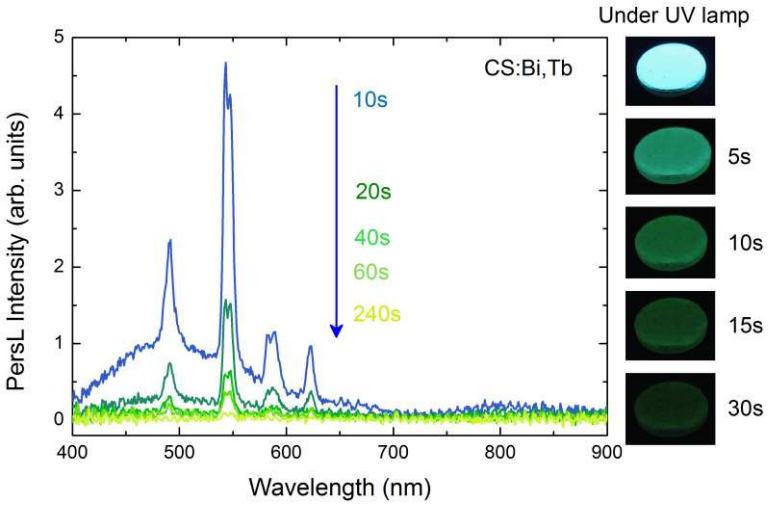

Figure 7.14 Persistent luminescence spectra of the CS:Bi,Tb sample as a function of time (10, 20, 40, 60, 240 s) after ceasing the exciting UV source.

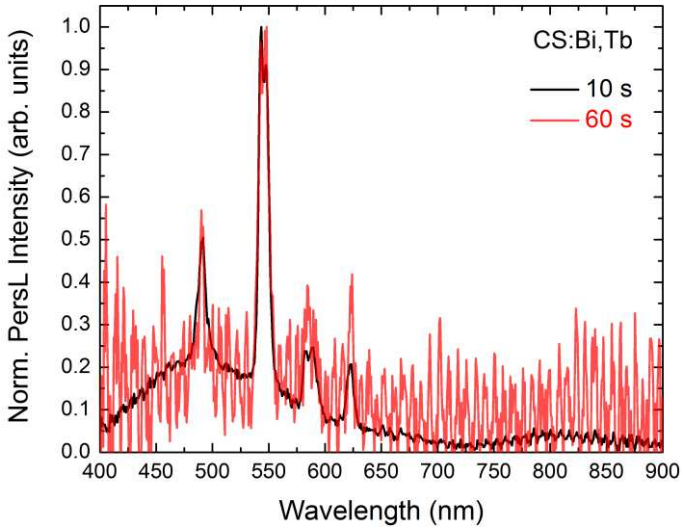

Figure 7.15 Comparison of the normalized PersL spectra collected 10 s and 60 s after ceasing of the UV lamp.

TL glow curve of the CS:Bi,Tb sample is shown in Figure 7.16. By means of the simple Eq. 7.2, a trap depth of 0.78 eV is estimated. The complete different shape of the TL glow curve respect to that one obtained for the Bi-single-doped sample of Figure 7.8 attests the different kind of trapping center induced by the non-equivalent substitution of Ca^{2+} with trivalent lanthanide ions like Tb^{3+} or by Bi^{3+}, reflecting the deeply different nature of the lanthanide ions respect to that of Bi^{3+}.

The peak at 391 K is in agreement with the TL peak at about 370-380 K reported by Liang *et al.*[56] for Tb^{3+}-doped $CaSnO_3$. However, it is remarkable that, in our case, the TL peak is very broad.

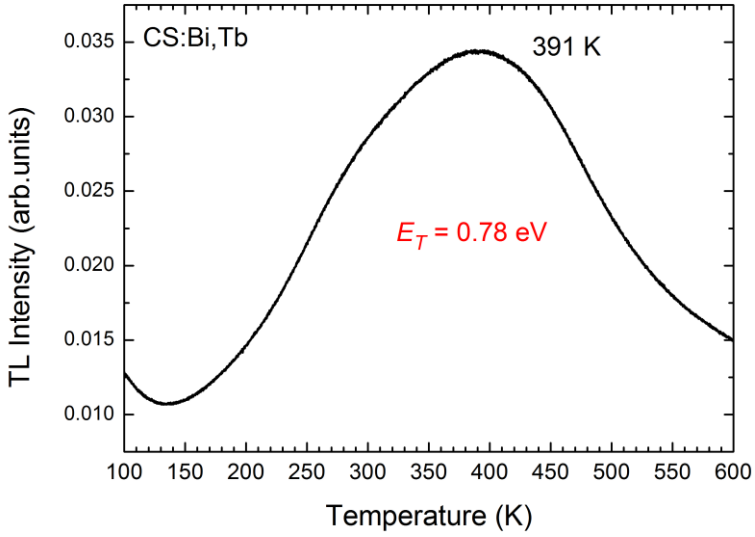

Figure 7.16 Thermoluminescence (TL) glow curve of the CS:Bi,Tb codoped sample.

For a better comprehension of the mechanisms involved in the luminescent properties of phosphors, we have previously demonstrated the potentialities of the VRBE diagram design. Therefore, as described in Section 2.6, the values reported by Dorenbos[62] for lanthanide ions in $CaSnO_3$ together with the description reported below for Bi-single-activated $CaSnO_3$ were used

to build the VRBE diagram of Tb^{3+}, Bi^{3+} codoped $CaSnO_3$ (see Figure 7.17). The different nature of the trap levels responsible for the PersL properties of the MMCT state and the Tb^{3+} could be responsible for the different ratio between the two luminescent center emissions in the steady-state PL and PersL spectra. Nevertheless, to date, the reason is not completely understood.

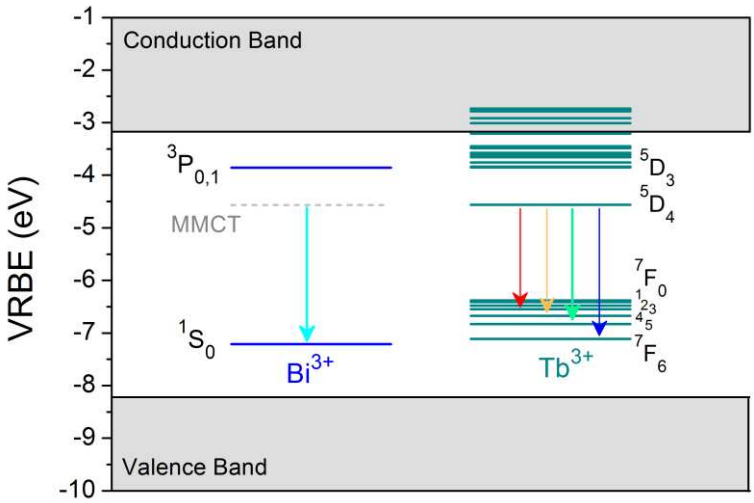

Figure 7.17 VRBE scheme of Bi^{3+} and Tb^{3+} respect to the energy of the bottom of the CB and the top of the VB of $CaSnO_3$ host.

In conclusion, a sample synthetized codoping with bismuth and chromium is prepared, showing a considerably different situation. First of all, it is interesting to point out the change of the powder color into pink-red (picture in Figure 7.18). The diffuse reflectance spectrum evidences that this behaviour can be linked to a very broad absorption band centered at about 520 nm. Even if red color usually suggested the stabilization of Cr^{3+}, on the other hand Cr^{4+} ion stabilization was demonstrated in this kind of perovskite structure, and in particular in the case of $CaSnO_3$.[65,66] The absorption feature at 520 nm is thus related to the Cr in 4+ state.

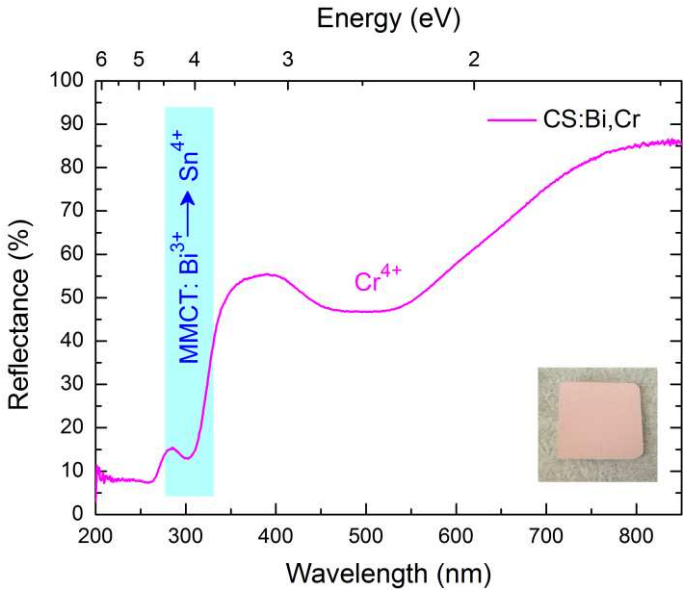

Figure 7.18 Diffuse reflectance spectrum of CS:Bi,Cr codoped sample and photograph of the sample.

As emerging from the spectra of Figure 7.19, we observe the enhancement of the emission band centered at 800 nm, presumably due to Bi^{2+} ion $^2P_{3/2}(1) \rightarrow {}^2P_{1/2}$ transition and the suppression of the blue emission at about 470 nm, due to the MMCT state. In addition, also the PersL spectrum consists of just a single band emission at 800 nm that can be collected for about 2 minutes (Figure 7.19b).

Even if these are only preliminary results, it is worth remarkable that the system shows a single persistent emission band that falls in the first biological window, with appealing properties as a probe for bioimaging applications.

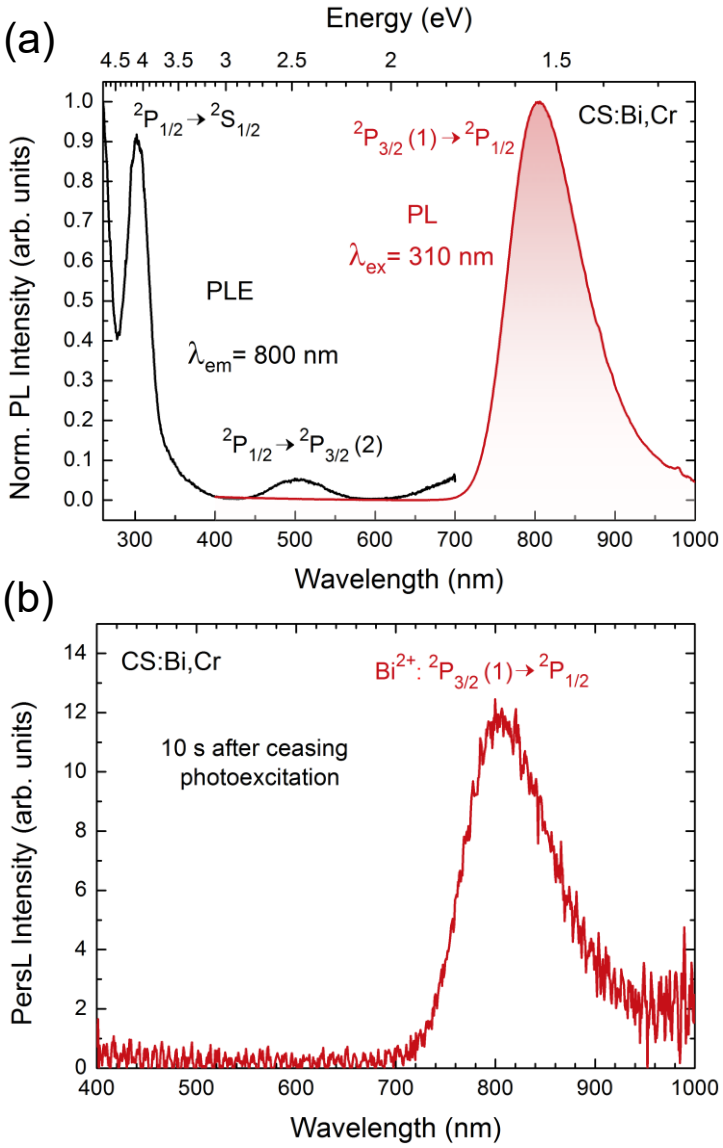

Figure 7.19 (a) PLE and PL spectra of the CS:Bi,Cr sample, collecting at 800 nm and exciting at 310 nm, respectively. (b) Persistent luminescent spectrum collected 10 seconds after ceasing the excitation source.

Finally, it should be pointed out that the reason of the enhancement of Bi^{2+} emission is still not completely understood. However, we have hypothesized two possible causes: (1) from one hand, an energy transfer from Cr^{4+} to Bi^{2+} could take place but (2) from the other hand, a chemical

stabilization of a higher number of Bi^{2+} ions induced by Cr^{4+} charge compensating effect, could be responsible of the NIR emission enhancement.

7.8 Conclusions

In conclusion, the luminescent properties of Bi-activated $CaSnO_3$ system was investigated. The steady-state luminescence properties were discussed by comparing experimental and theoretical data, showing the simultaneous emission from both MMCT state and Bi^{2+} ions. Moreover, a comparison of the orthorhombic perovskite Ca*B*O3:Bi systems (*B*=Ti,Sn,Zr) was provided, discussing the key parameters influencing the band emission nature. The design of the VRBE diagram, together with experimental PL temperature dependence analyses, were demonstrate to be an efficient way for a comprehensive investigation of the optical properties of luminescent materials.

$CaSnO_3$:Bi showed persistent luminescence, that, in principle, is rarely observed in Bi-activated phosphors. Therefore, the persistent luminescence performances were tested and discussed by means of the VRBE diagram constructed by considering the results of TL and PL analysis.

Finally, the effects of codoping with Tb or with Cr were explored, pointing out interesting properties for both the Bi-Tb and Bi-Cr pairs. The persistent features of CS:Bi,Tb sample evidenced an interesting behaviour with a different color output respect to the steady-state PL, suggesting a possible different pathway for MMCT and Tb^{3+}-related PersL, while the Cr^{4+} codoping has showed the enhancement of the near-infrared Bi^{2+} emission in the first biological window and the suppression of the blue emission band due to the MMCT state, resulting in a persistent NIR single-band emitting material with promising characteristics as label for bioimaging applications.

Materials and Methods

Experimental Details. The crystal phase was identified by XRPD measurement (Shimadzu, Kyoto, Japan; XRD6000). The diffuse reflectance spectra were collected by a spectrophotometer (Shimadzu, UV3600) equipped with an integrating sphere.

The photoluminescence excitation (PLE) spectra were collected exciting with a 300 W Xe lamp (Asahi Spectra, MAX-302) equipped with a monochromator (Nikon, G250) and detecting by Si photodiode (PD) detector (Electro-Optical System Inc., S-025-H) equipped with a monochromator (Shimadzu, 675 grooves/mm). Photoluminescence (PL) spectra were measured collecting with a CCD spectrometer (Ocean Optics, QE65Pro) connected with an optical fiber. All the PL spectra were calibrated by using a standard halogen lamp (Labsphere, SCL-600). Temperature dependence of PL and PLE (80-600 K) were investigated setting the sample in a cryostat (Helitran LT3, Advanced Research Systems).

The thermoluminescence (TL) glow curves were collected setting the samples in a cryostat (Helitran LT3, Advanced Research Systems) to control the temperature (starting from 100 K), then the samples were irradiated by D_2 lamp for 10 min and 10 minutes after the shout off of the excitation source the emissions were detected by a PMT detector (R11041, Hamamatsu Photonics & Co. Ltd.,) covered with 350 nm short-cut and 750 nm long-cut filters, with a heating rate of 10 K/min.

The persistent decay curve was recorded at RT (25 °C) after 5 min of UV irradiation with the same PMT detector.

References

1. E.M. Dianov. Bismuth-doped optical fibers: a challenging active medium for near-IR lasers and optical amplifiers. *Light Sci. Appl.* **2012**, 1, e12.
2. H.-T. Sun, J. Zhou and J. Qiu. Recent advances in bismuth activated photonic materials. *Prog. Mater. Sci.* **2014**, 64, 1-72.
3. F. Kang, H. Zhang, L. Wondraczek, X. Yang, Y. Zhang, D.Y. Lei and M. Peng. Band-gap modulation in single Bi^{3+}-doped yttrium-scandium-niobium vanadates for color tuning over the whole visible spectrum. *Chem. Mater.* **2016**, 28, 2692-2703.
4. R. Mohan. Green bismuth. *Nat. Chem.* **2010**, 2, 336.
5. A.B. Seabra and N. Durán. Nanotoxicology of metal oxide nanoparticles. *Metals* **2015**, 5, 934-975.
6. G.G. Briand and N. Burford. Bismuth compounds and preparations with biological or medicinal relevance. *Chem. Rev.* **1999**, *99*, 2601.
7. P. Riente, A. Matas Adams, J. Albero, E. Palomares and M.A. Pericàs. Light-driven organocatalysis using inexpensive, nontoxic Bi_2O_3 as the photocatalyst. *Angew. Chem. Int. Ed.* **2014**, *53*, 9613.
8. G. Blasse and A. C. van der Steen. Luminescence characteristics of Bi^{3+}-activated oxides. *Solid State Commun.* **1979**, 31, 993-994
9. G. Boulon, J.P. Faurie and C. Madej. Préparation, sites de symétrie et photoluminescence de l'ion Bi^{3+} dans les antimoniates de terres rares Y_2BSbO_7 (B=Ga, Lu, Y). *J. Solid State Chem.* **1974**, 10, 167-174.
10. G. Blasse. Classical phosphors: A Pandora's box. *J. Lumin.* **1997**, 72-74, 129-134.
11. G. Blasse. The ultraviolet absorption bands of Bi^{3+} and Eu^{3+} in oxides. *J. Solid State Chem.* **1972**, 4, 52-54.
12. E. Cavalli, F. Angiuli, F. Mezzadri, M. Trevisani, M. Bettinelli, P. Boutinaud and M. Brik. Tunable luminescence of Bi^{3+}-doped $YP_xV_{1-x}O4$ ($0 \leq x \leq 1$). *J. Phys.: Condens. Matter.* **2014**, 26, 385503.
13. P. Boutinaud. Revisiting the Spectroscopy of the Bi^{3+} Ion in Oxide Compounds. *Inorg. Chem.* **2013**, 52, 6028-6038.
14. P. Boutinaud and E. Cavalli. Predicting Metal-to-Metal Charge Transfer in Close-Shell Transition Metal Oxides doped with Bi^{3+} or Pb^{2+}. *Chem. Phys. Lett.* **2011**, 503, 239-243.

15. A.M. Srivastava and W.W. Beers. On the impurity trapped exciton luminescence in $La_2Zr_2O_7:Bi^{3+}$. *J. Lumin.* **1999**, 81, 293-300.

16. G. Blasse. Optical electron transfer between metal ions and its consequences. In *Complex chemistry* (Structure and bonding series) Springer, Berlin **1991**, Vol. 76, pp. 153-187.

17. M. Peng and L. Wondraczek. Bi^{2+}-doped strontium borates for white-light-emitting diodes. *Opt. Lett.* **2009**, 34, 2885-2887.

18. M.A. Hamstra, H.F. Folkerts and G. Blasse. Red bismuth emission in alkaline-earth-metal sulfates. *J. Mater. Chem.* **1994**, 4, 1349-1350.

19. G. Blasse, A. Meijerink, M. Nomes and J. Zuidema. Unusual bismuth luminescence in strontium tetraborate (SrB_4O_7:Bi). *J. Phys. Chem. Solids* **1994**, 55, 171-174.

20. L. Seijo and Z. Barandiarán. Blue absorption and red emission of Bi^{2+} in solids: strongly spin-orbit coupled 6p levels in low symmetry fields. *Phys. Chem. Chem. Phys.* **2014**, 16, 17305-17314.

21. Q. Zeng, T. Zhang, Z. Pei and S.U. Qiang. Luminescence of unusual bismuth in barium borates (BaB_8O_{13}:Bi). *J. Mater. Sci. Technol.* **1999**, 15, 281-282.

22. M. de Jong and A. Meijerink. Color tuning of Bi^{2+} luminescence in barium borates. *J. Lumin.* **2016**, 170, 240-247.

23. R. Cao, M. Peng and J. Qiu. Photoluminescence of Bi^{2+}-doped $BaSO_4$ as a red phosphor for white LEDs. *Opt. Express* **2012**, 20, A977-A983.

24. M. Peng, B. Sprenger, M.A. Schmidt, H.G.L. Schwefel and L. Wondraczek. Broadband NIR photoluminescence from Bi-doped $Ba_2P_2O_7$ crystals: Insights into the nature of NIR-emitting Bismuth centers. *Opt. Express* **2010**, 18, 12852-12863.

25. M. Peng and L. Wondraczek. Photoluminescence of $Sr_2P_2O_7:Bi^{2+}$ as a red phosphor for additive light generation. *Opt. Lett.* **2010**, 35, 2544-2546.

26. L. Li, M. Peng, B. Viana, J. Wang, B. Lei, Y. Liu, Q. Zhang and J. Qiu. Unusual concentration induced antithermal quenching of the Bi^{2+} emission from $Sr_2P_2O_7:Bi^{2+}$. *Inorg. Chem.* **2015**, 54, 6028-6034.

27. Y. Zhuang, J. Ueda and S. Tanabe. Enhancement of red persistent luminescence in Cr^{3+}-doped $ZnGa_2O_4$ phosphors by Bi_2O_3 codoping. *Appl. Phys. Express* **2013**, 6, 052602.

28. Y. Zhuang, J. Ueda and S. Tanabe. Tunable trap depth in $Zn(Ga_{1-x}Al_x)_2O_4$:Cr,Bi red persistent phosphors: considerations of high-temperature persistent luminescence and photostimulated persistent luminescence. *J. Mater. Chem. C* **2013**, 1, 7849-7855.

29. Y. Katayama, J. Ueda and S. Tanabe. Effect of Bi_2O_3 doping on persistent luminescence of $MgGeO_3:Mn^{2+}$ phosphor. *Opt. Mater. Express* **2014**, 4, 613-623.

30. C. Liu, Z. Xia, M.S. Molokeev and Q. Liu. Synthesis, Crystal structure, and enhanced luminescence of garnet-type Ca3Ga2Ge3O12:Cr3+ by codoping Bi3+. *J. Am. Ceram. Soc.* **2015**, 98, 1870-1876.

31. S.H. Pawar, A.V. Narlikar. Mechanism of luminescence in CaS:Bi phosphor. *Mater. Res. Bull.* **1976**, 11, 821-826.

32. D. Jia, J. Zhu and B. Wu. Improvement of persistent phosphorescence of $Ca_{0.9}Sr_{0.1}S:Bi^{3+}$ by codoping Tm^{3+}. *J. Lumin.* **2000**, 91, 59-65.

33. Y. Zhuang, J. Ueda and S. Tanabe. Photochromism and white long-lasting persistent luminescence in Bi^{3+}-doped $ZnGa_2O_4$ ceramics. *Opt. Mater. Express* **2012**, 2, 1378-1383.

34. Z. Yang, J. Liao, T. Wang, H. Wu, J. Qiu, Z. Song and D. Zhou. Ultraviolet long afterglow emission in Bi^{3+} doped $CdSiO_3$ phosphors. *Mater. Express* **2014**, 4, 172-176.

35. S. Zhang, Y. Hu, R. Chen, X. Wang and Z. Wang. Photoluminescence and persistent luminescence in Bi^{3+}-doped Zn_2GeO_4. *Opt. Mater.* **2014**, 36, 1830-1835.

36. X. Qin, Y. Li, D. Wu, Y. Wu, R. Chen, Z. Ma, S. Liu and J. Qiu. A novel NIR long phosphorescent phosphor: $SrSnO_3$:Bi^{2+}. *RSC Adv.* **2015**, 5, 101347-101352.

37. C.J. Howard and H.T. Stokes. Group-Theoretical Analysis of Octahedral Tilting in Perovskites. *Acta Crystallogr., Sec. B* **1998**, 54, 782.

38. M.W. Lufaso and P.M. Woodward. Prediction of the crystal structures of perovskites using the software program *SPuDS*. *Acta Crystallogr., Sec. B* **2001**, 57, 725-738.

39. A. Yangthaisong The Structural, Electronic and Elastic Properties, and the Raman Spectra of Orthorhombic $CaSnO_3$ through First Principles Calculations. *Chin. Phys. Lett.* **2013**, 30, 077101.

40. H. Mizoguchi, H.W. Eng and P.M. Woodward. Probing the Electronic Structures of Ternary Perovskite and Pyrochlore Oxides Containing Sn^{4+} or Sb^{5+}. *Inorg. Chem.* **2004**, 43, 1667-1680.

41. J.M. Henriques, E.W.S. Caetano, V.N. Freire, J.A.P. da Costa and E.L. Albuquerque. Structural, electronic, and optical absorption properties of orthorhombic $CaSnO_3$ through *ab initio* calculations. *J. Phys.: Condens. Matter* **2007**, 19, 106214.

42. J. Tauc, R. Grigorovici and A. Vancu. Optical properties and electronic structure of amorphous germanium. *Phys. Status Solidi*, **1966**, 15, 627-637.

43. P. Kubelka and F. Munk. Ein Beitrag zur Optik der Farbanstriche. *Z. Technische Physik*, **1931**, 12, 593-601.

44. H. Mizoguchi, H.W. Eng and P.M. Woodward. Probing the electronic structures of ternary perovskite and pyrochlore oxides containing Sn^{4+} or Sb^{5+}. *Inorg. Chem.* **2004**, 43, 1667-1680.

45. W. Zhang, J. Tang and J. Ye. Structural, photocatalytic, and photophysical properties of perovskite $MSnO_3$ (M=Ca, Sr, and Ba) photocatalysts. *J. Mater. Res.* **2007**, 22, 1859-1871.

46. A. M. Srivastava. Luminescence of Bi^{3+} in Orthorhombic Perovskites $CaB^{4+}O_3$ (B^{4+}=Zr, Sn): Crossover from Localized to D-State Emission. *Opt. Mater.* **2016**, 58, 89-92.

47. C.W. Struck and W.H. Fonger. Thermal Quenching of Tb^{3+}, Tm^{3+}, Pr^{3+} and Dy^{3+} $4f^n$ Emitting States in La_2O_2S. *J. Appl. Phys.* **1971**, 42, 4515-4517.

48. P. Boutinaud, L. Sarakha, E. Cavalli, M. Bettinelli, P. Dorenbos and R. Mahiou. About ref afterglow in Pr^{3+} doped titanate perovskites. *J. Phys. D: Appl. Phys.* **2009**, 42, 045106.

49. W. Jia, D. Jia, T. Rodriguez, D.R. Evans, R.S. Meltzer and W.M. Yen. UV excitation and trapping centers in $CaTiO_3$:Pr^{3+}. *J. Lumin.* **2006**, 119-120, 13-18.

50. F. Clabau, A. Garcia, P. Bonville, D. Gonbeau, T. Le Mercier, P. Daniard and S. Jobic. Fluorescence and phosphorescence properties of the low temperature forms of the $MAl_2Si_2O_8$:Eu^{2+} (M=Ca, Sr, Ba) compounds. *J. Solid State Chem.* **2008**, 181, 1456-1461.

51. T. Wang, J. Gou, X. Xu, D. Zhou, J. Qiu and X. Yu. Self-activated long persistent luminescence from different trapping centers of calcium germinate. *Opt. Express* **2015**, 23, 12595-12604.

52. Y.Q. Li, J.E.J. van Steen, J.W.H. van Krevel, G. Botty, A.C.A. Delsing, F.J. DiSalvo, G. de With and H.T. Hintzen. *J. Alloys Compd.* **2006**, 417, 273-279.

53. K. Van den Eeckhout, P.F. Smet and D. Poelman. Persistent luminescence in rare-earth codoped $Ca_2Si_5N_8:Eu^{2+}$. *J. Lumin.* **2009**, 129, 1140-1143.

54. P.F. Smet, N. Avci and D. Poelman. Red persistent luminescence in Ca_2SiS_4:Eu,Nd. *J. Electrchem. Soc.* **2009**, 156, H243-H248.

55. F. Urbach. Zur Lumineszenz der Alkalihalogenide: II. Messungmethoden. *Sitzungsberichte Akademie der Wissenshaften in Wien* **1930**, 139, 363.

56. Z. Liang, J. Zhang, J. Sun, X. Li, L. Cheng, H. Zhong, S. Fu, Y. Tian and B. Chen. Enhancement of green long lasting phosphorescence in $CaSnO_3:Tb^{3+}$ by addition of alkali ions. *Physica B* **2013**, 412, 36-40.

57. B. Lei, B. li, H. Zhang and W. Li. Preparation and luminescence properties of $CaSnO_3:Sm^{3+}$ phosphor emitting in the reddish orange region. *Opt. Mater.* **2007**, 29, 1491-1494.

58. K. Li and D. Xue. Estimation of electronegativity values of elements in different valence states. *J. Phys. Chem. A* **2006**, 110, 11332-11337.

59. A. H. Krumpel, P. Boutinaud, E. Van der Kolk and P. Dorenbos. Charge transfer transitions in the transition metal oxides $ABO_4:Ln^{3+}$ and $APO_4:ln^{3+}$ (A=La, Gd, Y, Lu, Sc; B=V, Nb, Ta; Ln=lanthanide). *J. Lumin.* **2010**, 130, 1357-1365.

60. R. Cao, T. Fu, H. Xu, W. Luo, D. Peng, Z. Chen and J. Fu. Synthesis and luminescence enhancement of $CaTiO_3:B^{i3+}$ yellow phosphor by codoping Al^{3+}/B^{3+} ions. *J. Alloys Compd.* **2016**, 674, 51-55.

61. E.G. Rogers and P. Dorenbos. Vacuum referred binding energies of the single 3d, 4d, or 5d electron in transition metal and lanthanide impurities in compounds. *ECS J. Solid State Sci. Technol.* **2014**, 10, R173-R184.

62. P. Dorenbos. The electronic structure of lanthanide impurities in TiO_2, ZnO, SnO_2, and related compounds. *ECS J. Solid State Sci. Technol.* **2014**, 3, R19-R24.

63. P. Dorenbos and E.G. Rogers. Vacuum referred binding energies of the lanthanides in transition metal oxide compounds. *ECS J. Solid State Sci. Technol.* **2014**, 3, R150-R158.

64. R.H.P. Awater and P. Dorenbos. X-ray induced valence chance and vacuum referred binding energies of Bi^{3+} and Bi^{2+} in $Li_2BaP_2O_7$. *J Phys. Chem. C* **2016**, 120, 15114-15118.

65. M. Kato, H. Unuma and M. Takahashi. Color modification of chromium-tin pink pigment by substitution of Ti for Sn. *J. Ceram. Soc. Jpn.* **2000**, 108, 478-481.

66. R.S. Pavlov, V.B. Marzá and J.B. Carda. Electronic absorption spectroscopy and colour of chromium-doped solids. *J. Mater. Chem.* **2012**, 12, 2825-2832.

CHAPTER 8

Bi,Er-codoped Y_2O_3 Nanocrystals: Broadband Sensitization of Erbium Fluorescence

Abstract The enhancement of the low absorption cross section and widening of the absorption range of the RE ions in the UV-blue region is still a challenge to develop optical systems with high performance. In this Chapter we present the synthesis of Bi,Er-codoped Y_2O_3 nanocrystals by means of Pechini type sol-gel process. X-ray powder diffraction (XRPD) and transmission electron microscopy (TEM) were performed to evaluate the nanocrystalline particle size and phase. Photoluminescence investigation in the UV-Vis and IR regions showed that the presence of Bi^{3+} ions promotes the strengthening of Er^{3+} emitter properties. In particular, an Er^{3+} sensitization process based on a broadband energy transfer mediated by the Bi^{3+} ions in the C_2 site was evaluated, resulting in a wavelength spread for the photostimulation of the rare earth emissions in the visible and NIR range. We pointed out a resonant type via a dipole-dipole interaction as the most probable mechanism of energy transfer. Moreover, the critical distance between the Bi^{3+} and Er^{3+} ions was estimated to be of about 8.5 Å.

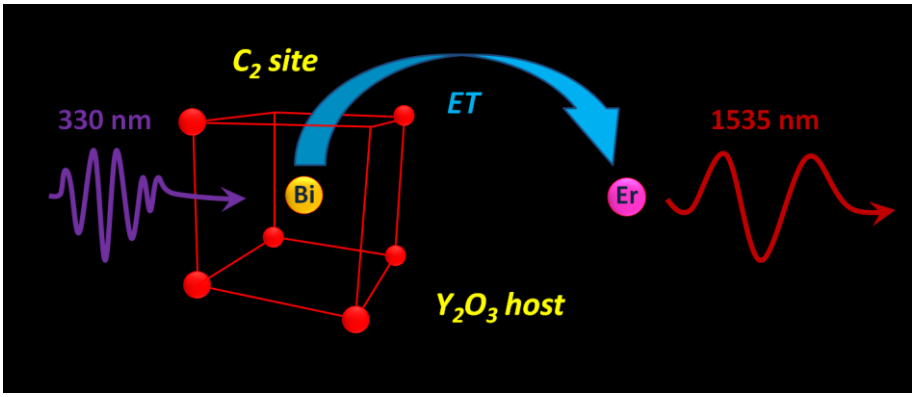

8.1 Introduction

Inorganic light-emitting materials have received much attention for their versatility in devices involving the artificial production of light such as fiber-optic amplifiers, waveguide lasers, and displays[1-3] but also in photovoltaic and biomedical applications.[4,5] The unique optical properties of the rare-earth (RE) ions-doped nanophosphors, like the narrow emission bands and the long radiative emission lifetimes,[6] due to their electronic configuration[7] had made them among the most studied systems.

The extensive use of Er^{3+} ion in optical systems is principally due to its $^4I_{13/2} \rightarrow {}^4I_{15/2}$ transition around 1540 nm, exploited in telecom technology.[8] Because of the current development of high speed optical communication systems, devices such as waveguide optical amplifiers are required.[9-11] An Er-doped fiber amplifier (EDFA) is a standard device for long-distance optical telecommunication, while the low solubility of the erbium ions represents a severe limitation for possible applications in the field of miniature integrated optics, where high optical gain performances over short distances are required.

In this context, the yttrium oxide (Y_2O_3) is a promising host because of the similarity of the Y^{3+} and Er^{3+} ionic radii and the same crystal structure of Er_2O_3 and Y_2O_3, allowing, in principle, the incorporation of a high Er concentration.[12] Moreover, Y_2O_3 exhibits suitable properties as a high refractive index, high melting point, low phonon energy, and high stability. Although this kind of system is widely studied and used, overcoming the intrinsic low absorption cross section of the RE ions in the UV-blue region can bring to a further improvement of the material optical performances. Moreover, since the RE ion absorption spectrum consists of a set of sharp lines, the widening of the Er3+ photoexcitation window is still a formidable challenge. In this regard, it is well-known that the incorporation in the Er-doped host of sensitizers like other RE ions,[13-15] Si,[16,17] or metal clusters[18-20] represents a way to enhance the Er luminescence properties in virtue of the broadening of the spectral excitation range and the increase of the effective absorption cross section.[21-24]

In the past decade, the study of bismuth-based materials has attracted growing interest because of the peculiar optical properties of the Bi^{3+} ion, making them particularly suitable materials for applications in various fields such as photocatalysis, photovoltaics, photonics, and sensors.[25-27] This ion has $6s^2$ electronic configuration ($^1S_0$ corresponds to the ground state, whereas $^3P_0$, $^3P_1$, and $^3P_2$ label the first three excited states), and the luminescence of bismuth-doped materials is strongly dependent on the host incorporating the Bi^{3+} ions. In the case of the Y_2O_3 matrix, the peculiarity of this system lies in two different sites hosting the Bi^{3+} ions (C_2 and S_6),[28-35] each showing a proper optical behavior. Although the optical behavior of the bismuth ion in yttria has already been object of several devoted studies, the investigation of the Bi- and Er-codoped Y_2O_3 system aiming at a strengthening of the Er absorption window and consequent photoemission enhancement is still missing, to the best of our knowledge. In this context, it is worth mentioning the study of Yang *et al.*[36,37] focused on the analysis of the upconversion properties shown by Bi-Er:Y_2O_3-based samples.

Therefore, this investigation deals with the synthesis and the characterization of structural and optical properties of Bi- and Er-codoped Y_2O_3 nanoparticles, highlighting the occurrence of an efficient energy transfer process between the ions of the two doping species. The resulting rare

earth sensitization and consequent improvement of the fluorescence properties suggests possible application in the field of Er-based optical and photonic devices.

8.2 Sample Preparation

Materials. $Y(NO_3)_3 \cdot 6H_2O$ (99.9%, Sigma-Aldrich), $Bi(NO_3)_3 \cdot 5H_2O$ (99.99%, Sigma-Aldrich), $Er(NO_3)_3 \cdot 5H_2O$ (99.9%, Sigma-Aldrich), citric acid (99%, Carlo Erba), ethylene glycol (99.5%, Acros Organics), and HNO_3 60% (Sigma-Aldrich) were used for the preparation of the samples without further purification.

Synthesis. The synthesis of monocrystalline nanoparticles was achieved by a modified Pechini-type sol-gel process, whose details has been accounted in Chapter 4. Briefly, the synthesis consists in the use of citric acid as complexing agent and chelating ligand for the Y^{3+}, Bi^{3+}, and Er^{3+} ions, following the reaction:

$$xY(NO_3)_3 + yLn(NO_3)_3 + HOC(COOH)(CH_2COOH)_2 + HOCH_2CH_2OH \xrightarrow{HNO_3,H_2O} Y_xO_3{:}Ln_y$$

where the molar proportions between the salts (x:y:z) were chosen according to the stoichiometry of Y_2O_3 and the desired dopant concentrations; the molar ratio between the salts, the citric acid, and the ethylene glycol was maintained in proportions of 1:3:4.5. The reaction was protracted for about 12 h at 120 °C, and the products were calcined in a muffle kiln at 780 °C in air for about 2 h to obtain the final samples. Table 9.1 reports the nominal compositions and the labels of the samples.

It is worth mentioning that the adopted range of the Er doping level was chosen in order to avoid any concentration quenching phenomena, detrimental for the rare earth luminescence activity.[36] Similar considerations have determined the choice of 1 at. % as Bi content for all the samples.[33]

Table 8.1 Composition, Cell Length, and Volume-Weighted Average Crystallite Size of the Samples Obtained from the Rietveld Refinements[a]

sample label	sample formula	*a* (Å)	crystallite size (nm)
Er0	$Y_{1.98}Bi_{0.02}O_3$	10.6094	41.5
Er0.25	$Y_{1.975}Bi_{0.02}Er_{0.005}O3$	10.6491	40.9
Er0.5	$Y_{1.97}Bi_{0.02}Er_{0.01}O3$	10.6487	44.1
Er1	$Y_{1.96}Bi_{0.02}Er_{0.02}O3$	10.6478	46.3
Er2	$Y_{1.94}Bi_{0.02}Er_{0.04}O3$	10.6470	45.9

[a]The uncertainties on the crystallites size of the samples are about 10%.

8.3 Structural and Morphological Analysis

It is well established that Pechini method allows to synthesize monocrystalline ions-doped yttrium oxide nanoparticles.[38-40] The presence of the single cubic phase ($Ia\bar{3}$ space group, #160890) upon the thermal treatment at 800 °C (Figure 8.1a) is in agreement with our expectations and demonstrates the effectiveness of the synthesis route. The two different sites characterizing the Y_2O_3 crystal structure are depicted in Figure 8.1b and c. If C_2 and S_6.

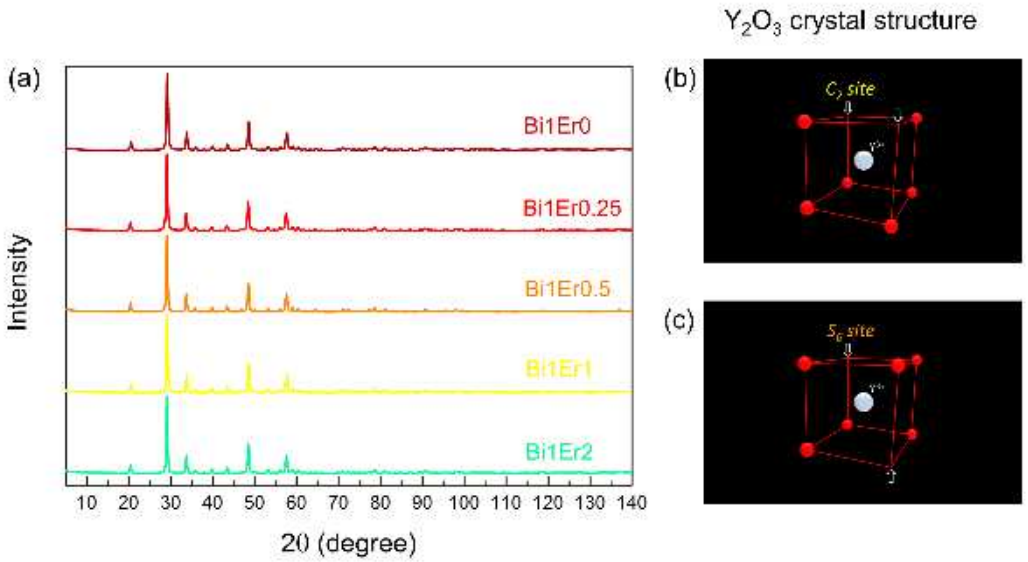

Figure 8.1. (a) XRPD patterns of the samples Bi1Er*x* with *x*=0, 0.25, 0.5, 1 and 2. (b,c) Scheme of the low symmetry site C_2 and the high symmetry site S_6 of Y^{3+} in Y_2O_3.

The results of the XRPD profile analysis by Rietveld full profile fitting method are summarized in Table 8.1. Figure 8.2 shows how the introduction of Er^{3+} in the lattice brings a shrinkage of the cell edge. The decrease of the cell parameter *a* with increasing the content of erbium is due to the smaller ionic radius of Er^{3+} with respect to that of Y^{3+} (114.4 and 115.9 pm, respectively, when these are coordinated to eight anions).

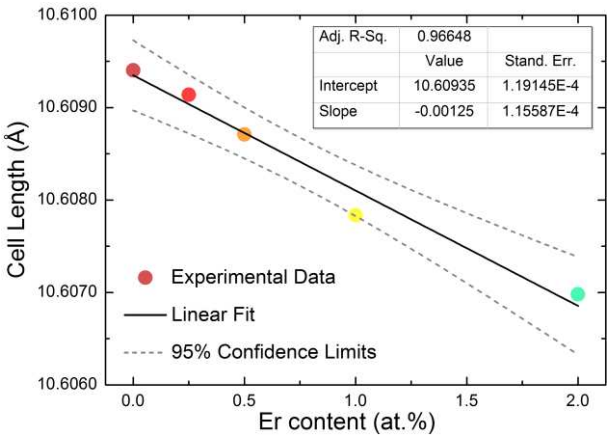

Figure 8.2. Plot of the cell length versus erbium content.

The high-resolution transmission electron microscope (HRTEM) micrograph reported in Figure 8.3 shows the synthesized nanoparticles of the sample Er2. As expected, the nanoparticles are monocrystallines with dimensions of about 40 nm, in agreement with the crystallite size estimated from the Rietveld analysis (reported in Table 8.1). The presence of bismuth and erbium after calcination was checked by EDS analysis (Figure 8.3c), confirming that the dopant amount is in agreement with the chemical formulas in Table 8.1.

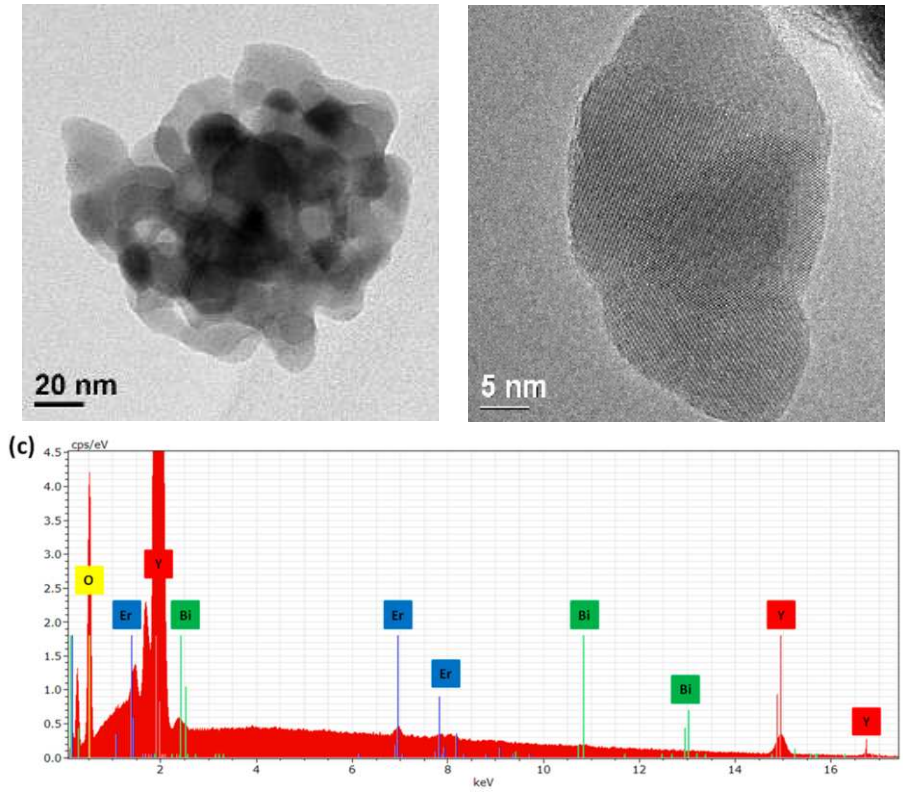

Figure 8.3 TEM and HR-TEM micrographs (a,b) and EDS spectrum (c) of the sample Er2.

8.4 Optical Analysis: Photoluminescence Spectra and Decay Curves

In principle, the optical properties of a doping ion are influenced by the symmetry of the site occupied in the crystalline host. The rare earth ions are not critically affected from the crystal field due to their particular electronic structure, while the Bi^{3+} ion is particularly sensitive, showing deep change in the optical properties due to the influence of the local host structure. The two sites (C_2 and S_6) in which the Bi^{3+} ions can substitute the Y^{3+} ions in the cubic yttrium oxide structure have different symmetry, with the C_2 site more asymmetric than the S_6 one.

The photoluminescence analysis regarded the optical properties of the system in a range going from the UV-vis edge up to the near-IR region. By choosing the appropriate excitation wavelength, it was possible to selectively excite the Bi^{3+} ions in the C_2 or in the S_6 sites (see Figure 8.4) and then to discriminate their behaviour in relation with the luminescence activity shown by the Er^{3+} ions.

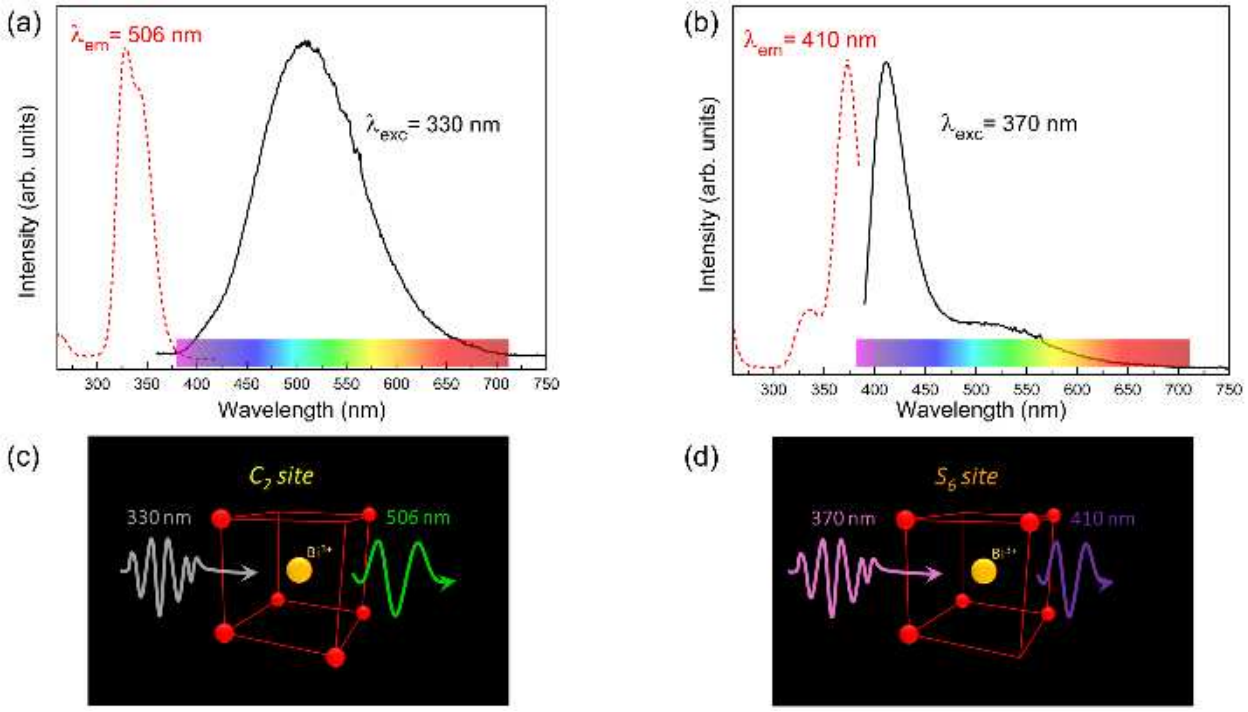

Figure 8.4 PL and PLE spectra of Bi^{3+} in C_2 (a) and S_6 (b) sites of Y_2O_3 and schematic representation of the optical properties of Bi^{3+} in the two different sites (c,d). PL and PLE spectra of Bi^{3+} in C2 site were collected exciting at 330 nm and following the 506 nm emission, respectively, while for Bi^{3+} in S_6 site excitation and emission at 370 nm and 410 nm, respectively, were selected.

The luminescence properties of bismuth(III) ion in Y_2O_3 have been the focus of theoretical[28,29] and experimental[30-35] studies, allowing to confirm the predictions of Boulon[41] on the energetic levels of the ion in two specific sites of the host labeled as C_2 and S_6. So, now it is well established that the Bi^{3+} ion optical properties in the UV-vis are determined by the transitions involving the $^1S_0$ ground state and the $^3P_1$ excited one.

Figure 8.5 shows the visible photoluminescence emission (b, d) and excitation (a, c) spectra of the single Bi-doped sample and the samples codoped with different content of erbium. Figure 8.5a,c shows an excitation band in the 300-400 nm range that is slightly shifted toward the UV in the case of Bi^{3+} ion in the C_2 site. On the other hand, in virtue of a more intense Stokes shift during the internal relaxation after light absorption, the $^3P_1 \rightarrow {}^1S_0$ emission band for the Bi^{3+} ion in the C_2 site results manifestly red-shifted with respect to the ion in the S_6 site, as can be seen in Figure 8.5b,d. Moreover, our measurements revealed that these two emissions are comparable in intensity. The PL spectra also include the sharp emission peaks of the Er^{3+} ions, corresponding to the $^2H_{11/2}/^4S_{3/2} \rightarrow {}^4I_{15/2}$ (green emission) and $^4F_{9/2} \rightarrow {}^4I_{15/2}$ (red emission) transitions.

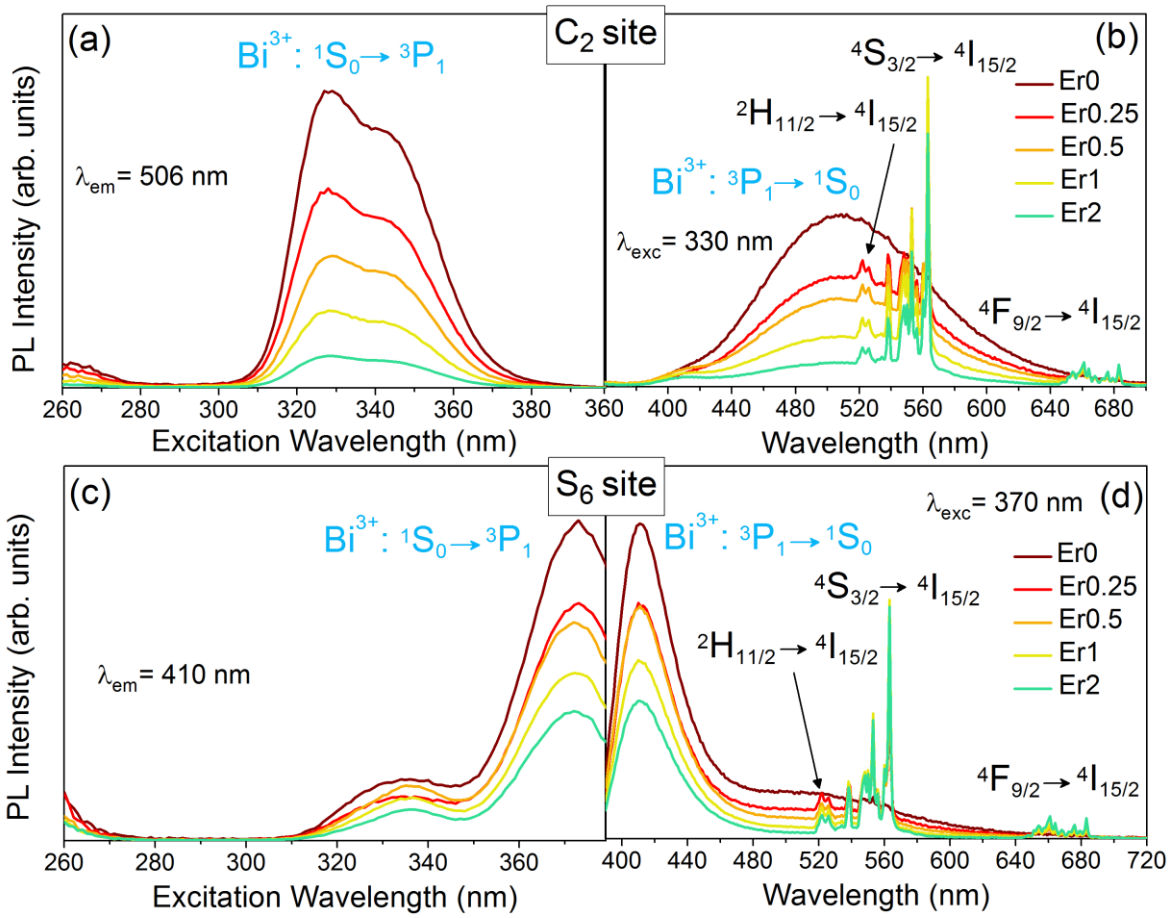

Figure 8.5 Luminescence analysis of the Bi^{3+} emission for the series of Bi-Er:Y_2O_3 samples: PLE (a, c) and PL (b, d) spectra collecting and exciting selectively the Bi^{3+} ions in the *C_2* (a, b) and *S_6* (c, d) site.

It is worth pointing out that the used excitation wavelengths are not strictly resonant with any of the rare earth absorption lines in the visible range. Therefore, this behavior suggests a possible energy transfer process involving Bi^{3+} and Er^{3+} ions. Moreover, the observation of a progressive decrease of the bismuth signal as the Er content increases can be taken as a further evidence of such an interaction mechanism between the two ions. This hypothesis seems to be supported by the analysis of the dynamics that characterizes the Bi^{3+} PL emission depending on the Er content.

Figure 8.6 reports the time-resolved PL curves at 506 nm by exciting the samples through the third harmonic (355 nm) of a Nd:YAG laser, a wavelength that well matches the spectral range for the Bi^{3+} photostimulation. The observed trend accounts for the decay of the PL signal generated by the Bi^{3+} ion located in the *C_2* site, and it is characterized by a progressive shortening of the excited state lifetime as the Er content increases. In fact, we estimate that the lifetime drops down from 0.6 μs for the Bi-doped sample up to 0.3 μs for the largest Er-doped one (Er2 sample). This behavior can be ascribed to a loose in effectiveness of the overall PL process, with consequent reduction of the Bi^{3+} $^3P_1$ excited state lifetime, in virtue of the competitive energy transfer mechanism when in the presence of the Er^{3+} ion.

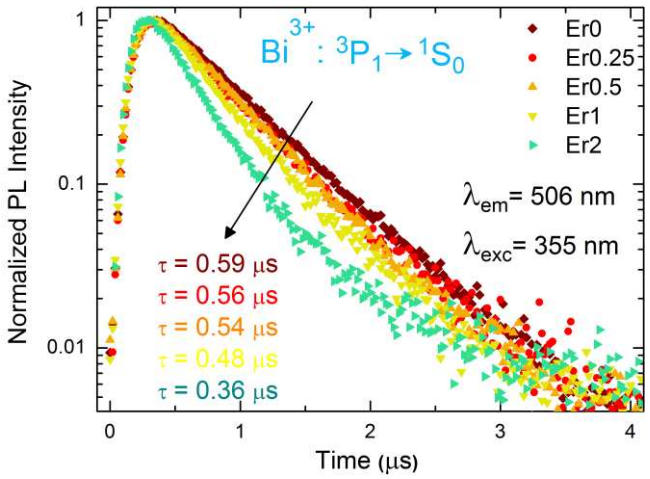

Figure 8.6 Time decay curves for the PL signal taken at 506 nm; samples were excited at 355 nm by means of the third harmonic of a Q-switched Nd:YAG laser.

From the point of view of the rare earth luminescence properties, Figure 8.7 reports the PL spectrum obtained by 379 nm excitation and then in resonant pumping condition with the Er^{3+} $^4I_{15/2} \rightarrow {}^4G_{11/2}$ transition. It must be underlined that the spectral shape does not vary with the erbium content. Moreover, it can be noted that a residual of the Bi^{3+} ion emission remains as a background where the Er^{3+} signal floats on and it almost disappears as the rare earth content was increased up to 2 at. %, in agreement to the behaviour evidenced above.

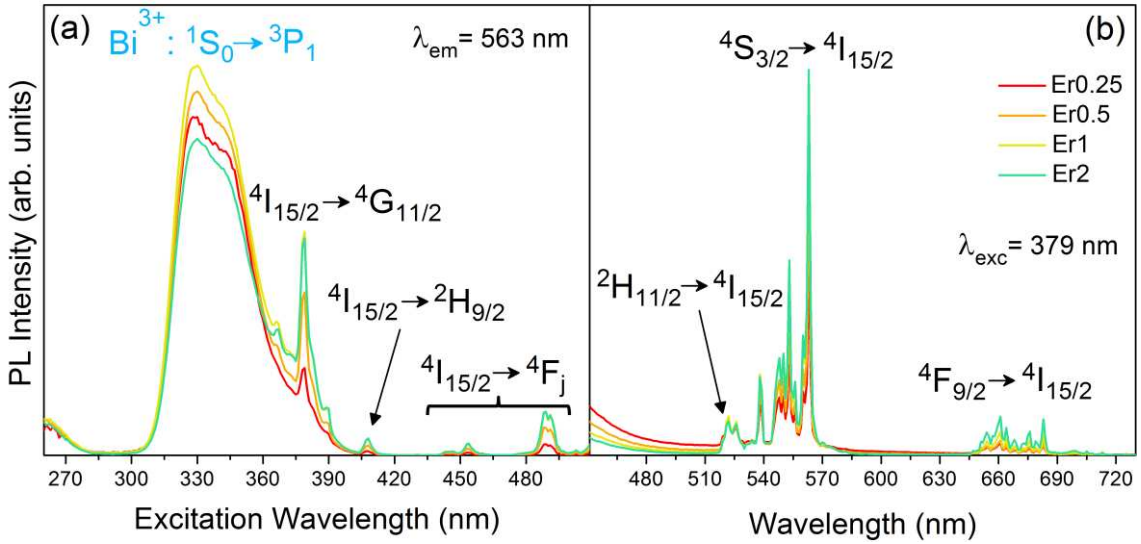

Figure 8.7 Luminescence analysis of the Er^{3+} green emission for the series of Bi-Er:Y_2O_3 samples: (a) comparison of the PLE spectra with light collection at 563 nm; (b) PL spectra under 379 nm excitation.

Concerning the PLE spectra for the green emission (peaked at 563 nm) of Figure 8.7, the main evidence is that not only the characteristic peaks in correspondence of the Er^{3+} ground-to-excited states transitions appear, but these also include the characteristic features of Bi^{3+} light absorption already showed in the PLE spectra of Figure 8.5, in particular the ones related to the C_2 site. This is another clear evidence of the energy transfer mechanism between the two ions, whose nature will be investigated later.

A similar behavior can be observed by analyzing the rare earth emission related to the $^4I_{13/2} \rightarrow {}^4I_{15/2}$ transition (NIR emission) falling around 1.5 μm, a wavelength range extremely appealing for purpose of photonic applications. As shown in Figure 8.8, the PL spectrum is constituted by a main peak centered at 1535 nm and a series of narrow features due to the Stark splitting effect. Concerning the excitation mechanism, the PLE spectra taken at the NIR emission peak reproduce the trend observed in the case of the green emission. The Er^{3+} ion can be stimulated even by out-of-resonance pumping mediated by strongly absorbing Bi^{3+} ions, predominantly in the C_2 state. This originates an enhancement of the NIR emission together with a broadening of the excitation spectrum, with interesting perspectives from a technological point of view.

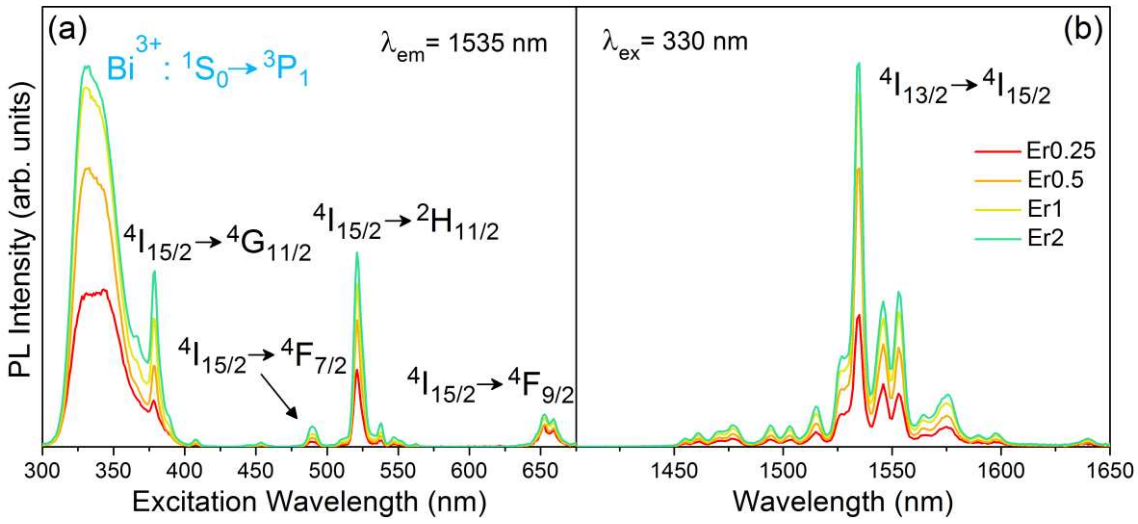

Figure 8.8 Luminescence analysis of the Er^{3+} NIR emission for the series of Bi-Er:Y_2O_3 samples: (a) comparison of the PLE spectra with light collection at 1535 nm; (b) PL spectrum under non-resonant 330 nm excitation.

The fact that the energy transfer mechanism seems to be mainly triggered by Bi^{3+} ions in the C_2 site can be due to a better spectral overlap with the rare earth energy levels than the ions in the S_6 site. In this regards, a careful observation of the PL spectra in Figure 8.5 suggests that the C_2 site's emission well matches the very sensitive absorption lines linked to the $^4I_{15/2} \rightarrow {}^4S_{3/2}$ and $^4I_{15/2} \rightarrow {}^2H_{11/2}$ transitions, whereas the S_6 site's one covers a weak Er photostimulation region. The diagram of Figure 8.9a is a scheme for the energy levels of the two ions and gives a sketch of a possible scenario for the discussed energy transfer mechanism.

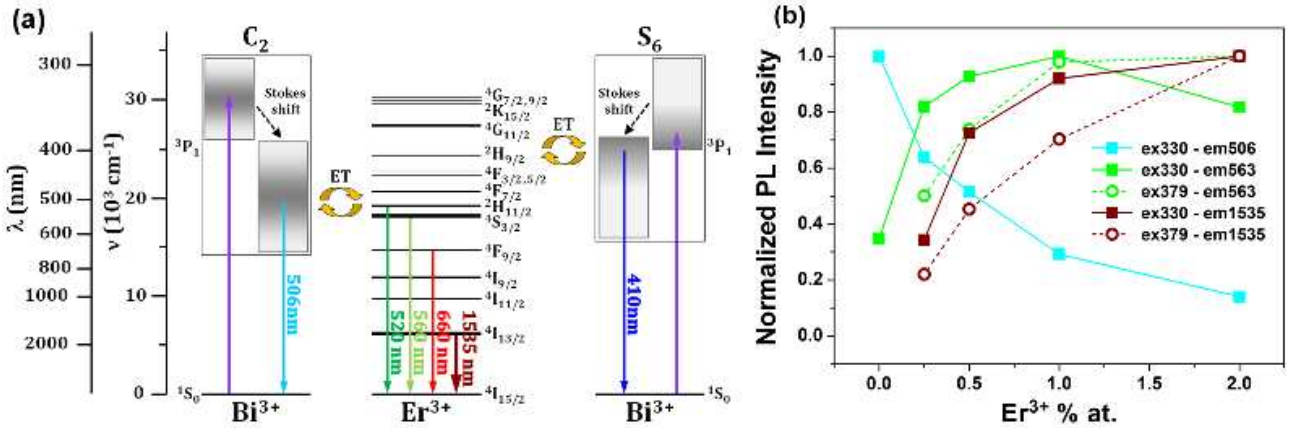

Figure 8.9 (a) Energy level diagram of the Bi-Er:Y_2O_3 system in which the possible absorption, emission, and energy transfer processes are depicted. (b) PL intensity vs Er content trend for signals taken under different excitation and emission wavelength conditions; for each series of data, PL values were normalized to the intensity of the most luminescent sample.

To summarize the above observations, Figure 8.9b reports the trend as a function of the Er content showed by the PL signal intensity for Bi^{3+} ion emission in the *C2* site and for both Er^{3+} green and NIR emissions. The first impressive feature is the opposite trend showed by bismuth and erbium green emissions when pumping directly on the absorption band of the post-transition metal ion: whereas the PL signal peaked at 506 nm promptly falls down, losing half of its intensity already with Er 0.5 at. % codoping level, the signal of the green emission increases with the rare earth content up to Er 1 at. %. The observed reduction of this emission for Er2 sample can be related to the fact that the PL signal at 563 nm includes also a component due to the tail of the Bi^{3+} emission that strongly shrinks with the Er content.

In this context, further considerations are achieved by analyzing the trend for the NIR emission. Since no emissions ascribable to the Bi^{3+} ions occur in this range, we expect a linear increase of the PL intensity at 1535 nm with the Er content. Actually, even though the increase is not fully linear under resonant pumping with the Er^{3+} $^4I_{15/2} \rightarrow {}^4G_{11/2}$ transition, then indicating possible Er concentration quenching effect beyond 1 at. %, on the other hand this saturation trend is more pronounced by non-resonant excitation at 330 nm.

To motivate this observation, we have to consider that a full sensitization effect is achieved only if the population of the Bi^{3+} ions acting as energy transfer mediators is so dense to interact with all the emitting Er^{3+} ions. Therefore, we hypothesize that this condition is lacking for the erbium richest sample due to a low bismuth doping level. As a counterproof, future experiments will regard the use of a larger Bi^{3+} ion content aiming at maximizing the enhancement of the Er luminescence properties. Moreover, since the Bi^{3+} ions in the *C2* sites, as the major promoters of the energy transfer process, are just a fraction of the overall content, the control of both the host structure and the dopant incorporation will be another key for increasing the optical performance of the system.

The interesting possibility of tuning the colour emission by controlling the Bi/Er ratio is underlined by the CIE x, y chromaticity diagram displayed in Figure 8.10a and the pictures of the Bi1 and Bi1Er1 samples under 366 nm lamp in Figures 8.10b and c.

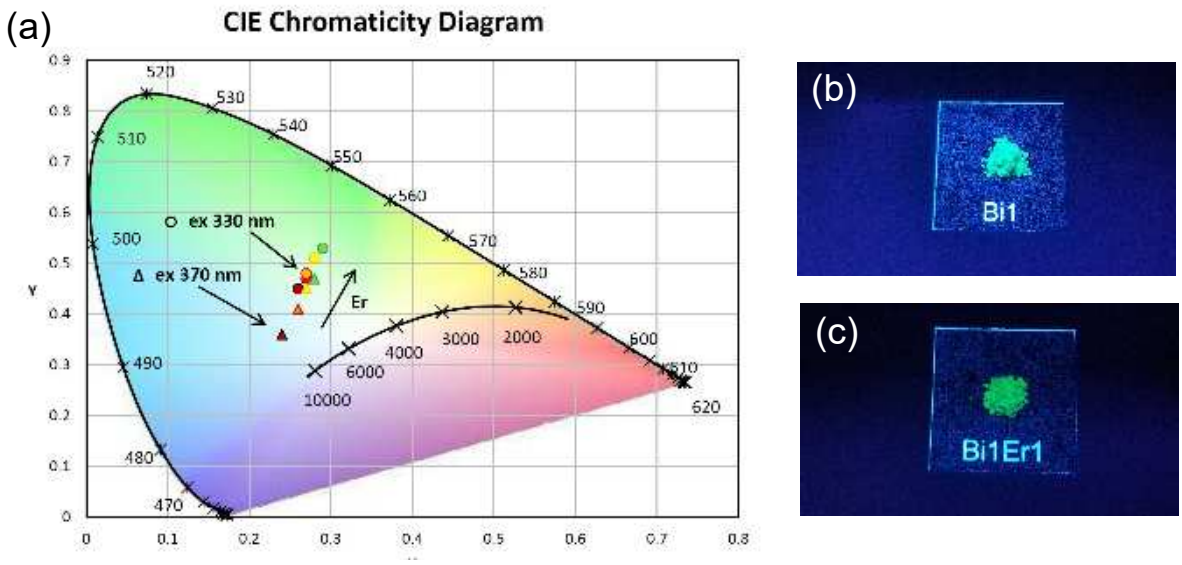

Figure 8.10 CIE chromaticity diagram for the synthesized samples excited at 330 nm (circles) and 370 nm (triangles) (a) and pictures of the Bi1 (b) and Bi1Er1 (c) samples under the 366 nm lamp.

Table 8.2 summarized the CIE colour coordinates (*x*,*y*) of the samples exciting at 330 nm or 370 nm.

Table 8.2 CIE Colour Coordinates (*x*,*y*) for the samples under 330 or 370 nm excitation.

Sample	CIE(*x*,*y*) λ_{ex} = 330 nm	CIE(*x*,*y*) λ_{ex} = 370 nm
Er0	(0.26,0.45)	(0.24,0.36)
Er0.25	(0.27,0.47)	(0.26,0.41)
Er0.5	(0.27,0.48)	(0.26,0.41)
Er1	(0.28,0.51)	(0.27,0.45)
Er2	(0.29,0.53)	(0.28,0.47)

8.5 Energy Transfer Mechanism

Accounting for the peculiar optical properties showed by the synthesized Bi- and Er-codoped Y_2O_3 nanoparticles, now we aim at getting deeper inside the energy transfer mechanism mediated by the Bi^{3+} ion in the C_2 site.

As reported in the literature[39,42] the energy transfer efficiency η_{ET} from Bi^{3+} to Er^{3+} in Y_2O_3 can be expressed by

$$\eta_{ET} = 1 - \frac{I_S}{I_{S0}} \tag{8.1}$$

where I_{S0} and I_S are the luminescence intensity of the sensitizer (Bi^{3+}) in the absence and presence of the activator (Er^{3+}), respectively. Figure 8.11 shows the η_{ET} trend for the $Bi^{3+}(C_2) \rightarrow Er^{3+}$

system, from which it is evident the increase of the energy transfer efficiency with increasing erbium concentration. A maximum value of about 90% is calculated for the Er2 sample.

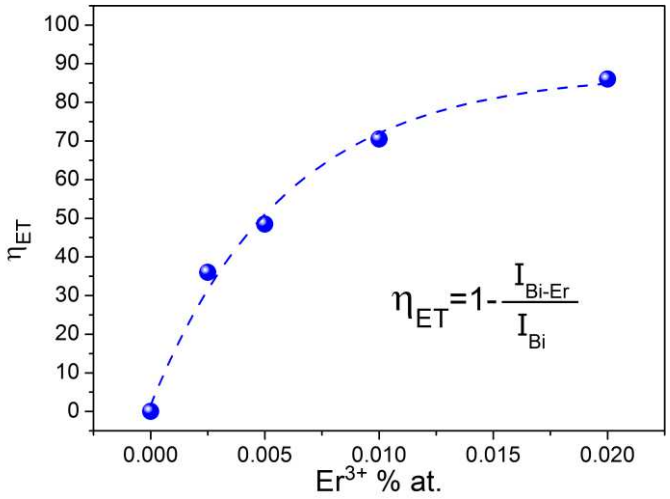

Figure 8.11 Energy transfer efficiency versus erbium content. The dashed line is a guide for the eyes.

As described in ref. 39, the estimate of the average separation between the doping ions considering a probabilistic approach from the discretization of the theory of Chandrasekhar[43] for the average distance $\bar{R}$ between the particles in a random distribution of them, and we took advantage of some specific geometric characteristics of the crystal under consideration.

We approximated the space group $Ia\bar{3}$ of Y_2O_3 with the space group $Fm\bar{3}m$ (both cubic), in order to describe the structure (designed as oxygen-free) as a series of concentric shells of yttrium atoms packed as cuboctahedrons like in Figure 8.12 (in a $Fm\bar{3}m$ crystal, the Y^{3+} ions are located in a face-centered cubic sublattice). This approximation consists in a small distortion of the $Ia\bar{3}$ in the more symmetrical $Fm\bar{3}m$ structure that brings to a negligible error in the calculation.

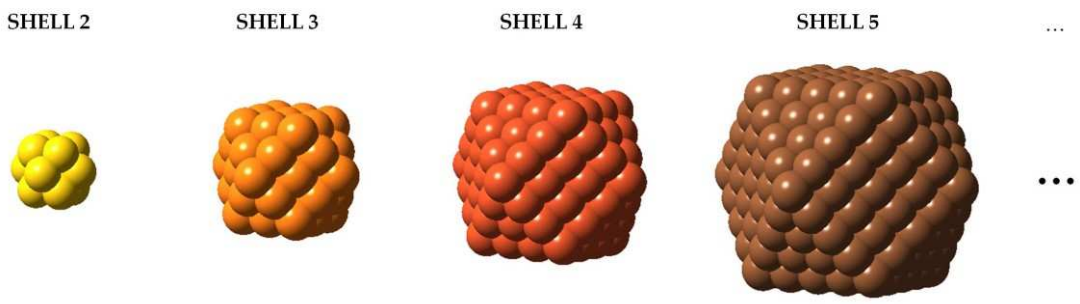

Figure 8.12 Series of cuboctahedral shells of yttrium atoms.

Because of the geometry of the cuboctrahedron with triangular faces, the total number of atoms $n(k)$ of the generic k-shell cuboctrahedral "cluster" (taking into account the central atom) and the number of atoms in the $(k+1)$th shell $n(k+1) - n(k)$, can be done by[44]

$$n(k) = \frac{10}{3}k^3 - 5k^2 + \frac{11}{3}k - 1 \tag{8.2}$$

$$n(k+1) - n(k) = 10k^2 + 2 \tag{8.3}$$

Following Chandrasekhar's idea, we describe the probability that the nearest neighbour to a particle occurs in at least one of the $n(k+1)$ sites of the $(k+1)$th shell (kth cuboctahedron) as the probability that no particles exist in the precedent k shells times the probability that at least one particle does exist between the sites of the $(k+1)$th shell:

$$w(k+1) = \left[1 - \sum_{k'}^{k} w(k')\right]\left[1 - (1-x)^{10k^2+2}\right] \tag{8.4}$$

where x is the atomic concentration of the acceptor ions. Thus, the average distance between Bi^{3+} and Er^{3+} ions can be calculated by

$$\bar{R} = \sum_{k=2}^{\infty} w(k)\,\bar{d}(k) \tag{8.5}$$

with $\bar{d}(k)$ the average distance of the ions in the kth shell from the central ion. The resulting average distance $\bar{R}_{Bi-Er}$ calculated from the last equation is 12.1, 8.5, 6.6, and 5.2 Å for x = 0.002, 0.005, 0.010, and 0.020, respectively. Moreover, defining a critical concentration x_C as the concentration at which the emission intensity of the Bi^{3+} ions is half of that of the sample in the absence of Er^{3+} ions (like in the Dexter's theory[45]), that in this system is estimated to be 0.005, we calculated the critical distance R_C for the Bi^{3+}-Er^{3+} energy transfer of about 8.5 Å.

The different ways in which an energy transfer between a sensitizer and an activator may take place are the exchange interaction, radiative transfer, and multipole-multipole interaction. A radiative energy transfer can be neglected for this two reasons: (i) no spectral dips are detectable in the emission bands of Bi^{3+} sensitizer ions in correspondence of the absorption lines of Er^{3+} acceptor ions; (ii) the lifetime of the Bi^{3+} PL emission is modified in the presence of the rare earth, showing a clear decrease as the Er content is raised. Moreover, exchange interaction is strongly influenced by the distance between the sensitizer and the activator, with typical values of the critical distance of about 3-4 Å,[46] half of the calculated value (8.5 Å), thereby excluding the possibility of an energy transfer via exchange interaction. On the basis of Dexter's energy-transfer expressions of multipolar interaction[45] and Reisfeld's approximation,[47] the following relation can be obtained:

$$\frac{\eta_{S0}}{\eta_S} \propto x^{n/3} \tag{8.6}$$

where η_{S0} and η_S are the luminescence quantum efficiencies of Bi^{3+} in the absence and presence of Er^{3+}, respectively, x is the total concentration of the Bi^{3+} and Er^{3+} ions, and n = 6, 8, and 10

correspond to dipole-dipole, dipole-quadrupole, and quadrupole-quadrupole interactions, respectively. In order to assess the type of multipolar interaction, the value of η_{S0}/η_S can be approximately replaced by the ratio of related luminescence intensities I_{S0}/I_S, so the equation becomes

$$\frac{I_{S0}}{I_S} \propto x^{n/3}. \tag{8.7}$$

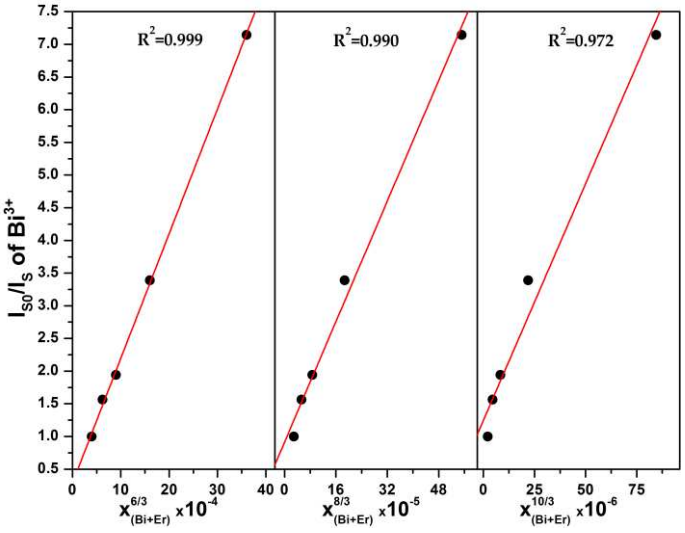

Figure 8.13 Dependence of I_{S0}/I_S on $x^{n/3}$ for n = 6, 8, and 10.

The good linear relationship in the I_{S0}/I_S-$x^{n/3}$ plot for n = 6 (Figure 8.13) proves the dipole-dipole interaction should be mainly responsible for the energy transfer from Bi^{3+} to Er^{3+} ions in the yttrium oxide.

8.6 Conclusions

In this Chapter, we reported about the synthesis of Bi- and Er-codoped Y_2O_3 monocrystalline nanoparticles by a Pechini-type process. A nanoparticle average size of about 40 nm was estimated from both the X-ray powder diffraction and TEM analysis. The optical properties of the samples were evaluated both in the visible and IR regions, showing the different optical behavior of the Bi^{3+} ion in the two sites of Y_2O_3 and the efficient energy transfer from the Bi^{3+} in the C_2 site to the Er^{3+} ions with an enhancement of the 1.54 μm transition of Er^{3+}.

The intriguing luminescence properties of the material highlight the Bi-Er-codoped Y_2O_3 system as a possible useful system for Er-based optical and photonic devices. The dipole-dipole resonant type interaction is the most probable mechanism for the Bi^{3+}-Er^{3+} energy transfer in Y_2O_3. Moreover, the new probabilistic approach based on the discretization of the theory of

Chandrasekhar for the distribution of the nearest neighbor in a random distribution of particles suggests a critical distance R_C of about 8.5 Å.

Materials and Methods

Experimental Details. The morphology of the particles was investigated by means of X-ray diffraction (XRD) and transmission electron microscopy (TEM).

The XRD patterns were collected at RT with a step size of 0.05° in the preset-time mode (10 s); in order to improve the signal-to-noise ratio, at least three runs were measured. A Philips diffractometer with a PW 1319 goniometer with Bragg-Brentano geometry, equipped with a focusing graphite monochromator on the diffracted beam and with a proportional counter with an electronic pulse height discrimination, was used.

TEM images were taken at 300 kV with a JEOL3010 instrument with an ultrahigh resolution (UHR) pole-piece (0.17 nm point resolution), equipped with a Gatan slow scan CCD camera (model 794). The powders were dispersed in isopropyl alcohol by means of sonication and then deposited onto a holey carbon film-coated copper grid. EDS analysis was carried out by a Carl Zeiss Sigma VP FE-SEM equipped with a Bruker Quantax 200 microanalysis detector.

Photoluminescence properties have been measured with a FluoroLog 3-21 system (Horiba JobinYvon) equipped with a 450 W xenon arc lamp as excitation source and selecting the excitation wavelength with a double Czerny-Turner monochromator. The detection system was composed of an iHR300 single grating monochromator alternatively coupled to a R928 or a liquid N_2-cooled R5509-73 Hamamatsu PMTs operating in the VIS and in the IR regions, respectively. All photoluminescence emission (PL) and excitation (PLE) spectra were recorded at room temperature using the same setup parameters.

For the time-resolved PL analysis, the sample excitation was provided by a homemade custom system including a Q-switched Nd:YAG laser coupled to a series of NLO crystals for the generation of the third harmonic at 355 nm. PL emission was collected to a Cinel 25 cm monochromator, converted into a current signal by a gated R928 Hamamatsu PMT, and sampled by a Tektronix TDS3032 oscilloscope.

References

1. A.J. Kenyon. Recent Developments in Rare-Earth Doped Materials for Optoelectronics. *Prog. Quantum Electron.* **2002**, 26, 225-284.
2. F. Auzel. Upconversion and Anti-Stokes Processes with f and d Ions in Solids. *Chem. Rev.* **2004**, 104, 139-173.
3. T. Jüstel, H. Nikol and C. Ronda. New Developments in the Field of Luminescent Materials for Lighting and Displays. *Angew. Chem., Int. Ed.* **1998**, 37, 3084-3103.
4. S. Gai, C. Li, P. Yang, and J. Lin. Recent Progress in Rare Earth Micro/Nanocrystals: Soft Chemical Synthesis, Luminescent Properties, and Biomedical Applications. *Chem. Rev.* **2014**, 114, 2343-2389.

5. J.-C. G. Bünzli. Lanthanide Luminescence for Biomedical Analyses and Imaging. *Chem. Rev.* **2010**, 110, 2729-2755.

6. B.R. Judd. Optical Absorption Intensities of Rare-Earth Ions. *Phys. Rev.* **1962**, 127, 750-761.

7. S.H. Liu. In *Handbook on the Physics and Chemistry of Rare Earth*; K.A. Gschneidner and L. Eyring, Eds.; North/Holland Publishing Company: Amsterdam, 1978; Vol. 1, pp 233-335.

8. P.C. Becker, N.A. Olsson, and J.R. Simpson. In *Erbium-Doped Fiber Amplifiers - Fundamentals and Technology*; Academic Press: San Diego, 1999; pp 131-200.

9. M. Ferrari and G.C. Righini. In *Physics and Chemistry of Rare-Earth Ions Doped Glasses*; N.S. Hussain and J.D. Santos, Eds.; Trans Tech Publication Inc.: Stafa-Zurich, 2008; pp 69−118.

10. E. Cattaruzza, G. Battaglin, F. Visentin and E. Trave. Er-Doped SiO_2 Films by rf Magnetron Co-Sputtering. *J. Non-Cryst. Solids* **2009**, 355, 1128-1131.

11. E. Cattaruzza, M. Back, G. Battaglin, P. Riello and E. Trave. Er-Doped Alumina Crystalline Films Deposited by Radiofrequency Magnetron Co-Sputtering. *Opt. Mater.* **2011**, 33, 1135-1138.

12. A. Polman. Erbium-Implanted Thin Film Photonic Materials. *J. Appl. Phys.* **1997**, 82, 1-39.

13. C. Strohhöfer, and A. Polman. Absorption and Emission Spectroscopy in Er^{3+}-Yb^{3+} Doped Aluminum Oxide Waveguides. *Opt. Mater.* **2003**, 21, 705-712.

14. J. Zhou, Y. Teng, X. Liu, S. Ye, Z Ma and J. Qiu. Broadband Spectral Modification from Visible Light to Near-Infrared Radiation Using Ce^{3+}-Er^{3+} Codoped Yttrium Aluminium Garnet. *Phys. Chem. Chem. Phys.* **2010**, 12, 13759-13762.

15. J. Zhou, J. Teng, X. Liu, S. Ye, X. Xu, Z Ma and J. Qiu. Intense Infrared Emission of Er^{3+} in $Ca_8Mg(SiO_4)_4Cl_2$ Phosphor from Energy Transfer of Eu^{2+} by Broadband Down-Conversion. *Opt. Express* **2010**, 18, 21663-21668.

16. M. Fujii, M. Yoshida, Y Kanzawa, S. Hayashi and K. Yamamoto. 1.54 μm Photoluminescence of Er^{3+} Doped into SiO_2 Films Containing Si Nanocrystals: Evidence for Energy Transfer from Si Nanocrystals to Er^{3+}. *Appl. Phys. Lett.* **1997**, 71, 1198-1200.

17. G. Franzò, V. Vinciguerra, and F. Priolo. The Excitation Mechanism of Rare-Earth Ions in Silicon Nanocrystals. *Appl. Phys. A: Mater. Sci. Process.* **1999**, 69, 3-12.

18. C. Strohhöfer, and A. Polman. Silver as a Sensitizer for Erbium. *Appl. Phys. Lett.* **2002**, 81, 1414-1416.

19. E. Trave, G. Mattei, P. Mazzoldi, G. Pellegrini, C. Scian, C. Maurizio and G. Battaglin. Sub-Nanometric Metallic Au Clusters As Efficient Er^{3+} Sensitizers in Silica. *Appl. Phys. Lett.* **2006**, 89, 151121-151123.

20. E. Cattaruzza, G. Battaglin, F. Visentin, E. Trave, G. Aquilanti and G. Mariotto. Enhanced Photoluminescence at λ=1.54 μm in Cu-Doped Er:SiO_2 System. *J. Phys. Chem. C* **2012**, 116, 21001-21011.

21. F. Enrichi, G. Mattei, C. Sada, E. Trave, D. Pacifici, G. Franzò, F. Priolo, F. Iacona, M. Prassas, M. Falconieri and E. Borsella. Evidence of Energy Transfer in an Aluminosilicate Glass Codoped with Si Nanoaggregates and Er^{3+} Ions. *J. Appl. Phys.* **2004**, 96 3925-3932.

22. A. Martucci, M. de Nuntis, A. Ribaudo, M. Guglielmi, S. Padovani, F. Enrichi, G. Mattei, P. Mazzoldi, C. Sada, E. Trave et al. Silver-Sensitized Erbium-Doped Ion-Exchanged Sol-Gel Waveguides. *Appl. Phys. A: Mater. Sci. Process.* **2005**, 80, 557-563.

23. C. Maurizio, E. Trave, G. Perotto, V. Bello, D. Pasqualini, P. Mazzoldi, G. Battaglin, T. Cesca, C. Scian and G. Mattei. Enhancement of the Er^{3+} Luminescence in Er-Doped Silica by Few-Atom Metal Aggregates. *Phys. Rev. B* **2011**, 83, 195430.

24. E. Trave, E. Cattaruzza and P. Riello. Er and Cu Codoped SiO_2 Films Obtained by Sputtering Deposition: Enhancement of the Rare Earth Emission at 1.54 μm Mediated by Metal Sensitizers. *Opt. Mater.* **2013**, 35, 2018-2022.

25. M. Mehring. From Molecules to Bismuth Oxide-Based Materials: Potential Homo- and Heterometallic Precursors and Model Compounds. *Coord. Chem. Rev.* **2007**, 251, 974-1006.

26. A. Kubacka, M. Fernández-Garciá and G. Colón. Advanced Nanoarchitectures for Solar Photocatalytic Applications. *Chem. Rev.* **2012**, 112, 1555-1614.

27. R.S. Devan, R.A. Patil, J.-H. Lin and Y.-R. Ma. One-Dimensional Metal-Oxide Nanostructures: Recent Developments in Synthesis, Characterization, and Applications. *Adv. Funct. Mater.* **2012**, 22, 3326-3370.

28. J. Schamps, J.P. Flament, F. Real and I. Noiret. Ab Initio Simulation of Photoluminescence: Bi^{3+} in Y_2O_3 (S_6 Site). *Opt. Mater.* **2003**, 24, 221-230.

29. F. Réal, B. Ordejón, V. Vallet, J.-P. Flament and J. Schamps. Improvement of the Ab Initio Embedded Cluster Method for Luminescence Properties of Doped Materials by Taking into Account Impurity Induced Distortions: The Example of Y_2O_3:Bi^{3+}. *J. Chem. Phys.* **2009**, 131, 194501-194516.

30. R.K. Datta. Luminescent Behavior of Bismuth in Rare-Earth Oxides. *J. Electrochem. Soc.* **1967**, 114, 1137-1142.

31. A.M. van de Craats and G. Blasse. The Quenching of Bismuth(III) Luminescence in Yttrium Oxide (Y_2O_3). *Chem. Phys. Lett.* **1995**, 243, 559-563.

32. A.M. van de Craats and G. Blasse. The Influence of d^{10} Ions on the Luminescence of Bismuth(III) in Solids. *Mater. Res. Bull.* **1996**, 31, 381-387.

33. L.G. Jacobsohn, M.W. Blair, S.C. Tornga, L.O. Brown, B.L. Bennett and R.E. Muenchausen. Y_2O_3:Bi Nanophosphor: Solution Combustion Synthesis, Structure, and Luminescence. *J. Appl. Phys.* **2008**, 104, 124303-124307.

34. L.G. Jacobsohn, B.C. Tappan, S.C. Tornga, M.W. Blair, E.P. Luther, B.A. Mason, B.L. Bennett and R.E. Muenchausen. The Effect of Hydrostatic Pressure on the Combustion Synthesis of Y_2O_3:Bi Nanophosphor. *Opt. Mater.* **2010**, 32, 652-656.

35. H. Fukada, K. Ueda, J. Ishino, T. Miyata and T. Minami. Blue PL and EL Emissions from Bi-Activated Binary Oxide Thin-Film Phosphors. *Thin Solid Films* **2010**, 518, 3067-3070.

36. M. Yang, Y. Sui, S. Lu, M. Wang, X. Wang, M. Wu, Y. Wang, T. Lu and W. Liu. Effect of Bi^{3+} Doping on the Quenching Concentration of $^2H_{11/2}$/$^4S_{3/2}$ Level of Er^{3+}. *J. Alloys Compd.* **2011**, 509, 8590-8594.

37. M. Yang, Y. Sui, M. Wang, X. Wang, Y. Wang, S. Lu, Z. Zhang, Z. Liu, T. Lu and W. Liu. Effects of Bi^{3+} Doping on the Optical Properties of Er^{3+}:Y_2O_3. *J. Alloys Compd.* **2011**, 509, 827-830.

38. M. Back, A. Massari, M. Boffelli, F. Gonella, P. Riello, D. Cristofori, R. Riccò and F. Enrichi. Optical Investigation of Tb^{3+}-Doped Y_2O_3 Nanocrystals Prepared by Pechini-Type Sol-Gel Process. *J. Nanopart. Res.* **2012**, 14, 792.

39. M. Back, M. Boffelli, A. Massari, R. Marin, F. Enrichi and P. Riello. Energy Transfer Between Tb^{3+} and Eu^{3+} in Co-Doped Y_2O_3 Nanocrystals Prepared by Pechini Method. *J. Nanopart. Res.* **2013**, 15, 1753.

40. R. Marin, M. Back, N. Mazzucco, F. Enrichi, R. Frattini, A. Benedetti and P. Riello. Unexpected Optical Activity of Cerium in Y_2O_3:Ce^{3+}, Yb^{3+}, Er^{3+} Up and Down-Conversion System. *Dalton Trans.* **2013**, 42, 16837-16845.

41. G. Boulon. Processus de Photoluminescence dans les Oxydes et les Orthovanadates de Terres Rares Polycristallins Activés par l'Ion Bi^{3+}. *J. Phys.* (Paris) **1971**, 32, 333-347.

42. P.I. Paulose, G. Jose, V. Thomas, N.V. Unnikrishnan and M.K.R. Warrier. Sensitized Fluorescence of Ce^{3+}/Mn^{2+} System in Phosphate Glass. *J. Phys. Chem. Solids* **2003**, 64, 841-846.

43. S. Chandrasekhar. Stochastic Problems in Physics and Astronomy. *Rev. Mod. Phys.* **1943**, 15, 1-89.

44. T.P. Martin. Shells of Atoms. *Phys. Rep.* **1996**, 273, 199-241.

45. D.L. Dexter. A Theory of Sensitized Luminescence in Solids. *J. Chem. Phys.* **1953**, 21, 836-850.

46. Y. Huang, H. You, G. Jia, Y. Song, Y. Zheng, M. Yang, K. Liu and N. Guo. Hydrothermal Synthesis, Cubic Structure, and Luminescence Properties of $BaYF_5$:RE (RE = Eu, Ce, Tb) Nanocrystals. *J. Phys. Chem. C* **2010**, 114, 18051-18058 (2010).

47. R. Reisfeld. In *Rare Earths, Structure and Bonding*; Springer: Berlin, 1973; Vol. 13, pp 53-98.

CHAPTER 9

Summary & Outlook

Ever new solutions required by the rapidly growing demand in the lighting industry, have prompted the ongoing research on new efficient phosphors. From the technological point of view, luminescent materials are used not only for standard lightning but also in new frontiers of photonics such as biomedical applications, energy harvesting systems and anti-counterfeiting. Hence, the design of new luminescent materials with suitable and ever improved performances, able to meet the requirements of the next-generation devices, is a challenge.

In this view, in this thesis we have proposed new bismuth-based luminescent materials, demonstrating outstanding properties and proposing new strategies for the design of next-generation classes of light emitting systems for a wide range of technological applications. New insights into the synthesis and the optical investigation of these materials are provided, discussing their applicability in different fields such as upconverting nanoparticles for bioimaging, ratiometric optical thermometer for biological environments, persistent luminescence in the visible and near-infrared regions and broadband Er^{3+} luminescence sensitization at the telecommunication wavelength via energy transfer. In addition, a combined experimental and theoretical approach was considered to ensure the reliability of the calculations presented, and some preliminary analyses aimed to assess the applicative potentialities of the synthesized materials were provided.

Chapters 4 and 5 deal with the development of two new classes of UCNPs. If in Chapter 4 we have proposed a new strategy to control the UC emission output by means of the bandgap engineering of Bi_2O_3 NPs, evidencing very promising UCQY, in Chapter 5 we have accounted for the occurrence of a peculiar Bi_2SiO_5@SiO_2 core-shell self-assembly process in bismuth impregnated MSNs, providing a tentative mechanism of formation on the basis of the resulting temperature and pore loading dependence of the investigated material properties. We have demonstrated the possibility to tune the UC luminescence output by finely controlling the bandgap of the Bi_2O_3 NPs in a wide range of energies. This new strategy of emission chromaticity tuning

through the bandgap engineering may be used to design smart luminescent nanosystems able to concentrate all the absorbed energy in a single emitting excited state, through controlled energy transfer processes. The stabilization of the different polymorphs of bismuth oxide, with crystal structure suitable to optimize the critical distances among the doping ions, can be an effective method to enhance the UCQY by increasing the energy transfer rate. Moreover, the development of new synthetic procedures able to stabilize monodisperse single phase bismuth oxide based NCs of controlled size is a challenge.

In perspective, we expect that the reported approach can be applied to a wide class of bismuth oxide based compounds and we believe that the intrinsic suitable nature of bismuth for multimodal probe (*e.g.* CT, PAT and SPECT) is an excellent starting point for the design of the next-generation multifunctional nanoplatforms.

From the technological point of view, it should be pointed out that nanocrystals allow to easily form transparent luminescent materials once dispersed in a plastic or liquid medium. In this view, if from one hand, the lanthanide-doped Bi_2SiO_5@SiO_2 UCNPs developed in Chapter 5, are characterized by suitable features, like low toxicity and easy surface functionalization, for the use as probe in biological environments, from the other hand, they give the possibility to be incorporated also into glasses with prospective applications, for example, in the anti-counterfeiting technology. The remarkable self-assembly process of the core-shell nanosystems is characterized by the formation of a glassy shell. This self-sealing process on the MSN outer shell is driven by bismuth-induced silica low melting point effect and can be used as a new strategy to incorporate different materials such as UV filters, magnetic nanoparticles, pigments or other luminescent nanocrystals, with the double aim to (i) avoid the contact of the active phase with the environment, drastically limiting undesired reactions (*e.g.* in the case of toxic or photocatalytic materials) and, at the same time, to (ii) prevent the degradation of the active materials in the core. A remarkable example consists in the expected suppression of the luminescent quenching due to the aging induced by humidity absorption into silica sol-gel coated luminescent materials. However, further investigations are needed in the future to confirm this statement.

Another interesting area of application for photonics materials is the thermal sensing. In Chapter 6 we have introduced the $Bi_2Ga_4O_9:Cr^{3+}$ system, demonstrating its unique characteristics as single-doped material for ratiometric optical thermal sensing in the NIR spectral region. The crystal field experienced by Cr^{3+} was assessed in detail by means of Tanabe-Sugano diagram, configurational coordinate diagram design and the comparison with energy level calculations derived from Cr-O bond lengths in the host. In view of future developments, the great agreement between the models and the experimental results opens the way to a real luminescence output design by careful choice of the host. In this regards, further analyses are needed to confirm the fundamental role of the lone pair of electrons, characteristic of Bi^{3+} ion electronic configuration, in the distortion of the typical Ga^{3+} and Al^{3+} ion sites, where Cr^{3+} is usually substituted. In fact, as in the case of $Bi_2Ga_4O_9$, the distortions induced by the Bi^{3+} lone pair can lead to unusual and unique optical properties, including peculiar luminescence activity as determined from the resulting overall energy level structure of the material.

An active research area in the field of thermal sensing is the development of ratiometric luminescent nanothermometry for the measurements of the intracellular temperature. In this optic, the material developed in Chapter 6 shows a unique set of characteristics, such as the single-doping nature, low toxicity, dual emission in the near-infrared region (matching the first biological window), good sensitivity and reproducibility, which are all suitable properties for a temperature sensor operating in the biological environment. Hence, the future research activity will consist mainly in the development of a protocol of synthesis for nanosized $Bi_2Ga_4O_9:Cr^{3+}$, and in tailoring the host crystal field through controlled incorporation of codoping species, to improve the luminescent response and then the critical thermometer parameters.

As briefly mentioned in Chapter 3, Bi-activated phosphors are recognized as promising luminescent materials due to a remarkable emission activity in the whole UV-visible-NIR range. In Chapters 7 and 8, we have reported two studies regarding the use of Bi^{3+} and Bi^{2+} ions as sensitizers and active centers. In particular, in Chapter 7, a new bismuth-doped persistent luminescent material is described, consisting in a perovskite $CaSnO_3$:Bi system in which both Bi^{3+} and Bi^{2+} are simultaneously stabilized. By means of VRBE diagram design, we have discussed the MMCT nature of the main blue emission band characterizing the material optical response, in comparison with the luminescent features of orthorhombic perovskite $CaBO_3$:Bi compounds class (B=Ti, Sn, Zr). The analysis suggested a trend for the relative energy position of the MMCT state and the Bi^{3+} first excited state with respect to the shortest distances between the B^{4+} site and the cation site available for Bi^{3+} (Ca^{2+} site). This trend should be confirmed by synthesizing new bismuth-activated compounds. In addition, the material showed a persistent luminescence behaviour in which the MMCT state seems to be the luminescent center. However, the transient nature of such a state would be in contrast to this possibility, suggesting a new mechanism that could be clarified by means of dedicated analyses (*e.g.* XPS and EXAFS). For this system, it must be underlined both the fact that the stabilization of Bi^{2+} ion is achieved in air, without the need of reductive atmosphere, and that the emission band falls at 800 nm, then in the first biological window. Moreover, as demonstrated in Section 7.7, the introduction of chromium as doping ion promotes the enhancement of the Bi^{2+} emission at 800 nm. In perspective, the optimization of the system will be attempted by further incorporation of doping species suitable to optimize the trap depth of the material, for example by substituting Ca^{2+} with Sr^{2+} ions; moreover further investigations will be considered to fully elucidate the role of Cr. The possibility to develop new systems acting on the starting material composition, is suggested by the notable advantage of bandgap tuning by compositional engineering via simply adjusting the cation species, exhibited by $A^{2+}B^{4+}O_3$ perovskites.

In Chapter 8, the well known potentialities of Bi^{3+} ion as sensitizer for lanthanide ions are proved to be effective also for the enhancement of the typical Er^{3+} emissions at the telecom wavelengths by promoting the broadening of the lanthanide absorption window. Even if the energy transfer processes were massively investigated by considering a plenty of combinations between donor-acceptor pairs and hosts, for the best of our knowledge this is the first time that Bi^{3+} ion is demonstrated to effectively act as sensitizer for the 1.54 μm emission of Er^{3+} in Y_2O_3. A preferential crystalline site hosting the Bi^{3+} ions mainly involved in the energy transfer process was assessed by site-selective analyses. Moreover, a simple model for the definition of the critical

donor-acceptor distance characterizing the energy transfer process was proposed, in virtue of the positions occupied by the two interacting ions into the crystal lattice.

The new insights and the relevant possibilities discussed in this thesis, have also raised questions to be answered, opening the door to future investigations. The host bandgap mediated UC PL output tuning, together with the refractive index influence on the radiative transition probability, will be deeply analyzed (*e.g.* by photoconductivity measurements) to spread light on the possibility to realize a new class of single-band emitting UC nanosystems. The role of the Bi^{3+} lone pair of electrons in crystal site distortion will be addressed, with particular care to the resulting effect on the energy level configuration of transition metal ions hosted in Bi-based oxide matrices. Moreover, the optical behaviour of the different bismuth ions (Bi^{+}, Bi^{2+}, Bi^{3+}) shows intriguing aspects still under debate, that require a challenging insight into the physicochemical properties of Bi-activated phosphors.

A critical step in the development of novel luminescent materials is to achieve a design route on the basis of modelling methods and empirical rules that allow to overcome the try and error method, thus saving resources. In this regard, a clear example is represented by the use of the vacuum referred binding energy diagram, discussed in Sections 2.6, 4.3.4 and 7.6, that leads to the selection of the suitable doping ions acting as electron or hole trap in the design of persistent luminescent materials. Another outstanding example is the use of the energy level diagram of Cr^{3+} and Mn^{4+} as a function of the Cr/Mn-O bond length, reported by Ogasawara (discussed in Section 6.8), to predict the relative energy level position of these luminescent ions on the basis of host structural parameters. In this scenario, concerning the luminescence of bismuth ions, further experimental and theoretical (first-principle calculations) investigations are needed to provide rules of thumbs for establishing guidelines in regard to the prediction of the optical response to external stimuli, and thus for the design of new bismuth-based luminescent materials with advanced properties.

Publications

Tuning the Upconversion Light Emission by Bandgap Engineering in Bismuth Oxide-based Upconverting Nanoparticles
M. Back, E. Trave, N. Mazzucco, P. Riello and A. Benedetti
Submitted

Formation and Controlled Growth of Bismuth Titanate Phases into Mesoporous Silica Nanoparticles: An Efficient Self-Sealing Nanosystem for UV Filtering in Cosmetic Formulation
G. Zaccariello, M. Back, M. Zanello, P. Canton, E. Cattaruzza, P. Riello, A. Alimonti and A. Benedetti
Submitted

Orthorhombic Phase Stabilization and Separation Phase Process in Zirconia Tantalum-doped Powders and Spark Plasma Sintering Systems
G. Sponchia, M. Boffelli, M. Back, W. Zhu, A.D. Rodríguez, G. Pezzotti, G. de Portu, P. Riello, and A. Benedetti
Submitted

Ratiometric Optical Thermometer Based on Dual Near-Infrared Emission in Cr^{3+}-doped Bismuth-based Gallate Host
M. Back, E. Trave, J. Ueda and S. Tanabe
Chem. Mater. **2016**, 28, 8347-8356

Energy Transfer in Color-Tunable Water-Dispersible Tb-Eu codoped CaF_2 Nanocrystals
M. Back, R. Marin, M. Franceschin, N. Sfar Hancha, F. Enrichi, E. Trave and S. Polizzi
J. Mater. Chem. C **2016**, 4, 1906-1913

Development of an Eco-Protocol for Seaweed Chlorophylls Extraction and Possible Applications in Dye Sensitized Solar Cells
S. Armeni Minicante, E. Ambrosi, M. Back, J. Barrichello, E. Cattaruzza, F. Gonella, E. Scantamburlo and E. Trave
J. Phys. D: Appl. Phys. **2016**, 49, 295601

Determining Europium Compositional Fluctuations in Partially Stabilized Zirconia Nanopowders: A Non-Line-Broadening-Based Method
R. Marin, G. Sponchia, M. Back and P. Riello
Acta Cryst. B **2016**, B72, 29-38

Energy Transfer in Bi- and Er-codoped Y_2O_3 Nanocrystals: An Effective System for Rare-Earth Fluorescence Enhancement
M. Back, E. Trave, R. Marin, N. Mazzucco, D. Cristofori and P. Riello
J. Phys. Chem C **2014**, 118, 30071-30078

Unexpected Behaviour of the 1.54 µm Luminescence in Er-doped Silica Films
E. Cattaruzza, M. Back, G. Battaglin and E. Trave
J. Non-Cryst. Solids **2014**, 401, 186-190

Oxygen Hole States in Zirconia Lattices: Quantitative Aspects of Their Cathodoluminescence Emission
M. Boffelli, W. Zhu, M. Back, G. Sponchia, T. Francese, P. Riello, A. Benedetti and G. Pezzotti
J. Phys. Chem. A **2014**, 118, 9828-9836

Patent

Silicati di Bismuto Luminescenti, Sintesi ed Uso degli Stessi
P. Riello and M. Back
Patent UB2015A001870, 2015

List of Presentations

Dual Near-Infrared Emission in Cr^{3+}-doped $Bi_2Ga_4O_9$: A New Candidate for Ratiometric Luminescence Thermometry
M. Back
Phosphor Safari 2016, Hong Kong, November 2016 (oral)

Cr^{3+}-doped $Bi_2Ga_4O_9$ for Ratiometric NIR Luminescent Thermal Sensing
M. Back
CerSJ-GOMD Joint Symposium on Glass Science and Technologies, Kyoto, November 2016 (oral)

Materiali Luminescenti Avanzati: Dalla Progettazione all'Applicazione
M. Back
1st LCCS Workshop, Ca' Foscari University, June 2016 (oral)

Development of Bismuth-based Oxide Materials with Advanced Optical Properties
M. Back
Seminar, Kyoto University, April 2016 (oral, invited)

Bandgap Engineering of Bismuth Oxide-based Nanoparticles: A New Strategy for Upconversion Emission Control
M. Back and E. Trave
LumiMat 2015, Kyoto, December 2015 (poster)

Bismuth Oxide as Host for Rare-Earth Dopants in UCNPs
M. Back, E. Trave and P. Riello
ICOM 2015, Budva, September 2015 (oral)

Bismuth Silicate Nanoparticles: Structural Control and Rare Earth Doping for Upconversion
M. Back, E. Trave, P. Canton and P. Riello
ICOM 2015, Budva, September 2015 (poster)

Exploring and Deepening the Use of Algal Chlorophylls into Dye Sensitized Solar Cells
E. Ambrosi, S. Armeli Minicante, M. Back, J. Barrichello, E. Cattaruzza, F. Gonella, E. Scantamburlo and E. Trave
ICOM 2015, Budva, September 2015 (poster)

Algal Chlorophylls for Dye Sensitized Solar Cells
S. Armeli Minicante, M. Back, J. Barrichello, E. Cattaruzza, F. Gonella and E. Trave
Symposium E of E-MRS, Lille, May 2015 (poster)

Zirconia Tantalum-doped Materials: An Initial Study About New Structure Stabilization
G. Sponchia, M. Back, T. Francese, M. Cillotto, M. Boffelli, W. Zhu, G. Pezzotti, P. Riello and A. Benedetti
NanotechItaly, Venice, November 2014 (poster)

Upconversion Process in Yb^{3+}-RE co-doped Bismuth Oxide Nanoparticles (RE=Er^{3+}, Ho^{3+}, Tm^{3+})
M. Back, R. Marin, N. Mazzucco, F. Enrichi, A. Benedetti, P. Riello and E. Trave
PRE'2014, San Sebastian, May 2014 (poster)

Acknowledgements

Infine la parte più sentita, i ringraziamenti! Questo lavoro non sarebbe stato possibile senza la guida, il confronto, la pazienza, il sostegno e l'amicizia di tutte le persone che ho avuto la fortuna di incontrare e con cui ho collaborato in questi tre anni. Riassumere in poche righe la gratitudine verso tutti voi è un compito difficile ma cercherò di fare del mio meglio.

Il mio più sentito ringraziamento va innanzitutto al Dr. Enrico Trave per la guida, il sostegno, la pazienza, le sentite discussioni scientifiche nonché per la disponibilità dimostrata in tutti questi anni. Lo ringrazio per avermi dato l'opportunità di confrontarmi con diverse realtà scientifiche supportando le trasferte a congressi e periodi all'estero. In particolare, lo ringrazio per avermi trasmesso la passione e la dedizione per la ricerca. In queste poche righe vorrei anche ricordare che questa tesi è stata testimone della gestazione e nascita dei due nani, Arturo e Gregorio, e vorrei cogliere l'occasione per ringraziare Susi per aver sopportato l'extra lavoro di Enrico a causa mia.

Un doveroso ringraziamento va al Prof. Pietro Riello e al Prof. Alvise Benedetti per avermi consentito di sviluppare parte della mia tesi presso i loro laboratori, ma soprattutto per la disponibilità e i loro consigli. Li ringrazio per le costruttive discussioni e il costante confronto scientifico e umano.

Un grazie sentito ai Prof. Francesco Gonella e Elti Cattaruzza, non solo per il costante supporto, le discussioni e il contributo scientifico a questa tesi, ma anche per le stimolanti discussioni su libri, musica e quant'altro. In generale grazie a tutti i compagni di Balcania, questo non si dimentica! Un grazie particolare va a Paolo Calvelli per il supporto in laboratorio durante le misure di luminescenza; al Prof. Alberto Quaranta per le misure di riflettanza; al Dr. Francesco Enrichi per la disponibilità delle attrezzature e per le analisi di luminescenza; alla Prof.ssa Patrizia Canton e a Davide Cristofori per le misure TEM; a Tiziano Finotto per le infinite analisi ai raggi-X (grande Tizi!); a Martina Marchiori per le analisi di fisisorbimento; al gruppo della Prof.ssa Loretta Storaro per le analisi di riflettanza; al Dr. Andrea Lausi, Dr. Jasper Rikkert Plaiseier e Dr. Mahmoud Abdellatief per il supporto alla linea MCX di Sincrotrone Elettra; al Dr. Lucio Ronchin per le misure di TG e DSC; un ringraziamento speciale al Dr. Jonas Joos e al Prof. Philippe Smet per le misure di efficienza quantica e le stimolanti discussioni.

Un ringraziamento sentito al Prof. Setsuhisa Tanabe per avermi concesso l'opportunità di lavorare presso il suo laboratorio e per avermi introdotto al mondo della spettroscopia. Lo vorrei ringraziare soprattutto per avermi trasmesso il fondamento su cui si basa la ricerca alla Kyoto University "La ricerca è libertà. Senza libertà non c'è ricerca.". Spero di avere la possibilità un giorno di poter utilizzare queste parole allo stesso modo. Un ringraziamento altrettanto sentito al Dr. Jumpei Ueda (presto Prof!) per aver condiviso le nottate di esperimenti, i dubbi scientifici, per la sua amicizia e avermi fatto sperimentare l'ospitalità giapponese. Come non ringraziare tutti i membri del team (il Tanabe's lab!) per l'aiuto in laboratorio e nella vita giapponese di tutti i giorni. Un grazie a Xu-san (magici pranzi con l'hamburger più buono del Giappone), ad Asami-san/John (un amico oltre che collega), Hoshino-san (il miglior sushi di mezzanotte di sempre), Maki-san (talkative Maki), Kobayashi-san (Federer number one, no way!), Yasuda-san (jazz, sempre e solo jazz!), Miyano-san (una è più che sufficiente…) e Kubo-san. Ringrazio inoltre il Prof. Peter A. Tanner per il tempo speso assieme a Kyoto durante il quale ho potuto ammirarne le competenze e la passione per la ricerca (la teoria dei gruppi salverà il mondo), nonché per la sua amicizia (Hong-Kong coffee per tutti!). Un grazie di cuore per il tempo e la pazienza spesi nel spiegarmi e rispiegarmi l'utilizzo della teoria dei gruppi in spettroscopia. Infine un ringraziamento a chi per certi versi (e forse a sua insaputa) ha reso possibile il mio periodo in Giappone, un grazie vivissimo al Prof. Bruno Viana.

Sono molti coloro che hanno allietato le lunghe giornate di via Torino con pause caffè, aperitivi, discussioni scientifiche e non. Un grazie infinito agli X-man Dr. Gabriele Sponchia e Dr. Riccardo Ottini, a Nicolò Mazzucco, al Dr. Emmanuele Ambrosi, a Enrico Pontoglio, al Dr. Marco Mardegan (evviva i beverdì), a Riccardo Marin, a Giulia Ricci, a Martina Zuena, alla Dr.ssa Eleonora Balliana e ad Anna Del Tedesco.

Questi tre anni non sarebbero stati gli stessi senza gli amici di sempre, pronti a festeggiare e rendere leggera ogni evenienza, bella o brutta che fosse. Grazie veramente fioi!

Un grazie speciale va ai miei genitori e alle sorelle per avermi sopportato, aiutato e consigliato in tutti questi anni. Questo lavoro non sarebbe mai stato possibile senza il vostro supporto.

Infine il mio più sentito ringraziamento va a chi ha condiviso con me gioie e dolori di un percorso meraviglioso in questi tre anni (ed è solo l'inizio!), chi ha sopportato con pazienza periodi difficili di lontananza e ha saputo darmi la forza nei momenti di difficoltà, un grazie infinito a te Gloria!

Estratto per riassunto della tesi di dottorato

Studente: Michele Back matricola: 812891

Dottorato: Scienze Chimiche

Ciclo: XXIX

Titolo della tesi: Bismuth-based advanced luminescent (nano)materials: from design to application.

Abstract:

Negli ultimi anni, le peculiari attività luminescenti esibite dagli ioni di Bi e le proprietà ottiche degli host a base di bismuto, assieme a interessati proprietà tecnologiche quali una bassa tossicità e costi contenuti, hanno reso i materiali luminescenti a base di bismuto tra i più promettenti per la progettazione di fosfori di nuova generazione. In quest'ottica, questa tesi è focalizzata sulla sintesi e caratterizzazione di nuovi materiali ossidi a base di bismuto, proponendo nuove strategie per il controllo della luce emessa per mezzo di un'accurata selezione degli ioni dopanti nonché la progettazione della struttura a bande dei composti host. Pertanto, la principale attività di ricerca è stata rivolta alla caratterizzazione ottica e, in particolare, alla determinazione e modellizzazione dei meccanismi di luminescenza caratterizzanti i sistemi studiati (processi di energy transfer, upconversion e luminescenza persistente). Allo scopo di descrivere in modo affidabile i processi ottici coinvolti, è stata considerato un duplice approccio sperimentale e teorico. Inoltre, al fine di aumentare l'efficienza e il controllo della risposta di emissione, la ricerca è stata focalizzata sull'ottimizzazione delle procedure di sintesi e il successivo trattamento del materiale finalizzato alla stabilizzazione strutturale più adeguata.

Bismuth-based luminescent materials have been recognized as promising candidates for the design of next-generation phosphors, in virtue of the peculiar emission activity exhibited by Bi ions and the optical characteristics of Bi based hosts, together with technologically appealing properties like low toxicity and low costs. In this view, this thesis is focused on the synthesis and the characterization of novel bismuth-based oxide materials, proposing new strategies of control of the light emission through careful dopant selection and host band structure tailor. Therefore, the main research activity has been devoted on the optical characterization and, in particular, on the determination and modeling of the luminescence mechanisms characterizing the studied systems (energy transfer, upconversion and persistent luminescence processes). With the aim to reliably describe the optical processes involved, a combined experimental and theoretical approach was considered. Moreover, in order to increase the efficiency and the manipulation of the emission response, the research has also focused on the optimization of the synthesis procedures and subsequent material processing for suitable structural modification.

Firma dello studente